THE MAGELLANIC – MILKY WAY MERGER: REVEALING DEFORMING DARK MATTER HALOES WITH STELLAR STREAMS

SOPHIA LILLEENGEN

Thesis submitted to the University of Surrey
for the degree of Doctor of Philosophy

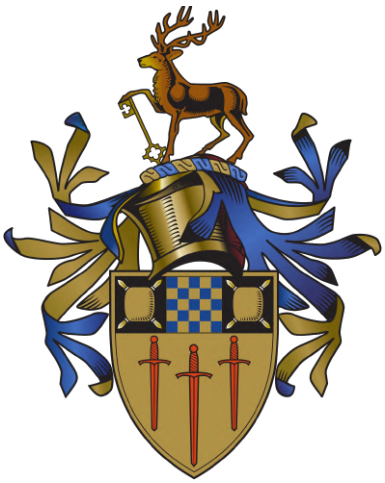

Astrophysics PhD

Supervisors:
Dr Denis Erkal
Prof. Justin Read

July 2023

Für Katja

Immer an meiner Seite

ABSTRACT

The nature of dark matter is one of the biggest open questions in modern-day astrophysics. Recent studies have shown that the dark matter halo of the Milky Way is deforming due to the infalling Large Magellanic Cloud (LMC). These two haloes serve as a dark matter 'collider'. This dark matter 'collider' provides a unique testbed for the nature of dark matter.

To make use of this opportunity, we need detectors in this 'collider'. Some of the most sensitive tracers to the gravitational potential of the Galaxy are stellar streams. Streams are disrupted globular clusters and dwarf galaxies (DGs), forming long, filament-like structures in the halo. In this thesis, we explore whether stellar streams are affected by the deforming Milky Way and LMC, which streams are particularly informative on these deformations, and how omitting these deformations biases stream fits.

First, we evolve a DG stream in a time-dependent Milky Way–LMC interaction described by basis function expansions (BFEs). We find that the stream is significantly perturbed by the deformations, predominantly by the Milky Way dipole. Then, we develop an information theory approach to find the most informative streams on the time-dependent Milky Way dipole. These streams are long and wide, with a large apocentre. The constraints for the perturbation are ~ 1 magnitude worse than for halo parameters. Then, we look into the bias of stream fits by fitting a stream evolved in the Milky Way–LMC simulation with current state-of-the-art, rigid techniques. We find an underestimated Milky Way mass, an overestimated LMC mass, and stronger flattening in the fits.

Finally, I will end with an overview of future directions for this field. Our results reveal the need for a time-dependent Milky Way model. To fit the Milky Way streams with these time-dependent models, we need to utilise the functionality of BFEs. This will enable us to probe how dark matter haloes deform and test different dark matter theories.

DECLARATION

This thesis and the work to which it refers are the results of my own efforts. Any ideas, data, images or text resulting from the work of others (whether published or unpublished) are fully identified as such within the work and attributed to their originator in the text, bibliography or in footnotes. This thesis has not been submitted in whole or in part for any other academic degree or professional qualification. I agree that the University has the right to submit my work to the plagiarism detection service TurnitinUK for originality checks. Whether or not drafts have been so assessed, the University reserves the right to require an electronic version of the final document (as submitted) for assessment as above.[1]

Work shown in Chapter 3 and Appendix A is published in Monthly Notices of the Royal Astronomical Society, Volume 518, Issue 1, January 2023, Pages 774–790 (Lilleengen et al., 2023).

Work shown in Chapter 4 and Appendix B is being prepared for submission to the Astrophysical Journal as *The Information Content in Stellar Streams in Time-Dependent Potentials*, Lilleengen, Price-Whelan, Bonaca, Erkal, Johnston and Hogg.

Work shown in Chapter 5 is being prepared for submission to Monthly Notices of the Royal Astronomical Society as *Stellar stream fitting methods are biased when ignoring the time dependence of the Milky Way*, Lilleengen, Erkal, et al.

1 This declaration is not in my own words but was downloaded from https://surrey-content.surrey.ac.uk/sites/default/files/2023-04/Handbook%202022-23%20Final%20v3.pdf

ACKNOWLEDGMENTS

First and foremost, I want to thank my advisor Denis Erkal. I thoroughly enjoyed working with you over the past few years. You are a great teacher and mentor. Thank you for always taking time for me and supporting me in science and in life, for always being optimistic and for your words of encouragement when I need them. I look forward to collaborating in the future. Second, I want to thank Mike Petersen. You not only support me enormously with my research, but you are always there for feedback, advice and any help I need. Thank you for being a collaborator, mentor, and friend! Thanks to Adrian Price-Whelan for working with me during my time as a predoc and afterwards. I learned so much from you, about research, coding and life. And thank you for always welcoming me back in NYC.

Thank you to Justin Read and Kathryn Johnston for guiding me in my research and my career. Justin, meeting you in Saas-Fee in early 2019 changed my life; otherwise, I would not have gone to Surrey for my PhD. Kathryn, you gave me the opportunity to come to NYC, to travel and network while I was there, and you supported me with my postdoc applications. Thank you for your sharing your insights with me!

I want to thank my examiners, Alessia Gualandris and Jason Sanders. Thank you for taking the time to read my thesis and examine me. I am looking forward to the viva, useful discussions of my work, and your feedback.

I will be forever grateful for my previous advisors and mentors, Wilma Trick, Glenn van de Ven, and Paolo Bianchini. You have introduced me to research and have shown me how much fun it is; you took a lot of time out of your schedules to teach me; you believed me, invested in me, and set me up to become a successful researcher.

Thanks to the collaborations I am a member of. To the S^5 collaboration, where we do exciting research on stellar streams. It was great finally meeting in a larger group recently, and I am looking forward to a collaboration meeting soon. To the B-BFE

collaboration, I am very excited to see all the research that will come from this. The collaboration meetings always instil new ideas and progress, and it is fun to be a part of this group.

Thanks to everyone in the Astrophysics group at the University of Surrey. David for becoming friends immediately and for all your technical support; Emily for all the mutual support, encouragement, celebration of achievements and for just being a great friend; Pol for letting me take over your desk and the 'speacial' journal club; Matt and Michele for wisdom, fun parties and a great office vibe; the streams group including Tariq and Madison; and to Noushin, Kate, Arman, Paula, Joanna, Ethan, Stacy and everyone else. I am also grateful to the Doctoral College at the University of Surrey for all their support for PGRs. Particularly, I would like to thank Emma Francis for all her support throughout organising the Doctoral College Conference and for helping me learn more about who I am. Meeting you brightened up my first year, especially when everything suddenly changed.

I was lucky enough to spend a substantial part of my PhD at the CCA in New York. Thanks again to Adrian and Kathryn for giving me the opportunity and for everyone making me feel so at home. The Dynamics group immediately welcomed me and offered great discussions, advice, and feedback. A special thank you to David Hogg for interesting and insightful conversations about information theory. I am so thankful for the friendships from that group, for Sarah, Nico, Jason, Emily, and Danny. I had a great time meeting and connecting with the other predocs, Manami, Alex, Mike, and Brent; you made the time here so much fun. I also want to thank my other astro friends that I made along the way, Chris for all the fun nights out, Nora for being a great role model and an even better collaborator and friend, Sabina for all the fun you bring into my life, Richard for giving me a chance to work with you, Alex for bringing me to Durham, and Sachi for pushing together through the thesis writing.

I also want to thank everyone behind the scenes of a PhD. This includes the admin staff at CCA, particularly Abby, and at Surrey. I want to thank everyone who keeps the offices and facilities running. My research relied heavily on the Eureka cluster at Surrey, the SAO/NASA Astrophysics Data System and the arXiv; I am thankful for everyone who puts in time and resources to keep these going.

Ein besonderer Dank geht an meine Freunde. Jill und Lea, ihr seid in meinem Leben seit ich denken kann. Svenja, für deine Freundschaft seit dem ersten Tag im Gymnasium. Caro und Alina, mit euch ist es immer als wäre keine Zeit vergangen. Julia, danke dass du so eine gute Freundin bist und unsere Freundschaft so sehr pflegst. Andi, danke dass du ein Teil unserer Familie bist! Lina, tusen takk for vennskapet vårt i Manchester. Jeg håper å se deg snart igjen.

Ohne meine Familie wäre ich nicht hier und hätte diese Arbeit nicht geschafft. Oma und Opa, danke euch für alles! Eure Geschichten inspirieren mich, die Welt zu entdecken und zu erleben. Oma, du bist mein größter Cheerleader und die erste, der ich meine guten Neuigkeiten erzähle. Opa, ich vermisse dich. Niko, danke, dass es dich gibt! Ich bin so froh, dass wir uns so gut verstehen, so viel Kontakt haben und immer füreinander da sind. Unsere Reise vor meinem PhD war eins der besten Erlebnisse in meinem Leben und die Erinnerungen haben mir über die letzten Jahre immer wieder Antrieb gegeben. Danke an den Rest meiner Familie, besonders Ute und Knut, Zeja und Milo, und Anneke. I want to thank Kerrie and Phil for welcoming me into their family, and always sending words of encouragement and support!

Lewis, the last four years with you have been incredible. We are a great team and bring out the best in each other. Thank you for being a great partner, and for your endless love and support. Your reassurance and belief in me keep me going. Thank you for letting me explore opportunities and sticking with me even if I move across an ocean. I enjoy every minute I spend with you and miss you every second I am not. I love you!

Mein größter Dank gilt meinen Eltern, Ivo und Sigrun. Diese Arbeit ist nur möglich durch eure Unterstützung. Ihr seid meine Vorbilder, habt mir alle Werte beigebracht und wegen euch bin ich wer ich bin. Dank euch weiß ich dass Familie das wichtigste ist, aber auch Unabhängigkeit und ein erfülltes Leben. Papa, wir verstehen uns ohne Worte und wissen immer was der andere denkt. Sigrun, takk for at du kom inn i livet vårt. Takk for at jeg ble din datter. Ich bin unendlich stolz und dankbar, eure Tochter zu sein.

CONTENTS

LIST OF FIGURES

LIST OF TABLES

ACRONYMS

BFE	basis function expansion
CDM	cold dark matter
CMB	cosmic microwave background
CRLB	Cramér–Rao lower bound
DES	Dark Energy Survey
DG	dwarf galaxy
DM	dark matter
FDM	fuzzy dark matter
GC	globular cluster
GSE	Gaia–Sausage–Enceladus
IC	initial condition
ΛCDM	Λ cold dark matter
LHC	Large Hadron Collider
LMC	Large Magellanic Cloud
LSST	Large Synoptic Survey Telescope
MCMC	Markov Chain Monte Carlo
mLCS	modified Lagrange Cloud Stripping
MOND	modified Newtonian dynamics
mSSA	multichannel singular spectrum analysis
NFW	Navarro–Frenk–White
OC	Orphan–Chenab
pdf	probability density function
S^5	Southern Stellar Stream Spectroscopic Survey
SIDM	self-interacting dark matter
SDSS	Sloan Digital Sky Survey
SMBH	supermassive black hole
SMC	Small Magellanic Cloud
WDM	warm dark matter
WIMP	weakly interacting massive particle

SOFTWARE

Astronomical research is built upon publicly available software often developed by other astronomers. This allows us to focus on research instead of software engineering and immensely improves the possibilities of what we can achieve as a community. In this thesis, I have made use of the following software packages:

- `AGAMA` (Vasiliev, 2019)
- `astropy` (The Astropy Collaboration, 2013, 2018, 2022)
- `corner` (Foreman-Mackey, 2016)
- `emcee` (Foreman-Mackey et al., 2013)
- `EXP` (Petersen et al., 2022a)
- `gala` (Price-Whelan, 2017; Price-Whelan et al., 2022)
- `h5py` (Collette, 2013)
- `imageio` (Klein et al., 2023)
- `IPython` (Pérez & Granger, 2007)
- `Jupyter` (Kluyver et al., 2016)
- `matplotlib` (Hunter, 2007)
- `mpi4py` (Dalcin & Fang, 2021)
- `numpy` (Harris et al., 2020)
- `pandas` McKinney (2010); Reback et al. (2020)
- `pybind11` (Jakob et al., 2017)
- `schwimmbad` (Price-Whelan & Foreman-Mackey, 2017)
- `scipy` (Virtanen et al., 2020)

We have published the simulations presented in Chapters 3 (Lilleengen et al., 2023) and 5 as an easy-to-use `Python` package with tutorials[2]. For the research carried on in Chapter 4, I have contributed to the galactic dynamics package `gala`[3] (Price-Whelan, 2017; Price-Whelan et al., 2022).

2 github.com/sophialilleengen/mwlmc
3 gala.adrian.pw

1

INTRODUCTION

1.1 COSMOLOGY AND STRUCTURE FORMATION

More than 95 per cent of the energy in the Universe is in a form which is unknown to us. In the Λ cold dark matter (ΛCDM) paradigm, our default cosmological model, the Universe is dominated by two invisible ingredients: dark matter (DM) and dark energy (Λ) (Peebles & Ratra, 2003). Dark energy is a negative pressure that is the source of the accelerating expansion of space and makes up ~ 69 per cent of the energy content in the Universe (Planck Collaboration, 2020). Dark matter is the material that forms cosmic structures. It contributes ~ 26 per cent to the energy content in the Universe and makes up ~ 85 per cent of all matter in the Universe. Baryonic matter, i.e. everything that we can observe, such as stars, planets and gas, contributes less than 5 per cent to the total mass-energy density. While the predictions of ΛCDM are successful at explaining the large-scale structure of the Universe and many phenomena on smaller scales, we have not detected a dark matter particle yet, and we have a poor understanding of the dark sector in general. Dark matter continues to be a hypothesis – with strong empirical evidence (e.g. Zavala & Frenk, 2019) – until its discovery.

1.1.1 *History and first evidence of dark matter*

The idea of dark matter came up 90 years ago when Fritz Zwicky applied the virial theorem to the galaxies in the Coma cluster and found that the velocity dispersion of these galaxies is a magnitude larger than expected, concluding with surprise that if these observations were confirmed dark matter is present and more abundant than luminous matter (Zwicky, 1933a). This is often referred to as the first usage of 'dark matter'. Bertone & Hooper (2018) present an extensive overview of the history of dark matter and remark that the expression 'dark matter' (i) was used at that time by as-

tronomers who studied the dynamics of stars in the Galaxy, such as Kapteyn, Oort and Jeans; and (ii) was already used by Zwicky before in a letter discussing the sources of cosmic rays (Zwicky, 1933b). Following that work, Zwicky (1937) extended the analysis of the Coma Cluster again with the virial theorem and inferred a very high mass-to-light ratio. The previous year, Smith (1936) estimated the mass of the Virgo Cluster, finding that the inferred mass-per-galaxy is two magnitudes larger than estimated by Hubble & Humason (1931). These results led to decades of scientific discussions (see Bertone & Hooper, 2018, for an insightful chronicle of dark matter and details of these discussions).

The next big breakthrough in the discovery of dark matter came from the rotation curves of galaxies. The rotation curve of the Andromeda galaxy (M31) has been measured several times in the first half of the 20th century (Bertone & Hooper, 2018). The first rotation curve was measured by Pease (1918) out to 2.5 arcminutes finding an approximately constant angular velocity. Their inferred mass for M31 was in agreement with other mass measurements in the local neighbourhood. Rotation curves only led to a problem with the understanding of galaxies in the 1970s. With the technological improvement of spectrographs, Rubin & Ford (1970) observed the rotation curve of M31 at a higher quality than ever before, out to 110 arcminutes. Over the course of the next few years, the rotation curves of many galaxies were observed in different regimes of the electromagnetic spectrum (radio observations to observe the 21cm hydrogen line and spectrography in the optical to infer velocities from emission, e.g. Roberts, 1966; Rubin & Ford, 1970; Rogstad & Shostak, 1972; Roberts & Rots, 1973). Particularly the 21 cm observations that measured velocities beyond the optical galaxy exhibited flat rotation curves that disagreed with predictions, interpreted by Freeman (1970) as an excess of undetected mass.

For a few years and with only a few galaxies, flat rotation curves were by some astronomers still seen as the exception and explanations for the unseen mass were e.g. low-luminosity material such as dwarf M stars in the other regions of those galaxies. By the end of the 1970s, new surveys presented rotation curves for 25 (Bosma, 1978) and 10 (Rubin et al., 1978) rotation curves. Almost all of them were flat. Vera Rubin recalls in Rubin (2004) that astronomers went from hoping in 1977 that dark matter could be avoided in answering why the rotation curves were flat to a 'decision' in 1978

that dark matter really exists. This is seen in a clearly worded review in the next year, where the abstract concludes that "the case for invisible mass in the universe is very strong and becoming stronger" (Faber & Gallagher, 1979). "[A]chievements since 1980 are science, not history" (Rubin, 2004).

1.1.2 *Gravitational lensing and the Lyman-alpha forest as further evidence and probes for dark matter*

Figure 1.1: The Bullet Cluster is a stunning example of a dark matter collider. Two galaxy clusters collided head-on, one passing through the other. Most of the baryonic matter is contained in the hot gas (pink), which was observed in the X-ray. The dark matter was reconstructed from weak-lensing observations (blue). The result is a clear separation between baryonic and dark matter. *Credit:* X-ray: NASA/CXC/CfA/M.Markevitch, Optical and lensing map: NASA/STScI, Magellan/U.Arizona/D.Clowe, Lensing map: ESO WFI.

Dark matter was established due to missing mass in galaxies and galaxy clusters. There are many more arguments for dark matter, including gravitational lensing. Gravitational lensing is based on the geometry of spacetime. As light follows the geodesics of spacetime according to Einstein's general theory of relativity, its path will be warped if spacetime is warped by gravity (Einstein, 1917). A heavy enough mass between the

light source and the observer will act as a lens that distorts the light. Analysing these distortions reveals the amount and distribution of the lensing mass. There are two forms of gravitational lensing: strong and weak lensing (e.g. Blandford & Narayan, 1992; Schneider et al., 1992; Bartelmann & Schneider, 2001). Strong lenses are massive perturbers that produce a large enough warping effect to bend the background source into arcs, rings or multiple sources. The effect in weak lensing is much smaller; therefore, a statistical sample of background lenses is necessary to infer the properties of the lens.

Lensing constrains the masses of dark matter haloes over many orders of magnitudes; it provides some of the strongest mass constraints on galaxies and galaxy clusters and can be used to detect dark matter subhaloes (Massey et al., 2010; Vegetti et al., 2010). Zwicky (1937) predicted that gravitational lensing was one of the best ways to determine the mass of galaxy clusters, and it turned out to be correct. A stunning example of the power of weak lensing is the Bullet Cluster (Figure 1.1; Clowe et al., 2006). The head-on collision of two galaxy clusters shows a clear separation between the hot gas observed with X-ray telescopes and dark matter (as reconstructed with weak lensing). While the less massive stellar components of both galaxies continued mostly unperturbed, the hot gas components of both clusters interact, slowing down the gas content. Dark matter traces the stellar component of the cluster, implying a collisionless nature. Systems like the Bullet Cluster allow putting limits on alternative dark matter and gravity theories that do not have a collisionless nature (e.g. Randall et al., 2008) or explain the missing mass by changing the laws of gravity instead of introducing exotic particles (e.g. Brownstein & Moffat, 2007).

As light travels through the Universe, it is not only perturbed by gravitational lenses, but it also interacts with clouds of neutral hydrogen gas, e.g. the intergalactic medium (reviewed in Meiksin, 2009). When a photon interacts with a neutral hydrogen atom, it can excite an electron to transition to another energy level, leading to an absorption line in the spectrum of the photon source. An electron's transition from the ground state to the first excited state is called the Lyman-alpha transition. Light from distant quasars travels through much intergalactic medium at different redshifts. Therefore, we can observe a whole 'forest' of redshifted Lyman-alpha spectral absorption lines (first observed in Lynds, 1971), called the Lyman-alpha forest, where each cloud leaves

its own 'fingerprint'. This allows us to map the large-scale structure of the Universe. Since the large-scale structure is highly sensitive to the underlying dark matter distribution, Lyman-alpha forest measurements can be used to constrain different dark matter models (e.g. Hernquist et al., 1996; Iršič et al., 2017a,b). But what is dark matter?

1.1.3 *What is dark matter?*

We do not know what dark matter is.

No, really, what is it?

The nature of dark matter is a big research focus both in astrophysics and particle physics. Astrophysical measurements inform types of possible dark matter candidates, and specific particle candidates have been proposed by particle physicists (reviewed by Bertone et al., 2005). For the large and small scale structure to develop into its observed form requires a cold, collisionless and stable particle: cold dark matter (CDM; Peebles, 1982; Blumenthal et al., 1984). A promising candidate for CDM for the past centuries is the weakly interacting massive particle (WIMP; e.g. Lee & Weinberg, 1977; Kolb & Turner, 1990; Jungman et al., 1996). It is a massive particle with weak interaction. WIMP were created thermally in the early Universe. When the Universe expanded and cooled below the WIMP mass (which varies for different candidate particles), formation declined exponentially; the WIMP density dropped, and annihilation rates became small, leading to a 'freeze-out' (Kolb & Turner, 1990). The relic density of WIMPs (and other massive DM candidates) constrains whether a proposed particle is abundant enough to be a dominant component of dark matter and the mass range of the particle. With a matching relic density, the WIMP particle has properties, specifically its high mass and its weak force interaction, that make it an outstanding candidate for experiments that search for and produce it. The mass and the cross-section of the WIMP particle line up with mass and cross-sections that are typical of the weak force, coining the term 'WIMP miracle'.

Several underground experiments are designed to specifically search for the WIMP via the recoil of atomic nuclei, e.g. the XENON (Aprile et al., 2018) and LUX (Akerib et al., 2017) experiments. Particle accelerators such as the Large Hadron Collider (LHC)

possibly produce WIMPs up to a certain mass; with the latest results of the direct detection experiments, the particle is heavier than the LHC could produce, and only the next generation of accelerators could achieve this (e.g. Aprile et al., 2018). In theory, while the detectors in the particle accelerators would not detect the particle itself, some amounts of energy and angular momentum would be missing due to the conservation of the total amounts, allowing conclusions on the properties of the particle. With a lot of focus over the past decades on these experiments and many null results, a large parameter space for these particles is now excluded; this motivated new theories of the nature of dark matter and calls to diversify the range of experiments (see e.g. Bertone & Tait, 2018).

A CDM alternative to WIMPs are axions (Peccei & Quinn, 1977). Axions arise from a postulated solution for the strong CP problem in quantum chromodynamics and match the requirements for a cold dark matter particle (Sikivie, 2008). As with WIMPs, experiments have been designed to search for them and to constrain their parameter space; so far, no axion has been found (Bertone & Tait, 2018).

Alternatives to cold dark matter from astrophysical problems

Cold dark matter is not the only possible type of dark matter. Problems in astrophysics, mainly by comparing cosmological simulations to observations, revealed problems with CDM and theories such as warm dark matter (WDM; Blumenthal et al., 1982), self-interacting dark matter (SIDM; Spergel & Steinhardt, 2000), and fuzzy dark matter (FDM; Hu et al., 2000) were developed. Bullock & Boylan-Kolchin (2017) provide an insightful review of these problems in the ΛCDM paradigm on small scales and their (proposed) solutions.

WDM (e.g. Bode et al., 2001; Lovell et al., 2014) behaves similarly to CDM on large scales but suppresses the formation of small-scale structures. WDM has a particle mass in the order of keV. Free streaming of these particles leads to a cutoff in the linear fluctuation power spectrum at a scale that corresponds to dwarf galaxies. It was proposed as a solution to the missing satellites problem (Klypin et al., 1999; Moore et al., 1999), where in numerical simulations, too many satellites were found compared to observations. The missing satellite problem is now considered solved. Improved simulations that include baryonic physics and stellar feedback have shown that subhaloes exist

that do not contain stars, and deeper observations found more satellites around galaxies (e.g. Simon & Geha, 2007; Sawala et al., 2016; Wetzel et al., 2016; Garrison-Kimmel et al., 2017). However, constraining WDM is still an active area of research. WDM particles are lighter than CDM particles, and a promising candidate is a sterile neutrino. Sterile neutrinos are 'right-handed' neutrinos and the counterpart to neutrinos, which is well-motivated from theory. An X-ray line at 3.5 keV (Bulbul et al., 2014; Boyarsky et al., 2014) gives rise to possible sterile neutrino candidates with masses of 3.5 keV (annihilating into two photons) or 7 keV (decaying into a photon and a neutrino) (Adhikari et al., 2017). Nevertheless, with an unknown mass of the sterile neutrino, they could be candidates for CDM as well. As with other DM candidates, they remain undetected.

Both SIDM (Spergel & Steinhardt, 2000) and FDM (Hu et al., 2000) were proposed to solve the core-cusp problem. The core-cusp problem is a discrepancy between the dark matter density profiles of dwarf galaxies (DGs) in simulations (cuspy) and observations (cored). In SIDM, (cold) dark matter interacts with itself with a high-enough cross-section but does not annihilate. This cross-section is the characteristic property of SIDM. It solves the core-cusp problem with the scattering between dark matter particles; it can heat up the centre of DGs, leading to lower, cored, central densities. On large scales, the behaviour is very similar to CDM (Rocha et al., 2013).

FDM particles are ultralight bosons. With a very low mass of $m \sim 10^{-22}$ eV, FDM follows the principles of quantum mechanics, i.e. it behaves like a wave, with a de Broglie wavelength of $\lambda = 1.2 \left(\frac{m}{10^{-22}\,\mathrm{eV}}\right) \left(\frac{100\,\mathrm{km\,s^{-1}}}{v}\right)$ kpc, which can be on the kpc scale. In this theory, the core-cusp problem is solved by a soliton core, where the quantum pressure prevents gravitational collapse (e.g. Hu et al., 2000; Mocz et al., 2019). Due to the quantum mechanic effects in FDM, it is harder to simulate and understand than most other DM models (e.g. Schive et al., 2014).

All these theories show that in order to understand the nature of dark matter, we need to constrain parameter spaces for different types of dark matter both from the astrophysics and from the particle physics aspect to find the candidates that are worth building new detectors and experiments (Buckley & Peter, 2018, provide a comprehensive overview bridging between astrophysics and particle physics). But what if we are wrong and dark matter does not exist?

What if dark matter does not exist? Could gravity be wrong?

By 1980, almost all astronomers were convinced that dark matter existed. They turned their focus on developing theories, and particle physicists turned their attention to experiments. Still, some did not see the need for dark matter. Instead of introducing an exotic form of matter, Milgrom (1983) proposed a modification to gravity called modified Newtonian dynamics (MOND) to explain flat rotation curves. The model states that at extremely low accelerations, the laws of gravity change and the acceleration is boosted by an acceleration constant, while at higher accelerations, MOND agrees with Newtonian dynamics. More alternative gravity theories emerged in order to avoid needing an unknown particle. While these theories agree with and even predict several observations (Famaey & McGaugh, 2012; Milgrom, 2020), they fail to explain e.g. the early Universe, galaxy clusters, and gravitational lensing (e.g. Natarajan & Zhao, 2008; Dodelson, 2011). Only with additional parameters and unseen matter can alternative gravity explain these phenomena (e.g. Sanders, 2003; Bekenstein, 2004; Skordis & Złośnik, 2021).

With ΛCDM being the standard and best-researched cosmology with a tremendous amount of evidence, despite a large parameter space for possible particles ruled out, I will now describe how structure forms in such a Universe.

1.1.4 *The history of the Universe*

The Universe was born a Hubble time ago; the Universe is $\sim$ 13.8 Gyr old (Planck Collaboration, 2020). Figure 1.2 presents the history of the Universe based on hierarchical structure formation (early work includes e.g. White & Rees, 1978; Guth, 1981; Blumenthal et al., 1984; Davis et al., 1985, and a detailed description of inflationary cosmology is presented in Liddle & Lyth, 2000). The Universe was created in the Big Bang. Within a fraction of the first second, there were at least 50 e-folds of cosmic inflation (Remmen & Carroll, 2014). Tiny quantum fluctuations during inflation were the seeds for later structure formation. While the theory of inflation provides a very good explanation of observations, it is not directly confirmed. The expanding Universe cooled down, allowing light and matter to form in a hot and dense plasma just one second after the Big Bang. During this time, DM evolved independently of baryonic

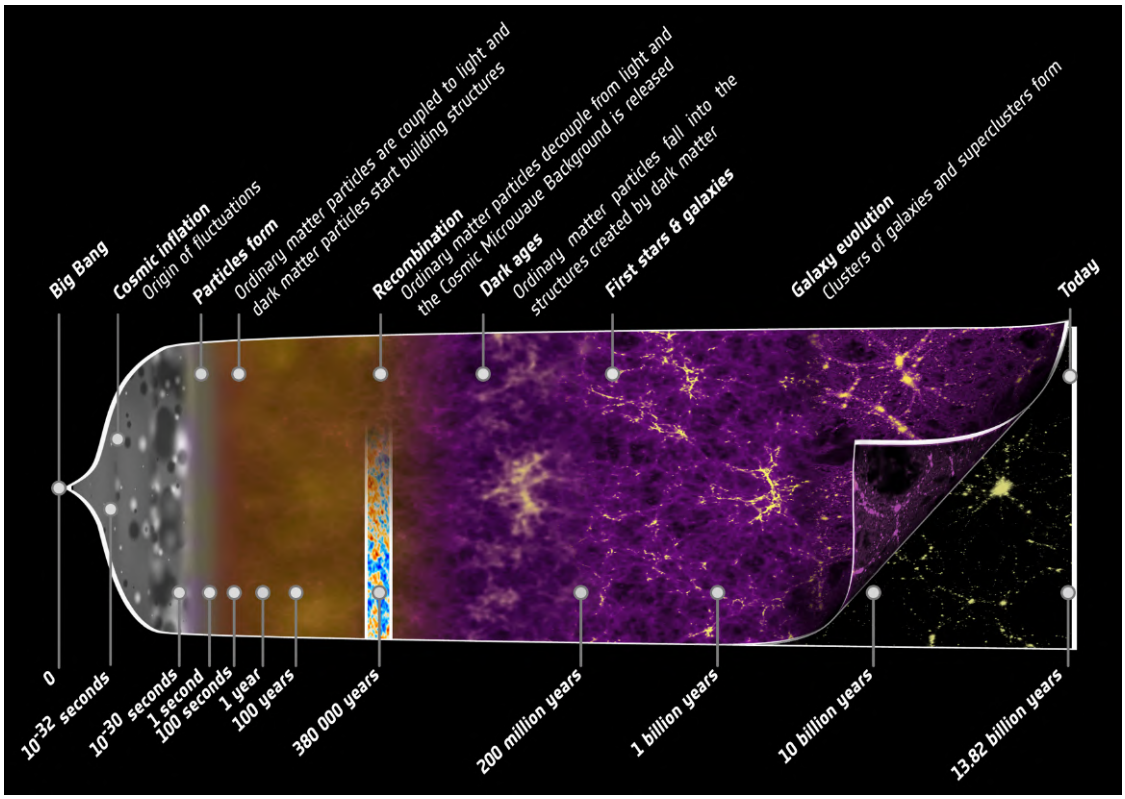

Figure 1.2: Schematic of the history of the Universe. It shows the state of the Universe at different times and explains the main events during that stage, from the Big Bang via recombination to the variety of structures we see today. The stages are explained in more detail in Section 1.1.4. *Credit:* ESA – C. Carreau.

matter. It clumped along the fluctuations from inflation and began to form a web of structure. The Universe was radiation-dominated until $\sim 47,000\,\mathrm{yr}$ when it became matter-dominated. With the Universe still being very hot, the baryonic matter formed a hot ionised plasma with which photons interacted after travelling only short lengths, making the Universe opaque. After 380,000 yr, in the epoch of recombination, protons and electrons started forming atoms, and the Universe became transparent. The first light from that period is imprinted on the cosmic microwave background (CMB). The CMB is a powerful probe of the early Universe and of cosmological models, allowing us to constrain many cosmological parameters as e.g. goal of the Planck mission (Planck Collaboration, 2020).

In the next period, without radiation pressure dominating the behaviour of baryons, atoms felt the gravity of the DM web and started falling into these structures. The Universe was filled with hydrogen atoms that absorb light at shorter wavelengths. No

other luminous material has formed yet; this period is dubbed the dark ages. With enough baryonic matter in the form of gas accreted along the cosmic web, the gas got dense enough to collapse to form the first stars (Bromm & Larson, 2004). While the first stars and galaxies formed along the cosmic web in dark matter haloes, their light broke the atoms of the gas apart and reionised the Universe. This lasted until around one Gyr after the Big Bang when almost all gas was ionised, and the Universe became transparent again.

From early recombination to around redshift $z \approx 0.5$, matter dominated the Universe (Frieman et al., 2008). Due to its gravity, the cosmic web got more and more clustered, and galaxies, galaxy clusters, and superclusters formed within this web. Galaxies grew from low mass to higher mass, both through intrinsic star formation and through mergers with other galaxies. A variety of galaxies emerged, with different types of spiral (younger) and elliptical (older) galaxies.

On large scales, the Universe is homogeneous – from every point in the Universe, the Universe looks the same – and isotropic – there is no preferred direction in the Universe and, therefore, no centre[1]. Distant galaxies move away from us at speeds proportional to their distance (Lemaître, 1927; Hubble, 1929), indicating that the Universe is expanding. Not only is the Universe expanding, but that expansion is accelerating (Riess et al., 1998; Perlmutter et al., 1999)[2]. The driver of this acceleration is dark energy; dark energy has dominated the Universe since redshift $z \approx 0.5$ (Frieman et al., 2008). This even less understood entity makes up most of the energy budget of the Universe. What exactly the future holds is not well understood but dark energy is expected to drive the Universe apart with ever-increasing acceleration until the only light reaching the Earth will be from local galaxies, which are bound to the Local Group.

1.1.5 *Simulating the Universe*

Much of this knowledge comes from cosmological simulations. Cosmological simulations are used to gain more understanding of how the Universe evolves and looks in DM theories and make predictions that can be compared to observations. These simulations have a long history, starting in the 1960s with only 10 to 1000 particles (e.g.

1 This also means that the Earth, the Sun, and even our Galaxy are neither special nor unique.
2 For this discovery, the Nobel Prize in Physics 2011 was awarded to Saul Perlmutter, Brian P. Schmidt and Adam G. Riess.

Aarseth, 1963; Ahmad & Cohen, 1973; Press & Schechter, 1974; White, 1976). An early CDM simulation of the large-scale structure is presented in Davis et al. (1985). The very popular Navarro–Frenk–White (NFW) profile that describes dark matter haloes stems from N-body simulations (Navarro et al., 1996, 1997). Another impressive breakthrough was the *Millenium Simulation* (Springel et al., 2005) with more than 10^{10} particles using the `GADGET-2` code (Springel, 2005). This code and its update are heavily used to this day. Since then, many different cosmological simulations have been carried out (for an overview, see Vogelsberger et al., 2020).

Cosmological simulations can roughly be split up into two pairs of categories: dark matter-only vs dark matter and baryonic, and large volume vs zoom-in. Dark matter-only simulations are generally N-body simulations whereas the ones including baryons are hydrodynamical with more complicated prescriptions (e.g. Somerville & Davé, 2015; Naab & Ostriker, 2017). Large-volume simulations (e.g. Vogelsberger et al., 2014; Hopkins et al., 2014; Schaye et al., 2015) are analysed for statistics while zoom-in simulations (e.g. Sawala et al., 2016; Wetzel et al., 2016; Grand et al., 2017) are run to understand details of e.g. galaxies. In large-volume simulations, everything within a box of a given size with the same resolution is simulated, while in zoom-ins, the focus is on a particular region (e.g. near a Milky Way-like galaxy) which is simulated with a much higher resolution. Areas of research include the cosmic web and the large-scale structure, the distribution of dark matter, the formation and evolution of galaxies, galaxy clusters, and many other aspects of astrophysics and cosmology. The majority of these simulations assume the ΛCDM cosmology, but other cosmologies are also investigated, often within the same simulation framework. As these simulations are very complex, there are a variety of approaches and choices to make. Vogelsberger et al. (2020) review the methodology and applications and give an extensive overview of current state-of-the-art simulations.

1.1.6 *Near-field cosmology*

The imprints of structure formation are found from large scales to small scales. On large scales, cosmology is constrained by statistics. Near-field cosmology studies resolved stars and galaxies in detail to complement these statistical predictions (e.g. Freeman & Bland-Hawthorn, 2002; Frebel & Norris, 2015). With the great wealth of

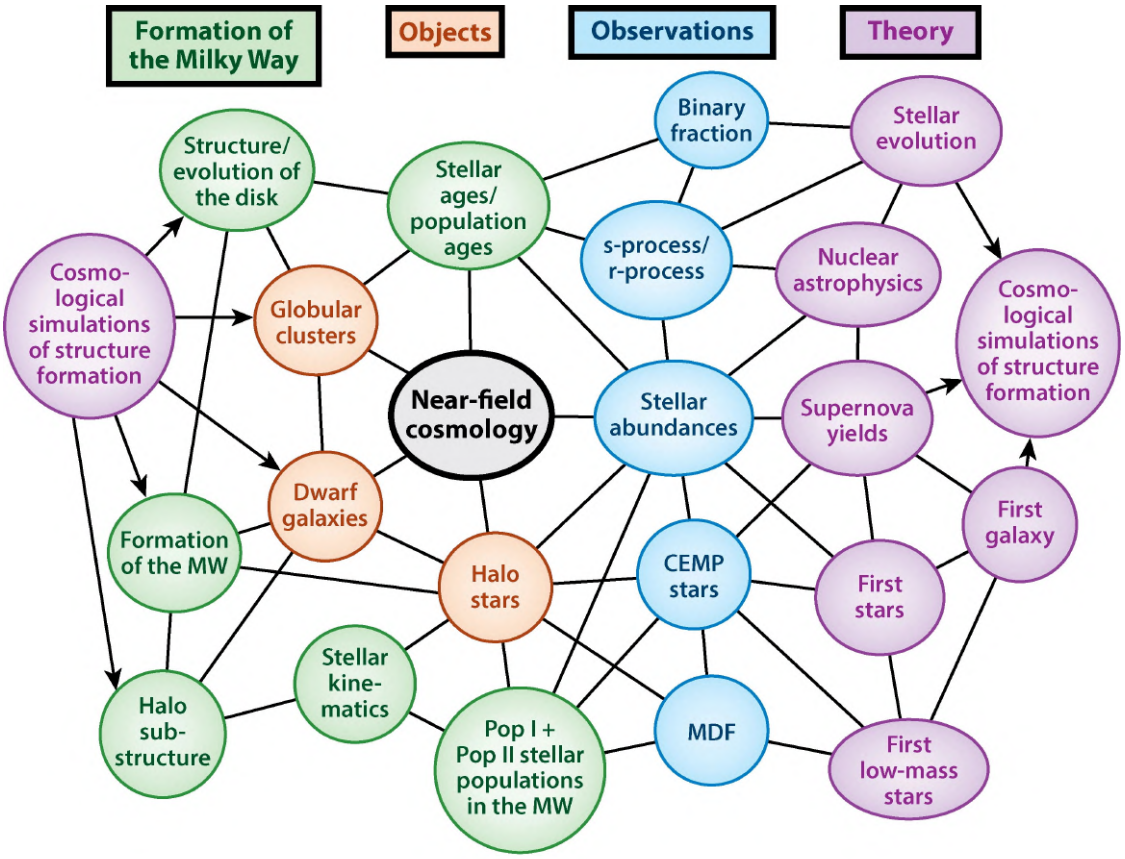

Figure 1.3: Overview of near-field cosmology. This diagram shows how near-field cosmology connects observations (blue) of different objects (orange) with the formation of the Milky Way (green) and theory (purple). This is both informed by cosmological simulations (left), and this generates new understanding to refine the simulations (right). Abbreviations: CEMP – carbon-enhanced metal-poor; MDF – metallicity distribution function; Pop I and Pop II – Population I and II. *Credit:* Frebel & Norris (2015).

spatial, kinematic, and chemical observations of stars, the goal is to reveal the structure and evolution of the Milky Way and nearby galaxies. Figure 1.3 shows how near-field cosmology learns from and informs theory and simulations by observing stars, star clusters, and galaxies. Old stars tell us about the first stars (Frebel & Norris, 2015); DGs are dominated by dark matter and tell us about low-mass DM haloes (Mateo, 1998); globular clusters (GCs) are some of the oldest structures in the Universe (Forbes et al., 2018). While predictions of cosmological simulations match the observed large-scale structure extremely well, their predictions for small scales are not solved yet (see Section 1.1.3) and offer opportunities to constrain the nature of dark matter. For many reasons explained in the next section, the Milky Way is an excellent environment for astrophysical dark matter experiments.

1.2 THE MILKY WAY

Like many other galaxies, the Milky Way is a spiral galaxy; but unlike many other galaxies, our position within it makes it a laboratory to gain unique insights into galaxy formation and evolution and allows us to probe cosmology and the nature of dark matter in new ways. *Gaia* (Gaia Collaboration, 2016, 2018, 2021a) has provided us with remarkable data on over one billion stars and significantly increased our knowledge of the Galaxy. It has uncovered just how much the Galaxy is in disequilibrium due to several galaxy infalls and mergers in its history (e.g. Antoja et al., 2018; Helmi et al., 2018; Haywood et al., 2018; Trick et al., 2019; Erkal et al., 2019; Naidu et al., 2020; Belokurov et al., 2020; Cantat-Gaudin et al., 2020). These new insights cause us problems where we previously described the Milky Way with equilibrium models but, more importantly, provide us with exciting opportunities to gain an understanding of the interplay of baryonic and dark matter.

1.2.1 *The components of the Milky Way*

The Milky Way is made up of baryonic and dark material with more than 100 billion stars, cold, warm and hot gas, and a supermassive black hole at its centre, embedded within a dark matter halo. An overview of the anatomy of the Milky Way is shown in Figure 1.4. This work focuses on the description of the stellar components and the dark matter halo. A review of the structural, kinematic and integrated properties of the Milky Way (pre-*Gaia*) can be found in Bland-Hawthorn & Gerhard (2016).

Stellar components

THE THIN AND THICK DISCS Most of the stars in the Milky Way reside in the thin and the thick disc where they are distributed in spiral arms. A distinction between the discs can be seen both geometrically and in their chemistry, with differences between the distinct discs in each space. Geometrically, the thin and the thick discs have roughly exponential mass profiles where the thick disc has a larger scale height and longer scale length than the thin disc (Yoachim & Dalcanton, 2006).

While the thick disc formed within the first 5 Gyr of the Milky Way until ~ 8 Gyr ago (Belokurov et al., 2020; Xiang & Rix, 2022), the thin disc started forming around that

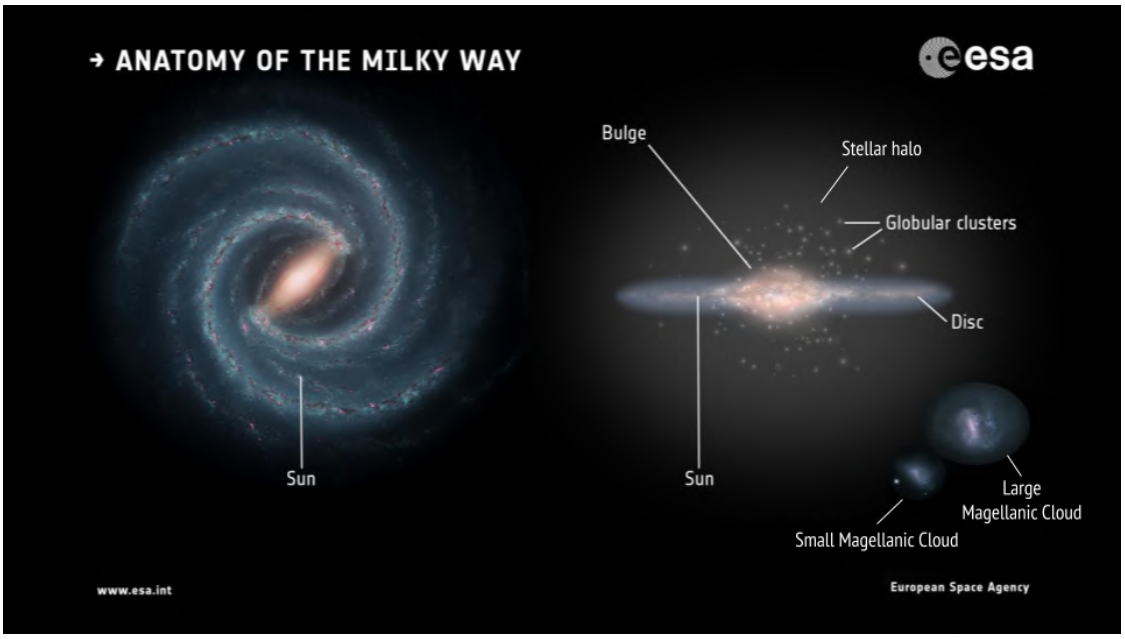

Figure 1.4: The anatomy of the Milky Way: showing the stellar components of the Milky Way. The stars in the Galaxy reside mostly in the spiral arms of the disc, including the Sun. Further components include the bulge and the stellar halo that contains substructures such as globular clusters and dwarf galaxies – the Magellanic Clouds are shown. *Credit*: Left: NASA/JPL-Caltech; right: ESA; layout: ESA/ATG medialab; adapted with credit for the LMC and SMC: ESA/Gaia/DPAC, CC BY-SA 3.0 IGO.

time (Haywood et al., 2013). The discs could be explained due to a two-infall model (e.g. Chiappini et al., 1997; Spitoni et al., 2019) where the infall of Gaia-Sausage-Enceladus (Belokurov et al., 2018; Helmi et al., 2018) possibly triggered star formation in the thick disc (Helmi et al., 2018) and Sagittarius at its pericentre repeatedly triggered star formation in the thin disc (Ruiz-Lara et al., 2020).

These different formation times are seen in two chemically distinct discs. While both have similar metallicities (with the thick disc slightly more metal-poor), there is a clear clustering in α abundances [α/Fe], with a high enhancement in [α/Fe] for the thick disc and a lower abundance for the thin disc (e.g. Haywood et al., 2013).

Gaia DR2 (Gaia Collaboration, 2018) has unveiled that the discs are in dynamical disequilibrium. An example is the phase-space snail in the vertical direction and velocity (Antoja et al., 2018), a possible response to a perturbation in the perpendicular direction such as the Sagittarius DG (Laporte et al., 2019). Further perturbations are seen e.g. as the warp of the Milky Way disc (Kerr, 1957; Schönrich & Dehnen, 2018) and ridges in action-angle space (Trick et al., 2019) due to resonances of the Galactic

bar and spiral arms. The examples and references mentioned here only cover a tiny space of the ongoing research on the Galactic discs.

THE BULGE, THE BAR, AND THE GALACTIC CENTRE The inner regions of the Galaxy host a bulge, a bar and a supermassive black hole at the Galactic centre. The bulge is a dense spheroid containing older and more metal-poor stars than the disc. The exact shape of the bulge and the (ranges of) metallicities and ages of its stars, and therefore the origin and the formation of the bulge, are still debated (e.g. Athanassoula, 2005; Barbuy et al., 2018). Currently, a hybrid formation scenario is favoured (e.g. Fragkoudi et al., 2020). The old and metal-poor 'classical' bulge was formed in violent processes, e.g. dissipationless collapse, mergers or clump migration at high redshifts, evident from the old ages of the stars inferred from colour-magnitude diagrams (e.g. Ortolani et al., 1995; Clarkson et al., 2008). The younger and more metal-rich 'boxy/peanut' bulge results from instabilities and resonances from a bar formation (McWilliam & Zoccali, 2010; Nataf et al., 2010; Wegg & Gerhard, 2013).

In spiral galaxies, bars are common structures in their centres (Eskridge et al., 2000). The formation, evolution, and dynamics of the bar and its interaction with other components of the Galaxy are complicated (Kormendy & Kennicutt, 2004); e.g. the rotation of the bar causes resonances in the disc, and the length of the bar is affected by the dynamical friction due to the Milky Way's dark matter halo. Still, the bar has a promising premise: inferring – non-trivial – bar properties allows conclusions about the amount of baryonic and dark matter in the inner Milky Way (Fragkoudi et al., 2021).

In the Galactic centre, there is a supermassive black hole (SMBH)[3]. It is surrounded by a nuclear star cluster, a small, dense and spherical collection of old and young stars (see e.g. Genzel et al., 2010; Neumayer et al., 2020). Observing the position of S2, a star that orbits the SMBH with a period of $\sim$ 16 yr, for decades (e.g. Ghez et al., 2008; Gillessen et al., 2017), has allowed conclusions on the mass and position of the SMBH and tests of predictions of general relativity (GRAVITY Collaboration, 2018, 2019, 2020). Furthermore, Event Horizon Telescope Collaboration (2022) impressively captured an image of the Milky Way black hole, revealing another stunning agreement with general relativity. The mass of the SMBH is $\sim 4 \cdot 10^6 M_\odot$ (Ghez et al., 2008; Genzel et al., 2010;

3 For its detection, Andrea Ghez and Reinhard Genzel were awarded the Nobel Prize in Physics 2020.

Event Horizon Telescope Collaboration, 2022) at a distance of $R_0 \sim 8.2$ kpc (GRAVITY Collaboration, 2020).

THE STELLAR HALO The Galactic halo is dominated by dark matter, and the stellar halo makes up only one per cent of the stellar mass in the Galaxy (Bland-Hawthorn & Gerhard, 2016). The stars are generally old and metal-poor and are contained in stellar substructure, both in-situ and accreted (Naidu et al., 2020). Examples of accreted substructures are DGs, GCs and stellar streams. Most of the accreted stars in the stellar halo come from two DGs, Gaia–Sausage–Enceladus (GSE; Belokurov et al., 2018; Helmi et al., 2018) and Sagittarius (Ibata et al., 1994). These stars, particularly the ones from the Gaia–Sausage–Enceladus (GSE) merger, are now distributed all over the stellar halo and identified by their chemo-dynamical properties. There are several intact DGs in the stellar halo, most prominent the Large Magellanic Cloud (LMC) and the Small Magellanic Cloud (SMC). There are 11 classical satellites of the Milky Way – the brightest satellite galaxies – and many more, fainter DGs (McConnachie, 2012; Pace et al., 2022). Furthermore, there are more than 150 GCs (Harris, 1996; Vasiliev & Baumgardt, 2021) and almost 100 detected stellar streams – disrupted DGs and GCs – in the halo (Mateu, 2023). These structures in the stellar halo, particularly stellar streams, are highly sensitive to the gravitational potential of the dark matter halo and have been used to infer its properties (e.g. Johnston, 1998).

Dark matter halo

Due to the nature of dark matter, the dark matter halo of the Milky Way cannot be directly observed. Since the potential of the dark matter halo is necessary for modelling anything that moves in the Milky Way halo, we need to constrain it. Only by carefully analysing baryonic matter in the Milky Way can we draw conclusions about the distribution of dark matter in the Milky Way. There are many different methods to infer the mass and the shape of the dark matter halo. Until recently, most of these methods assume equilibrium and time independence of the Milky Way. In the next section, I will describe some of these methods and their constraints, but throughout this thesis, I will show that the underlying assumptions might lead to significant biases.

1.2.2 *Mass and shape of the Milky Way halo*

Knowing the mass and the shape of the Milky Way halo is essential to many astrophysical problems utilizing methods of galactic dynamics, including many efforts in Galactic archaeology – unveiling the formation and merger history of the Milky Way. There are many different methods and tracers to infer the potential at different distances.

Wang et al. (2020a) provide a recent overview of methods and results of measuring the mass and shape of the Milky Way halo. As different tracers constrain the mass at different distances, Wang et al. (2020a) summarise results on enclosed mass measurements and extrapolate to virial mass estimates (when not done in the original work). The virial mass, M_{200}, is the mass within the virial radius R_{200}, where the density of the halo is 200 times the critical density of the Universe. It is often used in cosmological simulations, where it is straightforward to calculate, even though its observational calculation and application are debated as none of the tracers is observable to the virial radius. The estimates of the viral mass range between $0.5 - 2.5 \cdot 10^{12}$ $M_\odot$ (figure 1 in Wang et al., 2020a).

METHODS TO MEASURE THE MASS Most of the mass measurements of the Milky Way halo come from four different methods: (i) the rotation curve, (ii) spherical Jeans modelling of halo tracers such as GCs and DGs, (iii) distribution functions, and (iv) modelling stellar streams. Stellar streams are described in more detail in Section 1.4.

The rotation curve is used to constrain the mass in the inner Milky Way and its disc. Assuming that gas and young stars move on circular orbits in an axisymmetric potential within the solar orbital radius, there is a particular direction for the stars and ISM where the rotational velocity makes up the entire line-of-sight velocity and the peak velocity can be measured. These measurements make up the rotation curve of the interstellar medium and disc stars (e.g. van de Hulst et al., 1954; Gunn et al., 1979; Bovy et al., 2012; McMillan, 2017; Eilers et al., 2019) and are measured along the flat part of the rotation curve. The rotation curve depends on the distance to the Galactic centre and the enclosed mass but, due to the geometry of the observations, is complicated by other velocities (see e.g. figure 4 in Wang et al., 2020a), such as the Sun's velocity, the Local Standard of Rest, terminal velocities and the asymmetric drift (Binney &

Tremaine, 2008). The circular velocity is proportional to the square root of the radial derivative of the gravitational potential, for which then the mass can be calculated.

Spherical Jeans modelling (e.g. Jeans, 1922; Bahcall, 1984a,b; Binney & Tremaine, 2008; Read, 2014) assumes that the outer halo is spherical and in equilibrium, i.e. time-independent and collisionless – meaning that the force on a star is dominated by the contribution from many distant stars rather than a few close ones. Using the Jeans equations (Jeans, 1922; Binney & Tremaine, 2008), the circular velocity at any given distance can be calculated by the radial density profile, the radial velocity dispersion, and the velocity anisotropy of tracers in the system. The tracers that are used for this method are e.g. DGs (Watkins et al., 2010) and GCs (Watkins et al., 2019) that go further out than the tracers of the rotation curve method, up to 300 kpc.

For an assumed potential in equilibrium, again, time-independent and collisionless, distribution functions describe the number of objects, such as stars, on a given orbit, given either phase-space coordinates or actions, which are generally assumed to be constant in time (e.g. Jeans, 1915; Eddington, 1916; Lynden-Bell, 1962; Wilkinson & Evans, 1999; Binney, 2010; Deason et al., 2012; Sanders & Binney, 2015b). Objects such as DGs and GCs are modelled, where potential parameters such as the halo mass are fit parameters (e.g. Eadie & Harris, 2016; Posti & Helmi, 2019).

While the uncertainty on the Milky Way virial mass has decreased and results have moved within a factor of two with these methods and measurements from *Gaia*, the Hubble Space Telescope and other surveys, there is still no consensus on the true mass (Wang et al., 2020a). This is due to the different assumptions and tracers used in these different methods and that most of the methods assume that the Milky Way is in equilibrium. It has now become clear that the Milky Way is not in equilibrium due to its past and ongoing merger history with massive DGs causing significant perturbations.

1.3 THE LARGE MAGELLANIC CLOUD

The Magellanic Clouds are the most prominent DGs in the night sky and are visible to the naked eye in the Southern hemisphere. They have been the subject of science since early times, with the many indigenous cultures in the Southern hemisphere to scientists around the world today trying to understand them and their influence on our Galaxy.

1.3.1 *The clouds in a cultural context*

INDIGENOUS SCIENCE In many natives' cultures, mythologies, and sciences, the Magellanic Clouds played an important role. They inspired stories about the night sky but also lead to observations of both luminous and dark parts of the Galaxy. For the Australian Aborigines, the Magellanic Clouds were the camps of an old couple, Jukara (Filipovic et al., 1996). The man's camp was in the LMC, and the woman's in the SMC. They were unable to feed themselves, so other star beings caught fish in the "sky river" (the Milky Way) and brought it to them. In the Polynesian culture, there were many names for the clouds. Kokouri and Kokotea, Tioreore and Tikatakata who protect their people from the winds, purei ao and pukohukohu according to their appearance; Tahitians called them Mahu and natives from the Cook Group Ma'u (Best, 1922). South American people saw water features in the clouds. The Tupi-Guaranis, around today's Rio de Janeiro, called them fountains from which a tapir (Tapi'i Huguá, LMC) and a pig (Coxi Huguá, SMC) are drinking (Afonso, 2006; Dennefeld, 2020). My favourite interpretation comes from the Mapuche in Chile: Originally, there were three artificial water wells (Rüganko; from rvgan - dig, and ko - water). One is completely dissolved – possibly referring to the Coalsack Nebula – and the second is dissolving – could this be the SMC that is disrupting around the LMC (De Leo et al., 2020)?. Once the third has gone, it is the end of the world (Pozo Menares & Canio Llanquinao, 2014; Dennefeld, 2020).

EARLY RECORDED OBSERVATIONS The first time the LMC was mentioned in written text was in 964 by the Persian astronomer Abd-al-Rahman Al Sufi in the 'Book of Fixed Stars' – it also contained the first recorded observation of the Andromeda galaxy (Al Sufi, 964). He referred to the LMC as Al Bakr, the White Ox, of the southern Arab (as it was not visible in Northern Arabia) (Allen, 1963; Frommert, H. and Kronberg, C., 2007).

Around 500 years later, European explorers and settlers 'discovered' the Southern Sky when they began sailing in the Southern Hemisphere. They referred to the Magellanic Clouds as 'Cape Clouds' after arriving and seeing them at Cape Horn in South Africa (Allen, 1963). The first written records from Europeans come from the Italian

authors Peter Martyr d'Anghiera (von Humboldt, 1852) and Andrea Corsali (Kanas, 2012) in 1516. On Portuguese voyages, they saw and wrote about them; Corsali drew them in a letter to the Medici family. The drawing shows some stars, including the southern cross, and two 'nebulae'.

Europeans referred to these objects as 'nubecula major' and 'nubecula minor' (e.g. Johann Bayer in his book *Uranometria*, 1603, shown in Figure 1.5). Only at some point between the 18th and 19th century were the clouds called the 'Magellanic Clouds', after the Portuguese explorer Ferdinand Magellan whose chronicler Antonio Pigafetta reported them during their circumnavigation of the world in 1519–1522 (Pigafetta, 1522). Herschel (1847) wrote the first scientific publication using 'Magellanic Clouds' alongside 'Nubecula Major' and 'Nubecula Minor'.

Contrary to popular belief, Magellan did not finish his circumnavigation of the world as his voyage was cut short at the hands of Lapulapu, a datu (chief) of Mactan in the Visayas in the Philippines, and his men on 27 April 1521 who defeated the Spanish forces (Pigafetta, 1522). For this battle, Lapulapu is considered the first Filipino hero.

The naming of these galaxies, together with other namings that happen within astronomy, are an example of eurocentric and inconsiderate actions that lead to active exclusions of underrepresented scientists. Other examples are the naming of telescopes, such as JWST named after James Webb, who was in power during the active persecution of gay people in US government agencies, and more innocent yet possibly distressing namings, such as 'Orphan' in regard to things which do not seem to have a visible progenitor or history.

1.3.2 *The mass of the LMC*

The total mass of the LMC is not yet well-understood, and research into the orbit of the LMC over the past decade has led to revised mass estimates and new areas of research on the effects that the LMC infall has on the Milky Way. The mass of the LMC's stellar disc is $M_{LMC,disc} = 2.7 \cdot 10^9\,M_\odot$ (van der Marel et al., 2002) and the LMC is at an impressively well-constrained distance of $d = 49.59 \pm 0.09\,(\text{statistical}) \pm 0.54\,(\text{systematic})\,\text{kpc}$ (Pietrzyński et al., 2019). Based on the van der Marel et al. (2002) mass measurements, Bekki & Chiba (2005) assumed a total mass for the LMC, $M_{LMC} \sim 10^{10}\,M_\odot$, and simulations suggested an orbital period of $T \sim 2\,\text{Gyr}$ around the Milky Way.

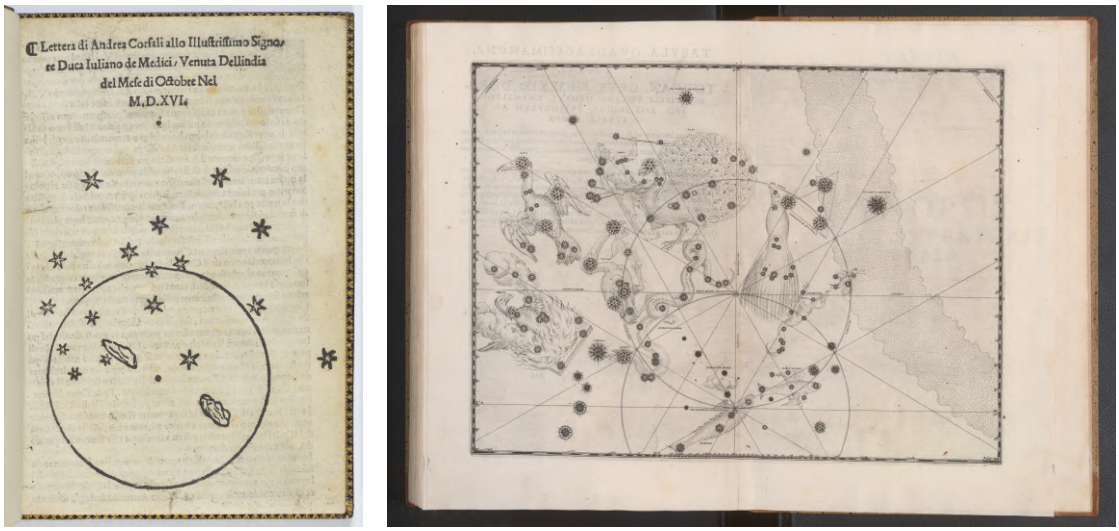

Figure 1.5: Early sketches of the clouds. *Left:* Sketch by Andrea Corsali of the Southern sky. This was part of a letter to the Medici family in 1516 and shows the Southern Cross and drawings of the clouds. *Right:* Excerpt from Johann Bayer's Uranometria (Bayer, 1603). The clouds are depicted at the bottom at the centre as nubecula major and nubecula minor. *Credit:* the State Library of NSW (*left*) and ETH-Bibliothek Zürich (*right*).

Since then, more simulations and observations of the Magellanic clouds have led to updated estimates for the orbit and mass of the LMC. Besla et al. (2007) and Kallivayalil et al. (2013) argued that the LMC is on its first infall with a total velocity of $320\,\mathrm{km\,s^{-1}}$ (Kallivayalil et al., 2006, 2013), changing implications for the LMC mass strongly; they found it must be a factor of 10 higher than previously estimated. Different methods to calculate the LMC mass all support this increased mass; models of the Magellanic system (Besla et al., 2010), the rotation curve around the LMC (van der Marel & Kallivayalil, 2014), LMC satellites – including the SMC (Jethwa et al., 2016; Kallivayalil et al., 2018; Erkal & Belokurov, 2020), and stellar streams that are perturbed by the LMC (Erkal et al., 2019; Shipp et al., 2021; Vasiliev et al., 2021). Shipp et al. (2021) estimated the mass of the LMC with closely passing stellar streams to be $M_{LMC} = 1.88 \cdot 10^{11}\ M_\odot$, corresponding to 23 per cent of their assumed Milky Way mass. This increased mass of the LMC affects the Milky Way halo drastically.

1.3.3 *The effect of the LMC on the Milky Way*

There are several effects the LMC has on the Milky Way, and there is current research into more of them[4] and gaining a better understanding, including this thesis. One con-

4 A recent review can be found in Vasiliev (2023).

sequence of the infalling LMC is the reflex motion of the Milky Way disc. The disc has a shorter dynamical time scale than the halo; therefore, the LMC pulls it down as one component, while the halo does not experience this pull (Gómez et al., 2015; Petersen & Peñarrubia, 2020). Since we observe from within the disc and it is our rest frame for observations, we observe an upwards motion of the halo that needs to be taken into account when analysing any motions in the stellar halo (Erkal & Belokurov, 2020; Erkal et al., 2020). With different populations of tracers in the stellar halo, Petersen & Peñarrubia (2020) measure the reflex motion velocity at $v_{\rm travel} = 32^{+4}_{-4}\,{\rm km\,s^{-1}}$ with respect to the outer halo, moving towards the past orbit of the LMC, consistent with measurements in Erkal et al. (2021).

Another consequence is the deformation of the stellar and dark matter halo, visible in their densities. Garavito-Camargo et al. (2021a) describe two modes of response. The first is due to resonances that only damp slowly over time (Weinberg, 1994). They identify this response in an overdensity, mainly in the Northern hemisphere. They call this the 'Collective Response' and explain this with the displacement of the disc. The other response is the 'Wake' of the LMC due to dynamical friction (Chandrasekhar, 1943). This is a non-resonant response that damps quickly. These overdensities were observed in the stellar halo by Conroy et al. (2021), even though the distribution and strength of overdensities do not match the Garavito-Camargo et al. (2019, 2021a) simulations, revealing the need for both more simulations and observations.

These responses so far are only seen in stellar tracers that possibly could be explained due to other theories such as alternative gravity. To prove the existence of dark matter, our aim is to find a direct, observable effect of the deforming dark matter haloes. Since stellar streams are very sensitive to the gravitational potential they move in (Erkal et al., 2019; Koposov et al., 2023), they are some of the best objects to test the effect of the deforming dark matter haloes. In Chapter 2, I explain the tools to describe the Milky Way–LMC interaction and how we model stellar streams. In the next section, I introduce stellar streams in the Milky Way.

1.4 STELLAR STREAMS

Stellar streams are filament-like structures on the haloes of galaxies. There are currently 97 observed streams around the Milky Way (Mateu, 2023) and many around nearby ex-

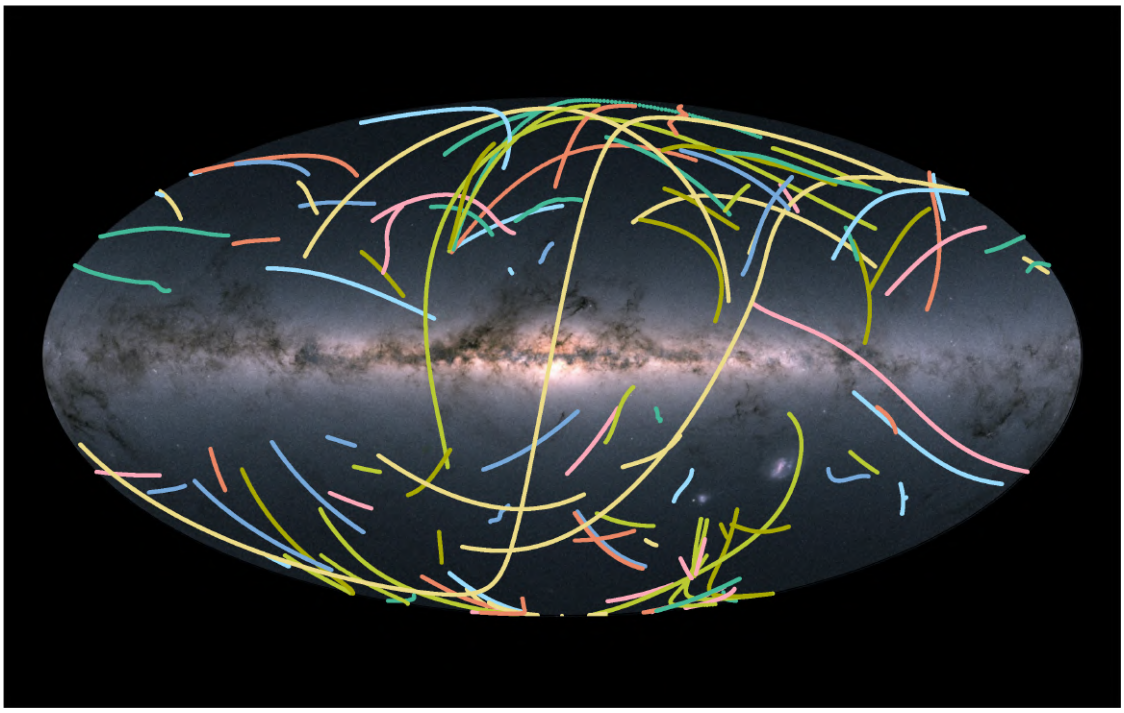

Figure 1.6: Tracks of the 97 stellar streams in the Milky Way from `galstreams` (Mateu, 2023) with the *Gaia* Milky Way view in the background. These streams have a range of lengths, widths, distances, orbits and other properties. They are complex objects, often with features in the streams, and are used to understand the disruption of infalling satellites, to reconstruct the assembly of the Milky Way, and to constrain properties of dark matter. *Credit for the background image:* ESA/Gaia/DPAC.

ternal galaxies. Streams are the results of disrupting GCs and DGs in the gravitational potential of the galaxy that accretes them, such as the Milky Way. They are excellent probes to the Galactic potential due to their orbital configuration and location within the Milky Way's dark matter halo.

1.4.1 *Introduction to stellar streams*

The first stellar stream, the Sagittarius stream, was found almost 30 years ago by Ibata et al. (1994). Over the next 20 years, ~ 20 more streams were found (Grillmair & Carlin, 2016), many with the Sloan Digital Sky Survey (SDSS; York et al., 2000). Since then, the number of known stellar streams has almost quintupled. This is due to telescopes and surveys such as *Gaia* and the Dark Energy Survey (DES; Dark Energy Survey Collaboration, 2016), and due to improved stream finding techniques and algorithms, particularly `STREAMFINDER` (Malhan & Ibata, 2018).

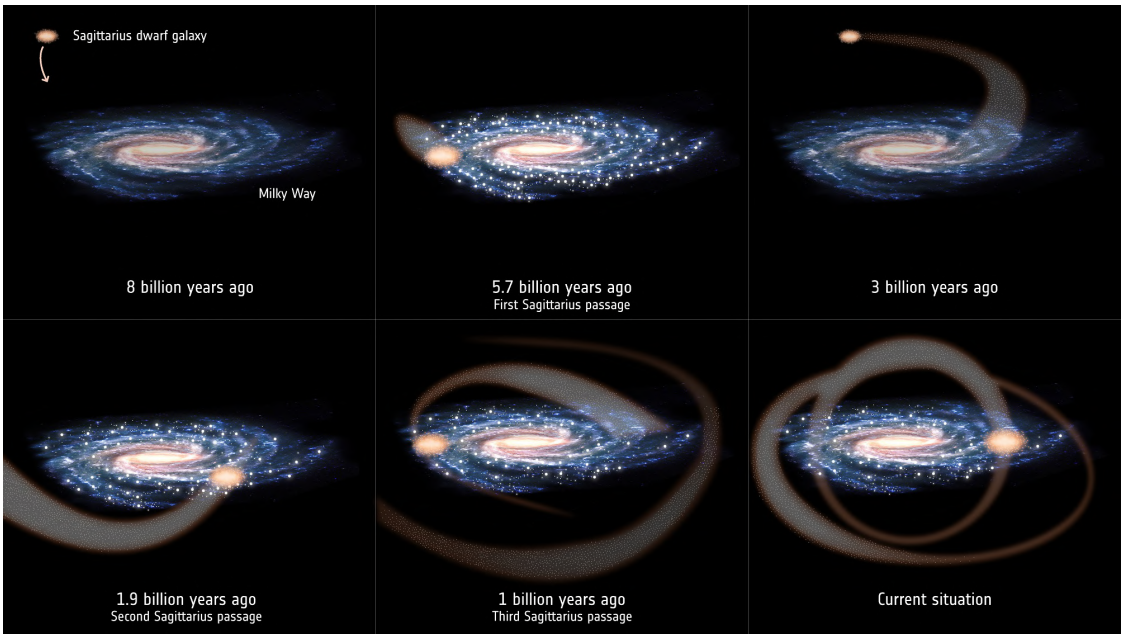

Figure 1.7: Schematic of the disruption of the Sagittarius dwarf galaxy around the Milky Way and the build-up of its stream. Over several orbits, stars leave the progenitor galaxy and form trailing and leading arms. *Credit:* ESA.

STREAM FORMATION Stellar streams are infalling GCs and DGs that are disrupted by the tidal field of the Milky Way or other galaxies. The stars of the streams are initially bound to their progenitor, having slightly varying energies due to the velocity dispersion of the progenitor. When entering a galaxy, stars are stripped from the progenitor. Figure 1.7 shows an artist's impression of the infall of the Sagittarius DG and the formation of its stream. Their stripping time and their position in the stellar stream depend on their energy, position and velocity in the progenitor. Fundamentally, stars that leave the progenitor and are closer to the Galactic centre have shorter orbital periods and thus move ahead of the progenitor while stars further away from the centre have longer orbital periods, therefore, move behind the progenitor. Therefore, stars with a lower velocity or that are closer to the Galactic centre will have a lower energy in the Galactic potential and move faster, forming the leading arm of the stream. Stars further away from the Galactic centre or with higher velocities have a higher energy in the Galactic potential and will orbit more slowly, forming the trailing arm.

In reality, the build-up of the tidal tails from a progenitor, particularly from DGs, is more complex. The internal dynamics and structure of the stellar populations of the progenitor can affect the stripping process (e.g. Peñarrubia et al., 2010; Niederste-

Ostholt et al., 2012; Gibbons et al., 2014). Moreover, a DG can fall in with several GCs (e.g. Massari et al., 2019; Bonaca et al., 2021; Malhan et al., 2022a). These can have started disrupting around the DG before being accreted by the Milky Way and forming more complex stream structures (Malhan et al., 2021, 2022b). The host potential and other large substructures also affect how streams form and evolve (discussed in Section 1.4.2). To understand the detailed build-up of the streams and to learn about the environment it evolves in, we need sophisticated stream modelling techniques that take these more complex effects into account. I will describe several stream modelling methods, including the ones used in this thesis, in Section 2.2.

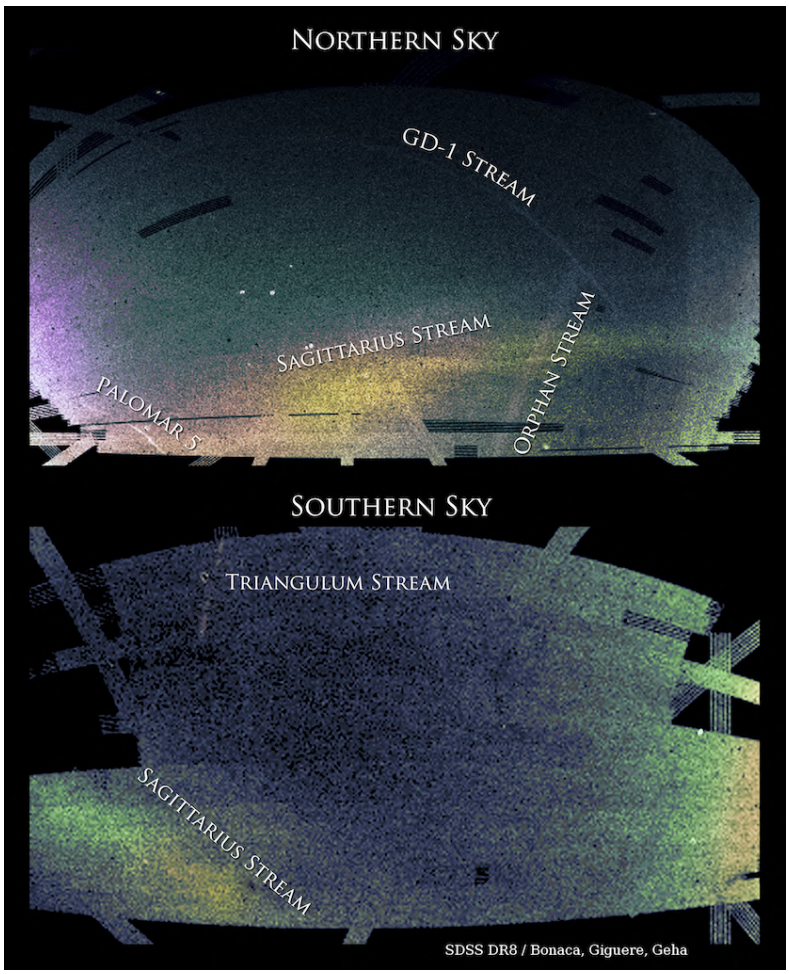

Figure 1.8: The field of streams, originally from Belokurov et al. (2006) and updated by Bonaca et al. (2012) to include the Southern sky. The figure shows the SDSS footprint and several Milky Way streams that were discovered in SDSS.

DETECTING STELLAR STREAMS There are different methods to detect stellar streams in larger data sets. The simplest and earliest ones include finding objects on great circles that have high contrast against the background (Johnston et al., 1996); and cuts in colour and magnitude to select blue main-sequence turnoff stars, e.g. leading to the field of streams (Figure 1.8, Belokurov et al., 2006; Bonaca et al., 2012).

A more elaborate method is the matched-filter technique (Rockosi et al., 2002). This technique uses the fact that stellar streams are disrupted GCs or DGs and therefore follow an isochrone consistent with an old and metal-poor population on the colour-magnitude diagram. Then, by filtering small sections of the sky – any known populations such as the LMC, the Sagittarius stream and the Galactic disc are removed – in a series of distance modulus bins, streams can be detected and verified in residual density maps, where the smoothed Milky Way foreground is subtracted. With this method, Shipp et al. (2018) discovered 11 new stellar streams in the DES footprint.

With the amount of data that all-sky surveys such as *Gaia* and Large Synoptic Survey Telescope (LSST; Ivezić et al., 2019) provide, machine-learning algorithms are being developed to detect stellar streams in an automated and systematic way. The algorithm leading to many recent stream detections in the *Gaia* dataset is `STREAMFINDER` (Malhan & Ibata, 2018), aiming to find dynamically cold and thin streams, i.e. GC streams. It looks for coherent structures in 6D phase-space hypertubes where missing information, such as radial velocities and parallaxes, are estimated or sampled, For each star, a stream membership likelihood is calculated. With this algorithm, more than 40 stellar streams were detected (Malhan et al., 2018; Ibata et al., 2019, 2020; Martin et al., 2022). Another machine-learning approach to discovering stellar streams in survey data is based on the fact that (unperturbed) streams almost delineate orbits and, therefore, can be found as lines on the sky and corresponding clumps and overdensities in the proper motions and photometric data. This idea is implemented in `VIA MACHINAE` (Shih et al., 2022) and its update `Via Machinae 2.0` (Shih et al., 2023). Shih et al. (2023) identified 90 candidate streams using this algorithm on *Gaia* DR2 data[5]. The idea of finding streams as linear structures is also applied to external galaxies (Pearson et al., 2022a) and will be particularly useful for finding streams with the Nancy Grace Roman Space Telescope.

5 At the time of this writing, this paper has not been peer-reviewed yet.

STREAMS AS ARTEFACTS IN GALACTIC ARCHAEOLOGY The stellar halo is a time capsule conserving the memory of the assembly history of the Milky Way. Stars that belonged to the same group before their infall have similar integrals of motion (conserved quantities such as energy, angular momenta and actions) and similar chemical abundance patterns, even if they are scattered across the sky. Therefore, finding groups by chemo-dynamical tagging of stars is one of the main methods to disentangle the infall history of the Milky Way and to "reconstruct the galactic past" (Eggen et al., 1962). Many mergers have been found like this, most prominently the GSE merger[6] (Belokurov et al., 2018; Helmi et al., 2018), or followed up with chemo-dynamical investigations (e.g. Naidu et al., 2020).

Streams offer another window into exploring the history of the Milky Way as they fill the gap between the smooth halo and intact satellite galaxies. Taking spectroscopic measurements of stream members is challenging: they have low surface density and a large extent on the sky. The Southern Stellar Stream Spectroscopic Survey (S^5) takes spectroscopic observations of several streams in the Southern sky, aiming to identify stream members and map their kinematics and chemistry (Li et al., 2019). Li et al. (2022) study a population of 12 streams to further our understanding of Galactic archaeology. They infer the properties of the disrupted progenitors and find possible associations with other Milky Way satellites. They discuss the implications of the streams' infall orientation and find a pile-up at peri- and apocentres. Combining metallicities and orbits of streams, they find clear trends between different progenitors and a difference between GC streams and GCs that are still intact, possibly due to a different origin or accretion history. By comparing these results to cosmological simulations, they find a possible extension of the 'too big to fail' problem from satellites to streams — meaning there are not enough DG streams in the Milky Way. This was solved by Shipp et al. (2022) as a detection limit problem. This shows that streams are powerful artefacts in Galactic archaeology. Due to their location in the Galactic halo and their sensitivity to the gravitational potential they move in, they are also powerful probes of the dark matter distribution around the Milky Way.

6 GSE was first identified as a 'sausage'-like structure in the radial and azimuthal velocity space in Belokurov et al. (2018).

1.4.2 *Stellar streams and dark matter*

Stellar streams are some of the leading objects with which to study the distribution of dark matter around the Milky Way and other galaxies. Particularly in the Milky Way, there are two aspects of dark matter that can be studied; the global dark matter distribution and the distribution of dark matter substructure. The global dark matter profile affects the overall orbit and shape of the stream. Dark matter subhaloes create gaps in streams when passing by closely and with a similar velocity to the stream. In external galaxies, currently, stellar streams are used to constrain the mass and shape of their dark matter haloes.

GLOBAL POTENTIAL The Milky Way's gravitational potential, particularly the properties of its dark matter halo, is still an open question, as discussed in Section 1.2.2. Stellar streams provide a localised constraint of the dark matter halo (Bonaca & Hogg, 2018), with prime streams being the Sagittarius, the OC, and the GD-1 stream[7].

The Sagittarius stream is an extremely interesting case. It has a clear progenitor, the Sagittarius DG (Ibata et al., 1994), it spans a large part of the halo, and it has many features along the stream that are still not explained, such as bifurcations (e.g. Fellhauer et al., 2006; Ramos et al., 2022). Many attempts at fitting the stream and the Galactic potential were only partly successful, and models were preferring opposing results for the halo shape (prolate – Helmi, 2004; Law et al., 2005; oblate – Johnston et al., 2005; triaxial, but nearly oblate – Law & Majewski, 2010; Vasiliev et al., 2021). While the triaxial solution from Law & Majewski (2010) was more successful than the axisymmetric solutions, the configuration of their triaxial shape is dynamically unstable and unlikely to be the true shape of the Milky Way (Debattista et al., 2013). Vasiliev et al. (2021) allow for a more flexible profile, with a different inner and outer flattening. More importantly, they include the LMC in their fits. With these adaptations, they match the observed data pretty well, even though there are still some caveats present, such as an offset of $\sim 2°$ between the model and the data in the leading arm of

7 I will discuss these streams and some of their fit results here but will refrain from listing specific mass measurements since determining a specific number for the Milky Way mass and shape is not a goal of this thesis but rather understanding where biases can affect these methods and results.

the stream track. The LMC affects more than just this stream, as described in the next section.

The GD-1 stream (Grillmair & Dionatos, 2006) is another interesting stream. Like the Sagittarius stream, it was discovered in SDSS. It is a GC stream, the coldest and longest observed to date (more than 100°, Mateu, 2023). It has many features like a spur, a blob, a wiggle, and gaps along the streams (Price-Whelan & Bonaca, 2018), making it an important stream to understand the effect of other structures such as dark matter subhaloes (Bonaca et al., 2019), the Sagittarius DG (de Boer et al., 2020), and even disruption that started in a previous host galaxy (Malhan et al., 2019, 2021). Furthermore, its length and thinness make it a great stream to constrain the gravitational potential in the inner Milky Way halo (Malhan & Ibata, 2019, find GD-1's apocentre at $R = 20.8$ kpc). First to constrain the Milky Way potential with GD-1 were Koposov et al. (2010) with an orbit fitting technique [8], as did Malhan & Ibata (2019). Bovy et al. (2016) fit GD-1 and the Milky Way halo with an action-angle modelling approach, while Bowden et al. (2015) use a Lagrange point stripping method to generate streams that they fit to GD-1. All find oblate halo shapes for the inner Milky Way (in the region that GD-1 spans).

A third stream used to fit the potential is the Orphan–Chenab (OC) stream (Grillmair, 2006; Belokurov et al., 2007b). The OC stream is a DG stream and the first detected stream without a progenitor, hence its name. Recently, it has become one of the most interesting streams to infer the Galactic potential with, since it is highly affected by the LMC. Before the effect of the LMC became obvious, Newberg et al. (2010) and Hendel et al. (2018) fit the OC stream with orbits. With better data from *Gaia*, and models that include the infalling LMC, the reflex motion of the disc and more flexible potential description, Erkal et al. (2019) and Koposov et al. (2023) present fits that not only constrain the Milky Way halo – preferring an oblate flattening – but also the mass and orbit of the LMC.

SUBSTRUCTURE AND SUBHALOES In cosmological models with cold dark matter, dark matter haloes exist with masses of orders of magnitudes below where galaxies form (Wang et al., 2020b). Galaxies can only form in haloes with masses of at least $\sim 10^8 - 10^9$ $M_\odot$ (e.g. Efstathiou, 1992; Sawala et al., 2015). Finding dark subhaloes less

8 The modelling methods are explained in the Chapter 2.2.

massive than 10^8 $M_\odot$ would confirm these dark matter predictions; measuring the population of subhaloes to get a halo mass function would put strong constraints on the nature of dark matter as the number of subhaloes at different halo masses varies significantly in different dark matter theories (Angulo et al., 2013). These subhaloes populate the Milky Way halo and are expected to interact with stellar streams, altering the streams' morphology (Johnston et al., 2002; Ibata et al., 2002). These features in streams, such as gaps and spurs, can be used twofold in dark matter research; high-confidence investigations of individual features to put strong constraints on the properties of the perturber and statistical studies of gaps to constrain the population of subhaloes (Erkal et al., 2016; Bovy et al., 2017). For the latter, there are not enough features in different streams identified yet to carry out these studies. This is expected to change with LSST data, which will provide deeper photometry for many low surface brightness streams. For studies of individual streams and perturbers, thin and cold streams such as GD-1 (Grillmair & Dionatos, 2006), ATLAS–Aliqa Uma (Koposov et al., 2014; Shipp et al., 2018), and Palomar 5 (Odenkirchen et al., 2001) are well-suited streams as they possess these features.

Dark matter subhaloes are not the only type of substructure that can produce these features. Other possibilities are both nonimpact scenarios and luminous objects as perturbers. Nonimpact perturbations come e.g. from the disruption process itself, where patterns come from epicyclic motions of the stars around the progenitor's orbit (Küpper et al., 2008, 2010, 2012); from a chaotic potential in which the streams evolve (Price-Whelan et al., 2016a), e.g. a potential containing a rotating bar or spiral arms (Pearson et al., 2017; Erkal et al., 2017; Banik & Bovy, 2019); and from initial disruption around a different host (Malhan et al., 2019, 2021). Luminous perturbers can be DGs, GCs, giant molecular clouds (Amorisco et al., 2016), and the stream crossing the Galactic disc. To confirm that a dark perturber caused a specific feature, these other possibilities need to be investigated and ruled out.

Many of these streams have been studied in great detail. The ATLAS–Aliqa Uma stream was initially detected as two streams, as there is a significant shift of the stream in the on-sky track. Li et al. (2021) show that the stream is connected and was massively perturbed to produce this 'kink'. They test possible perturbers and find that only an encounter with the Sagittarius DG can cause this feature. Ongoing research is

investigating impact scenarios with dark perturbers. They also find several 'broadenings' along the stream that might be the result of dark perturbers. Palomar 5 exhibits gaps, and its tidal arms have different lengths. Erkal et al. (2017) interpret the gaps as impacts from dark perturbers, while Pearson et al. (2017) finds that the asymmetry of the arm lengths and the gaps can be explained by the rotating bar. Bonaca et al. (2019) show that the spur and gap in GD-1 can be produced by an encounter with a massive, dense object. They also explore whether any luminous perturbations or nonimpact scenarios are likely and find that the dark perturber is the most probable solution. To confirm the encounter scenarios for the streams, better data of the perturbed regions of the streams, particularly kinematical data, are needed.

STREAMS IN EXTERNAL GALAXIES In the Milky Way, we have the most abundant and highest-quality data on stellar streams, allowing for complex investigations on dark matter. But just focusing on the Milky Way totals a sample size of $N_{\text{galaxies}} = 1$ and $N_{\text{streams}} \approx 100$. Extending research to external galaxies will (1) increase the sample of streams with features that could originate from dark substructures and (2) probe the dark matter haloes of an increasing number of galaxies.

The first observed external DG stream is the Giant stream around M31 (Ibata et al., 2001). Another prominent example is a DG stream around the closest ($D \sim 3.8$ Mpc) massive elliptical galaxy Centaurus A (Crnojević et al., 2016). With the `Hough Stream Spotter`, Pearson et al. (2022a) have identified candidate GC streams around M31. The 'Stellar Tidal Stream Survey' Martínez-Delgado et al. (2010, 2012, 2015) is a citizen science project where high-quality amateur observatories hosting a variety of mostly small reflector telescopes are taking coordinated observations of streams in the Local Universe complimentary to streams around the Milky Way and M31. The 'Stellar Stream Legacy Survey' (Martínez-Delgado et al., 2023) follows up on this work examining deep imaging data from the DESI Legacy Imaging Surveys (Dey et al., 2019), finding 24 new candidates of streams around galaxies at distances of $30 \text{ Mpc} \leqslant D \leqslant 100$ Mpc. A dedicated survey to take ultra-low surface brightness images of the haloes of nearby galaxies, ARRAKIHS (Analysis of Resolved Remnants of Accreted galaxies

as a Key Instrument for Halo Surveys), was selected as the new ESA fast mission, scheduled to launch in the early 2030s[9].

With new telescopes, particularly the Vera Rubin Observatory (LSST; Ivezić et al., 2019), Euclid (Laureijs et al., 2011), and the Nancy Grace Roman Space Telescope (Spergel et al., 2013), the discovery of thousands of extragalactic tidal features is expected. To make the most of this wealth of data, new methods need to be developed. This ranges from identifying streams in these datasets to understanding the information in these streams, given that most systems will not have distance or velocity measurements.

Firstly, there is a need for new and updated discovery algorithms. Any method that requires more than a stream track – therefore, most of the methods used to discover streams in the Milky Way – is not applicable to external galaxies. While extended observational surveys, also including citizen science surveys, deliver deep imaging of some streams, software that scans survey data to find streams more efficiently is necessary to build up a statistical sample. Algorithms that look for stream-like features such as the `Hough Stream Spotter` will be successful in discovering both DG and GC streams (Pearson et al., 2022a) in the survey data.

Secondly, with a variety of external streams and only track data available for their majority, it is important to understand the information they contain about their host and how they can be used to constrain its dark matter halo. Pearson et al. (2022b) show models of the stream around Cen A (Crnojević et al., 2016). They put a lower mass limit on Cen A and show that with only one radial velocity measurement, the constraints get more substantial, demonstrating the need for targeted radial velocity measurements in external streams. Nibauer et al. (2023) present an interesting approach to constraining the hosts' halo shape. They identify a connection between the curvature of a stream and the acceleration field of the host, allowing them to infer the shape parameters without the need for more expensive forward models of the stream. These are two recent examples. Over the next few years, in preparation for and with the data from the new telescopes, more ideas on how to discover and model external streams will be developed and published.

9 https://cosmos.esa.int/web/call-for-missions-2021/selection-of-f2

1.4.3 *The effect of the LMC on stellar streams*

Coming back to the Milky Way, we study stellar streams with complex models that allow us to understand the impact other substructures have on streams. The biggest substructure in the Milky Way halo is the LMC. As mentioned in the previous section, it emerged as necessary to include the LMC in fits to stellar streams in order to match observations. This opens up opportunities to put constraints on the gravitational potential of the LMC and on its orbit. Knowing these properties accurately will open new near-field cosmology opportunities.

THE EFFECT ON THE OC STREAM In an unperturbed stream, the proper motions of stars should point along the stream, while in a perturbed stream, they can point away from the track. The OC stream exhibits a strong misalignment of its track and its proper motion, particularly in the southern part of the stream. Erkal et al. (2019) and Koposov et al. (2023) show that the perturber is the LMC and present models that include an infalling LMC and the resulting reflex motion of the Milky Way, while the shapes of the galaxies are kept rigid. Fitting the OC stream with this model reveals an oblate Milky Way on the lower mass end of current estimates and an LMC with a mass of ~ 17 per cent of the Milky Way's. The model matches many data points well, yet it does not reproduce some observed quantities perfectly. For the halo shape, they find very flattened solutions for both oblate and prolate haloes, with a preference for the oblate solution. In Erkal et al. (2019), the orientation of the oblate halo is consistent with the orientation of the orbital angular momentum vector of the LMC, and the orientation of the prolate halo is consistent with the present-day vector to the LMC. While this still holds for the prolate halo in Koposov et al. (2023), the oblate halo shows a misalignment. The shapes being aligned with the LMC in any way is suspicious and a sign that we are missing something in the potential description. These strongly flattened solutions where the disc is not aligned with the short or long axis are not stable (Debattista et al., 2013). Given that the LMC probes the outer regions of the halo, the inner regions could have a different shape (see e.g Shao et al., 2021, for how the Milky Way halo shape can change with radius). Another possibility, which is explored in this thesis, is that with these strong flattenings, the fits might try to account for

the time-dependent deformations of the dark matter haloes of the Milky Way and the LMC, which are not included in the model.

Koposov et al. (2023) further find that the closest approach of the stream to the LMC was ~ 350 Myr ago with a distance of less than 10 kpc. This close approach of the OC stream and the LMC results in a narrower distribution of possible past orbits of the LMC than e.g. calculating the LMC orbits in a subset of realisation of the widely used McMillan (2017) Milky Way potential. The orbit of an infalling satellite depends on dynamical friction (Chandrasekhar, 1943). Dynamical friction has varying descriptions in different dark matter particle theories. Therefore, a well-constrained orbit of the LMC will be a powerful discriminator between different theories.

THE EFFECT ON THE SAGITTARIUS STREAM The OC stream is not the only stream affected by the LMC. Without the LMC, the notoriously difficult-to-model Sagittarius stream requires a highly flattened and unstable halo configuration (Law & Majewski, 2010) to match at least some observables. Vera-Ciro & Helmi (2013) create simple models of the stream that included an LMC, and Gómez et al. (2015) include the LMC in a suite of N-body simulations of the stream without attempting to fit it. Both find that including the LMC has a significant effect on the properties of the stream and how its tidal tails form. For the first time, Vasiliev et al. (2021) present a well-matching fit to the Sagittarius stream that includes the LMC and the reflex motion of the Milky Way disc. Allowing for triaxial shapes, the inferred Galactic halo changes its shape with radius, from oblate in the inner regions to almost oblate in the outer halo but with a significantly changing orientation of the halo. As Erkal et al. (2019), they find the orientation of the short axis aligned with the orbital pole of the LMC. Koposov et al. (2023) show that there is a clear offset in the orientations of the Milky Way halo in different stream fits and that the inferred shapes from the Sagittarius stream and the OC stream are inconsistent.

THE EFFECT ON OTHER STREAMS IN THE SOUTHERN HEMISPHERE With the OC and the Sagittarius stream, two significant streams are affected by the LMC. Generally, streams that pass closely to the LMC with a small enough velocity difference are perturbed. After discovering new streams in DES (Shipp et al., 2018), which has a footprint

covering the recent orbit of the LMC, Shipp et al. (2019) find a significant proper motion offset for some streams. Based on this discovery, Shipp et al. (2021) model the affected streams and infer strong LMC mass constraints from all but one of these streams. This shows how useful some stellar streams are by not only containing information on the Milky Way but also on the LMC and opens an opportunity to learn even more about the dark matter distribution around our Galaxy.

1.5 STELLAR STREAMS IN DEFORMING HALO POTENTIALS – THESIS OVERVIEW

Recent work has shown that the LMC is on its first approach and that it has a substantial dark matter halo. Thus, the Milky Way–LMC system is effectively a dark matter collider. This opens new avenues of testing and constraining the nature of dark matter. Stellar streams are sensitive probes to the Galactic potential and are possible detectors in this dark matter collider. In this thesis, I aim to answer several questions:

- Are stellar streams affected by the deformation of the haloes of the Milky Way and the LMC?
- Which of the galaxies' haloes has a more significant effect?
- What are the modes of the deformations that perturb the streams?
- Which streams are the most affected? Is there a specific stream property that determines this?
- Are stream models that do not include the deformations biased? Could this be an explanation for the very flattened DM haloes inferred from fits?
- Finally, to be answered in the long term, can we, with the help of stellar streams, explicitly prove that the dark matter haloes of both galaxies are time-dependent?

To answer these questions, I utilise two main technological tools: stream models and simulations that describe the deforming Milky Way–LMC system; these are introduced in Chapter 2. In Chapter 3, I present how the OC stream is affected by the deforming Milky Way–LMC system. There, I investigate which galaxy and which mode of deformation are the most significant perturbers. Chapter 4 contains a statistical approach

to finding the properties of streams that hold the most information on the deformations on the haloes. The results will guide future fits of the time-dependent Milky Way. Current fits that do not include these deformations might be biased. In Chapter 5, I investigate the extent of the bias in stream fits; which parameters are likely wrong and by how much? Finally, in Chapter 6, I summarise the results of the thesis and give an outlook on the exciting research that will follow.

2

METHODOLOGY

2.1 BASIS FUNCTION EXPANSIONS

In order to understand how the merger of the Milky Way and the Large Magellanic Cloud (LMC) affects stellar streams, we need a way to describe the time-dependent deformations of both galaxies. This description should be easily accessible for force evaluations for fast stream models. Basis function expansions (BFEs) are well-suited to tackle this task. They describe the dynamical evolution of a gravitational system with a set of functions and coefficients that act as weights for these functions. This functional representation makes it quick and easy to access and evaluate quantities of the system, such as the potential, density, and acceleration, allowing for a wide range of applications. In this section, I describe where BFEs are used, provide a qualitative explanation, the history of their developments, and the specific BFE code we use for our work, `EXP` (Petersen et al., 2022a).

2.1.1 *The need for basis function expansions*

BFEs enable stream models in the deforming Milky Way–LMC system

The aim of this thesis is to explore how stellar streams in the Milky Way halo are impacted by the Milky Way–LMC interaction, particularly by their deforming dark matter haloes. We aim to answer questions such as:

- Are stellar streams affected by this interaction?
- Which streams are affected by this interaction?
- How much does the dark matter halo of each galaxy affect stellar streams?
- Which modes of deformation have the biggest impact on stellar streams?

To dissect the time-dependent Milky Way and LMC haloes into their respective modes of deformation and to quantify their potential and acceleration fields to allow for quick stream models, we need non-parametric descriptions of this interaction, i.e. BFEs.

The BFEs which we use in this work come from simulations of the LMC infall onto a Milky Way-like galaxy. In these simulations, we use three separate expansions: one for the Milky Way's dark matter halo, one for the Milky Way's disc and bulge, and one for the LMC. These coefficients are time-dependent and describe the time-dependent deformations of both systems. We compute these coefficients with N-body simulations of the Milky Way and LMC (described below). Once they have been computed, we can then use the coefficients to evaluate the properties of the galaxies, such as potential, density, and forces, as functions of position and time. This allows us to run efficient and inexpensive stream models in the presence of this interaction. Each degree and order of deformation is described by one coefficient, where the degree is e.g. the dipole, and the order quantifies the shape and direction. Setting a coefficient to zero in the expansion eliminates the effect of that mode, allowing us to only select the modes we are interested in. With descriptions for each component and the possibility to select a subset of coefficients that describe different modes of deformations, we are equipped with the tools to answer these questions.

BFEs as a tool to study dynamical interactions

BFEs are used to study a variety of interactions in and around the Milky Way. While this work focuses on the effect of the Milky Way–LMC interaction on stellar streams, there are many other effects the LMC has on the Milky Way. For example, two currently observable effects that the Milky Way is experiencing are the reflex motion of its disc and over- and underdensities in the stellar halo. We will discuss these effects before moving on to stellar streams.

The LMC's gravitational pull affects the inner MW halo more strongly than the outer halo, due to the inner halo's shorter dynamical time (e.g. Erkal et al., 2020). The centre of mass of the inner halo is accelerated towards the LMC and shifts with respect to the outer halo. This is known as the reflex motion of the disc. In a Galactocentric coordinate system, this movement is roughly downwards. As observers in the disc, we see this as an upward motion of the stellar halo. This effect was first predicted by

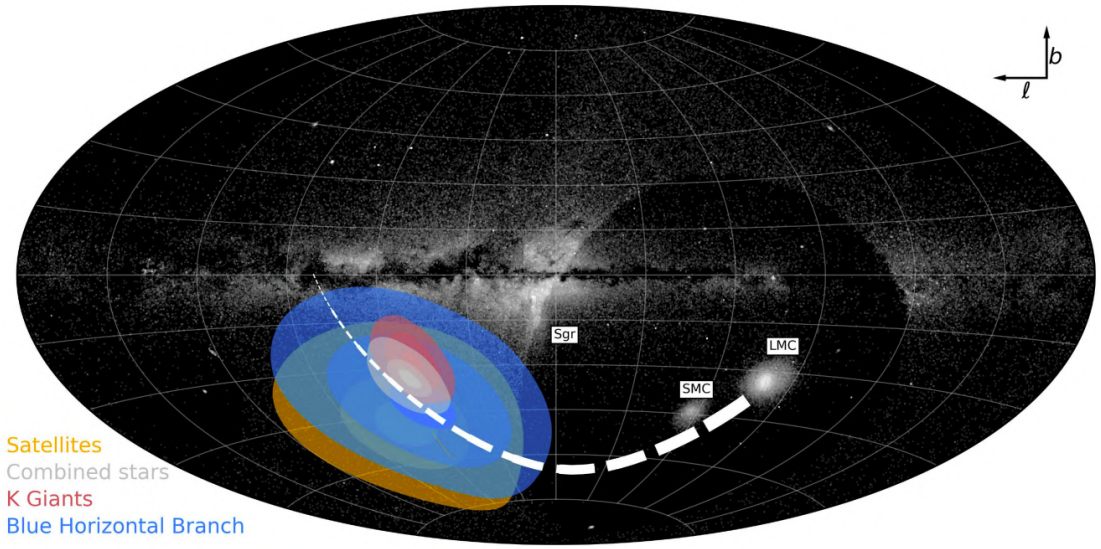

Figure 2.1: The direction of the reflex motion of the stellar disc, inferred from different sets of distant halo tracers shown in differently coloured contours. The black-and-white background represents RR Lyrae stars from Pan-STARRS DR1 (Sesar et al., 2017) and *Gaia* DR2 (Holl et al., 2018; Rimoldini et al., 2019). The disc moves towards the past orbit of the LMC (indicated by the white dashed line). *Credit:* Petersen & Peñarrubia (2021).

Gómez et al. (2015) when the total mass of the LMC was less constrained. With better constraints of the LMC mass due to e.g. fitting it with the OC stream (Erkal et al., 2019), Petersen & Peñarrubia (2020) – using BFE simulations – and Erkal et al. (2020) – with a set of semi-analytic simulations – made predictions on the dipole signature in the halo and the reflex motion of the disc. Erkal et al. (2021) detected this effect in the radial velocities of distant halo stars, and Petersen & Peñarrubia (2021) detected this signature in different samples of distant halo tracers; Petersen & Peñarrubia (2021) find that the disc moves with $v_{\rm travel} = 32 \pm 4\,{\rm km\,s^{-1}}$ with respect to the outer halo towards the past orbit of the LMC (Figure 2.1).

Next, we discuss the overdensities in the stellar halo. Garavito-Camargo et al. (2019) present N-body simulations of the Milky Way–LMC interaction run with GADGET-3 (Springel et al., 2008). In Garavito-Camargo et al. (2021a), they fit the snapshots with BFEs to investigate the response of the Milky Way halo. They identify a global response of the halo that is revealed by a density asymmetry between the Northern and Southern hemispheres *(collective response)*. They also recover a wake due to the dynamical friction of the LMC along its past orbit. Belokurov et al. (2019) show that the Pisces overdensity is consistent with the wake of the LMC in the stellar halo. In Conroy et al. (2021), these

predictions for overdensities in the Milky Way halo were followed up with observations of distant halo stars, finding overdensities both in the Northern hemisphere and along the LMC's past orbit. However, the amplitude of the overdensities and the shape of the collective response differ from the simulations This suggests the need for a bigger observational sample and more simulations of the Milky Way–LMC interaction.

Applications to cosmological simulations

With the ability of BFEs to describe perturbed and time-dependent systems in a cheap and accessible way, another important application for them is the description of cosmological simulations. They offer such an insightful environment that it would be useful to replay them in order to e.g. disrupt substructures as if they were evolving in the initial simulation. But due to the nature of cosmological simulations, i.e. evaluating forces between all particles ideally in high-resolution on large scales, it is expensive to rerun them. Expanding snapshots of the simulation with BFEs provides a quick and computationally efficient description of the simulation; integrating structure in this cosmological context is now possible.

For the first time, Lowing et al. (2011) expanded a dark matter halo from an already simulated dark matter halo – the Aquarius simulation, a Milky Way-sized dark matter-only simulation (Springel et al., 2008). They expanded the simulation with a spherical basis (see Section 2.1.3) and introduced subhaloes into this potential that evolve as if they were in the original Aquarius simulation. More recently, Sanders et al. (2020) expanded cosmological simulations with BFEs over a range of times. They show two applications of their machinery. First, they investigate the effect of the time dependence on the orbit of satellites and find that assuming a time-independent halo introduces a 15 per cent uncertainty in their orbital properties. Second, they examine the build-up of planes of satellites. They do not find a significant effect from the time dependence of the halo and find that the plane is affected more by its alignment with the triaxial halo (which can be affected by the time dependence of the halo).

Along similar lines, Ngan et al. (2015, 2016) expand the Via Lactea II halo (Diemand et al., 2008) at redshift $z = 0$ to investigate the disruption of globular clusters (GCs) and investigate the effect of the presence of other subhaloes. Dai et al. (2018) expand the *Eris* simulations (a hydrodynamical simulation; Guedes et al., 2011) at $z = 0$ and

infer its halo shape with GD-1 and Pal5-like streams. They find that streams evolved in a halo that includes baryonic physics match the observed data, while streams evolved in the dark matter-only *ErisDark* halo (Pillepich et al., 2014) do not. These studies investigate how streams evolve in a cosmological context, but by only expanding the $z = 0$ snapshot, the resulting potentials are time-independent. Furthermore, these simulations are not directly matched to the Milky Way, i.e. they do not match the Milky Way potential, and they do not have an LMC equivalent. The aim of my thesis is to examine the evolution of stellar streams in a realistic Milky Way potential that includes the LMC. As a first step towards modelling this, we use BFEs to simulate and describe the Milky Way–LMC system and to evolve stream models in it.

Other science cases with BFEs

Systems that are described by BFEs have a broad application for a variety of astrophysical questions, ranging from predictions for observations, addressing current problems in cosmology, and informing direct and indirect dark matter searches. Petersen et al. (2022b) predict the extent of the LMC halo in the search for tidally stripped stars, finding several candidates up to 68° from the LMC. Garavito-Camargo et al. (2021b) find a possible explanation of the plane of satellite problem; infalling massive satellites can induce a transient pile-up of the orbital poles of other satellite galaxies. They are also used to predict how the local dark matter distribution is affected by the LMC debris (Donaldson et al., 2022; Smith-Orlik et al., 2023) and where to expect gamma-ray excesses from dark matter annihilation due to the deformations of the haloes (Eckner et al., 2023).

2.1.2 *A qualitative introduction to basis function expansions*

In this section, I explain how basis function expansions can describe complicated, non-parametric potential and density fields. First, I will explain how the potential and density are described in a self-consistent way, following Petersen et al. (2022a). Then, I will schematically show how BFEs use different moments to build up the deformations of a perturbed galaxy.

Potential and density described by functions and coefficients

With BFEs, the potential and the density of the system are described by a set of functions (the basis). The functions for the potential ϕ_μ and the density ρ_μ[1] are related through the Poisson equation, $\nabla^2\phi_\mu = 4\pi G\rho_\mu$. These potential–density pairs are required to be biorthogonal. This means that the pair is an indexed family of functional vectors in some topological functional vector space with the inner product of the pair being the Kronecker delta, noted as $\langle\tilde{v}_i, \tilde{u}_j\rangle = \delta_{i,j}$. Together with the relation through the Poisson equation, this is constructed for BFEs as

$$\int d\vec{x}\phi_\mu(\vec{x})\rho_\nu(\vec{x}) = 4\pi G\delta_{\mu\nu}. \tag{2.1}$$

A linear sum of M of these potential functions approximates the potential Φ, likewise for the density ρ, where each function is weighted by a coefficient a_μ:

$$\Phi(\vec{x}) = \sum_{\mu=1}^{M} a_\mu\phi_\mu(\vec{x}) \tag{2.2}$$

$$\rho(\vec{x}) = \sum_{\mu=1}^{M} a_\mu\rho_\mu(\vec{x}). \tag{2.3}$$

In an N-body simulation with N particles, the coefficients a_μ are calculated following

$$a_\mu = \frac{1}{N}\sum_{i=1}^{N}\phi_\mu(\vec{x}_i) \tag{2.4}$$

where $(\vec{x}_i)$ are the positions of the particles. The choice of functions and the complexity of the system determines how many functions and, therefore, coefficients are necessary. In a time-dependent system, the basis, generally, stays constant while the coefficients vary to describe the changing system[2].

The functions are selected to match the system they describe. For example, a spherical system can be described by functions that evaluate the potential and density at a radius and at the polar and azimuthal angles. One radial (indexed by n) and two

1 Note that Petersen et al. (2022a) and others often refer to the density in the biorthogonal system as d_μ. Their notation is used in Chapter 3.

2 If the system changes significantly over the evolution, one could find a new set of functions that matches the system better.

angular functions (indexed by l, m) are necessary to calculate the potential $\phi_n^{lm}(\vec{x})$ and density $\rho_n^{lm}(\vec{x})$ and their coefficient a_n^{lm}. In an N-body simulation, the coefficients are selected in such a way that they approximate the potential described by each subset summed over all particles (Equation 2.4). The potential and density are initialised from the underlying unperturbed model, and then the coefficients are updated at the next full time-step. Once the coefficients for the whole course of the simulation are calculated and tabulated, the expansion of the system is completed.

Now we want to access the expansion at any time and position to evaluate densities, potentials and forces. This is done by accessing the tabulated coefficients and multiplying them with their respective functions. The fields at a time and position are evaluated by summing over all coefficients at that time (linearly interpolated between the nearest tabulated time steps if necessary[3]) multiplied with the corresponding functions evaluated at the position. To isolate the effect of different contributions to the perturbation, the coefficients of other functions can be set to zero. With this, in the next section, I show a visual guide on how we build up a spherical expansion of increasing complexity from the different functions.

Constructing complicated fields from a simple model with BFEs

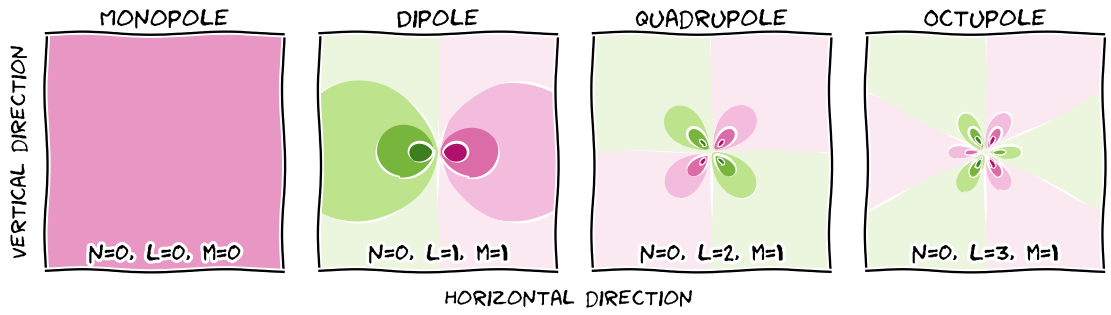

Figure 2.2: Sketch of the density differences with respect to the monopole from different spherical harmonics at zeroth radial order $n = 0$. These are contextual visualisations in a cartesian coordinate system; they are not to scale. The monopole is compared to itself; thus, there is no or a constant offset. The dipole, which has the index $l = 1$ and is shown here for the order $m = 1$, adds and subtracts an equal amount along a symmetry axis. The symmetry axis is set by the order m of the spherical harmonic. The quadrupole and the octupole at $m = 1$ each add a symmetry axis. In other orders and higher degrees, spherical harmonics become increasingly more complex.

3 See Petersen et al. (2022a, section 4.2) for a detailed description.

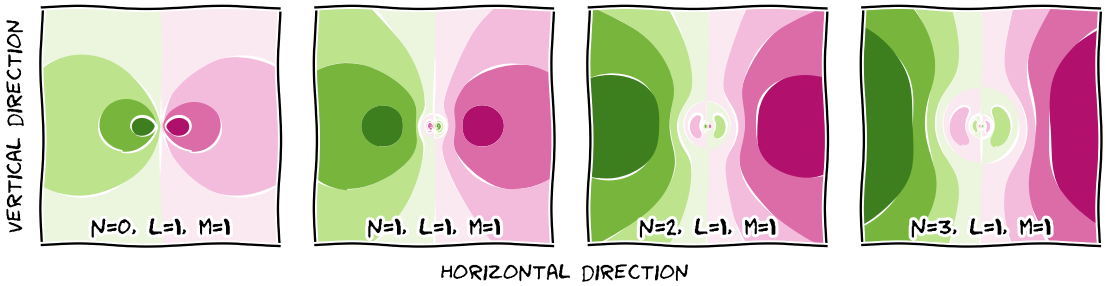

Figure 2.3: Sketch of the density offset of the dipole calculated at different radial orders n. The left panel shows the dipole from Figure 2.2. Each panel shows the dipole of order $m = 1$ described for an increasing radial order n. The zeroth radial order adds the most offset in the central parts; higher n shift the bulk of densities at increasingly larger radii while adding some alternating density offsets in the central parts. When a large offset in the dipole is induced, it is best described by the zeroth radial order. Higher radial orders are necessary to describe perturbations further out. As these perturbations are usually smaller, the weight of higher radial orders is usually smaller than the weight of the zeroth order.

In this section, I will show how different basis functions build up a perturbed LMC-like galaxy. Both a BFE-simulated Milky Way and LMC are introduced and shown in Chapter 3; here, I use the LMC as an example due to its larger visual perturbation.

BFEs that describe a spherical system, e.g. a Plummer (Plummer, 1911), Hernquist (Hernquist, 1990) or Navarro–Frenk–White (NFW; Navarro et al., 1996) profile, are well-represented by spherical harmonics as their angular functions and a series of eigenfunctions of the Sturm–Liouville equation as the radial solutions (a mathematical description can be found in Weinberg, 1999; Petersen et al., 2022a).

In a series of figures, I sketch the density profiles introduced by spherical harmonics (Figure 2.2) and by radial functions (Figure 2.3). Then, for the simulated LMC, I show how the combinations of these functions produce a highly perturbed LMC-like galaxy (Figure 2.4) and how that deformation builds up with time (Figure 2.5).

Figures 2.2 and 2.3 are produced with the self-consistent field method implemented in `gala` (Price-Whelan, 2017; Price-Whelan et al., 2022). The contours are the relative density offset compared to the monopole following Garavito-Camargo et al. (2021a), $\Delta\rho = \left(\rho - \rho_0^{00}\right)/\rho_0^{00}$. The LMC in Figures 2.4 and 2.5 is taken from a Milky Way–LMC simulation with the BFE technique `EXP`; the technique is explained in Section 2.1.4, and the details of the simulation are described in Section 3.2.

Spherical harmonics allow BFEs to capture different types of deformations; e.g. the dipole can be interpreted as a result of the dislocation of the Milky Way disc, and the

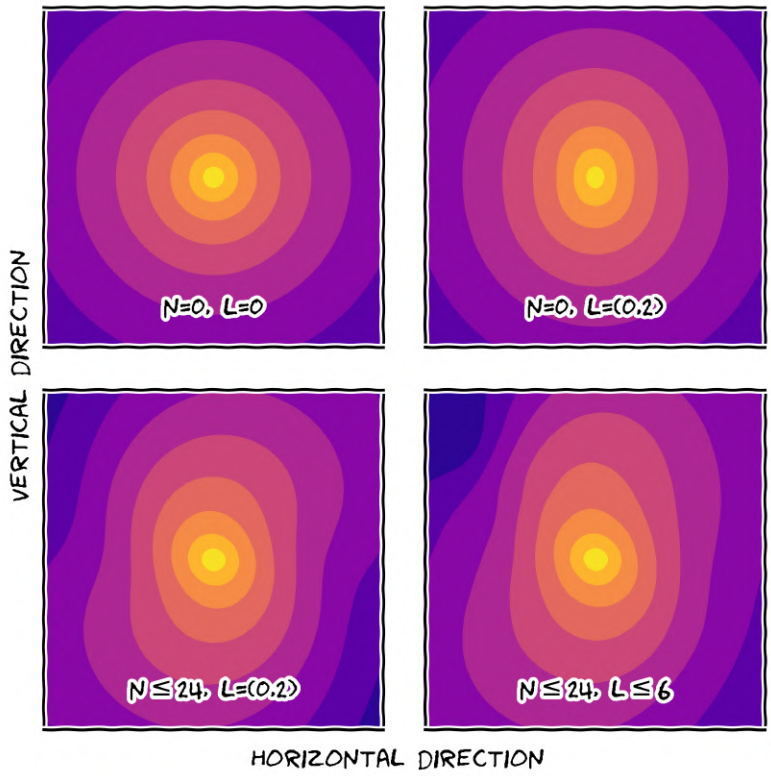

Figure 2.4: A schematic illustration of how different radial terms and degrees of spherical harmonics are combined to build a perturbed halo, shown as density contours. The top left panel shows the monopole of a spherical halo, $l = 0$, with only the zeroth-order radial order, $n = 0$. The top right panel shows these density contours with an added $n = 0$ quadrupole, $l = 2$. This stretches the galaxy in the vertical direction. The bottom row shows the deformations with many radial orders. The bottom left panel shows the monopole and quadrupole. The halo is now stretched and twisted but still mostly symmetric. The fully deformed galaxy is shown in the bottom right corner. For this galaxy, adding more degrees of spherical harmonics leads to more intricate changes on smaller scales and introduces more asymmetry. This shows how with BFEs that consist of different spherical harmonics and different radial orders, complicated deformations can be described in an efficient way.

quadrupole has an intuitive physical application as the flattening of a galaxy. Higher-order moments describe more localised details of the deformations. The radial orders, even though they act globally, shift the distance of the bulk of the deformation described by the spherical harmonic function. The weight that is applied to each function ρ_n^{lm} generally decreases with increasing radial and angular orders.

Figure 2.4 shows that in order to get a highly-detailed description of deformations, a combination of several radial and angular terms is needed. While the functions $\phi_n^{lm}(\vec{x})$ and $\rho_n^{lm}(\vec{x})$ (Equations 2.2 and 2.3) do not change over time, their weights a_n^{lm} (Equa-

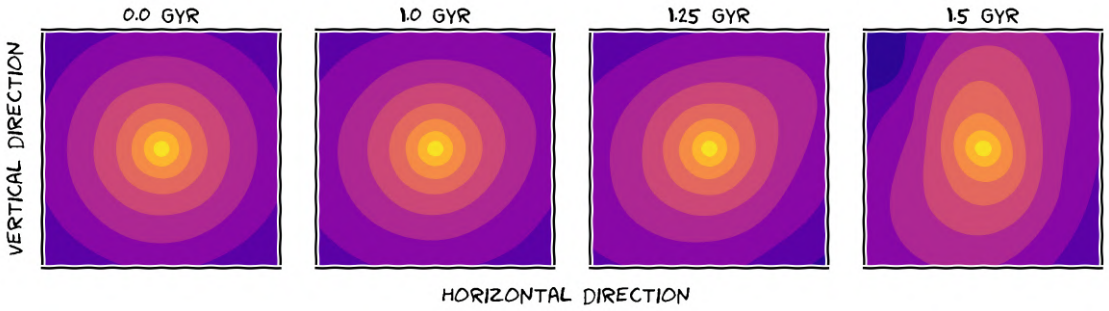

Figure 2.5: Density evolution of a fully deforming galaxy parametrised by BFEs, shown in Figure 2.4. All l, m, n are included up to their respective highest orders. In this system, the galaxy stays almost spherical for the first Gyr and only experiences some stretch. Over the next 250 Myr, the stretch becomes more distinct and asymmetric. At the final snapshot, after 1.5 Gyr, the system is stretched, twisted and asymmetric. The orientation of the system rotates as it orbits the host galaxy that is responsible for the perturbations. This time-evolution is based on the LMC in a Milky Way–LMC simulation run with `EXP`, which is introduced in Sections 2.1.4 and 3.2. The final snapshot and the full evolution of both the LMC and the Milky Way densities is shown in Figure 3.2. This drastic deformation from an initially spherical system shows that we need to explore its effect on other structures in the halo.

tion 2.4) do as the particles in the simulations are in motion. This allows BFEs to capture the evolution of a deforming system as shown in Figure 2.5.

2.1.3 *Brief history of biorthogonal expansions*

The idea to use biorthogonal basis sets to computationally describe stellar dynamics was suggested 50 years ago by Clutton-Brock (1972, 1973). Over the next 25 years, 'analytical' sets of biorthogonal functions were developed where the underlying zeroth order describes a known model. For spherical systems, the Clutton-Brock (1973) zeroth-order basis matches a Plummer profile (Plummer, 1911) while the Hernquist & Ostriker (1992) zeroth-order basis is a Hernquist profile (Hernquist, 1990). Hernquist & Ostriker (1992) dubbed this method the self-consistent field method. Similarly, expansions for two-dimensional cylindrical systems (Clutton-Brock, 1972; Kalnajs, 1976), and even for three-dimensional cylindrical systems (Earn, 1996) were developed. More recently, Lilley et al. (2018a) developed a 'super-NFW' potential with a finite mass that is used as the zeroth-order term for an expansion that represents the (flattened) NFW (Navarro et al., 1997) model in Lilley et al. (2018b). Lilley et al. (2018c) present a 'super-family' of spherical basis sets that have double-power law density profiles (including

the bases found in e.g. Clutton-Brock, 1973; Hernquist & Ostriker, 1992; Lilley et al., 2018b), and a new methodical approach to finding these basis sets.

Still, these expansions only cover a small subset of zeroth-order radial profiles. Weinberg (1999) developed an efficient numerical solution of the Sturm–Liouville equation in order to match a wide variety of density profiles. This is implemented in the EXP code (Petersen et al., 2022a) that was developed ever since (Weinberg & Katz, 2002; Holley-Bockelmann et al., 2005; Weinberg & Katz, 2007a,b; Choi et al., 2007, 2009; Petersen et al., 2016) and is close to being publicly released. Other 'designer' basis functions are developed in Saha (1993) and in Lilley & van de Ven (2023), where they tailor the basis in the radial direction.

Since *Gaia* has revealed that the Milky Way is in disequilibrium, both due to internal (e.g. the bar and spiral arms) and external (the LMC, Sagittarius, and GSE) perturbers, BFE methods have experienced a large uptake. The Hernquist & Ostriker (1992) expansion has a good accuracy compared to other expansions (Sanders et al., 2020), thus it is widely used (e.g. Johnston et al., 2002; Lowing et al., 2011; Ngan et al., 2015; Garavito-Camargo et al., 2021a). The EXP technique has several advantages over the Hernquist & Ostriker (1992) basis and is used in this work. In the next section, I will give a brief summary of the EXP method.

2.1.4 *The EXP code*

The EXP code[4] (Petersen et al., 2022a) is a BFE-based N-body solver. With that functionality, it also allows expanding other arbitrary distributions with BFEs, e.g. cosmological zoom simulations. The basis of an expansion is adapted to the input mass distribution. This is a powerful feature as it enables EXP to expand highly non-spherical components such as discs and bars. I present a short overview of some specifics but refer to Petersen et al. (2022a) for a detailed introduction to the theory and to Weinberg (1999) for the initial development of this method.

Bases

The unique advantage of EXP is that adaptive bases are constructed that describe the equilibrium distribution of the system in one or, at most, a few basis functions. Higher-

4 michael-petersen.github.io/papers/exp/exp.html

order terms are then only necessary to describe the perturbations to the system. If a system consists of multiple geometries on different scales, the system can be decomposed into different components that are each described by a set of basis functions.

In EXP, adaptive bases are found by describing a target particle distribution with a set of potential functions. With increasing moments μ, the weights on the functions become less important to capture the contributions in the smallest number of terms; thus, the coefficients should converge towards zero. Transforming this to a new orthogonal basis might give a quicker convergence. The goal is to find a basis that contains the largest amount of gravitational field energy in the smallest number of terms, i.e. to optimise the basis in a *least-square sense* (Weinberg, 1996). The initial 'guess' of the basis is often an already existing basis, e.g. Petersen et al. (2022a) show how to construct a cylindrical basis from a spherical basis. Further details and a mathematical description of this adaptive basis conditioning are given in Petersen et al. (2022a).

Advantages and disadvantages of the EXP code

EXP is a great tool to study galactic dynamics as it delivers several benefits and some advantages to previous simulation suites:

- EXP is fast. The simulations scale as $\mathcal{O}(N)$, in contrast to direct techniques that scale as $\mathcal{O}(N^2)$ or tree-based techniques as $\mathcal{O}(N\log N)$, where N is the number of particles in the N-body simulations. This means more simulations at fixed computational cost or more parameter space that can be covered.

- EXP has a particular but controllable bias-variance trade-off. One can get more accurate potentials out of EXP at fixed particle number (Petersen et al., 2022a). This is particularly important in the outer halo, where particle-based methods (i.e. direct or tree) can have huge noise and variance.

- EXP can be re-run infinitely to produce exactly the same potential and force fields: a BFE approximation of a tree code will not do this but will instead 'bake in' the tree gravity noise.

- EXP can be directly compared with results from applying linear perturbation theory to the Milky Way–LMC interaction, e.g. Rozier et al. (2022).

- EXP can be used to simulate different dark matter models. EXP allows us to choose the scales of interest for evolution; thus, one can mock up coupling between different gravitational scales. Furthermore, one can create effective solutions by not having nodes in the centre, or create warmer dark matter by having a very smooth distribution in the outskirts, i.e. by not inducing subhaloes, which are roughly injected by particle discreteness in current implementations.

As with any N-body solver, there are limitations; for some problems, other solvers are more appropriate. Most importantly, due to the nature of BFEs, EXP is not fully adaptive and cannot integrate arbitrary systems, such as systems with self-gravitating regions or have complex geometries, e.g. major mergers. For this, a tree-based code is a more suitable solution. Artefact patterns are another disadvantage. As an example, they can be seen in the density evolution of the Milky Way–LMC system in the video[5] of Figure 3.2. Care needs to be taken to ensure that these artefacts do not have an influence on the evolution of the system.

Having established that BFEs are powerful techniques to study galactic dynamics and that EXP is an adequate tool for our purpose of studying the Milky Way–LMC interaction, I will give an overview of stellar stream modelling. Combining both tools will enable us to study stellar streams in the deforming Milky Way–LMC system.

2.2 MODELLING STELLAR STREAMS

An analytical or numerical description of stellar streams allows us to understand and use many aspects of their dynamics. Scientific goals include constraining the parameters of the Galactic halo and of the LMC, understanding the impact and constraining the parameters of perturbing substructures, and studying the disruption and the structure of a stream in great detail. There are different methods to model streams. Some are quick and computationally cheap but have less detail, while others are more detailed but expensive. The choice of method depends on the scientific goal, the structure of the stream, and the available computational power.

5 https://youtu.be/KMeGVMXfLTw

2.2.1 *Overview of stream-modelling methods*

Stream models are generally based on the assumption that the debris closely follows the progenitor's orbit (Dehnen et al., 2004; Eyre & Binney, 2011) but not exactly (Sanders & Binney, 2013a) and is therefore highly sensitive to the gravitational potential. Different methods include the orbit-fitting technique, action-angle-frequency methods, N-body simulations, and particle-spray methods. A review of these techniques can be found in Johnston (2016) and of how they are used to probe dark matter in Johnston & Carlberg (2016).

ORBIT-FITTING TECHNIQUE This technique fits orbits to streams. It is a very fast method, as only the progenitor particle is integrated in the gravitational potential to calculate the orbit. The model input consists of the parameters of the gravitational potential and a 6D phase-space coordinate of the particle. It is often used to fit the Milky Way halo with the GD-1 stream (e.g. Koposov et al., 2010; Malhan & Ibata, 2019). While this method is very fast, it is not very accurate as on a perfect orbit, a stream would not build up with time but rather have an oscillating length between peri- and apocentre. It can introduce biases in the fitted parameters (Sanders & Binney, 2013a).

ACTION-ANGLE-FREQUENCY METHODS Actions are orbit labels, and angles represent the positions of the particles along the orbit (see Binney & Tremaine, 2008 for an introduction to actions and Sanders & Binney, 2016 for an overview of action estimation methods). Actions are calculated from the gravitational potential and orbital parameters such as the phase-space position or the peri- and apocentre. To be able to calculate actions, the gravitational potential needs to have separable Hamilton–Jacobi equations (Stäckel potentials), limiting the possible potentials to spherical potentials. Clever tricks such as the Stäckel Fudge (Binney, 2012; Sanders & Binney, 2015a) allow non-spherical potentials to be estimated as separable Stäckel potentials. For streams, however, computing the actions from an orbit integration is a more suited method (Sanders & Binney, 2016). Frequencies are the rate at which the angles increase. Since the orbits of stream particles follow the progenitor's orbit to an extent (Sanders & Binney, 2013a), their action-angle coordinates are only marginally offset from the progenitor's (Tremaine, 1999; Helmi & White, 1999; Eyre & Binney, 2011; Sanders & Bin-

ney, 2013b). These offsets propagate into the particles' frequencies, driving the growth of the stream. The gravitational potential is constrained by fitting these frequencies, which conveniently follow simple lines (Bovy, 2014; Sanders, 2014).

In an adiabatically growing potential, the slopes of the frequency and angle lines of a stream change, affecting the stream's morphology (Buist & Helmi, 2014, 2015). While Buist & Helmi (2015) propose to use this angle-frequency misalignment to infer the growing rate of the potential, Buist & Helmi (2017) find that these misalignments are mostly attributed to using a wrong potential. Only with the correct present-day potential of the Milky Way – which is still debated – the evolution of the potential could be constrained with this method.

Another way to utilise the actions of stream members without fitting the stream is 'adaptive dynamics' (Binney, 2005). It calculates the actions of stream members assuming an underlying gravitational potential without the need to integrate an orbit or a stream, therefore discarding a lot of information that is held by the highly correlated phase-space distribution of the stream. This method assumes that the actions are most clustered in the correct gravitational potential. Therefore, maximising the clustering leads to the best constraints (e.g. Sanderson et al., 2015; Reino et al., 2021, 2022). However, taking into account the time dependence of the accreting galaxy reveals biases in this method (Lilleengen et al., 2020; Arora et al., 2022).

N-BODY SIMULATIONS The most accurate model of stellar streams is achieved with N-body simulations, e.g. with `NBODY6` and its extensions (Aarseth, 2003; Wang et al., 2015). The forces each particle experiences are from the potential of the host galaxy, the progenitor potential and from the other particles in the stream. Therefore, this method is only insightful with a robust knowledge of the progenitor. A great advantage of this method is that it correctly matches the scattering of stars, and it can even include stellar evolution (e.g. Gieles et al., 2021). As they are computationally expensive to run, they are not very well-suited for fits to stellar streams. The largest N-body simulations suite to fit a stellar stream was carried out by Law & Majewski (2010) to fit the Sagittarius stream. More effective methods to fit a stream with a full stream model have been developed since, such as the method described in the next paragraph. Still, N-body

simulations are insightful in exploring the details of the stream's formation and its structure and comparing them to observations.

PARTICLE-SPRAY METHODS In order to explore a large parameter space when fitting stellar streams, particle-spray methods are used to create realistic stream models (e.g. Küpper et al., 2008, 2010, 2012; Gibbons et al., 2014; Fardal et al., 2015). The input parameters include the phase-space position of the progenitor, the underlying gravitational potential, and a progenitor potential This technique releases massless stream particles from the progenitor at its tidal radius. The released particles experience the potential from the host galaxy (and in recent implementations from the progenitor) but not other stream particles. The morphology of the resulting stream compares remarkably well to N-body simulation streams. Furthermore, this method is strikingly faster than N-body simulations since it does not rely on calculating the forces between the stream particles (Gibbons et al., 2014). However, as for the N-body simulations, some knowledge about the progenitor is necessary. Since the progenitor is often completely disrupted, it is an unknown input quantity, but it can be marginalised over (Price-Whelan et al., 2014). I use this method throughout this thesis and describe it in more detail in the next section.

NON FORWARD-MODELLING STREAMS All presented methods are parametric models of stellar streams, i.e. they require a choice of gravitational potential and progenitor initial conditions (ICs). There are some methods to investigate streams and to fit the gravitational potential that deviate from these methods. Streams form naturally in zoom-in cosmological simulations with high enough particle resolution. Currently, the resolution limits only allow for massive dwarf galaxy (DG) streams to form (e.g. Panithanpaisal et al., 2021). Once streams are identified (e.g. Panithanpaisal et al., 2021, for streams in the FIRE simulations), they can be studied in a cosmological context. Shipp et al. (2022) analyse the FIRE streams in regard to the 'too big to fail' question brought up by Li et al. (2022) and find that the detection limit currently prevents us from finding more massive streams around the Milky Way.

Another approach to constraining the acceleration field of the Milky Way is taken by Nibauer et al. (2022) who do not need to make assumptions on the underlying

gravitational potential. They treat streams as a mixture of orbits where neighbouring parts of the stream have similar orbits, but the orbits can change significantly along the stream. Using a neural network, they construct a path through the stream in all observables. This path is differentiable, allowing them to calculate the acceleration vector along the stream. Combining the accelerations for different streams allows them to infer a global acceleration field and, with that, a global potential.

2.2.2 *The modified Lagrange Cloud Stripping method*

In a series of papers, Küpper et al. (2008, 2010, 2012) developed a particle spray method called Lagrange Cloud Stripping. It is a forward-modelling method; first, the progenitor is rewound in the gravitational potential of the host system. The rewind time is chosen so that the stream will be long enough to cover the whole data range. Then, the progenitor is integrated forward in time, as are the escaping stream particles.

In the Lagrange Cloud Stripping method, particles leave the progenitor in the Lagrange points x_L, where the gravitational potential of the progenitor equals the gravitational potential of the host galaxy Φ,

$$x_L = \left(\frac{GM}{\Omega^2 - \partial^2\Phi/\partial R^2} \right)^{1/3}, \tag{2.5}$$

with the gravitational constant G, the mass of the progenitor M, the progenitor's angular velocity about the Galactic centre Ω, and the progenitor's Galactocentric distance R (King, 1962; Küpper et al., 2010, 2012; Gibbons et al., 2014). There are two Lagrange points in a progenitor along a line connecting the progenitor to the Galactic centre at $R \pm x_L$. Particles leaving the progenitor in the closer Lagrange point form the leading arm, while particles escaping in the Lagrange point further away form the trailing arm.

The Küpper papers develop the methods for star clusters, i.e. GCs. They assume that once a particle has left the progenitor, it only feels the gravitational potential of the host galaxy. In order to adapt this method to DGs, Gibbons et al. (2014) show that it is necessary to include the gravitational potential of the progenitor, modelled as a Plummer sphere (Plummer, 1911), by comparing their modified Lagrange Cloud Stripping (mLCS) method to N-body simulations. They find that with these modifications, the method reproduces the simulated streams very well while being substantially faster

and cheaper. Erkal et al. (2019) further modify this method to include the infalling LMC as a rigid potential, i.e. it is moving but not deforming, and the reflex motion of the Milky Way disc. With ever-improving data quality, stream fits require more complicated models and this method keeps on being modified, e.g. with a more complicated description of the Milky Way halo potential in Koposov et al. (2023). For parts of this thesis, in particular for the work presented in Chapter 3, I modified this method to evaluate forces at the positions of the progenitor and the stream particles in the BFE representation of the deforming Milky Way–LMC system.

2.2.3 *Fitting stellar streams*

With a method at hand to produce a suite of stream models, we can fit the stream ICs and other free parameters in that model, e.g. the parameters of the Milky Way and LMC halo profiles, by comparing the model streams to the stream observables. Stream observables are often rotated into a coordinate system that is aligned with the stream. In that coordinate system, the observables are (i) the stream track comprising of the angle along the stream ϕ_1 and the angle perpendicular to the stream ϕ_2, (ii) the distances d, (iii) the radial velocities v_r, and (iv) the proper motions along and perpendicular to the stream $\mu^\star_{\phi_1}$ [6] and μ_{ϕ_2}. An example of these stream observables is shown in Figure 3.4. The stream models are generated in Galactocentric coordinates $(\vec{x}, \vec{v})$. When comparing the models to data, to avoid covariances between observational uncertainties, the models are converted into stream coordinates.

The fit is based on a maximum-likelihood approach. In this method, a likelihood is formulated that describes how well the modelled stream matches the observed data in all observables $\mathtt{obs}$ with their observational uncertainty, $\sigma_{\mathrm{obs},i}$, and model uncertainty $\sigma_{\mathrm{model},i}$:

$$p(\mathrm{data}_i|\mathrm{model}) = \frac{1}{\sqrt{2\pi\left(\sigma^2_{\mathrm{obs},i} + \sigma^2_{\mathrm{model},i}\right)}} \exp\left(-\frac{\left(\mathrm{obs}_{\mathrm{model}}(\phi_{1,i}) - \mathrm{obs}_{\mathrm{data},i}\right)^2}{2\left(\sigma^2_{\mathrm{obs},i} + \sigma^2_{\mathrm{model},i}\right)}\right) \quad (2.6)$$

6 The star at this proper motion indicates that it was corrected for the convergence of meridians towards the North and the South Celestial Pole, i.e. $\mu^\star_{\phi_1} = \mu_{\phi_1}\cos\phi_2$ in stream coordinates and $\mu^\star_\alpha = \mu_\alpha \cos\delta$ in celestial coordinates.

for a data point i along the track ϕ_1. The total probability P is the product of the likelihood evaluation at each data point for each observable.

In order to find the best-fit model parameters and their uncertainties, we need to explore the likelihood surface. For this, we use the Markov Chain Monte Carlo (MCMC) Ensemble sampler `emcee` (Foreman-Mackey et al., 2013)[7]. In `emcee`, a number of walkers explore the log-likelihood space – we, therefore, implement the log of Equation 2.6 and sum over each data point and each observable. The walkers are initialised as a parameter vector over a range around the expected truth of each parameter. At each step, stream models are generated, and their log-likelihood is calculated. The likelihood function should also include an evaluation of the log-prior probability density function (pdf). The log-prior function can be 'flat' (returning 0) or include boundary conditions that return negative infinity if the parameter is out of bounds, e.g. for a negative mass parameter $M < 0$. Examples of how to implement this are given in the `emcee` documentation[8].

The likelihood is compared to the prior step, and roughly speaking, the walker either stays put if the likelihood is better and it passes an acceptance test – the parameter vector is accepted – or goes back and goes in a different direction if the likelihood is worse – the parameter vector is rejected[9]. This way, the walkers will climb towards regions of high likelihood in parameter space.

The result is a posterior chain with the parameter vectors. This method requires that walkers are independent. This can be ensured by implementing a 'burn-in': throwing away a few times the number of steps it takes until the walkers 'forget' where they started – the autocorrelation time. Then, to present the best-fit stream, we select the parameter vector with the highest log-likelihood as the best solution. Results that quote the uncertainty of a parameter are given as the median of the chain, with the 16th

7 As the developers of this package note in Hogg & Foreman-Mackey (2018), a bad reason to use this package is to optimise the likelihood as one should use an optimiser for this. Nevertheless, we not only aim to find the highest-likelihood solution but also to robustly estimate the parameter uncertainties. Since the particle-spray stream modelling technique is highly numerical, it does not meet the requirements for many other likelihood estimators. Therefore, until there is significant technical development for stream modelling techniques, `emcee` is still the best tool for our objectives.

8 emcee.readthedocs.io

9 An easy-to-understand tutorial with more depth aimed at junior undergraduates can be found here: prappleizer.github.io/Tutorials/MCMC/MCMC_Tutorial.html.

and 84th quantiles as uncertainty values. The fitting routine presented here is used in Chapter 5.

How to tweak the fits

For many different reasons, fitting stellar streams is not trivial. Here, I will give an overview of different features that may affect stream models and can be tweaked to improve the fits and possible pitfalls of the methods. This know-how comes from people with substantial fitting experience who have faced these problems and passed on the knowledge (e.g. Denis Erkal, Adrian Price-Whelan, and Wilma Trick). As this is not written down in a concise form anywhere, this aims to become some kind of guidance.

UNITS A first step for testing and debugging code is to make sure the units are correct. Often, simple mistakes can be found this way without much debugging. A very helpful tool to keep track of the units is `astropy.units`[10] (The Astropy Collaboration, 2013, 2018, 2022). This applies not just to fitting routines and models but to any quantitative research.

STREAM MODEL The stream model is subject to many choices and features that affect the fits to the data. They can be split up into choices regarding the progenitor, the orbit integration, and the particle release mechanism.

- *Progenitor:* For many streams, the progenitor is unknown. We estimate its mass and scale radius from stream properties, i.e. whether the progenitor was a GC or a DG. The progenitor mass is chosen to match the stream widths in whatever parameters have been measured, most typically the width on the sky. Another assumption is to have a constant mass loss of the progenitor so that it reaches complete disruption at the end of the integration time (if the stream does not have a progenitor anymore). This is generally good enough for fits that aim to constrain the Galaxy's potential parameters. If the aim is to study perturbations along the stream, more care needs to be taken in modelling the progenitor.
- *Particle release mechanism:* The particle release mechanism follows the mLCS method. Given that the progenitor is modelled as an analytic potential and not a collection

10 docs.astropy.org/en/stable/units/

of particles, there needs to be a prescription of when particles are released from the Lagrange points. There are different prescriptions to choose from: constant release of particles, e.g. $N_1 = N_{\rm total}/N_{\rm step}$ particles at every integration step (implemented in the stream models in Chapters 3 and 4), or releasing particles at times drawn from a Gaussian centred on each pericentre with the total number of particles released per pericentre $N_2 = N_{\rm total}/N_{\rm pericentres}$ (implemented in Chapter 5). $N_2 \gg N_1$ should be true; otherwise, the time steps of the orbit integration might be too long. The choice of $N_{\rm total}$ affects the model shot noise uncertainty, as it scales with $\sigma_{\rm model} \sim 1/\sqrt{N_{\rm total}}$. We require that this shot noise is much smaller than the observational noise to avoid adding additional model uncertainty.

- *Orbit integrations:* The orbit integration comes with two main choices: the integration time of the stream and the time steps along that integration. The integration time should generally be chosen so that the stream model covers the whole data range. The integration time affects the number of peri- and apocentres the stream completes. For fitting the gravitational potential, the exact integration time is not significant as long as it is long enough. An exception is fitting the Palomar 5 stream, where the number of pericentres seems to affect the stream morphology (Küpper et al., 2015).

  The time steps in the orbit can either be constant or adaptive. Constant time steps need to be small enough to recover the orbit when the particle is moving fastest at the pericentre. As particles move slower when further away from their pericentre, the time steps can be larger and, therefore, constant time steps are computationally more expensive than necessary. Adaptive time steps take this into account and calculate the optimal size at each step within some boundaries. This is particularly useful when stream models are more complicated and take longer to calculate, e.g. when evaluating forces from the Milky Way–LMC BFEs.

LIKELIHOOD SURFACE Ideally, in a fit, the likelihood is a smooth surface that has a clear maximum at the parameter with the highest likelihood. Generating streams is a numerical process, which affects the likelihood surface and makes it noisy. This can be seen as an uneven 'edge' of the likelihood, i.e. the maximum likelihood over the allowed range of a parameter can be patchy. Furthermore, this process can result in

local maxima of the likelihood in which the walkers can get 'stuck' (this problem is discussed towards the end of this chapter). When analysing the results of fits, it is recommended to inspect the likelihood given a parameter (e.g. as a scatter or contour plot) to ensure a smooth surface. If the likelihood appears noisy, there are several 'hacks' one could try: increase the number of stream particles, introduce nuisance parameters or increase the number of walkers. None of these hacks guarantees a smooth likelihood surface, though, and it might be necessary to introduce some more significant changes to the fitting process.

ERRORS AND NUISANCE PARAMETERS There are different types of errors evaluated in the fits, and one needs to be careful to select the right one(s). The first type of error or uncertainty regards the data. Depending on the number of available data points along the stream, the data and its uncertainty are either reported for each star or for a mean track that is fit to a bin along the track. When calculating the uncertainty in the likelihood, the model uncertainty needs to be taken into account by being combined in quadrature with $\sigma = \sqrt{\sigma_{\rm obs}^2 + \sigma_{\rm model}^2}$. The selection of the model uncertainty depends on the type of data uncertainty. If the data are individual observables for each star, the model uncertainty is the width of that observable, e.g. the width of the stream on the sky. If the data are mean track data, then the model is fitted with a line in each bin, and the model uncertainty is the uncertainty of the mean.

In order to avoid numerical artefacts affecting the stream models, the uncertainty of the model needs to be significantly smaller than the uncertainty of the observational data. When looking at mean quantities in the data, e.g. the mean stream track, as a rule of thumb, the observational uncertainty should be at least five times as large as the model uncertainty at the parts of the stream with the smallest data uncertainties.

Lastly, if a fit does not seem to converge, has a very bumpy likelihood surface, or gives dubious results, it is possible to add nuisance parameters to try to improve the fit. These are an additional unaccounted-for source of error in the model (or in the data) which is added in quadrature with the other Gaussian spreads. These parameters allow the fit to add uncertainties to observables that are not included in the model uncertainties. As an example, these nuisance parameters are included in the fits in Chapter 5.

CHOICE OF FITTING METHOD As mentioned in a footnote, MCMCs and `emcee` are not tools to fit data. More on fitting and MCMCs can be learned in Hogg et al. (2010), an in-depth overview and tutorial on fitting techniques, and in Hogg & Foreman-Mackey (2018), a 'user manual' for using MCMC methods. However, if one chooses to fit with `emcee`, there are several considerations one needs to be aware of. Section 4 in Foreman-Mackey et al. (2013) provides a useful discussion and tips for using `emcee`. This is a (likely incomplete) overview of the choices and features I have encountered in regard to stream modelling.

- *Initialisation of the walkers:* For most MCMC methods, including `emcee`, the walkers need to be initialised. For a successful MCMC run and a not-too-long burn-in time, the position where the walkers are initialised should not be completely random but somehow informed. On the other hand, it should not be exactly at the optimum of the posterior pdf as the walkers might not explore enough of the parameter space then. One approach is to sample from the prior distribution. This distribution can e.g. be taken from the results of previous fits to the stream that is being modelled.

- *Number of walkers:* The number of walkers should be large! Hundreds ideally. Otherwise, particularly with tens or more parameters, the walkers could get 'stuck' on local maxima on the N_{param}-dimensional likelihood surface. Obviously, increasing the number of walkers slows down the burn-in – it scales with the number of walkers – and, therefore, the whole fit. Foreman-Mackey et al. (2013) suggests choosing the greater number of (i) the smallest number of walkers that provide a good acceptance fraction and (ii) the resulting number of samples. As a rule of thumb, for a given number of model parameters, N_{param}, for which the likelihood is explored, there should be at least N_{param}^2 or even N_{param}^3 walkers.

- *Number of steps:* The number of steps should be not too many and not too few. Too many steps will just unnecessarily increase the run time. Once the samples are independent, the walkers have taken enough steps. This usually happens after a few (maybe 10) autocorrelation times[11] (Foreman-Mackey et al., 2013). On the other hand, too few steps will not produce independent samples.

11 emcee.readthedocs.io/en/stable/tutorials/autocorr/

- *Useful tools:* There are two tools within `emcee` that I found to be incredibly helpful when fitting streams, particularly when running them on a computing cluster: the possibility to parallelise the run[12] and saving the state of the chain to a file[13]. The parallelisation can be either distributed over several cores of a machine using the `multiprocessing` tool[14] or on a computing cluster using `schwimmbad`[15] (Price-Whelan & Foreman-Mackey, 2017). The chains are saved in an HDF5 file using the `h5py` package (Collette, 2013). These files can be used to initialise the walkers at their last step when restarting a fitting run after e.g. a cluster timeout. They are also useful for checking on the chains during the fit, analysing preliminary results, and estimating the autocorrelation time and the number of necessary steps. Many times, I adjusted my fitting routine (in regards to any of the points mentioned in this section) and completely restarted them based on checking preliminary results.

But beware, if you have a *multi-modal posterior space* – the walkers finding more than one likely solution – `emcee` will perform badly as walkers might get 'stuck' in different modes. It is suggested to split up the parameter space into single-mode regions and to sample them independently. For streams, multimodal solutions are possible for the halo flattening. Therefore, fits are often split up into fitting an oblate, a prolate and a spherical halo independently and then comparing their likelihoods (Erkal et al., 2019; Koposov et al., 2023, and in Chapter 5).

12 emcee.readthedocs.io/en/stable/tutorials/parallel/
13 emcee.readthedocs.io/en/stable/tutorials/monitor/
14 docs.python.org/3/library/multiprocessing.html
15 schwimmbad.readthedocs.io

3

THE EFFECT OF THE DEFORMING DARK MATTER HALOES OF THE MILKY WAY AND THE LARGE MAGELLANIC CLOUD ON THE ORPHAN-CHENAB STREAM

It has recently been shown that the Large Magellanic Cloud (LMC) has a substantial effect on the Milky Way's stellar halo and stellar streams. Here, we explore how deformations of the Milky Way and the LMC's dark matter haloes affect stellar streams, and whether these effects are observable. In particular, we focus on the Orphan-Chenab (OC) stream which passes particularly close to the LMC and spans a large portion of the Milky Way's halo. We represent the Milky Way–LMC system using basis function expansions that capture their evolution in an N-body simulation. We present the properties of this system, such as the evolution of the densities and force fields of each galaxy. The OC stream is evolved in this time-dependent, deforming potential, and we investigate the effects of the various moments of the Milky Way and the LMC. We find that the simulated OC stream is strongly influenced by the deformations of both the Milky Way and the LMC and that this effect is much larger than current observational errors. In particular, the Milky Way dipole has the biggest impact on the stream, followed by the evolution of the LMC's monopole, and then the LMC's quadrupole. Detecting these effects would confirm a key prediction of collisionless, cold dark matter, and would be a powerful test of alternative dark matter and alternative gravity models.

Work shown in this chapter is accepted for publication and presented in Lilleengen et al. 2023, MNRAS.

3.1 INTRODUCTION

Despite its ubiquity, dark matter continues to evade direct (e.g. Aprile et al., 2018), indirect (e.g. Gaskins, 2016), and collider searches (e.g. Kahlhoefer, 2017). To date, the only evidence of dark matter has come from its gravitational effect on astrophysical probes (e.g. Zwicky, 1937; Rubin & Ford, 1970; Read, 2014; Planck Collaboration, 2016). Merging galaxy clusters, which effectively serve as huge dark matter colliders, have proven a particularly fruitful testing ground for the collisionless nature of dark matter (e.g. Clowe et al., 2004; Markevitch et al., 2004; Bradač et al., 2008; Jee et al., 2014). The most iconic of these is the Bullet Cluster (Markevitch et al., 2002). It shows a clear offset between the dark matter (as measured with weak lensing) and the gas (as measured with X-rays) which has been used both as evidence of dark matter (e.g. Clowe et al., 2004) and to set constraints on self-interacting dark matter (e.g. Markevitch et al., 2004; Robertson et al., 2017).

Evidence is mounting that the ongoing merger of the Large Magellanic Cloud (LMC) and the Milky Way may serve as a similarly useful dark matter collider. The LMC is believed to be on its first approach to the Milky Way (Besla et al., 2007) and appears to still have a substantial dark matter halo consistent with what is expected from abundance matching, $\sim 2 \times 10^{11}$ $M_\odot$ (e.g. Moster et al., 2013; Behroozi et al., 2013). Such a massive halo would have a large effect on structures in the Milky Way, and such effects have recently been detected. For example, in order to explain the nearby presence of the Small Magellanic Cloud (SMC) and other Magellanic satellites, an LMC mass of $> 10^{11}$ $M_\odot$ is needed (e.g. Kallivayalil et al., 2013, 2018; Erkal & Belokurov, 2020; Patel et al., 2020). An LMC mass of $\sim 2.5 \times 10^{11}$ $M_\odot$ is needed to explain the timing argument with M31 and the nearby Hubble flow (Peñarrubia et al., 2016). The LMC's effect has also been detected in the Milky Way's stellar halo, both in terms of kinematics (Erkal et al., 2021; Petersen & Peñarrubia, 2021) and overdensities in the stellar halo (e.g. Belokurov et al., 2019; Garavito-Camargo et al., 2019; Conroy et al., 2021), all consistent with LMC masses of $\sim (1-2) \times 10^{11}$ $M_\odot$. Finally, the LMC has perturbed many stellar streams in the Milky Way, allowing for a precise measurement of its mass, $\sim (1.3-1.9) \times 10^{11}$ $M_\odot$ (Erkal et al., 2019; Koposov et al., 2019; Shipp et al., 2019, 2021; Vasiliev et al., 2021).

These large LMC masses correspond to roughly $10-20$ per cent of the Milky Way mass (e.g. Wang et al., 2020a). As such, this substantial merger will create significant tidal deformations in the dark matter haloes of both the Milky Way and the LMC (e.g. Weinberg, 1989, 1998; Laporte et al., 2018; Garavito-Camargo et al., 2019, 2021a). Garavito-Camargo et al. (2021a) quantified these deformations by first running an N-body simulation of the Milky Way–LMC encounter and then fitting basis function expansions (BFEs) to the present-day snapshot of a Milky Way–LMC realisation. Their analysis showed that the dark matter haloes of both the Milky Way and the LMC deform substantially. For their Milky Way model, these effects were comparable to the expected halo triaxiality seen in cosmological simulations (e.g. Chua et al., 2019) and thus would need to be understood in order to robustly measure the shape of the Milky Way halo. Furthermore, previous works have shown that the detailed structure of these deformations would also depend on the nature of dark matter (e.g. Furlanetto & Loeb, 2002; Hui et al., 2017; Lancaster et al., 2020).

In this chapter, we show that stellar streams are sensitive to the deforming dark matter haloes of both the Milky Way and the LMC. Stellar streams form as globular clusters and dwarf galaxies disrupt in the presence of their host galaxy. They are powerful probes of the host's gravitational potential (Johnston et al., 1999; Helmi & White, 1999): the collection of stars in the stream roughly delineate orbits in the host potential (Sanders & Binney, 2013a), allowing us to infer the accelerations that the stars experience (and hence the host's gravitational field) without having to directly measure the acceleration[1]. Many streams in the Milky Way have already been used to fit the Galactic potential (e.g. Law & Majewski, 2010; Koposov et al., 2010; Vera-Ciro & Helmi, 2013; Bonaca et al., 2014; Gibbons et al., 2014; Küpper et al., 2015; Bovy et al., 2016; Erkal et al., 2019; Malhan & Ibata, 2019; Vasiliev et al., 2021).

In this chapter, we focus on the Orphan-Chenab (OC) stream (Grillmair, 2006; Belokurov et al., 2006; Shipp et al., 2018; Koposov et al., 2019). This stream is particularly well-suited to study the deformations of the Milky Way and the LMC since it has experienced a close passage with the LMC ($\sim$15 kpc, Erkal et al., 2019) and spans a

1 See, however, Quercellini et al. (2008); Silverwood & Easther (2019); Chakrabarti et al. (2020) for efforts to directly measure accelerations of bright, nearby stars with upcoming spectrographs, Gaia Collaboration (2021b) for a measurement of the solar system's acceleration with quasars, and Chakrabarti et al. (2021) for a measurement of the local acceleration within ~ 1 kpc with binary pulsars.

large portion of the Milky Way (Koposov et al., 2019). Erkal et al. (2019) have used this stream to measure the potential of both the Milky Way and the LMC. Their fits prefer a Milky Way dark matter halo that is misaligned with the Milky Way's disc and either strongly oblate or strongly prolate. Interestingly, the oblate halo is roughly aligned with the orbital plane of the LMC and the prolate halo is aligned with the present-day position of the LMC, hinting that the inferred halo shape may be connected to the LMC. Furthermore, the oblate halo of Erkal et al. (2019) is similar to the triaxial (but nearly oblate) haloes inferred with the Sagittarius stream (Law & Majewski, 2010; Vasiliev et al., 2021). We note that while the fits in Erkal et al. (2019) and Vasiliev et al. (2021) allow the Milky Way to move in response to the LMC, both of these fits assume that the dark matter haloes of the Milky Way and the LMC are rigid (i.e. time-independent)[2]. This leads to the question; how exactly are streams affected by the deformation of the dark matter haloes of the Milky Way and the LMC?

In order to understand how the OC stream is affected by these deformations, we study the interaction of the Milky Way and the LMC with N-body simulations. The N-body simulations use basis function expansions to compute the density, potential, and forces that each particle experiences as a function of time and are performed using the basis function expansion software toolkit `EXP` (Petersen et al., 2022a). This provides us with time-dependent BFEs that we can use to evolve stellar streams in this disturbed system. The time-dependent BFEs allow us to explore how the different orders of both the Milky Way and the LMC expansion (in particular the multipole orders) affect the stream.

This chapter is organised as follows. In Section 3.2, we describe the BFE technique and our Milky Way–LMC model. In Section 3.3, we present the OC stream data and models and describe how they are affected by different moments of the deforming Milky Way–LMC model. Then in Section 3.4, we discuss our results, how tracing these deformations with stellar streams could allow us to distinguish between several dark matter and alternative gravity models, and the possible influence of the SMC on the Milky Way–LMC model. We summarise our findings and conclude in Section 3.5.

2 We note that Vasiliev et al. (2021) performed the MCMC exploration of the Milky Way and LMC parameters using rigid haloes. They then ran live N-body simulations and provided time-dependent potentials for some sets of the best-fit parameters.

3.2 BASIS FUNCTION EXPANSIONS

3.2.1 *EXP*

To model orbits for stellar stream particles in the combined (and evolving) Milky Way–LMC environment, we require a description of the potential and forces at any arbitrary point in the system (and through time). Unfortunately, analytic potentials will not describe deformations in the dark matter haloes of the Milky Way or the LMC. We, therefore, seek a flexible alternate method to describe the density, potential, and forces as they evolve through time: basis function expansions. Basis function expansions have proved a viable method to produce flexible models of the Milky Way (e.g. Petersen et al., 2016; Dai et al., 2018; Petersen et al., 2019; Petersen & Peñarrubia, 2020; Garavito-Camargo et al., 2021a). We use the basis function expansion machinery implemented in `EXP` (Petersen et al., 2022a) to both run N-body simulations, as well as to resimulate the fields ex post facto.

Briefly, basis function expansions model a target distribution as the sum of *orthogonal basis functions*, represented by the index μ, each of which adds an additional degree of freedom to the system. Each function has an associated *coefficient*, A_μ, which is the contribution of the function to the total description of the system. The total system at any given time is parameterised by the functions and their coefficients. We vary the coefficients through time to describe the evolving potential and keep the functions fixed in their initial forms.

In the case of a three-dimensional distribution of masses, one forms biorthogonal potential-density pairs that solve Poisson's equation[3]. The Hernquist basis set (Hernquist & Ostriker, 1992) is one such set of basis functions, which efficiently expands the Hernquist density distribution (Hernquist, 1990). Another standard method to expand an input model spherical distribution, $\rho_{\text{model}}(r, \phi, \theta)$, uses spherical harmonics Y_l^m to describe the (ϕ, θ) angular dependence, and eigenfunctions of the Sturm-Liouville equation (of which Poisson's equation is a special case, see Weinberg, 1999) to describe the three-dimensional radial dependence (indexed as n). The radial basis index, n, corresponds to the number of nodes in the radial function. For $l = 0$, n is equal to

3 That is, pairs of indexed potential and density functions $(\phi_i(\vec{x}), \rho_i(\vec{x}))$ satisfy the following equations: $\nabla^2\phi_i = 4\pi G\rho_i$ and $\int d\vec{x}\, \phi_i(\vec{x})\rho_j(\vec{x}) = 4\pi G\delta_{ij}$, where δ_{ij} is the Kronecker delta.

the number of nodes in each radial function. For $l > 0$, the number of nodes in the radial function is $n + 1$. Each spherical basis function may be represented by the triple $\mu \equiv (l, m, n)$, and the entire spherical coefficient set is of size $(l_{max} + 1)^2 \cdot (n_{max} + 1)$ at each timestep. Previous work using EXP demonstrated high force reconstruction accuracy when modelling the Milky Way using $l_{max} = 6$, $n_{max} = 17$ for the halo (Petersen et al., 2022a). As the LMC is undergoing a more significant deformation than the Milky Way, we model the LMC using a modestly larger number of radial functions to resolve the deformation. Guided by previous models for the Milky Way and LMC (Petersen & Peñarrubia, 2021), we choose $l_{max} = 6$, $n_{max} = 17$ for the Milky Way and $l_{max} = 6$, $n_{max} = 23$ for the LMC[4]. The basis functions are defined to be biorthogonal (Weinberg, 1999), such that the inner product of the density and potential functions for each component is the sum of the power computed from the entire coefficient set. The physical interpretation of the coefficient power is then that of gravitational energy, which allows one to interpret power as the self-gravity of the system represented by the different functions. Throughout, we will describe individual *harmonic subspaces*, referring to the $l = 0$ terms as the monopole, the $l = 1$ terms as the dipole, and the $l = 2$ terms as the quadrupole[5]. The lowest-order monopole function ($l = n = 0$) is tailored to match the density profile of the target mass distribution, such that $\rho_{lmn}(r) = \rho_{000}(r) = \rho_{model}(r)$ (and equivalent relationships for the potential Φ).

While a spherical object, such as the dark matter haloes of the Milky Way and the LMC, may be straightforwardly expanded using a spherical basis, a cylindrical mass distribution such as a stellar disc would necessitate extremely high l orders to approximate a thin structure. We, therefore, use the adaptive basis technique in EXP to derive a basis that more closely matches a target stellar density distribution. The cylindrical basis is selected from a high-order ($l_{max} = 64, n_{max} = 63$) spherical expansion by finding the optimal meridional functions through eigendecomposition. The cylindrical basis functions are described by two cylindrical coordinates, R and z, with the angular dependence coming from a Fourier expansion in azimuthal harmonics m. As in the case of the spherical expansions, the lowest-order monopole function

4 For all expansions, we index the lowest-order radial function as $n = 0$, meaning that the Milky Way (LMC) has 18 (24) radial functions per harmonic order. The harmonic functions (indexed by l in the spherical case and m in the cylindrical case) both also begin at 0.

5 Higher l orders will be simply described as $l = 3, \ldots, l_{max}$.

($m = n = 0$) will closely resemble the equilibrium density of the target mass distribution, $\rho_{mn}(R, z, \phi) = \rho_{00}(R, z, \phi) \approx \rho_{\text{model}}(R, z)$. For the total cylindrical expansion, we retain functions and coefficients up to $m_{\text{max}} = 6$ and $n_{\text{max}} = 17$. The cylindrical coefficient set is then of size $(2m_{\text{max}} + 1) \cdot (n_{\text{max}} + 1)$ at each timestep.

Representing the system as the linear sum of solutions to Poisson's equation is a so-called *global basis*, that has the principal benefits of describing the self-gravity in a given correlated evolutionary mode of the system. The downside of global bases is their susceptibility to aliasing[6]. Further, owing primarily to finite-N effects in the models, there is uncertainty on the coefficients of a given basis function. In practice, this will add numerical noise to the (re-)simulation, as well as create scatter in the coefficients.

Despite these limitations, careful use of basis function expansions provides a computationally efficient and flexible means to describe an evolving model. In the next section, we introduce the models from which we obtain the basis functions and coefficients in order to model the OC stream.

3.2.2 *N-body models*

We build our model Milky Way–LMC from three components: a Milky Way stellar component (a disc and bulge), a Milky Way dark matter halo, and an LMC dark matter halo. The dark matter profiles are selected to be the best fit, but reflexive, spherical potential (labelled 'sph. rMW+LMC') from table A1 of Erkal et al. (2019): an Navarro–Frenk–White (NFW) (Navarro et al., 1997) Milky Way dark matter halo with $M_{\text{MW halo}} = 7.92 \times 10^{11}\ M_\odot$, $r_s = 12.8$ kpc, and $c = 15.3$, a Miyamoto-Nagai (Miyamoto & Nagai, 1975) stellar disc with $M_{\text{MW disc}} = 6.8 \times 10^{10}\ M_\odot$, $a = 3.0$ kpc, and $b = 0.28$ kpc, a Hernquist (Hernquist, 1990) stellar bulge with $M_{\text{MW bulge}} = 5 \times 10^{9}\ M_\odot$, $r_s = 0.5$ kpc, and a Hernquist LMC dark matter halo with $M_{\text{LMC}} = 1.25 \times 10^{11}\ M_\odot$

6 Aliasing formally owes to the truncation of the infinite series; in practice, regions with low sampling (i.e. low density) are the most affected. Fortunately, these regions are low-density and therefore tend to have little impact on the evolution, but may cause structures that are obvious by eye. In an idealised test of a deformed model, Petersen et al. (2022a) demonstrate that regions at $r > 5r_s$, mismatch in the outskirts of models may contribute a 1% error to the forces. These regions do not strongly affect the evolution of the OC stream.

and $r_s = 18.43$ kpc[7]. While we do not apply a truncation to the Hernquist profile of the LMC, we add a truncation to the Milky Way halo potential to counteract the infinite mass of the NFW potential. We truncate the profile by multiplying the density profile by a normalised error function such that the final Milky Way profile is $\rho_{\text{Milky Way}}(r) = 0.5\rho_{\text{NFW}}(r)\,(1 - \text{erf}\,[(r - r_{\text{trunc}})/w_{\text{trunc}}])$ where $r_{\text{trunc}} = 430$ kpc and $w_{\text{trunc}} = 54$ kpc. The models are realised with $N_{\text{MW halo}} = 10^7$, $N_{\text{LMC}} = 10^7$, $N_{\text{MW disc}} = 10^6$ particles, following the procedures in Petersen et al. (2021). We define the bases for each component using the basis selection techniques in EXP. The Milky Way and LMC dark matter haloes are represented as spherical bases; the Milky Way stellar disc and bulge mass distributions are combined and represented by a single cylindrical basis, as introduced in Section 3.2.1.

The N-body models are evolved using EXP, which uses the basis functions for each component to obtain the forces (see Petersen et al., 2022a, for details). We have checked that the distance between the expansion centre of the Milky Way halo and the Milky Way stellar component (consisting of the disc and the bulge) is smaller than the minimum node spacing in the Milky Way halo expansion (i.e. the node spacing in the $l = 0$, $n = 17$ Milky Way basis function). To realise the trajectory, we first run point-mass models of the Milky Way and the LMC in reverse from their present-day locations to obtain a rough trajectory. We specify the present-day centre position and velocity of the LMC using $(\alpha_{\text{LMC}}, \delta_{\text{LMC}}) = (78.76° \pm 0.52, -69.19° \pm 0.25)$, with proper motions $(\mu_{\alpha^*,\text{LMC}}, \mu_{\delta,\text{LMC}}) = (-1.91 \pm 0.02\ \text{mas/yr}, 0.229 \pm 0.047\ \text{mas/yr})$ from Kallivayalil et al. (2013), the distance from Pietrzyński et al. (2019), $d_{\text{LMC}} = 49.59 \pm 0.54$ kpc, and the line-of-sight velocity from van der Marel et al. (2002), $v_{\text{los, LMC}} = 262.2 \pm 3.4\,\text{km}\,\text{s}^{-1}$. We find that we recover a qualitatively similar orbit to the best-fit reflexive spherical model from Erkal et al. (2019). Individual model realisations may be run on modest-sized supercomputers owing to the computational efficiency of EXP. However, in order to obtain a realisation that is sufficiently close to the present-day Milky Way–LMC pair, we run a grid of 15 live N-body models around the rewound point mass models and select the model which best matches the present-day observables. We note that these live N-body models self-consistently include the dynamical friction the LMC experi-

7 In the publication, we quote $r_s = 14.9$ kpc. After the chapter was published, we found a mistake in the conversion between virial and physical units and the scale radius of the NFW halo is, in fact, $r_s = 18.43$ kpc.

ences in the presence of the Milky Way, in contrast to the initial point-mass models, which do not include any dynamical friction prescription. Future models may reach quantitatively better matches to the luminous positions of the Milky Way and the LMC, but for our purposes, the match of the Milky Way–LMC pair is sufficient to study the effect of deformations on stellar stream observables.

For computational convenience, we convert the physical units of the simulation into virial units ($G = T_{virial} = M_{MW} = 1$). In these units, we allow maximum timesteps of $dt_{max} = 0.002\ T_{virial}$, with smaller timesteps decided by adaptive criteria, down to a minimum of $dt_{min} = 0.000125\ T_{virial}$. At each minimum timestep in the simulation, the coefficients for each function are tabulated from the present distribution of the particles and recorded for later use. The live simulation starts at $T = -1.2\ T_{virial} (= -2.5$ Gyr) before the present day ($T = 0$). When representing the density/force/potential fields of the system at times prior to the start of the live simulation, we set the coefficients for each component to be their initial values, and place the LMC on a coasting orbit determined by extrapolating the $T = -1.2\ T_{virial}$ velocity vector of the LMC backwards in time[8]. The simulation qualitatively resembles the present-day snapshots of both other simulated (Garavito-Camargo et al., 2019, 2021a) and numerical (Rozier et al., 2022) models of the Milky Way–LMC interaction.

3.2.3 *Dipole/quadrupole evolution*

Figure 3.1 is a global view of the Milky Way–LMC interaction, as represented by our BFE. To summarise the Milky Way and LMC systems, we compute the squared sum of coefficients $\sum_{n,m} |A_{lmn}|^2$ over all radial functions n and $m \in [-l, \ldots, 0, \ldots, l]$ for each l harmonic subspace to compute a measure of the self-gravity in each harmonic subspace, A_l. The power values themselves are model-dependent, so we choose to normalise the power in each harmonic subspace to the total power in the monopole ($l = 0$) harmonic subspace, $P_l/P_0 = A_l^2/A_0^2$. Given this normalisation, we interpret the series of power over time as the relative influence of each harmonic order to represent the global system and describe percentages of self-gravity represented by particular harmonic subspaces. We inspected harmonic subspaces as a function of radial order

8 A `python` interface to integrate orbits and access the expansion model for the simulation can be found here: https://github.com/sophialilleengen/mwlmc.

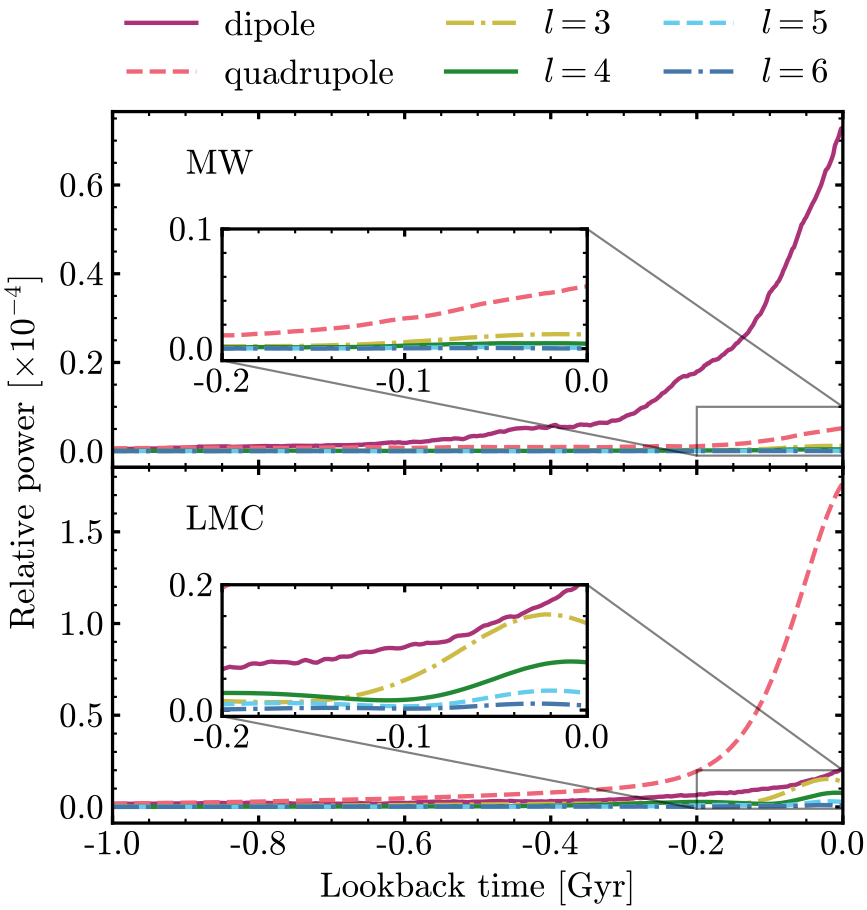

Figure 3.1: Time evolution of the relative power in non-monopole harmonic orders of the Milky Way halo *(top)* and the LMC *(bottom)*. The power in each harmonic order is normalised by the monopole ($l = 0$) power. Power may be interpreted as the amount of self-gravity in a particular harmonic order, such that larger power values indicate more influence. Insets show a zoom-in focusing on the 200 Myr preceding the present day. The strongest multipole order in the Milky Way is its dipole which has been slowly increasing over the last 500 Myr and more rapidly over the last few hundred Myr. The LMC is dominated by a sharply rising quadrupole over the last 200 Myr, with contributions of the higher orders becoming nonzero in the last 100 Myr.

n and found that the amplitudes decrease monotonically (that is, the $n = 0$ order is the largest, $n = 1$ the next largest, and so on). Therefore, we report only the sum over each harmonic subspace throughout the chapter. We include a visual breakdown of sums over n order in Appendix A.1. While the power is an efficient parametrisation of the total system, streams are inherently a local (or restricted) measure of the potential, which we will explore below. Nevertheless, concisely describing the Milky Way–LMC system gives insight into the dynamics of the interaction.

The upper panel of Figure 3.1 demonstrates that the dipole is the largest deformation in the Milky Way. The magnitude of the dipole owes to the 'stretching' of the Milky Way towards the LMC as the LMC approaches from beyond the virial radius. The dipole power becomes nonzero approximately as the LMC crosses the virial radius, and continues increasing until rising rapidly during the last few hundred Myr. Other harmonic orders are strongly subdominant, peaking below a tenth of the dipole power.

In contrast, the lower panel of Figure 3.1 shows that the quadrupole is the largest deformation of the LMC over the past 500 Myr, owing to the strong tidal forces experienced by the LMC near pericentre. While the strength of the quadrupole dominates the recent LMC response, other harmonic subspaces, including up to $l = 6$, also contribute to the response. Prior to the past 500 Myr, the dipole deformation of the LMC also dominates, with nonzero power on a similar timescale as the Milky Way.

In both panels, the estimation noise from finite-N effects is visible in the coefficient series. This noise creates the smallest variations, most visible in the $l = 1$ curves, with amplitudes of order 0.01×10^4 in the normalised power units. However, there are larger amplitude variations as well (of order 0.05×10^4 in the normalised power units), that are likely the result of real dynamical evolution. As we cannot control the natural dynamical evolution of the models, we expect some secular evolution dynamics to also be encoded in the coefficient series.

3.2.4 *Density*

We can use the basis function expansions to investigate how the Milky Way and the LMC deform in response to one another. We expect the biggest effect of deformations due to the LMC in its orbital plane since this is the plane in which the LMC's material spreads out the most (e.g. see figure 10 in Erkal et al., 2019). In order to best show the

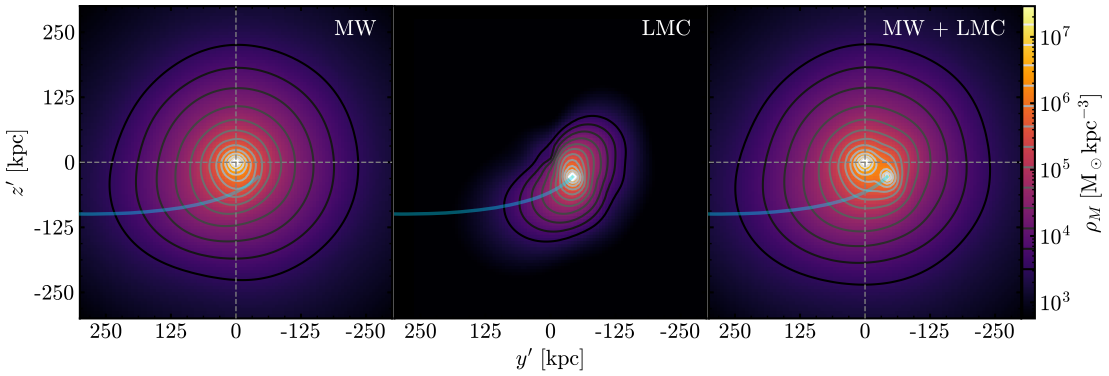

Figure 3.2: Density of the Milky Way halo (*left panel*), the LMC (*middle panel*), and combined (*right panel*) of the BFE simulations in the orbital plane of the LMC at the present time. The density is projected over a 10 kpc thick slab. The contour lines show the densities with a constant multiplicative spacing of ~ 2. The Milky Way exhibits deformations and a twist along the past orbit of the LMC (blue line). The dashed grey vertical and horizontal lines show the Milky Way centre to highlight asymmetries in the Milky Way halo. The LMC is heavily elongated along its orbit and twisted towards the centre of the Milky Way. A video of the LMC infall and the galaxies' deformations over the past 1.5 Gyr can be found here.

LMC's effect, especially when it is far from the Milky Way, we rotate coordinates to be aligned with the LMC's orbital plane; this rotation is explained in Appendix A.2. While the LMC's orbital plane is very close to the Galactic yz-plane, it differs by 5.8° in the x-direction, 4.3° in the y-direction, and 3.9° in the z-direction.

Figure 3.2[9] shows the densities of the Milky Way halo, the LMC halo, and their combined densities from the full BFE expansions. While their dark matter haloes are initialised to be spherical, over time (see video link in Figure 3.2 caption), the Milky Way deforms where the LMC is falling in. This leads to a twist along the LMC's past orbit. The general shape of the Milky Way is governed by its dipole (as seen in Figure 3.1 and Figure A.1). The Milky Way's density is lopsided and the density contours are compressed in the positive z'-direction and expanded in the opposite direction, shifting the Milky Way's density downwards beyond ~ 25 kpc.

The LMC's first visible deformation is the quadrupole in the leading part of the LMC. Around 500 Myr ago, with the increase of power in the quadrupole, the whole LMC starts elongating along the direction of its orbit. Over the last 100 Myr, the inner LMC twists towards the Milky Way, which is described by the higher radial terms of the quadrupole (see the third row in Figure A.1). The LMC has some deformations, partic-

9 Video link: https://youtu.be/KMeGVMXfLTw

ularly towards the Milky Way, that need the higher harmonic orders to be described. These densities for both the Milky Way and the LMC are similar to other simulations of this interaction, e.g. in Erkal et al. (2019) and in Garavito-Camargo et al. (2021a).

3.2.5 *Forces*

While the density is useful for highlighting the deformations, the density itself is not directly observable. Instead, the aim of this chapter is to show that the force fields generated by these deformations can be detected with stellar streams. In order to showcase how the deformations affect these forces, we consider several different expansions of our haloes throughout this chapter. First, we consider the present-day monopole which captures the spherical behaviour of the halo. This is useful for comparing our deforming models to other modelling techniques used to represent the Milky Way and the LMC which assume the Milky Way and the LMC do not deform (e.g. Erkal et al., 2019; Vasiliev et al., 2021; Shipp et al., 2021). We compare this with the 'live' model which includes all orders of the multipole expansion.

Using the BFEs, we evaluate the forces from the dark matter haloes of the Milky Way and the LMC for the monopole and the live simulations. Since the monopole haloes are spherical, any aspherical forces in the live haloes must result from the deformations. The strength of the aspherical force is given by

$$F_{\text{aspherical}} = |\hat{r} \times \vec{F}| \tag{3.1}$$

and the strength of the radial force is given by

$$F_{\text{radial}} = |\hat{r} \cdot \vec{F}| \tag{3.2}$$

where $\hat{r}$ is the normalised position vector relative to the centre of the galaxy we considered. We take the absolute values of these forces to understand the magnitude of the effect of the deformations.

In Figure 3.3[10], we compare the aspherical and radial forces in the live and monopole haloes. In order to aid the comparison, we normalise the difference in these forces

10 Video link: https://youtu.be/im930X6O33s

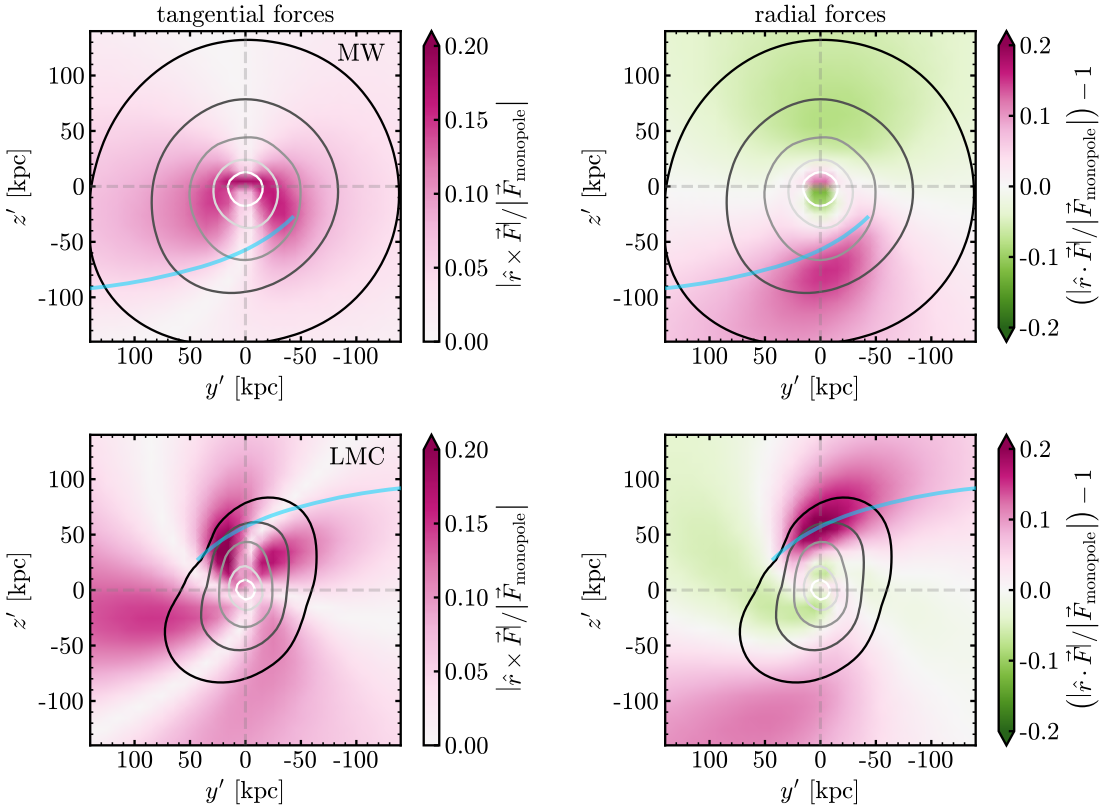

Figure 3.3: Aspherical and radial force differences between the live and monopole haloes for the Milky Way (*top row*) and the LMC (*bottom row*) in the orbital plane of the LMC at the present time. To aid the comparison, we normalise the force differences by the force from the monopoles at the present day. The orbit of the other galaxy is indicated by the blue line. The grey dashed lines show the centres of each halo. The grey-scale contours show the halo densities with a constant multiplicative spacing of ~ 3.8. *Top left panel:* For the Milky Way, the aspherical forces are up to 18 per cent of the monopole force and, therefore, could have a significant impact on objects in the affected parts. The maximum aspherical forces are around the centre of the Milky Way, oriented towards and away from the LMC, again showing the strong dipole. *Top right panel:* The radial forces in the North are lower while in the South, the radial forces are higher than the monopole forces, particularly following the LMC and its past orbit. Its change of force is higher compared to the Northern part. The first-order symmetry in both panels is due to the Milky Way's dipole. *Bottom left panel*: The aspherical forces of the LMC are split into four parts, indicating the prominent quadrupole. The borders of the quadrupole force shapes lie along the long and the short axis of the LMC's density distribution. The strongest parts of the aspherical force are at the leading part of the LMC, closest to the Milky Way, until ~ 300 Myr ago. Since then, the force field on the part opposite the Milky Way grew stronger. The aspherical forces of the LMC are up to 23 per cent of its current monopole's force. *Bottom right panel:* The quadrupole of the LMC is visible in the radial forces as well. The strongest change in the radial forces is again where the Milky Way falls in. Very recently, the opposite direction gains radial force as well. The losses in the other two parts of the quadrupole are not as strong. A video of the infall centred on each galaxy and the galaxies' force fields over the past 0.7 Gyr can be found here.

by the force from the monopole halo as a function of position. There are significant aspherical forces, up to 18 per cent and 23 per cent of the monopole forces of the Milky Way and the LMC, respectively. The LMC experiences enhanced aspherical and radial forces, particularly at its leading arm for the last ~ 300 Myr. While the Milky Way's dipole and the LMC's quadrupole are visible throughout the whole evolution, they become particularly significant over the last 100 Myr. Any objects that move in the areas of enhanced aspherical forces should be affected by the deformations. We also notice features in the Milky Way at small radii ($r < 20$ kpc) that likely correspond to the interaction of the disc and inner halo. Furthermore, over the course of the interaction and as seen in the top right panel of Figure 3.3, the Milky Way halo gets more centrally concentrated. For the purposes of this chapter, the small-scale features do not figure into the results. To understand the effects of the large-scale deformations better, in the next section, we evolve and analyse a stellar stream in this time-dependent potential.

3.3 THE OC STREAM IN LIVE POTENTIALS

In this section, we explore how the deforming Milky Way and LMC dark matter haloes affect the OC stellar stream (e.g. Grillmair, 2006; Belokurov et al., 2006; Newberg et al., 2010; Shipp et al., 2018; Koposov et al., 2019). We make this choice because the OC stream is one of the streams most strongly perturbed by the LMC (e.g. Erkal et al., 2019; Shipp et al., 2021) and because its observed extent covers a wide range of radii in the Milky Way. As a result, we stress that we are only exploring the effect of the deformations on the small set of orbits that the OC stream inhabits as a demonstration of what is possible. Streams and structures on other orbits will also be strongly affected by these deformations and we will explore the effects on other streams in future work.

3.3.1 *Stream data*

With proper motions from *Gaia* EDR3 (Gaia Collaboration, 2021a), radial velocities from the Southern Stellar Stream Spectroscopic Survey (S^5; Li et al., 2019), and distances from RR Lyrae (e.g. Koposov et al., 2019), we now have a 6D view of the OC stream. The presentation and detailed analysis of these data is published in Koposov et al. (2023). The measurements of various observables are done through modelling of unbinned

data as a function of angle along the stream track by cubic splines, similar to Erkal et al. (2017) and Koposov et al. (2019). The number of likely spectroscopic members, from which the proper motions and radial velocities are measured, is 379. The number of likely RR Lyrae stars, from which the distance modulus is measured, is 120. The splines are specified in terms of their values at a sequence of knots. In Figure 3.4, we show the values at the knots with grey error bars. The stream coordinate system (ϕ_1, ϕ_2) is defined in Koposov et al. (2019) and the rotation matrix is given in their Appendix B. Since there is little covariance between neighbouring data points, we treat these as independent measurements of the OC stream observables.

3.3.2 *Stream modelling*

To model the OC stream, we use the modified Lagrange Cloud Stripping (mLCS) method originally developed in Gibbons et al. (2014), which was further modified in Erkal et al. (2019) to include the force from the LMC and the reflex motion of the Milky Way. The progenitor is modelled as a Plummer sphere with an initial mass of 10^7 $M_\odot$, approximately matching the observational mass constraint from Koposov et al. (2019), and a scale radius of 1 kpc, to roughly match the width of the OC stream (Erkal et al., 2019). We rewind the progenitor in the combined presence of the Milky Way and the LMC for 4 Gyr. The orbital period of our OC stream model is 1.15 Gyr. The system is then evolved forwards and tracer particles are released from the progenitor's Lagrange points to generate a stream. The Lagrange radius is estimated by computing

$$r_t = \left(\frac{GM_{prog}}{\Omega^2 - \frac{d^2\Phi}{dr^2}} \right)^{\frac{1}{3}} \tag{3.3}$$

where M_{prog} is the mass of the progenitor, Ω is the angular velocity of the progenitor relative to the Milky Way, and $\frac{d^2\Phi}{dr^2}$ is the second derivative of the Milky Way potential computed along the radial direction (King, 1962). These ejected particles feel a force from the Milky Way, LMC, and progenitor. Due to the low mass of the progenitor, we do not model its dynamical friction in the presence of the Milky Way.

We model the Milky Way and the LMC with the BFE potentials described in Section 3.2. We evaluate the forces of each expansion (Milky Way halo, Milky Way stellar component, LMC halo) at each timestep for each particle. Motivated by the results of

Dehnen & Read (2011), we compute two separate time scales for each particle. To capture the orbit around the Milky Way, we compute $\Delta t_{i,\,\mathrm{orbit}} = \eta\sqrt{\frac{r_i}{|\vec{a}_i|}}$ where i is an index for the stream particles, r_i is the distance to the Milky Way, $\vec{a}_i$ is the acceleration experienced by the particle due to the Milky Way, and $\eta = 0.01$. To capture the orbit around the progenitor, we compute $\Delta t_{i,\,\mathrm{prog}} = \eta\sqrt{\frac{r_{i,\,\mathrm{prog}}}{|\vec{a}_{i,\,\mathrm{prog}}|}}$ where $r_{i,\,\mathrm{prog}}$ is the distance to the progenitor and $\vec{a}_{i,\,\mathrm{prog}}$ is the acceleration due to the progenitor. We then compute the minimum timestep over all of the particles, $\Delta t = \min_i\left(\Delta t_{i,\,\mathrm{orbit}}, \Delta t_{i,\,\mathrm{prog}}\right)$ with a minimum timestep of 0.5 Myr. The timesteps range up to 3 Myr. This is the same time-step criterion as used in Erkal et al. (2019). We note that also including a time-step criterion for the orbit relative to the LMC makes no observable difference to the stream.

Due to the long computation time of the force evaluations for each particle relative to an analytic force (i.e. as in Erkal et al., 2019), we do not attempt to fit the data with these stream models. Instead, we find the best model from a grid search over the parameter space around the initial conditions for the progenitor in a spherical Milky Way halo with reflex motion from table A1 in Erkal et al. (2019). The streams created with these initial conditions are compared to the data in each observable (i.e. track, proper motions, distance, and radial velocity) following Erkal et al. (2019). We use a right-handed coordinate system with the Sun's position at $x_\odot = (-8.249, 0, 0)$ kpc (distance to the Galactic centre from GRAVITY Collaboration, 2020) and take its velocity to be $v_\odot = (11.1, 245, 7.3)\,\mathrm{km\,s^{-1}}$ (with the peculiar velocity from Schönrich et al. 2010, and basing the rotation velocity on proper motion measurements of Sgr A* Reid & Brunthaler 2004). For each data point i, we select all model particles within 2° in ϕ_1. We fit a line as a function of ϕ_1 to these particles. This maximum-likelihood fit returns the mean $m_{i,\mathrm{mod}}$ and uncertainty on the mean $\sigma_{i,\mathrm{mod}}$ at the location of the data point i. The uncertainty on the mean results from the finite number of particles in the stream model. We compare these fits to the data points in each observable using the log likelihood[11]

$$\log \mathcal{L}_i = -\frac{1}{2}\log\left(2\pi\left(\sigma_{i,\mathrm{obs}}^2 + \sigma_{i,\mathrm{mod}}^2\right)\right) - \frac{1}{2}\frac{\left(m_{i,\mathrm{obs}} - m_{i,\mathrm{mod}}\right)^2}{\sigma_{i,\mathrm{obs}}^2 + \sigma_{i,\mathrm{mod}}^2} \tag{3.4}$$

with the observed values $m_{i,\mathrm{obs}}$ and observed uncertainty $\sigma_{i,\mathrm{obs}}$. We sum these log-likelihoods together and select the stream with the highest likelihood as the best-

11 Where log denotes the natural logarithm.

matching stream. We use these initial conditions for all stream models shown in this chapter. These initial conditions for the stream progenitor are $\phi_1 = 6.340°$, $\phi_2 = -0.456°$, $d = 18.975$ kpc, $v_r = 93.786\,\mathrm{km\,s^{-1}}$, $\mu_\alpha^* = -3.590$ mas yr^{-1}, $\mu_\delta = 2.666$ mas yr^{-1}, following the notation of Koposov et al. (2019) and Erkal et al. (2019). The stream track coordinates (ϕ_1, ϕ_2) are given in a coordinate system aligned with the OC stream provided in Koposov et al. (2019). This coordinate system follows a great circle with a pole at $(\alpha_{OC}, \delta_{OC}) = (72°, -14°)$, and has its origin at $(\alpha_0, \delta_0) = (191.10487°, -62.86084°)$. The rotation matrix to this coordinate system is given in Appendix B of Koposov et al. (2019).

The stream observables of the best-matching stream are shown in Figure 3.4. The model follows the overall trends of the observed stream well but there are quantitative discrepancies, in particular the radial velocities in the Northern part of the stream ($\phi_1 > 0°$). We note that Erkal et al. (2019) did not use radial velocities when fitting the stream. Since our simulated Milky Way and LMC are initialised with the potentials Erkal et al. (2019) obtained from their fits, a grid around their best initial conditions therefore might limit our capacity to fully match the radial velocities. Furthermore, including radial velocities could yield different potentials in which we would match the data better. This may explain part of the discrepancy. In addition, our potentials evolve due to the interaction of the Milky Way and the LMC. As a consistency check, we let the stream evolve in the initial potential with the initial conditions of Erkal et al. (2019) and find that the stream matches the stream track, distance, and proper motions as in Erkal et al. (2019) which is much better than the live model presented here. However, for the scope of this chapter, the live model stream resembles the OC data close enough. We stress that this chapter does not aim at fitting the data, but rather at investigating how the best-matching OC stream model is affected by the deformations of the Milky Way and the LMC.

3.3.3 *Stream tracks in increasingly complex potentials*

One of the advantages of BFEs is that for each expansion, we can select different moments to evaluate the contribution of different harmonic orders and radial subspaces. In order to better understand how the different terms of the BFEs affect the stream, we now selectively turn off the contribution from certain functions in the total expansion.

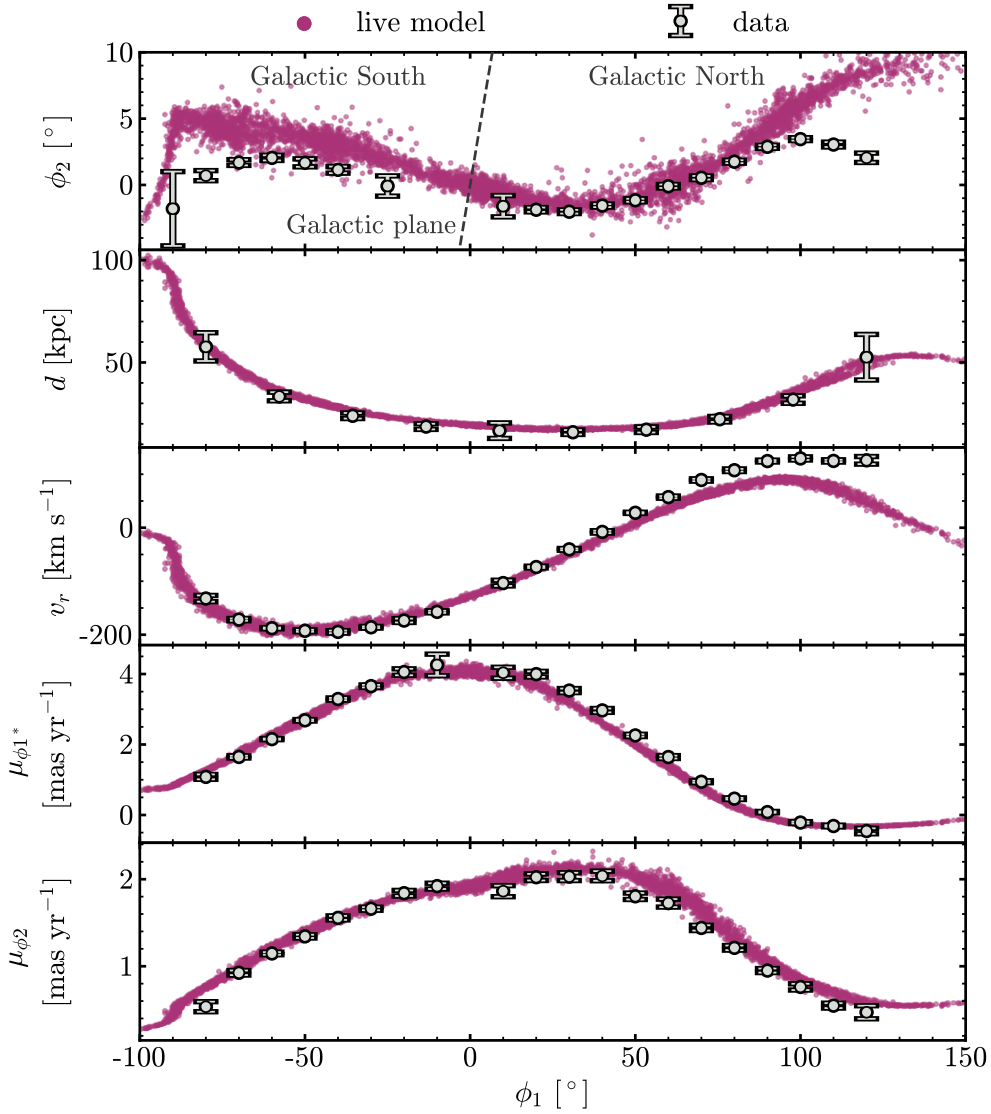

Figure 3.4: Observables of the best-matching OC stream model and data. The rows show the stream in sky coordinates, heliocentric distance, radial velocity in the Galactic standard of rest, and proper motions in stream coordinates, not reflex-corrected, respectively. The grey points with error bars show the observed stream from Koposov et al. (2023), and the purple points are the simulated stream particles of the best-matching stream in the fully evolving Milky Way–LMC simulations. The model stream matches the trends of the observed stream well but there are some quantitative differences.

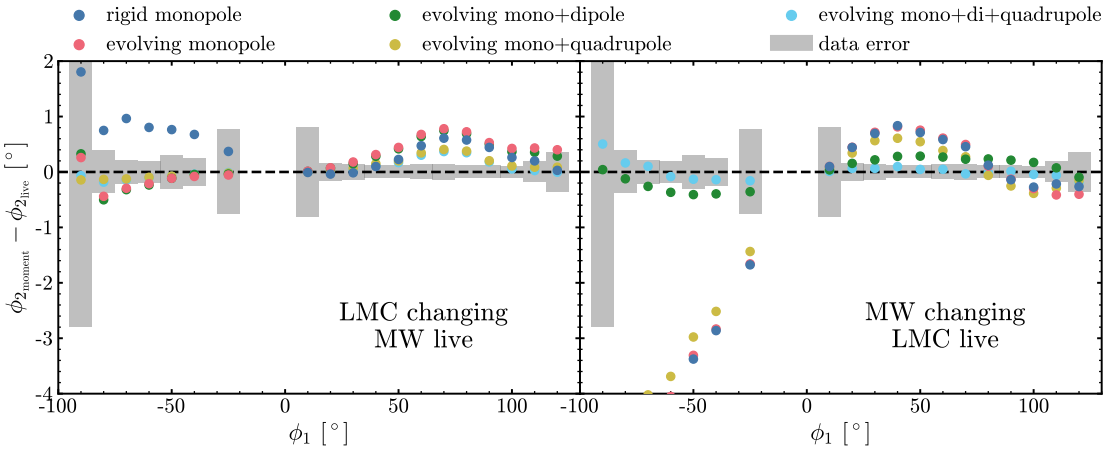

Figure 3.5: Tracks of the simulated OC stream in different LMC and Milky Way potentials compared to the fully live potential. In the left plot, the Milky Way is live and different moments of the LMC are selected as the potential. In the right plot, the LMC is live and we vary the Milky Way. All potentials include the live Milky Way disc. The moments are the rigid monopole (blue), evolving monopole (red), then, in addition to the monopole, the dipole (green) and quadrupole (yellow). Finally, we combine monopole, dipole and quadrupole (cyan). The grey bars show the size of the uncertainty on the mean ($\pm 1 \mathrm{sigma}$) for the observed stream track. All stream tracks are binned as explained in Section 3.3.2, at the same positions in ϕ_1 as the data. The errors of the mean observable tracks of the model, which depend on the number of particles in the model, are smaller than the size of the markers, and therefore not shown. For the LMC, the strongest effect results from turning on the time dependence (blue to red). From the higher moments, the quadrupole determines most of the live track (red to yellow). In the Northern part, between $\sim 50^\circ < \phi_1 < 80^\circ$, the live track indicated by the black dashed line differs from the others by a significant amount. The Milky Way's most important moment is the dipole (red to green). The tracks of the most affected configurations are shown in the top panels of Figure A.3. Some of these effects, in particular the Milky Way dipole's effect, are much greater than the observed errors.

To see how the inclusion or exclusion of these moments affects the OC stream, we run the model with the same initial conditions for the progenitor in the different potential setups. Figure 3.5 shows these different OC stream models. In order to isolate the effect of each term in the expansion, we keep one galaxy live, while we change the moments of the second galaxy, from a rigid monopole to the evolving lower order moments, to the fully live case. We note that the Milky Way disc is kept live in all cases.

First we consider the monopole which describes the spherical shape of each galaxy. Since the monopole is time-dependent, we first consider the final monopole at the present day (i.e. $t = 0$ Gyr) which we dub the 'rigid monopole'. This is to be contrasted with the 'evolving monopole' which includes the monopole's time dependence. The OC stream in the rigid monopole and evolving monopole are shown in blue and red respectively in Figure 3.5. Interestingly, using a rigid monopole for either the Milky Way or the LMC results in a significantly different stream than the full live stream. Furthermore, including the evolving monopole does not fully remedy this, showing that the higher order terms are also important. The other moments shown are the evolving dipole, quadrupole, and dipole+quadrupole together in green, yellow, and cyan, respectively. For all higher moments, the evolving monopole is included so that the additive effect of each component can be seen. The 'evolving mono+di+quadrupole' model captures all effects with $l \leqslant 2$. Given current observational uncertainties, it is indistinguishable from the live model, suggesting that higher order terms (i.e. $l \geqslant 3$) would not be necessary to describe the deforming Milky Way.

For the LMC, the biggest effect on the Southern part of the OC stream is from turning on the time-dependence of the monopole (blue to red), followed by the quadrupole (red to yellow). In the Northern part of the stream, between $\sim 50^\circ < \phi_1 < 80^\circ$, there is an offset between the 'evolving mono+di+quadrupole' and the live model, showing that higher order moments are playing a significant role.

For the Milky Way, the biggest impact comes from including the dipole (i.e. green and cyan points), showing the impact of the aspherical forces. The forces from the dipole pull the OC stream up in the South and down in the North. This effect is larger than the effect from any orders of the LMC's expansion, showing that accounting for the Milky Way's dipole deformation is the next most important effect to consider for the OC stream. We stress that the differences between the moments are much larger

than the uncertainty in the data which shows that fits to the OC stream should be sensitive to these deformations. We note that we have focused on changes in the stream track since these produce the largest effect compared to observational uncertainties. We show the differences in all observables in Appendix A.3 for comparison.

While this shows how different moments affect the stream track, it has an important caveat. When we change the BFE, the orbit of the progenitor also changes. This might affect the resulting stream tracks which complicates the comparison of the different expansion orders. To make a cleaner comparison, we next investigate the contribution of each moment of each galaxy towards the forces experienced by the live stream.

3.3.4 *Integrated absolute forces*

In the previous section, we explored how the different components of the BFE affect the stream track with the understanding that their orbits slightly differ. To more directly explore the impact of each component, we now compare the integrated absolute forces from the different moments on the same stream.

In order to dissect the contributions of each moment to the total force each stream particle experiences, we first run our best model stream in the fully live potential. We save the forces due to each moment from each galaxy on each stream particle every 20 Myr. We then sum the absolute values of these forces over all the snapshots to get the integrated absolute force on each particle:

$$F_{\sum \text{tot}} = \sum_{t} |\vec{F}| dt. \tag{3.5}$$

We also include the integrated absolute force on the progenitor up to the time when each particle was stripped to account for the forces the particles experienced before they left the progenitor. We consider different components of the force to better understand how the stream is affected. The total force is the force each particle experiences from each galaxy. The aspherical force is the force the particles experience from the non-spherical components,

$$F_{\sum \text{aspherical}} = \sum_{t} |\hat{r} \times \vec{F}| dt. \tag{3.6}$$

As discussed in Section 3.2.5, the Milky Way and the LMC haloes are initially spherical and do not exhibit aspherical forces. Any aspherical forces come from deformations and therefore these are an indication of how dark matter deformations affect the OC stream.

The forces from the LMC and the Milky Way are shown in Figure 3.6. The total force of the LMC is higher on the stream particles that passed closer to the LMC and roughly similar for all potential setups. The Milky Way exerts more force on the Northern part of the stream because it is the leading arm of the stream and hence has a smaller pericentre and thus a larger force. Since the monopoles only exert radial forces, the aspherical forces can only be due to deformations of the haloes and are thus more instructive for comparing the different expansions. The moments contributing most to the live force are the dipole for the Milky Way and the quadrupole for the LMC. Interestingly, for $\phi_1 > -45°$, the aspherical forces exerted by the LMC need the contribution of all higher moments to build up to the live forces showing that high multipole orders ($l \geqslant 3$) are needed to adequately capture the LMC's effect.

The ratio of the aspherical forces to live forces is up to 10 per cent for the LMC while only up to 1.8 per cent for the Milky Way. We stress that this does not directly translate to the impact of the deformations on the stream since the OC stream orbits the Milky Way throughout the whole integration time (4 Gyr). However, the Milky Way has only been deforming for the last ~ 500 Myr (see e.g. Figure 3.1). Therefore, the OC stream has experienced only radial forces for 3.5 Gyr and they make up most of the integrated absolute forces. If we restrict to the most recent 1 Gyr, the ratio of aspherical to total forces for the Milky Way reaches 5.5 per cent. In contrast, the LMC is already deforming when it gets close to OC so this metric should capture the relative strength of the aspherical forces. We discuss this in more detail in the next Section.

3.4 DISCUSSION

3.4.1 *The effect of deformations on streams*

Due to its length, OC experiences different effects from the deformations along the stream at different times. In Figure 3.7, we show the distance and time of the closest approach for each stream particle. While the Southernmost part of the stream passed

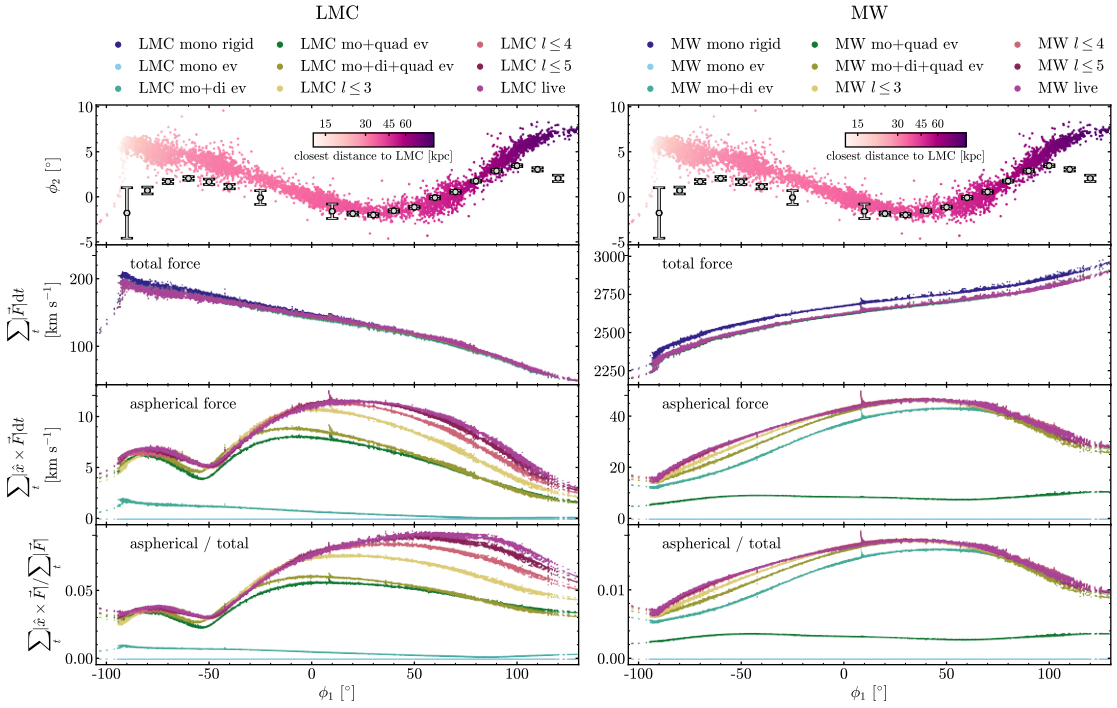

Figure 3.6: Integrated absolute forces of different moments of the LMC (*left*) and the Milky Way (*right*) on each particle of the stream. The *top row* shows the stream track, colour-coded by the closest approach distance to the LMC. The Southern portion of the stream ($\phi_1 < 0°$) passes the closest to the LMC, within 15–30 kpc. The *second row* shows the total integrated absolute forces. The colours indicate the moments whose forces are evaluated, going from blueish colours for the spherical components to reddish colours for the live potentials. Between the different moments, there is almost no difference. The total force of the Milky Way on the stream is more than a magnitude higher than the LMC's force since the Milky Way is more massive and since the OC stream orbits the Milky Way during the whole integration time (4 Gyr) while it is only impacted by the LMC over the most recent several hundred Myr. The *third row* shows the integrated aspherical forces. These forces are particularly interesting since these can only be a result of aspherical deformations. The moments with the highest marginal change are the quadrupole (green) for the LMC and the dipole (teal) for the Milky Way. In the LMC, the quadrupole contributes to most of the live forces on the Southernmost part of the stream ($\sim \phi_1 < -40°$). The Northern part of the stream is affected by higher moments beyond the quadrupole to build up to the live forces. In the Milky Way, the dipole and then quadrupole make up the majority of the live forces. The apparent spike at $\phi_1 \sim 10°$ is caused by particles that have just left the progenitor. The *bottom row* shows the ratio of aspherical to total integrated absolute forces. For the Milky Way, the aspherical forces are up to 1.8 per cent of the total forces while for the LMC they are up to 10 per cent.

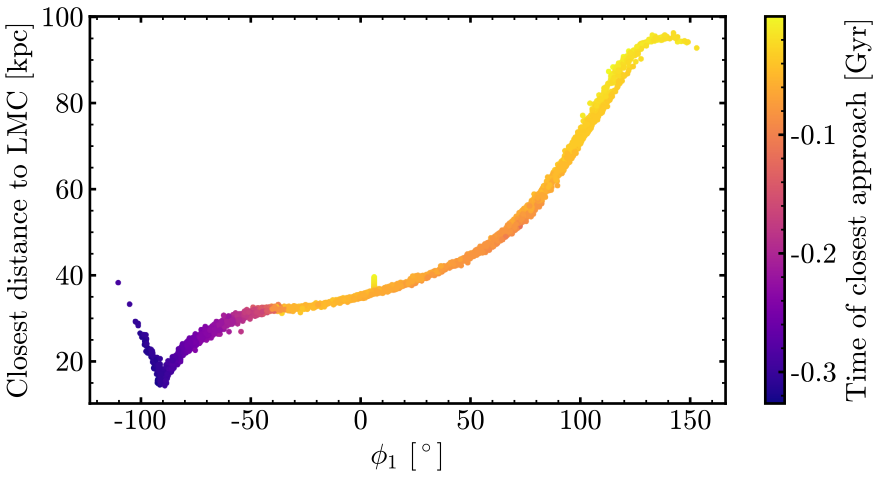

Figure 3.7: Distance and look-back time of the closest approach of the OC stream particles and the LMC. The plot shows the closest distance to the LMC along the stream colour-coded by the look-back time when this approach happened. The Southernmost part ($\phi_1 < -45°$) came closest to the LMC ($10-30$ kpc), around $200-300$ Myr ago while the rest of the stream had its closest interaction more recently ($<$ 100 Myr ago) and experienced a more strongly deformed LMC.

by the LMC around 300 Myr ago, the rest of the stream had its closest passage only within the last 100 Myr. There is a sharp cut between these time scales at $\phi_1 = -45°$. At this point in the stream, there is a dip in the aspherical forces experienced by the stream due to the LMC (see Figure 3.6). The aspherical forces on the left side of this dip are governed by the quadrupole which started growing around the time that this portion of OC had its closest passage to the LMC (~300 Myr ago, see Figure 3.1).

The particles with $\phi_1 > -45°$ had their closest approach to the LMC recently, and at a greater distance than the Southernmost part of the stream. Over the last 100 Myr, the quadrupole of the LMC increased significantly, but so did the higher moments (see Figure 3.1). These particles experienced an increased effect, not only by the quadrupole but also by the higher terms that allow for deformations on smaller scales (see bottom two rows of Figure A.1). We observe this effect in the aspherical forces from the LMC on the stream in Figure 3.6. While the quadrupole still makes up approximately half of the summed absolute aspherical forces, the contributions of all higher moments are necessary to get to the absolute sum of aspherical forces on the live stream.

Shipp et al. (2021) have modelled the OC stream in the presence of the LMC with rigid Milky Way and LMC models. Interestingly, at the position of the dip in the aspherical forces ($\phi_1 = -45°$), Shipp et al. (2021) find a sudden change in the orientation

of the LMC's perturbation on the OC stream (see their figure 5). They approximate perturbations with velocity kicks split up into different components: along the angular momentum of the stream, and in the radial and tangential direction of the orbit of the stream. For the OC stream, the velocity kick in the angular momentum direction is the strongest along most of the stream, but at the position of the dip, the offset in angular momentum has a sharp dip while the tangential offset has a quick rise. Moreover, their figure 8 shows the position of the stream with respect to the LMC at the time of the closest approach. The OC stream is split up into two unconnected parts at different positions and orientations. This is the same split that we see in the colours of Figure 3.7. These results from Shipp et al. (2021) and our results show that different regions of the stream are sensitive to different parts of the LMC.

3.4.2 *Possible bias in Milky Way and LMC halo measurements*

In this chapter, we have shown that the deforming Milky Way and LMC haloes have a significant effect on the OC stream. These effects have been ignored in all previous stream fits which have been done with rigid haloes for the Milky Way and the LMC (i.e. Erkal et al., 2019; Vasiliev et al., 2021). Interestingly, the change in the on-sky position from including the deformations ($\sim 1°$, see Figure 3.5) is similar to the change when allowing for the Milky Way halo to be flattened ($\sim 0.5°$, see figure 9 in Erkal et al., 2019). This suggests that at least some of this flattening could be due to deformations instead of the intrinsic shape of the Milky Way. This could be an explanation of the peculiar halo shapes inferred with the OC stream and Sagittarius stream which are strongly flattened and not aligned with the disc (Erkal et al., 2019; Vasiliev et al., 2021). Alternatively, if these measurements of the halo are robust, they could indicate that the Milky Way halo is twisted and aligned with the LMC's orbital plane as in Shao et al. (2021). We will investigate these potential biases in future work by fitting the stream models generated in this chapter with the same rigid haloes that are used to fit real streams (e.g. Erkal et al., 2019).

3.4.3 *Future directions*

Ultimately, we want to measure the Milky Way and LMC's time-dependent haloes by fitting streams in the Milky Way with models that include these effects. On the data side, we already have precise measurements for the Sagittarius stream (e.g. Ibata et al., 2020; Ramos et al., 2020; Vasiliev et al., 2021) and the OC stream (e.g. Koposov et al., 2019, 2023). These are the longest streams in the Milky Way that, along the stream, experienced different effects of the deformations at different times. Both have been used for fits of the Milky Way (e.g. Law & Majewski, 2010), recently including models of the LMC (e.g. Erkal et al., 2019; Vasiliev et al., 2021). There are also several shorter streams that have been affected by the LMC (Shipp et al., 2019). Shipp et al. (2021) have shown that the LMC has a significant impact on the OC stream and four additional streams in the Southern Galactic hemisphere, and has used them to fit the mass of the LMC. These streams had their last closest approach to the LMC between $\sim$ 100 Myr to $\sim$ 10 Myr ago, with closest approach distances ranging between $4-40$ kpc. As an ensemble, these streams pass through different parts of the deforming Milky Way and LMC at differing times and thus we should be able to use them to measure the time-dependence of the Milky Way and LMC haloes with upgraded BFE technology.

To be able to fit these streams, we need interpolatable BFEs. For this, we need a set of simulations with different Milky Way and LMC masses and, ultimately, different initial halo shapes. With these simulations, we then need to be able to interpolate between the coefficients to vary all parameters and fit the haloes with stellar streams. At each timestep, these simulations have 2058 coefficients to describe the haloes and 234 coefficients to describe the disc. To be able to fit these potentials, we need to improve our understanding of the importance of different terms in the expansion. One promising avenue for understanding and decomposing the time-dependence of the basis function expansions is with multichannel singular spectral analysis (Weinberg & Petersen, 2021). This non-parametric technique had some success isolating important dynamical effects but is still being developed.

3.4.4 *Implications for dark matter and alternative gravity models*

In this chapter, we have argued that the OC stream is sensitive to the deformed dark matter haloes of the Milky Way and the LMC. Detecting these deformations would allow us to test a robust prediction of the collisionless nature of cold dark matter and would allow us to constrain alternative dark matter and alternative gravity models.

In self-interacting dark matter (SIDM), the LMC and Milky Way dark matter haloes would experience additional forces during their interaction. Early work by Furlanetto & Loeb (2002), who approximated the SIDM as a perfect fluid, found that the structure of the wakes created in the dark matter haloes depends on whether the interaction is subsonic or supersonic. It remains to be seen what these effects look like in SIDM models with smaller cross-sections that do not assume a perfect fluid. We note that the Milky Way–LMC system will also be useful for constraining velocity-dependent SIDM models (e.g. Ackerman et al., 2009; Kaplinghat et al., 2016) since the velocities are much smaller than those of cluster-scale systems which are currently providing some of the most stringent limits (e.g. Tulin & Yu, 2018). Similarly, the effect of dynamical friction and the gravitational wake created is different in fuzzy dark matter models (e.g. Hui et al., 2017; Lancaster et al., 2020).

In alternative gravity models, e.g. modified Newtonian Dynamics (MOND, e.g. Milgrom, 1983; Bekenstein & Milgrom, 1984), the outer Milky Way has no dark matter halo to deform but still has a stellar halo and a hot gaseous corona (Gatto et al., 2013; Miller & Bregman, 2015). Since the stellar halo and corona densities have a different radial dependence than the dark matter halo (e.g. Miller & Bregman, 2015; Xue et al., 2015) they would presumably also deform differently. In addition, since dynamical friction behaves differently in the cold dark matter paradigm and MOND (e.g. Ciotti & Binney, 2004; Nipoti et al., 2008), the orbit of the LMC is quite different (e.g. Wu et al., 2008; Schee et al., 2013) which would also affect how the outer Milky Way deforms. As a result, we expect that detecting a deformed Milky Way potential with stellar streams would likely provide a powerful discriminator between dark matter and alternative gravity models. In order to confirm this, more work is needed to understand how the Milky Way deforms in alternative gravity models and how these deformations affect stellar streams.

3.4.5 *The effect of the Small Magellanic Cloud*

Our present study neglects the presence of the SMC in our model of the Milky Way–LMC interaction. One can make estimates for the possible bias our models incur from this omission from simple BFE-based arguments. In essence, we ask: can the SMC be responsible for levels of deformation in the LMC that would be detectable in our expansion, particularly at spatial locations that would be important for the OC stream? While the SMC is likely responsible for the deformations observed in the luminous component of the LMC, the deformations in the LMC dark matter halo are likely dominated by the interaction with the Milky Way.

Following the LMC–SMC models developed in Cullinane et al. (2022), we choose a mass ratio of $M_{SMC}/M_{LMC} = 2.5 \times 10^9\ M_\odot / 7.17 \times 10^{10}\ M_\odot = 0.03$ to represent their present-day masses. If we assume that the LMC expansion absorbs the contribution from the SMC, the mass ratio projects immediately into the monopole term, increasing the monopole by the mass ratio fraction (i.e. making the LMC heavier). More interesting are the implications for the higher-order terms in the expansion. If we assume that the SMC is represented by a Hernquist spherical mass distribution with $r_s = 10$ kpc centred on the current location of the SMC, the contribution to the amplitude of the dipole terms in the spherical expansion is of order 0.1 per cent relative to the LMC, i.e. an order of magnitude smaller than the deformations induced by the Milky Way. In this simple scenario, the SMC does not contribute to even-order spherical harmonics, which are the most influential for the evolution of the OC stream.

It is likely that the SMC had a higher mass in the past, but repeated interactions with the LMC have stripped much of the mass from the SMC (e.g. Besla et al., 2012; De Leo et al., 2020). This mass will be distributed around the LMC, with the primary contribution being to the monopole and likely having little impact on higher-order harmonics. Future models should investigate the possible geometries of stripped SMC dark matter mass around the LMC.

We note that this global view of the influence of the SMC on the LMC does not describe the forces orbits near the SMC might feel; thus we caution that for orbits that pass near the SMC at any point in the past (e.g. smaller than the LMC–SMC separation), the influence may be much larger (e.g. SMC's effect on orbits of dwarfs;

Patel et al., 2020; Simon et al., 2020). In order to test this, we injected the SMC as a tracer particle in our simulation. We find that, compared to the LMC, it has a more distant approach to the OC stream, suggesting it will have a negligible effect. Along similar lines, Koposov et al. (2023) explore this in more detail by modelling the gravitational effect of the SMC on the OC stream and find that it has almost no effect on the stream.

3.4.6 *The complex landscape of the Milky Way potential*

Although we have focused on the interaction of the Milky Way and the LMC, there are many other effects which can perturb streams and other tracers in the Milky Way, and thus complicate our ability to measure the potential. For example, the Sagittarius dwarf was likely much more massive when initially accreted onto the Milky Way, $\gtrsim 6 \times 10^{10}$ $M_\odot$ (e.g. Bland-Hawthorn & Tepper-García, 2021; Gibbons et al., 2017). The stripped dark matter of Sagittarius could have a substantial effect on the potential as well as on streams that pass through it (Bovy et al., 2016). Similarly, the accretion of Gaia-Sausage-Enceladus (GSE, Belokurov et al., 2018; Helmi et al., 2018) likely deposited a substantial amount of dark matter in the inner halo. Han et al. (2022) argue that this may cause a long-lived tilt in the dark matter halo that supports the orbits of stars in the Hercules Aquila Cloud (e.g. Belokurov et al., 2007a; Simion et al., 2014) and Virgo Overdensity (e.g. Vivas et al., 2001; Newberg et al., 2002). On slightly larger scales, Valluri et al. (2021) have shown that the expected figure rotation of the Milky Way's dark matter halo can also affect streams. On smaller scales, many works have shown that the bar and spiral arms of the Milky Way can perturb streams (e.g. Hattori et al., 2016; Price-Whelan et al., 2016b; Erkal et al., 2017; Pearson et al., 2017; Banik & Bovy, 2019).

Going forward, it will be crucial to identify which of this myriad of effects is the most important in each region of the Milky Way. Ideally, there will be a leading order effect in each region, e.g. the bar and spiral arms in the inner Milky Way, and the LMC in the outer Milky Way. This would allow us to search for and convincingly measure these effects without having to build overly complex models that contain all of these perturbations.

3.5 CONCLUSIONS

The Milky Way and the LMC are in disequilibrium (e.g. Garavito-Camargo et al., 2019, 2021a; Erkal et al., 2020, 2021; Conroy et al., 2021; Petersen & Peñarrubia, 2021; Petersen et al., 2022b), and several stellar streams in the Milky Way halo are affected, particularly the OC stream (Erkal et al., 2019; Koposov et al., 2019; Shipp et al., 2021). In this chapter, we have explored the effect of deformations of the dark matter haloes of these galaxies on a simulated OC stream using basis function expansions. We presented a N-body simulation of the interaction between the Milky Way and the LMC run with the BFE code `EXP` (Weinberg, 1999; Petersen et al., 2022a). This allowed us to evaluate the time-dependent forces at any position in the system, and thus evolve the OC stream in a deforming Milky Way and LMC system. We compared our simulations to the exquisite 6-D phase-space map of the OC stream from *Gaia* and the S^5 survey (Koposov et al., 2023).

Equipped with these BFEs, we investigated several aspects of the effect of the deformations on the OC stream. Our results are the following:

- The Milky Way deformations owe primarily to the dipole, which has grown in strength over the last ~ 500 Myr. In contrast, the LMC deformations owe primarily to the quadrupole, which steeply gained power over the last ~ 200 Myr. During the last ~ 100 Myr, the LMC's higher moments have also gained some power (see Figure 3.1). These multipoles are also visible in the density and force field plots and videos of the Milky Way and the LMC (see Figures 3.2 and 3.3).

- The OC stream changes significantly when evolved in the presence of different moments (and therefore different potentials) with the same initial conditions for the stream progenitor. These effects are much larger than the current observational uncertainties so models that ignore these effects may be biased. The biggest change is induced by the Milky Way's dipole, followed by the time-evolving monopole of the LMC and the LMC's quadrupole (see Figure 3.5).

- In order to isolate the impact of each multipole, we evolve the stream in the live potential and calculate the force contributions, with a particular emphasis on the aspherical forces that are due to deformations (see Figure 3.6). Again, the dipole

contributes the most to the Milky Way force while the LMC forces are dominated by the quadrupole. Interestingly, for the Northern part of the OC stream, higher moments of the LMC expansion ($l \geqslant 3$) make a significant contribution to the force it exerts on the OC stream.

- The OC stream is sensitive to the time-dependent deformation of the LMC. This is due to the fact that different parts of the OC stream experience their closest passage with the LMC at different times (Figure 3.7), and that the high-order multipoles of the LMC are growing over the past $\sim$ 100 Myr (Figure 3.1). As a result, the Northern and Southern components of the OC stream experience different force contributions from the multipole orders (see Figure 3.6).

In summary, we have shown that the OC stream acts as a sensitive detector in the Milky Way–LMC dark matter collider. If our models are correct, these effects are already present in the data since they are much larger than the observational uncertainties of the OC stream. Progress is now needed on the theory side to fully utilise this data to measure the time-dependent haloes of the Milky Way and the LMC. In particular, we need an improved understanding of BFEs so that we can interpolate over the properties of both haloes in a computationally efficient way. Detecting the existence of and characterizing these effects would be a spectacular test of the collisionless nature of dark matter and would offer another window to probe alternative dark matter and alternative gravity models.

ACKNOWLEDGEMENTS

SL would like to thank L. Whitehouse for useful discussion relating to the analysis in this chapter. We would like to thank the referee for their careful and insightful review that helped improve the clarity of this manuscript. This chapter includes data obtained with the Anglo-Australian Telescope in Australia. We acknowledge the traditional owners of the land on which the AAT stands, the Gamilaraay people, and pay our respects to elders past and present.

MSP acknowledges grant support from Segal ANR-19-CE31-0017 of the French Agence Nationale de la Recherche (https://secular-evolution.org). This chapter has made use of data from the European Space Agency (ESA) mission *Gaia* (https://www.cosmos.

esa.int/gaia), processed by the *Gaia* Data Processing and Analysis Consortium (DPAC, https://www.cosmos.esa.int/web/gaia/dpac/consortium). Funding for the DPAC has been provided by national institutions, in particular the institutions participating in the *Gaia* Multilateral Agreement.

Facilities: Anglo-Australian Telescope (AAOmega+2dF), Institute for Astronomy *cuillin* supercomputer (https://cuillin.roe.ac.uk), University of Surrey *Eureka* High Performance Computing cluster

Software: `astropy` (The Astropy Collaboration, 2013, 2018), `EXP` (Petersen et al., 2022a), `IPython` (Pérez & Granger, 2007), `Jupyter` (Kluyver et al., 2016), `matplotlib` (Hunter, 2007), `mpi4py` (Dalcin & Fang, 2021), `numpy` (Harris et al., 2020), `pandas` (McKinney, 2010; Reback et al., 2020), `pybind11` (Jakob et al., 2017), `scipy` (Virtanen et al., 2020)

DATA AVAILABILITY

The data underlying this article is published in Koposov et al. (2023). The stream models will be shared on reasonable request to the corresponding author. A `python` interface to integrate orbits and access the expansion model for the simulation can be found here: https://github.com/sophialilleengen/mwlmc.

4

INFORMATION CONTENT IN STELLAR STREAMS IN TIME-DEPENDENT POTENTIALS

The Milky Way is surrounded by stellar streams, with nearly 100 detected to date and more expected with future surveys. These streams hold a wealth of information about the gravitational potential they move in, i.e. the Milky Way's dark matter halo. Recently, it has become clear that the Milky Way's dark matter halo experiences a perturbation due to the infalling Large Magellanic Cloud (LMC). This perturbation is strong enough to affect stellar streams. This paper explores the information streams hold about this time-dependent perturbation. We build a simple toy model of the Milky Way halo and an external perturbation inspired by the LMC's perturbation in which we evolve Milky Way mock streams. We implement a Fisher information or Cramér–Rao lower bound (CRLB) approach to estimate the best-case uncertainty that stream model parameters can have given realistic data uncertainties. We first investigate one of the most informative streams, a mock of the Orphan–Chenab (OC) stream, which spans 40 kpc in the Milky Way halo. We find that most information lies in the stream track, but future data with better velocities will contribute to the information content. We find that the CRLBs for the perturbation are always worse than they are for halo parameters. The longer and wider a stream is, the more information on the time-dependence it contains; thus, dwarf galaxy streams will be more suited to fit a time-dependent Milky Way potential.

Work shown in this chapter is being prepared for publication by Lilleengen, Price-Whelan, Bonaca, Erkal, Johnston, and Hogg in The Astrophysical Journal.

4.1 INTRODUCTION

The Milky Way is surrounded by stellar streams that hold a wealth of information about the Milky Way's dark matter halo. Currently, there are almost 100 observed Milky Way streams (Mateu, 2023), and more detections are expected with upcoming surveys such as the Large Synoptic Survey Telescope (LSST; Ivezić et al., 2019). Each stream is unique in its orbital and morphological properties, e.g. its length, width, orbital properties, and the part of the galaxy in which it resides. Given these properties, some streams are particularly suited to constrain properties of the Milky Way's gravitational potential.

Shortly after the first stellar stream was detected (Sagittarius; Ibata et al., 1994), Johnston et al. (1999) suggested that these tidal tails can be used to infer properties of the Milky Way halo. Since then, many streams have been used to fit the Milky Way potential, including Sagittarius (e.g. Ibata et al., 1994; Newberg et al., 2002; Majewski et al., 2003), Orphan–Chenab (OC) (Grillmair, 2006; Belokurov et al., 2007a), Palomar-5 (Odenkirchen et al., 2001), and GD-1 (Grillmair & Dionatos, 2006). Different methods exist for these models: orbit-fitting techniques (e.g. Koposov et al., 2010; Malhan & Ibata, 2019), action-angle tracks (e.g. Bovy, 2014; Sanders, 2014), clustering of actions (Sanderson et al., 2015; Reino et al., 2021, 2022), particle-spray methods (Küpper et al., 2008, 2010, 2012; Bonaca et al., 2014; Gibbons et al., 2014; Fardal et al., 2015) and N-body simulations (e.g. Law & Majewski, 2010; these are usually too expensive to fit a stellar stream). All of these assume some form of analytic, rigid potential.

Recently, it has become clear that the infalling Large Magellanic Cloud (LMC) perturbs the Milky Way and its stellar streams. The LMC is heavy enough to substantially accelerate the Milky Way's disk. This reflex motion points along the past orbit of the LMC (e.g. Erkal et al., 2021; Petersen & Peñarrubia, 2021). Overdensities in the stellar halo are observed along the path of the LMC due to dynamical friction and as the collective response in the northern hemisphere sustained by resonances (Garavito-Camargo et al., 2019, 2021a; Conroy et al., 2021). Stellar streams are pulled off of their tracks by the LMC, which is seen in a misalignment between the stream track and the proper motions (Erkal et al., 2019; Shipp et al., 2021; Koposov et al., 2023). Due to this interaction, the dark matter haloes of both the LMC and the Milky Way are expected

to be deforming (Garavito-Camargo et al., 2019, 2021a; Petersen & Peñarrubia, 2020). Chapter 3 (Lilleengen et al., 2023) show that these deformations have a significant effect on the OC stream, particularly on the stream track.

While this effect has great potential in expanding our understanding of dark matter if we can find direct evidence of the deformations in stellar streams, it also causes great problems for modelling stellar streams. Chapter 3 shows that the deformations change the stream by more than the observational uncertainties, and thus, there may be biases if these effects are not included. Current data already exceeds our ability to fit them with rigid models as the fits in Erkal et al. (2019); Koposov et al. (2023) could not reproduce all of the features in the OC stream. While we can implement increasing complexity in the rigid models, we need to understand the effect of the deformations on stellar streams. We want to ask the questions, *what exactly are streams measuring*? Can streams constrain the time dependence of the halo?

These questions can be answered using concepts of information theory. Bonaca & Hogg (2018) developed an approach to calculate the information content in stellar streams. They calculated Cramér–Rao lower bounds of the uncertainty of model parameters given the quality of a data set. This is done by taking derivatives of a mock stream at the 'true' parameter value. For a simple analytic Milky Way potential, they found best-case uncertainties at the percent level when simultaneously fitting multiple stellar streams. They added more freedom to their models by using basis function expansions. These expansions could describe complicated deformations of the potentials. They found that, in this case, the information becomes restricted to the current position of the stream. While they added this description to the model, they kept the value of the coefficients that set the perturbations at zero and took derivatives there. In this chapter, we build upon Bonaca & Hogg (2018) and expand it to time-dependent perturbations. We investigate streams in perturbed potentials inspired by the LMC's effect and the information they contain on the time dependence of the halo.

This paper is organised as follows. In Section 4.2, we explain the information theory approach, the implementation of the perturbations to the potential, the generation of mock streams, and the calculation of the information content in stellar streams. Then, in Section 4.3 we present how this information looks in streams that are evolved in static and time-dependent perturbed potentials. We investigate different aspects of the

interpretation of the information in Section 4.4. We discuss these results in Section 4.5 and conclude in Section 4.6.

4.2 METHODOLOGY

4.2.1 *Information theory*

Stellar streams are often used to infer properties of the Milky Way's dark matter halo (e.g. Johnston et al., 1999; Law & Majewski, 2010; Koposov et al., 2010; Bovy, 2014; Sanders, 2014; Erkal et al., 2019; Vasiliev et al., 2021; Nibauer et al., 2022; Koposov et al., 2023). To do this, a model that describes the properties of the Milky Way and the progenitor of the stellar stream is generally necessary[1]. Identifying the most constraining streams for these model parameters will allow us to select the best streams for modelling the Galaxy most precisely. We use information theory to understand how much information observables of different stellar streams hold about the parameters of the underlying model. Bonaca & Hogg (2018) have developed this framework for stellar streams in static potentials. This chapter extends their approach to stellar streams in time-dependent potentials to allow for new strategies for mapping the Milky Way's dark matter halo.

In this approach, information is described as the best-case uncertainty that can be inferred for a model parameter given the quality of observational data and is described by the Cramér–Rao lower bound (CRLB; Cramér, 1946; Rao, 1945) as matrix C_x. The inverse of that matrix is Fisher information which describes the amount of information an observable carries about a model parameter. For a vector of observables $\vec{y}$ and a vector of model parameters $\vec{x}$, the Fisher information matrix (Fisher, 1925) is given by

$$C_x^{-1} = \left(\frac{d\vec{y}}{d\vec{x}}\right)^T C_y^{-1} \left(\frac{d\vec{y}}{d\vec{x}}\right) + V_x^{-1}. \tag{4.1}$$

Here, $\left(\frac{d\vec{y}}{d\vec{x}}\right)$ denotes the derivative of the observables of an object with respect to the model parameters, C_y represents the covariance matrix of the observed data and V_x a matrix containing any prior information.

1 Though in Nibauer et al. (2022), a model for the Galactic potential does not need to be specified; in some cases, accelerations can be measured from streams directly.

We aim to find stellar streams that contain information about the time-dependent Milky Way halo. Currently, models that can be used to fit the time-dependent Milky Way halo do not exist yet and still need to be developed. Therefore, we use a simplified potential model to present this technique and show its capabilities so that it can be applied to more complex models in the future. In the next sections, we describe the potential model and how we generate stream models and mocks before explaining how we apply Equation 4.1 to stellar streams.

4.2.2 *Perturbed potentials*

In order to gain an intuition for the effects of time dependence, we use a simple toy model as the underlying potential. We describe the dark matter halo with an Navarro–Frenk–White (NFW) profile (Navarro et al., 1997). We choose an NFW with a mass of $M_{NFW} = 7.92 \times 10^{11}\ M_\odot$ and a scale radius of $r_s = 12.8$ kpc based on the results in Erkal et al. (2019). This NFW mass translates to a scale mass of $M_{scale} = 4.28 \times 10^{11}\ M_\odot$ implemented in `gala` (Price-Whelan, 2017; Price-Whelan et al., 2022).

In order to describe perturbations to this potential, we use a multipole expansion (see e.g. Binney & Tremaine, 2008). They can be split up into the potential internal and external to a perturbation. Since in the Milky Way, the perturbation is caused by an infalling, i.e. external, dwarf galaxy, we assume an external perturbation. Therefore we use the potential internal to the perturbation (Binney & Tremaine, 2008). The perturbing potential depends on spherical harmonics, $Y_l^m(\theta, \phi) \propto P_l^m(\cos\theta)\, e^{im\phi}$ that use the Legendre polynomials $P_l^m(\cos\theta)$, and the maximum l order l_{max} and follows

$$\Phi_{int}^{l_{max}}(r, \theta, \phi) = \sum_{l=1}^{l=l_{max}} \sum_{m=0}^{m=l} r^l \left(\alpha_{lm} \cos m\phi + \beta_{lm} \sin m\phi\right) P_l^m(\cos\theta) \tag{4.2}$$

where α_{lm} and β_{lm} are the coefficients for the degree l and order m. Following Hernquist & Ostriker (1992), we combine terms with opposite signs of m to express the potential in real terms.

We explore two types of perturbations: static and time-dependent. The time-dependence is introduced by describing the coefficients α_{lm} and β_{lm} by the polynomials

$$\alpha_{lm}(t; n) = \sum_{i=0}^{n} \alpha_{lmi} \cdot t^i \tag{4.3}$$

$$\beta_{lm}(t; n) = \sum_{i=0}^{n} \beta_{lmi} \cdot t^i \tag{4.4}$$

where n is the degree of the polynomial. The static potential[2] is described by static coefficients with $n = 0$.

These coefficients describe the strength and the shape of the perturbation. Chapter 3 showed that the biggest effect of the Milky Way–LMC perturbation is the dipole induced in the Milky Way halo. They simulate the time-dependent Milky Way–LMC system using `EXP` (Petersen et al., 2022a) that describe the Milky Way halo, disc, and the LMC with basis function expansions (BFEs). To get a similar Milky Way dipole as in Chapter 3, we fit a polynomial to the time-evolution of the Milky Way halo dipole coefficients from their Milky Way halo expansion. The resulting coefficients are best described by a 9th-degree polynomial shown in Figure B.1. Then, we scale the resulting polynomial coefficients so that the ratio of the forces due to the perturbation and the forces due to the fiducial halo match the equivalent ratio for the Lilleengen et al. (2023) Milky Way dipole on large scales up to 50 kpc shown in Figure B.2. For this, we keep the mass and scale radius for the perturbing potential the same as the NFW potential parameters and then scale it with the value of the first coefficient of the time-dependent dipole (α_{100}) and a scale factor. The force fields of the perturbation of BFE simulation and the scaled multipole expansion are shown in Figure B.2. The simulated dipole contains more detail and more complex deformations. For the sake of a simple toy model, matching the perturbation force field on large scales is enough.

For the static perturbation, we use the first polynomial coefficient for each degree and order we investigate. Since the strength of the coefficients only increased recently (see Figure 3.1), this leads to a stronger deformation over time and along a stream's orbit than the time-dependent perturbation. A stronger deformation is more illustra-

2 We implemented the static perturbation potential in gala.

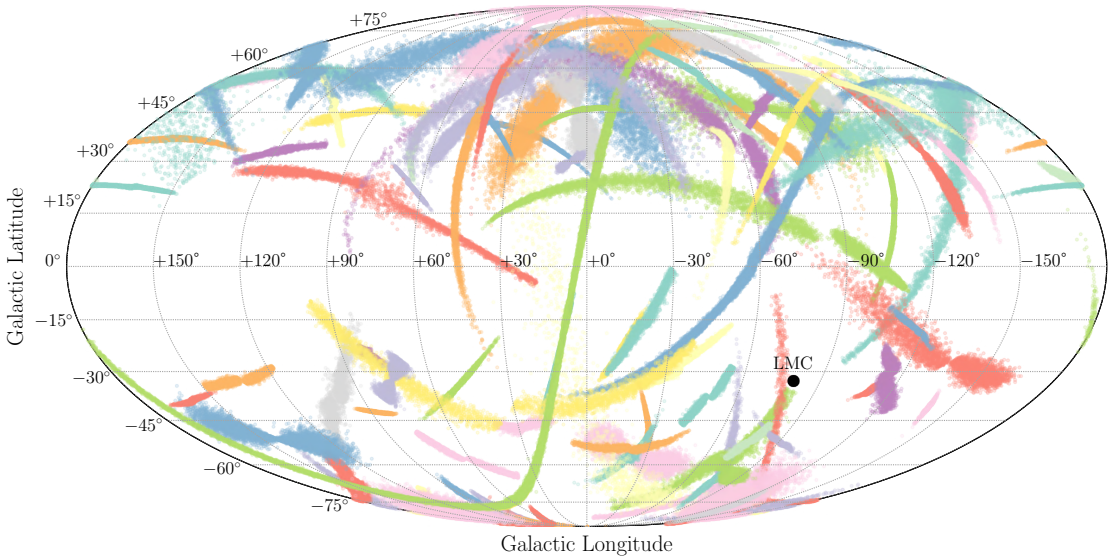

Figure 4.1: All-sky view of mock streams that are analyzed in this paper. The streams are based on the `galstreams` catalogue (Mateu, 2023) containing 97 streams. Each stream is generated based on the midpoints of the catalogue tracks and evolved in the static NFW potential described in Section 4.2.2 with the `MockStreamGenerator` implemented in `gala` (Price-Whelan, 2017). Mass, scale radius, and integration time depend on the stream length, as explained in the text. A black circle marks the position of the LMC.

tive and helpful for using the static case as a toy model since we are ultimately only interested in a realistic time-dependent perturbation.

The model parameters for the potential are the mass and scale radius of the NFW halo and the perturbation coefficients. The coefficients are either one number per degree l and order m in the static case, indicated by $S_{lm} (\equiv \alpha_{lm0})$, or several polynomial coefficients per order and mode for the time-dependent perturbation i, indicated by α_{lmi}.

4.2.3 *Stellar stream models and mock data*

Mock stream models

In this paper, we calculate the information of mock streams spanning a range of different initial conditions of the progenitor. To have a similar distribution of initial conditions, we use stream properties collected in `galstreams` (Mateu, 2023). For all 97 listed streams, we use the midpoint values as progenitor initial conditions. We integrate the streams using the `MockStreamGenerator` implemented in `gala` (Price-Whelan, 2017). The evolution of the streams is modelled with the particle spray method pre-

sented in Fardal et al. (2015). Particles are released near the Lagrange points of the progenitor with a position and velocity dispersion set by the progenitor's mass and orbit. This method reproduces stream morphologies that match N-body simulations of stellar streams.

To generate mock streams similar to the observed ones, we choose mass, scale radius and integration time according to the stream's length. Streams with observed lengths smaller than 60 degrees are assumed to be globular cluster streams with $M_{prog} = 10^4\ M_\odot$ and $r_{s,prog} = 10\,pc$. Longer streams are assumed to be dwarf galaxy streams with $M_{prog} = 10^6\ M_\odot$ and $r_{s,prog} = 100\,pc$. We find the minimum integration time necessary to produce the stream length by generating each stream in steps of 0.5 Gyr until it surpasses the observed length. We cut the streams to the length of the according `galstream` stream. Since our toy potential is not representative of the Milky Way, these streams evolve differently. A notable example throughout this paper is GD-1, whose mock is wider than the observed stream, making the results of this paper not directly applicable. Moreover, the mock streams might show different orientations, but they should give a representative picture of the information contained in the stream population. Figure 4.1 shows an all-sky view of the mock streams, colour-coded by distance.

Observables of stellar streams

To analyze stellar streams, they are often rotated into a system where they follow a 'great circle' shape, defined by a pole and optionally a zero point for each stream individually. In this coordinate frame, the stream observables are the stream track (ϕ_2), distance, radial velocity (v_r), and proper motions along ($\mu_{\phi_1^*}$) and perpendicular (μ_{ϕ_2}) to the stream along the angle of the stream (ϕ_1). A stream observables plot for the example stream from Figure 4.1 is shown in Figure 4.2. The observational error of these observables is one of the components to calculate the best-case parameter uncertainty, described in the next section.

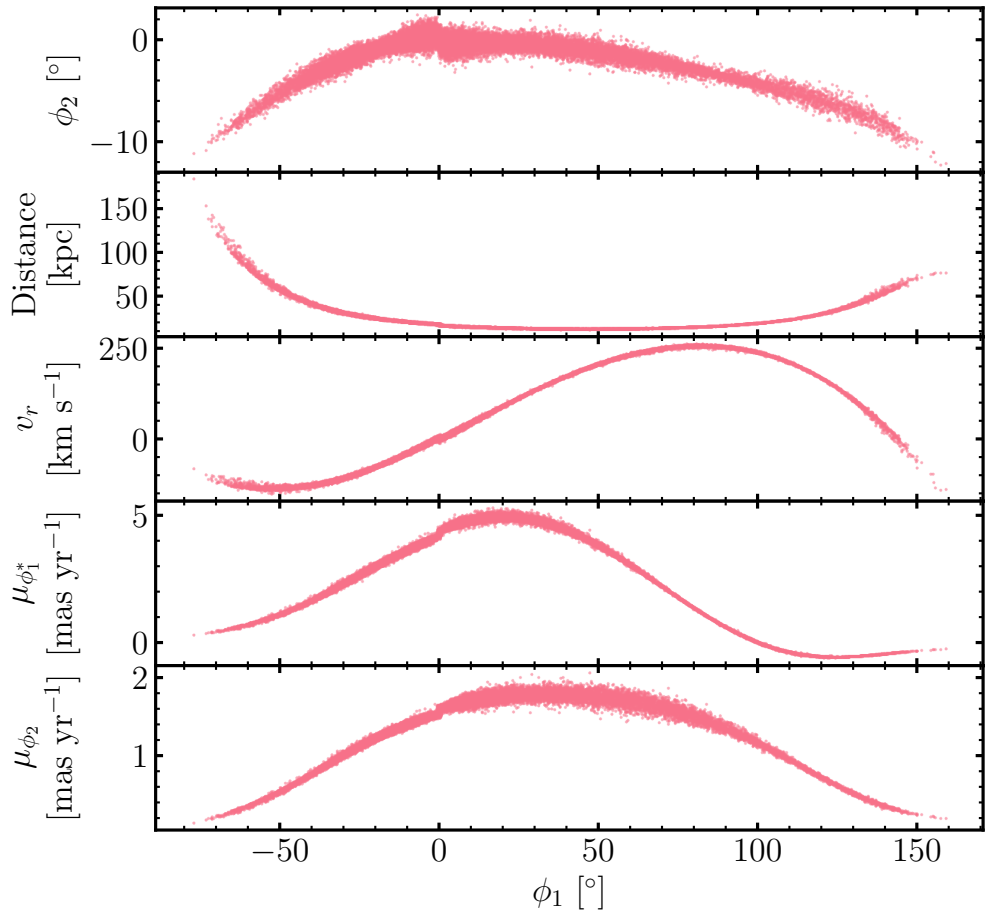

Figure 4.2: Observables of the mock OC stream. The panels show the stream track in stream coordinates *(first panel)*, the heliocentric distances *(second panel)*, the radial velocities *(third panel)*, and the proper motions along *(fourth panel)* and perpendicular to the stream *(fifth panel)*. This presentation is often used to visualise a stellar stream.

4.2.4 *Information content in stellar streams*

The best-case uncertainty of model parameters is described by the CRLB (Cramér, 1946; Rao, 1945). It is the inverse of the maximum information that observables contain on model parameters, quantified by Fisher information. The Fisher information matrix is given by Equation 4.1, for which we need to determine the different components in the context of stellar streams.

First, we calculate the numerical derivative of the streams $d\vec{y}/d\vec{x}$, where $\vec{y}$ is a vector containing the observational (mock) data and $\vec{x}$ a vector of the model parameters. For each parameter, we generate two streams with an offset Δx in both directions of the initial value. We explain how we calculate Δx in the next paragraph. Then, we calculate the distance between the observables of these two stream models for randomly selected particles along the stream, following this expression:

$$\left.\frac{dy_i}{dx_j}\right|_{\xi_k} = \left.\left(\frac{y_i\left(x_{0,j}+\Delta x_j\right) - y_i\left(x_{0,j}-\Delta x_j\right)}{2\Delta x_j}\right)\right|_{\xi_k} \tag{4.5}$$

for the stream observable y_i, model parameter x_j and stream particle ξ_k.

The offset Δ_x is calculated individually for each parameter for each stream, following the approach of Bonaca & Hogg (2018). We calculate the derivatives over seven magnitudes of Δx. For each step size Δx, we calculate the deviation of the derivatives from the adjacent step sizes, $\Delta\dot{y}$, following

$$\Delta\dot{y} = \sum_i \left(\left.\frac{dy_i}{dx}\right|_{\Delta x_j} - \left.\frac{dy_i}{dx}\right|_{\Delta x_{j-1}}\right)^2 + \sum_i \left(\left.\frac{dy_i}{dx}\right|_{\Delta x_j} - \left.\frac{dy_i}{dx}\right|_{\Delta x_{j+1}}\right)^2 \tag{4.6}$$

with the stream observables y_i. We select the step size with the smallest $\Delta\dot{y}$.

The matrix C_y contains data variances and covariances. When assuming no covariances, it is a diagonal matrix populated with $\sigma^2_{y_i}$ for all observables. In the Fisher information matrix, the inverse of this matrix is used. We can remove the observable from the analysis by setting the inverse of its uncertainty to zero. We use uncertainties of current and future surveys and summarise these in Table 4.1. Prior information is contained in V_x, but for this chapter, we do not assume any.

Table 4.1: Assumed uncertainties of stream observables for current (DR3) and future (DR5) *Gaia* data qualities.

Stream observables	*Gaia* DR3	*Gaia* DR5
σ_{ϕ_2} [deg]	0.1	0.1
σ_d [kpc]	2	2
σ_{v_r} [km s^{-1}]	5	1
$\sigma_{\mu_{\phi_1^*}}$ [mas yr^{-1}]	0.1	0.015
$\sigma_{\mu_{\phi_2}}$ [mas yr^{-1}]	0.1	0.015

With these components, we can calculate the Fisher information matrix C_x^{-1} using Equation 4.1. The stream derivative is calculated for particles along the stream, and the information matrix describes the information along the stream. To get the information the whole stream contains, we add the information up over the individual particles. Finally, to get the CRLB matrix, we invert the Fisher information matrix[3].

Within the CRLB matrix C_x, the best-case uncertainty for parameter i is given by $\sqrt{C_{x,ii}}$. The correlation of best-case uncertainties of two parameters can be described by an ellipse with rotation angle θ, width w, and height h with

$$\theta = \arctan\left(\frac{V_{1,0}}{V_{0,0}}\right) \tag{4.7}$$

$$h = 2\sqrt{v_0} \tag{4.8}$$

$$w = 2\sqrt{v_1}. \tag{4.9}$$

V_k are the eigenvectors with $V_{k,l}$ the l component of the eigenvector k and v_k the corresponding eigenvalues of a slice of the CRLB matrix $M_{ij} \equiv \left[\left[C_{x,ii}, C_{x,ij}\right], \left[C_{x,ji}, C_{x,jj}\right]\right]$. These ellipses visualise the Cramér–Rao Lower Bound, i.e., the parameters' best-case uncertainty, and the correlation between different model parameters.

4.3 INFORMATION IN AN EXAMPLE STREAM IN PERTURBED POTENTIALS

With the tools at hand to investigate the information in streams, we first build intuition by exploring the information on all model parameters in a potential with a static and a time-dependent perturbation.

3 `np.linalg.inv` has improved so that even with a large condition number of the matrix, we do not need any matrix inversion tricks as, e.g. were necessary for Bonaca & Hogg (2018).

4.3.1 *Static perturbation*

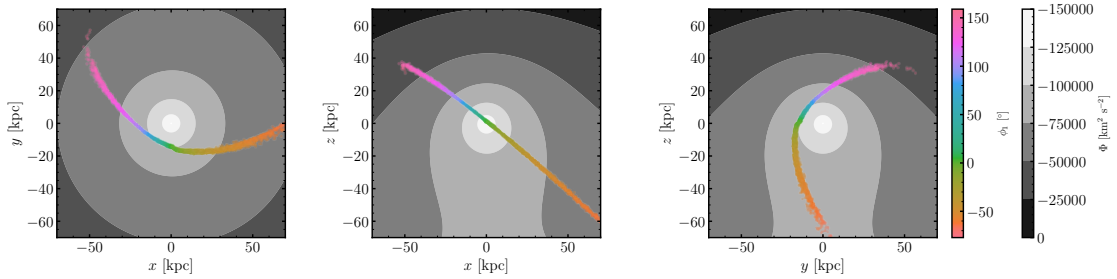

Figure 4.3: Contours of the perturbed potential in Galactocentric coordinates. The perturbation lies mainly within the $m = 0$ mode in the z-direction of the potential, shown in the middle and right panels. A smaller perturbation in the $m = 1$ mode is seen along the x-axis in the left and middle panels. The mock OC stream is overplotted and is colour-coded with the angle along the stream, corresponding to the top panel of Figure 4.2. For the static perturbation, the stream evolves in this potential. In the time-dependent perturbed potential, the strength and the shape of the deformation change over time, with the strongest deformation at the current time, $t = 0$ Gyr. The time-evolution of the coefficients is shown in Figure B.1.

First, we generate a stream model of the example mock stream in the potential with a static perturbation. We calculate the stream observables' information on the halo and perturbation parameters. Figure 4.3 shows the potential contours and the stream's current-day position. As mentioned in Section 4.2.2, this perturbation exceeds the expected level of the Milky Way perturbation for demonstrative purposes.

Figure 4.4 shows a visualisation of the CRLBs of the model parameters for an OC-like stream evolved in the potential with a static perturbation. The ellipses in each panel show the covariant CRLB for each pair of coefficients. They are centred on the true value of the parameter. The parameters shown are the progenitor's position and velocity in Galactocentric coordinates, the scale mass and radius of the NFW halo, and the coefficients of the dipole shown in Equation 4.3 with the coefficients S_{lm} noting the static perturbation for the modes $m = 0$: $S_{10} = \alpha_{100}$; and $m = 1$: $S_{11} = \alpha_{110}$. The stronger the ellipse, the higher the covariance. There are covariances between the parameters of the progenitor position and velocity, the progenitor's phase-space parameters and the NFW scale radius, the NFW scale mass and S_{11}, and between the two perturbation coefficients S_{10} and S_{11}.

We note that the amplitudes of the uncertainties with respect to the value of the true parameters are generally very small, significantly smaller than the single stream CRLBs from Bonaca & Hogg (2018). We have tested several model setups that could influence

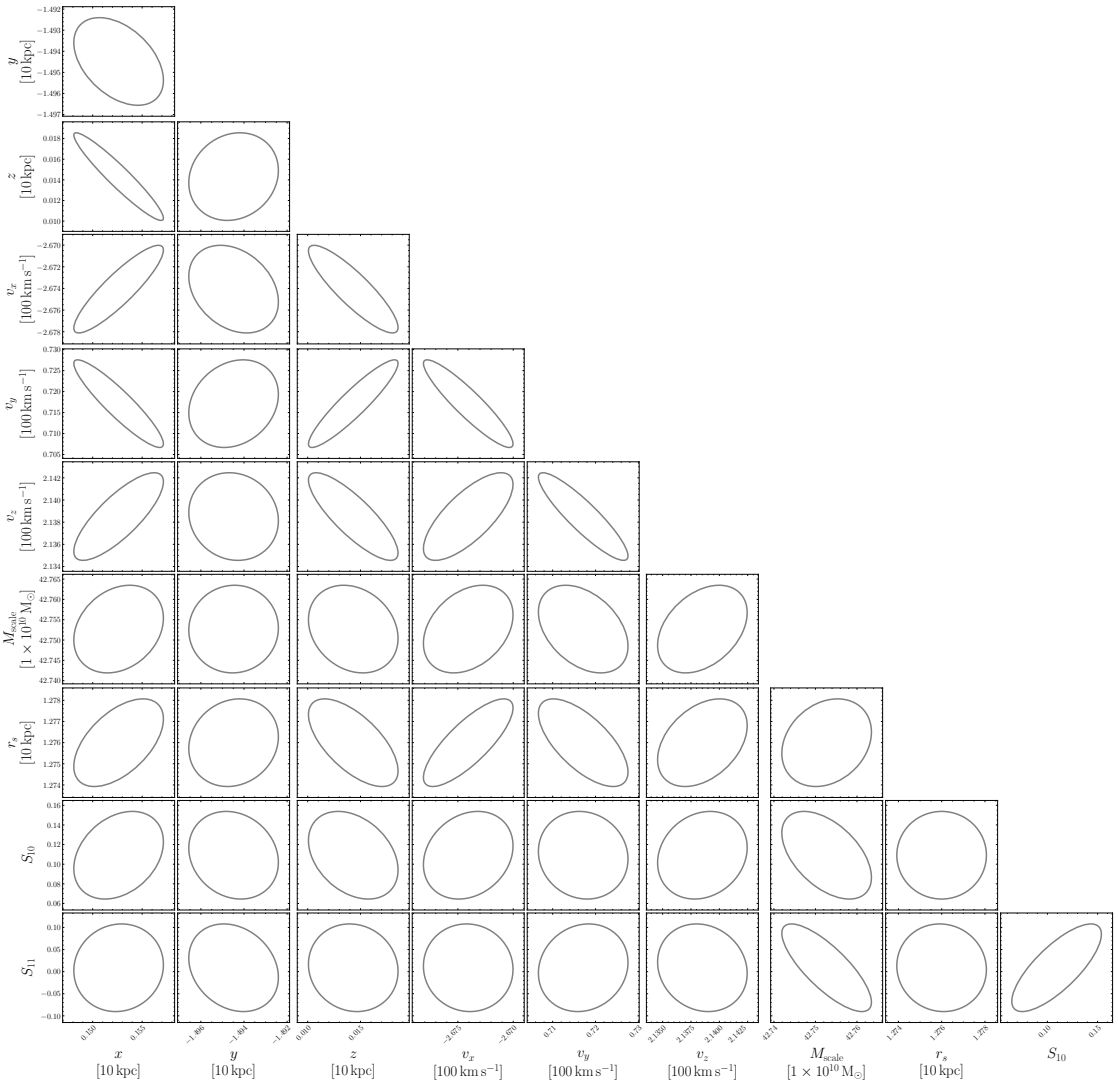

Figure 4.4: Visualisation of the Cramér–Rao Lower Bound ellipses for the parameters of the different components of the toy model inferred for an OC–like stream. The ellipses are centred on the true parameter values. The first six columns show the position and velocity of the stream progenitor in Galactocentric coordinates. The spherical NFW halo is described by its scale mass $M_{\rm scale}$ and radius r_s. The static perturbation is a dipole with two modes, S_{10} in the z–direction and S_{11} in the x–direction. Circular ellipses represent little correlation between the model parameters, while elliptical ellipses show a strong correlation between the model parameters.

this uncertainty, i.e. calculating halo uncertainties for a stream evolved in an unperturbed potential and adding a stellar disc and bulge to the toy model. Nevertheless, the uncertainties stayed very low. An explanation could be the number of particles we calculate the information for. With selecting a particle in each 0.5° bin, longer streams will have more evaluations of the derivatives following Equation 4.5, increasing the total information. As this study aims for a qualitative understanding of how well streams can constrain the perturbation vs the halo parameters and which stream properties are constraining, these CRLBs should not be interpreted quantitatively. While we show all model parameters in this figure, we will focus on the halo and perturbation parameters in the remainder of the paper.

4.3.2 *Time-dependent perturbation*

Next, we evolve the same stream in a potential with a time-dependent perturbation and compare its CRLB matrix to the one from the static case. Figure 4.5 shows the best-case uncertainty of the halo parameters and the zeroth polynomial dipole coefficients for both m modes, α_{100} and α_{110}. The stream evolved in the halo with a static perturbation constrains the halo parameters better, while the stream evolved in the time-dependent potential constrains the perturbation parameters significantly better. The latter is likely due to the stream experiencing different shapes and strengths of the deformations that affect parts of it differently, while in the static case, the stream always experiences the same potential at a given position. For both cases, the relative constraints on halo parameters are around a magnitude better for the halo parameters than for the perturbation parameters.

As the Milky Way is deforming due to the LMC, its perturbation is time-dependent. In simulations of the Milky Way–LMC system (Lilleengen et al., 2023), the dipole grows significantly over the last few hundred Myr (see Figure B.1). In the next section, we investigate different aspects of the information in streams on the time-dependent perturbation. We focus on the $m = 0$ dipole mode, in particular on its first two polynomial coefficients. The first polynomial coefficient, α_{100}, quantifies the power of the dipole at $t = 0\,\mathrm{Gyr}$. The second polynomial coefficient, α_{101}, affects the linear time dependence of the dipole. To recover the dipole from the Milky Way–LMC simulation from Lilleengen et al. (2023) by eye, ten polynomial coefficients are necessary. With ongoing

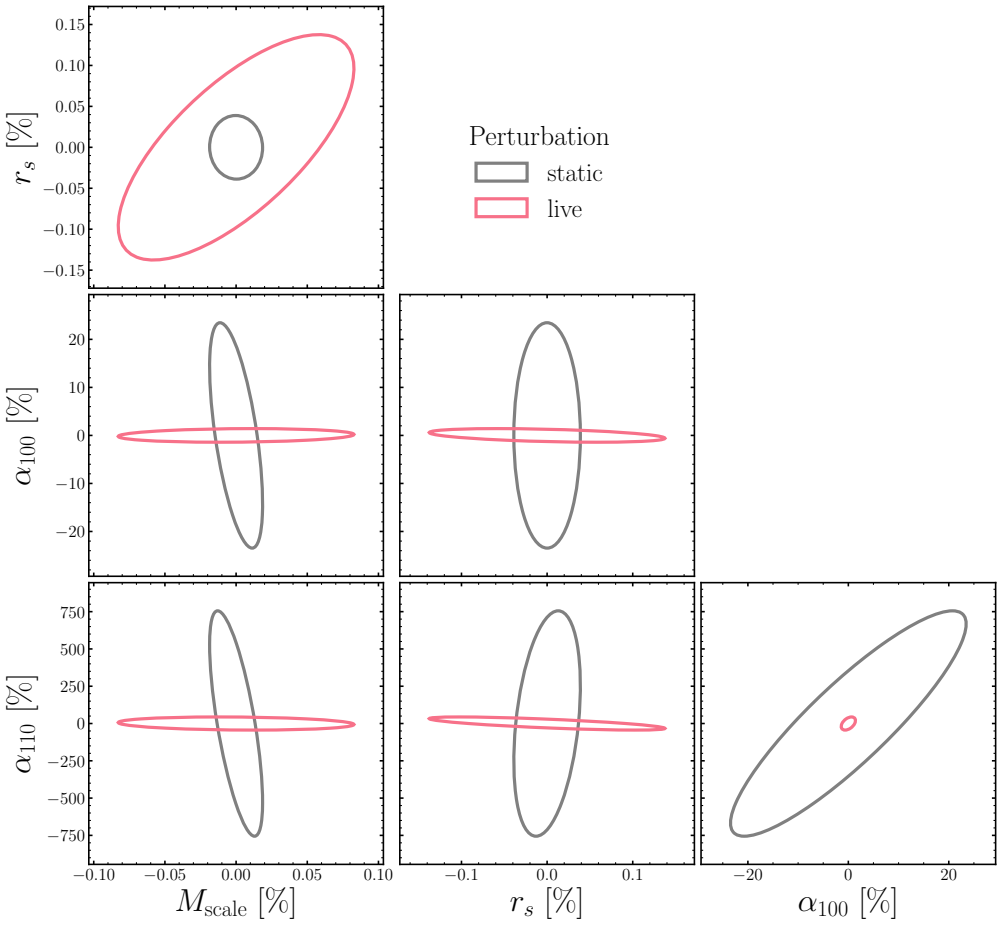

Figure 4.5: CRLBs of halo and perturbation parameters for an OC-like stream evolved in a potential with a static *(grey)* and live *(red)* perturbation. For this stream, evolving it in a potential with a static perturbation decreases the uncertainty on the halo parameters. The stream evolved in a time-dependent potential constrains the perturbation parameters much better.

work focused on finding dynamical features in such simulations (Weinberg & Petersen, 2021; Johnson et al., 2023), we forgo to improve our description for this qualitative toy model.

4.4 INFORMATION CONTENT IN VARIOUS ASPECTS OF STELLAR STREAMS

The information content framework and the visualisations of the CRLBs with ellipses show that streams have information on the perturbations of the halo potential, even if it is less than the information on halo parameters. In this section, we investigate different aspects of the information in streams. We show which observables hold the information, how the information will improve with future data, and how the information looks in different streams and along their stream tracks.

4.4.1 *Information in different observables*

First, we investigate which stream observables contain the bulk of the information. Again, we evolve the OC mock stream in the time-dependent potential. When calculating the Fisher information, the inverse data uncertainties of the excluded observables are set to zero, removing the contribution of that observable to the CRLB. Figure 4.6 shows the CRLB ellipses for these data dimensions. The OC-like stream has almost all of its information in the stream track. This is supported by Lilleengen et al. (2023), who found that the deformations of the Milky Way and LMC halo mainly affect the stream track, and other observables are not significantly affected.

This result depends on our estimates for the data uncertainties where we assume the uncertainty $\phi_2 = 0.1°$. Increasing that uncertainty decreases the strong constraint from the track. Furthermore, we generally assume these uncertainties for all `galstreams` mock streams. With their different morphologies, these uncertainties can be under or overestimated compared to the observed data quality for some streams. When using this method to select target streams, those streams should be modelled more realistically and assigned observationally informed uncertainties. This can lead to a relative decrease in the information in the stream track and to a relative increase in the information in other observables.

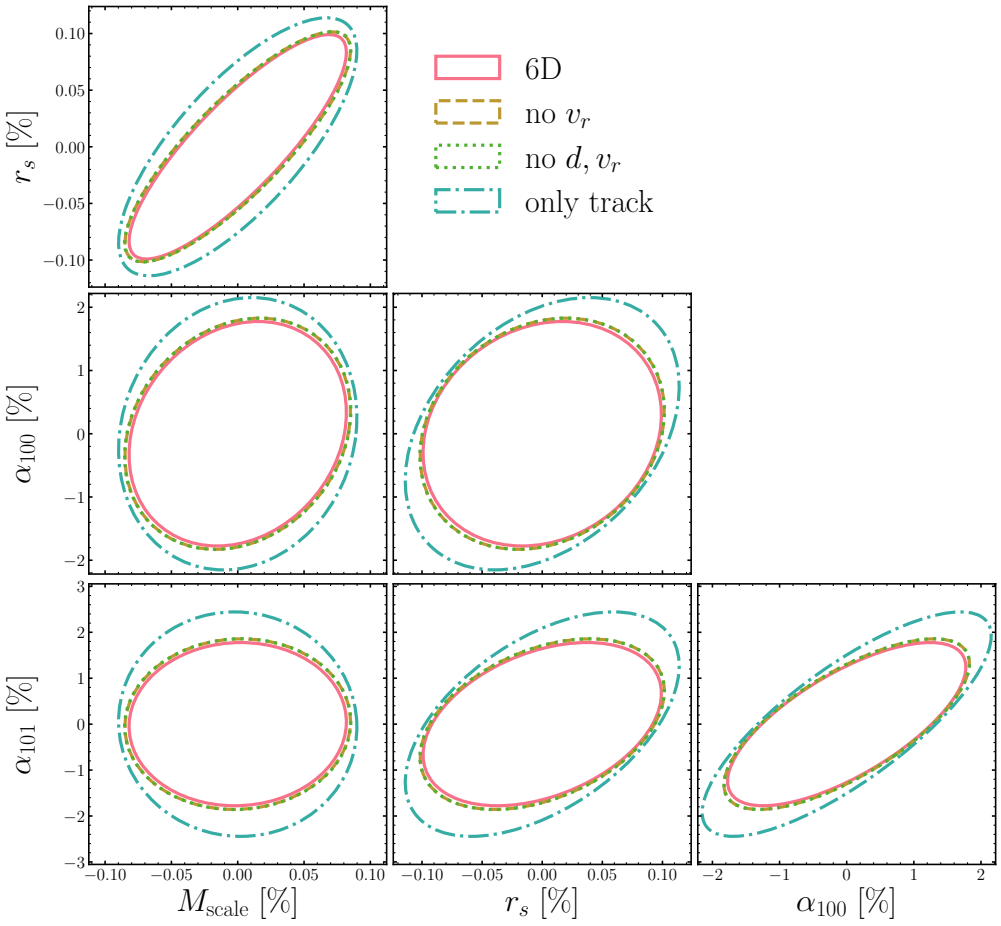

Figure 4.6: CRLBs of the model parameters for the OC mock stream in the time-dependent potential with different observable dimensions. The dimensions are full 6d observables *(red)*, 5d without radial velocities *(gold)*, 4d additionally without distance *(green)* and 2d only including the stream track *(blue)*. For this stream, for all shown model parameters, all of the information lies in the stream track.

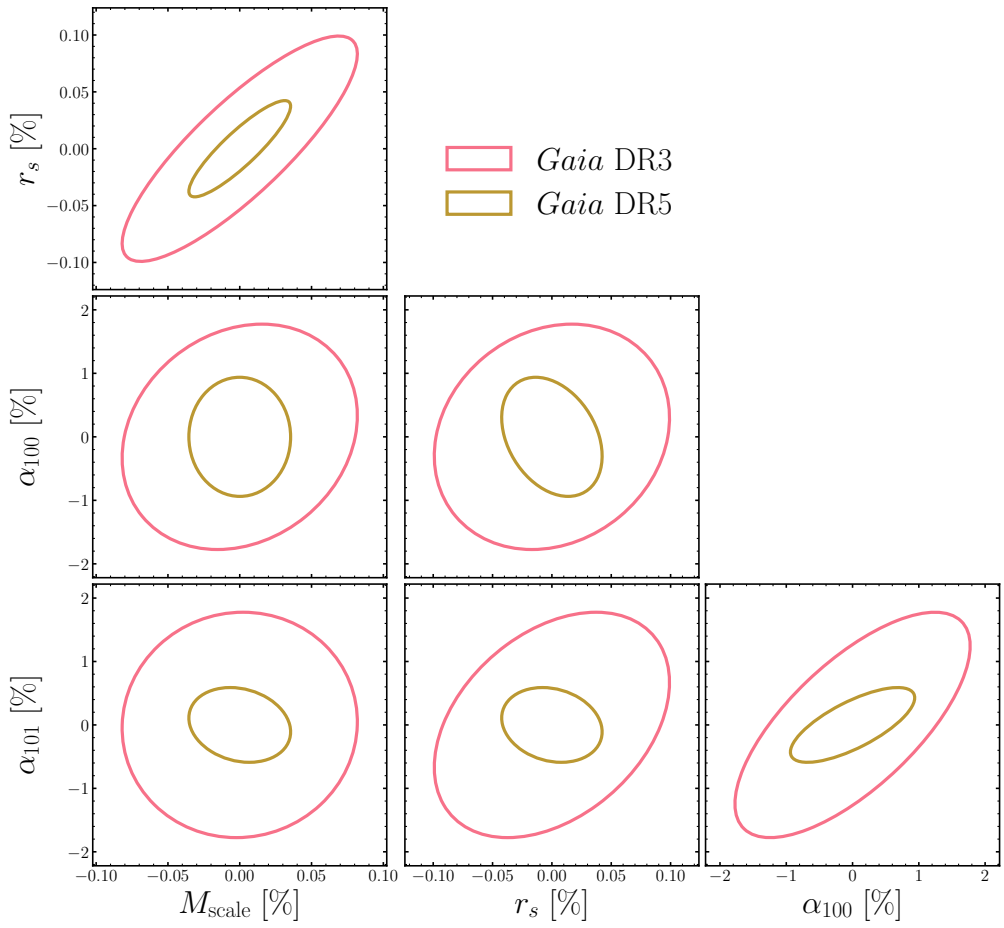

Figure 4.7: CRLB ellipses for halo and perturbation parameters constrained from an OC-like stream with estimated current *Gaia* DR3 *(red)* and future DR5 *(gold)* uncertainties. We assume the decrease of the proper motion uncertainties with a factor of 6.75 and a decreasing factor of 5 for the radial velocity uncertainties, both estimated with `pygaia`. We do not assume any improvements on the track or distances with *Gaia* DR5. Even though the velocities improve considerably, the CRLBs for all parameters only decrease with a factor of 2-3.

4.4.2 *Information with future data*

With most of the information contained in the stream track, we next show how the information in streams will improve with future data, particularly with *Gaia* DR5. For this, we use `pygaia`[4] to estimate the improvement of proper motion and radial velocity uncertainties. A red giant with a g magnitude of 15 mag will have 6.75 times better proper motion measurements and roughly 5 times better radial velocity measurements. We do not expect significant improvements for the stream track and the distance. Figure 4.7 shows the CRLBs for the current and future uncertainty estimates

4 https://pygaia.readthedocs.io/en/latest/

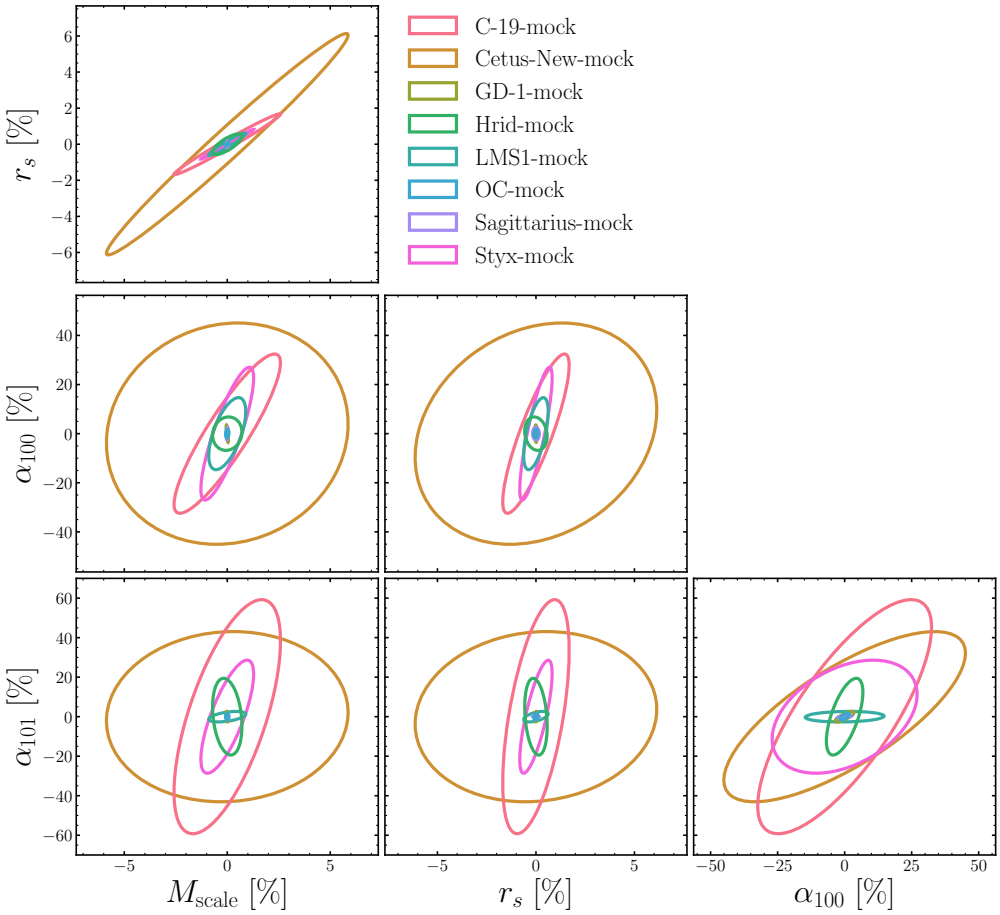

Figure 4.8: Best-case uncertainties of halo and perturbation parameters from several streams evolved in a time-dependent perturbed potential. Streams like OC, GD-1, and Sagittarius are the most constraining streams for all shown parameters. Generally, the goodness of constraints for a given stream compared to the other streams stays the same for all model parameters. The streams show similar correlations for the parameters, and the halo parameters have lower relative CRLBs than the perturbation parameters.

for an OC-like mock stream. Even though the velocities will have more than 5 times improved measurements, the information will only improve by a factor of 2-3. This shows that there will still be much information in the stream track, but velocities will add information.

4.4.3 *Information in different streams*

So far, we have focused on only the mock OC stream. The OC stream is affected by the presence of the LMC (Erkal et al., 2019; Koposov et al., 2023) and by the deformations of the LMC and the Milky Way halo, particularly the Milky Way dipole (Chapter 3). Since we mimic the dipole effect of Chapter 3, we chose the OC stream as we expected it to

be one of the most informative streams. Now we extend our analysis to include other streams that were selected because they have different levels of information. These streams are mock streams of C-19 (Ibata et al., 2021), Cetus-New (Yanny et al., 2009; Newberg et al., 2009; Yuan et al., 2022), GD-1 (Grillmair, 2006; Ibata et al., 2021), Hrid (Ibata et al., 2021), LMS-1 (Yuan et al., 2020), Sagittarius (Ibata et al., 1994; Antoja et al., 2020) and Styx (Grillmair, 2009). The generation of mock streams described in Section 4.2.3 does not guarantee that the mock streams have the same morphologies as the observed streams.

Figure 4.8 shows the CRLB ellipses for the halo and perturbation parameters constrained from the set of streams. We find that streams that constrain halo parameters well also constrain the perturbation parameters well. Different streams also have similar correlations between different model parameters. For all streams, the relative halo parameters are better constrained than the relative perturbation parameters.

4.4.4 *Information along stream tracks*

So far, the information in the streams was quoted for the entire stream. Now we present the information along the stream tracks. This will inform where in the stream we want to have the best data to constrain the perturbations the best. Figure 4.9 shows the stream tracks of the previously shown streams that are colour-coded by the Fisher information. The Fisher information is calculated as stated in Equation 4.1. The CRLB matrix is then calculated by summing over the bins along the stream and inverting the Fisher information matrix. The streams containing the most information are the OC, GD-1 and Sagittarius streams. Bins furthest away from the progenitor (located at $\phi_1 = 0\,\mathrm{deg}$) are the most informative. Stars in these bins left the progenitor the earliest, therefore, orbited in the host perturbed potential the longest, having more time to collect information than stars that only recently left the progenitor (that are closer to $\phi_1 = 0\,\mathrm{deg}$). This trend is seen in all streams, even the less informative ones. Observing stream stars as far as possible from the progenitor, particularly in long streams, will improve constraints on the model parameters.

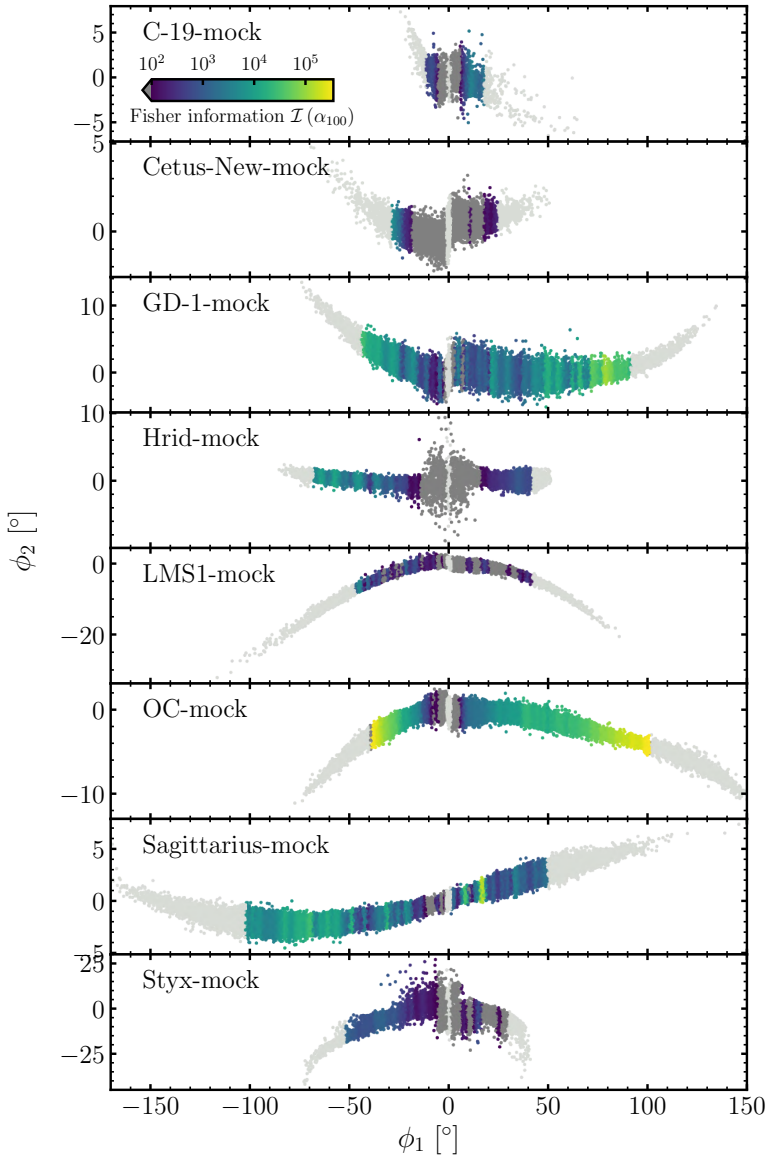

Figure 4.9: Stream tracks of different streams, colour-coded by the Fisher information for α_{100} inferred along the stream in bins of 0.5 deg. The Fisher information is described in Equation 4.1 and is calculated for each bin as a first step before summing over the bins and inverting the matrix to calculate the CRLBs. The light grey parts of the streams are the last 5th percentile of stream particles and the bins directly around the progenitor position at $\mathrm{abs}(\phi_1) \leqslant 1°$ that are excluded when calculating the information. Particles with information smaller than the colour range are coloured in dark grey. The shorter and thinner streams contain little information in each bin. The GD-1, OC, and Sagittarius streams contain the most information. The most informative bins containing are the furthest away from the progenitor. The stars in these bins have left the progenitor the earliest and orbited the perturbed potential the longest. Stars close to $\phi_1 = 0$ deg left the progenitor only recently and did not have much time to experience the host potential.

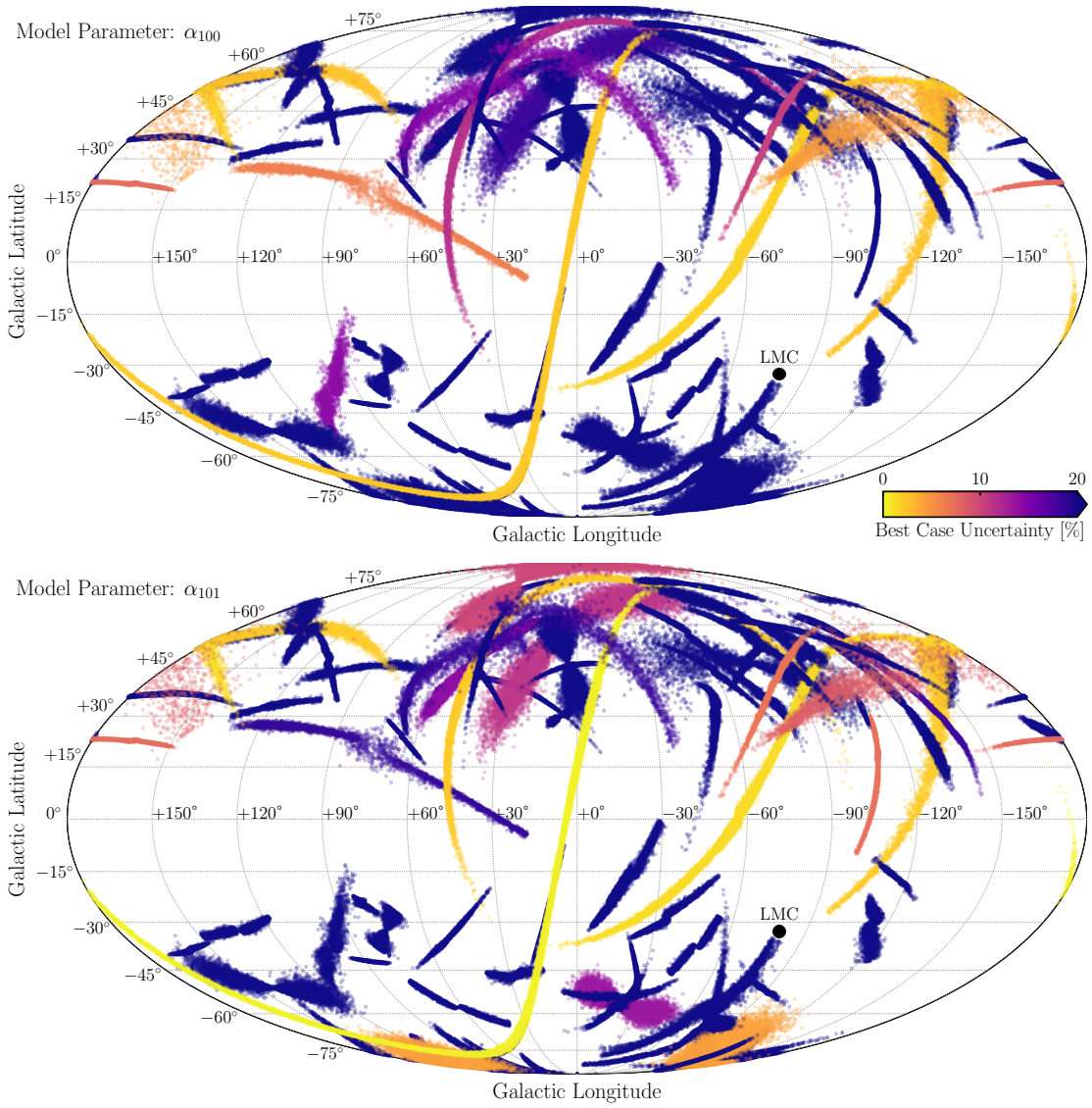

Figure 4.10: All-sky figure of the `galstreams`-based mock streams colour-coded by relative information about the polynomial coefficients described by Equation 4.3, α_{100} *(top)* and α_{101} *(bottom)*. Some streams shown in Figure 4.1 are missing since the information contains nan values due to peculiar stream morphologies. The longest streams are the most informative for both parameters. A few shorter streams are only informative for one of the parameters.

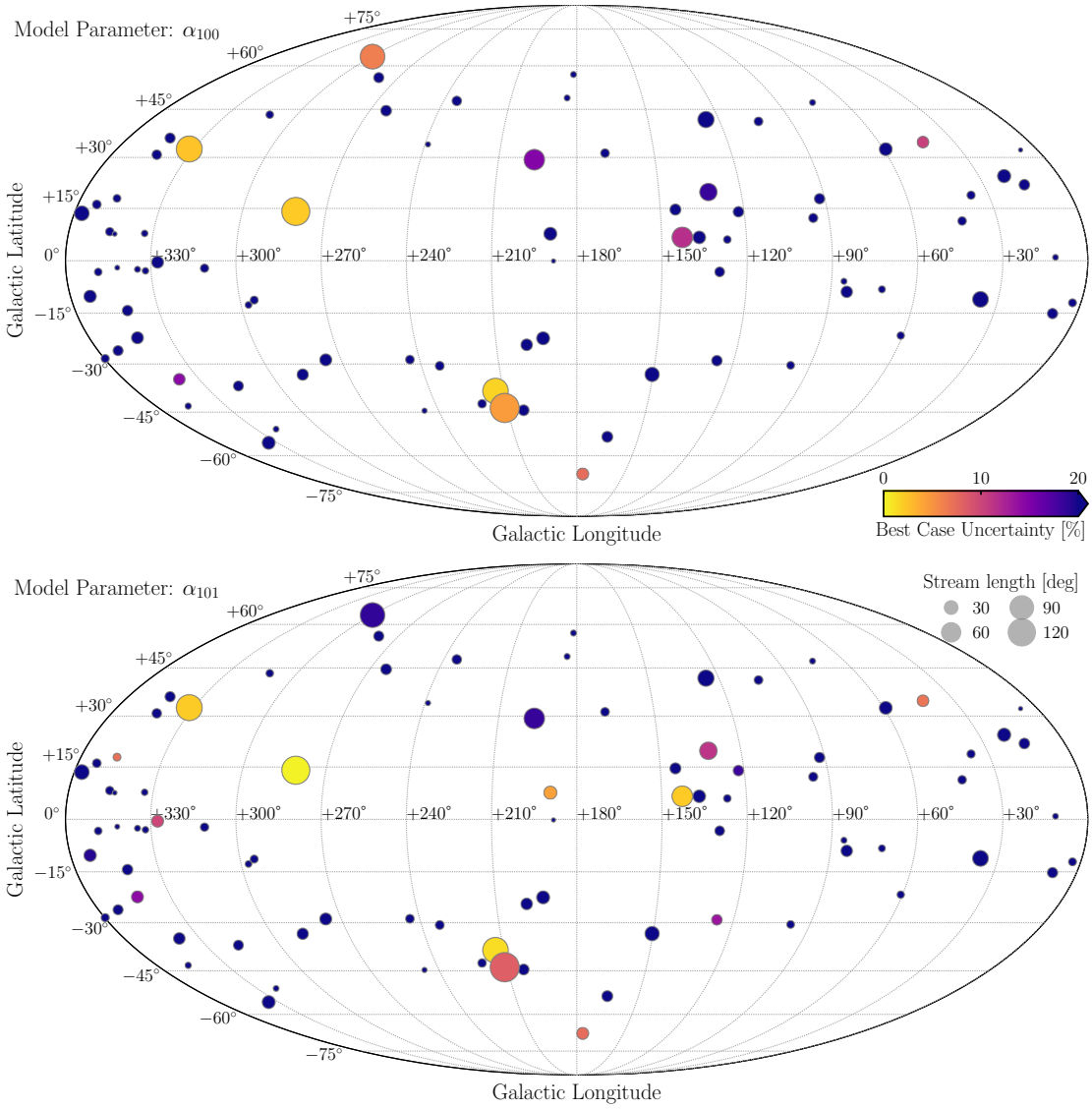

Figure 4.11: All-sky figure of the orbital poles of the mock streams colour-coded by relative information about the polynomial coefficients described by Equation 4.3, α_{100} *(top)* and α_{101} *(bottom)*. The sizes of the markers are proportional to the streams' lengths. The most informative streams are the longest streams. There is no obvious relation between the orbital poles and the information the streams contain.

4.4.5 *Information in all mock streams*

With almost 100 streams available in the Milky Way (Mateu, 2023), we now investigate them all individually to find relations between stream properties and the information on the perturbation coefficients. First, we calculate the information on the perturbation polynomial coefficients α_{100} and α_{101}, shown in Figure 4.10. Long streams generally have significantly more information on both parameters, with some shorter and wider streams also constraining the parameters with 10-20 per cent uncertainty. Some streams are only constraining for one of the parameters. The coefficient α_{101} has better absolute uncertainties than α_{100}. The parameter α_{100} only becomes relevant very recently (see Figure B.1) while α_{101} determines the linear time dependence of the polynomial coefficient, therefore relevant over the entire evolution of the streams. Therefore, streams with longer integration times have increased information about α_{101}.

Next, in Figure 4.11, we show the orbital poles of the streams to see whether there is a correlation with the information. The size of the points corresponds to the stream length, as that seems to be a very informative property seen in Figure 4.10. The streams that contain much information are mostly long streams. Interestingly, the orbital poles have no particular direction of information in the streams. In the next section, we explore the correlation between more stream properties and the contained information.

4.5 DISCUSSION

4.5.1 *Correlation between stream properties and information*

One of our goals is to identify correlations between stream properties and the information that streams contain about the perturbation. As seen in the previous section, the stream length is very significant to the stream's information, whereas the orbital poles of the streams are not. In Figure 4.12, we show the information in all streams shown in Figure 4.10 given several stream properties. These are the streams' heliocentric distances, their peri– and apocentres, the streams' lengths and widths, and the stream orbits' eccentricities. The stream distance is quoted from the mid-point distance of the observed stream in `galstreams` that is also used as the distance for the progenitor's initial condition. The stream width is calculated by binning the stream and fitting a line to the particles in each bin. We assign the median of the standard deviations of

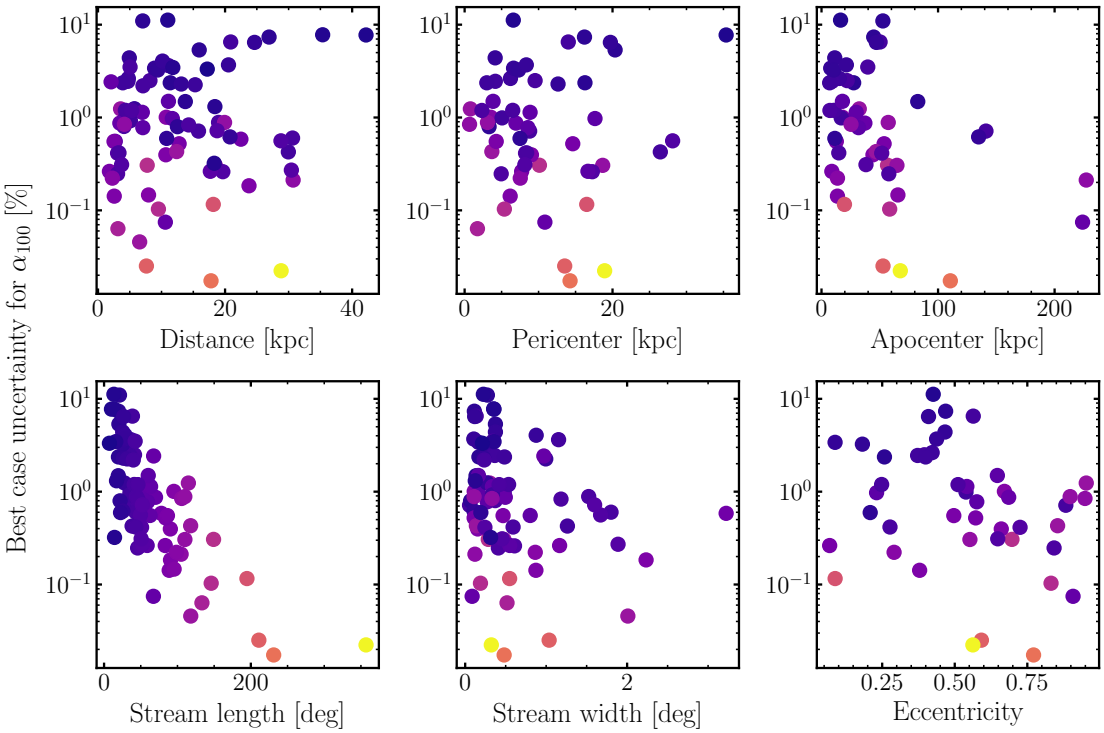

Figure 4.12: Properties and CRLB of α_{100} of all mock streams for which the information was calculated. The stream properties are distance, pericentre, and apocentre in the *top row*, and stream length and width, and the orbit's eccentricity in the *bottom row*. The markers are coloured by the stream length, shown in the bottom left panel. This is the property with the clearest correlation with information. Wider streams (bottom middle) and streams with a large apocentre (top right) are also informative, even if the streams are shorter. The streams lose information with increasing heliocentric distance to the progenitor (top left).

all line fits as the stream's width. The stream's orbit properties, peri– and apocentre, and eccentricity, are calculated by integrating the progenitor's orbit in the unperturbed potential in `gala`.

A stream's length and width have the clearest correlation with the CRLB for α_{100}, with longer and wider streams being more informative. Longer and wider streams are dwarf galaxy streams, while thinner streams are globular cluster streams. Furthermore, there is a correlation between the apocentre and the CRLB. The perturbation added to the NFW potential increases mainly in the z-direction with distance. Streams with large apocentres experience a stronger perturbation, thus holding more information on the perturbation's coefficients. The stream distances reveal a trend that streams get less informative with larger distances. At larger distances, the proper motion errors we include in Equation 4.1 to calculate the CRLBs translate to larger total velocity errors that decrease the information in the stream.

4.5.2 *Combining streams to improve constraints on parameters*

Bonaca & Hogg (2018) find that combining streams improves the constraints on halo parameters. Each stream is treated as an independent experiment, and the likelihood for any combination of these events is the product of the individual likelihoods. This means that the combined Fisher information matrix is the sum of the individual streams Fisher matrices (given by Equation 4.1),

$$C_x^{-1} = \sum_i \left(\left(\frac{d\vec{y}}{d\vec{x}} \right)_i^T C_{y,i}^{-1} \left(\frac{d\vec{y}}{d\vec{x}} \right)_i \right) + V_x^{-1} \tag{4.10}$$

where i denotes the individual stream.

We follow their approach and combine the Fisher information of the streams shown in Figures 4.8 and 4.9 for all possible combinations of the streams. Figure 4.13 shows the CRLBs of the halo and perturbation parameters for these combinations. As this is a qualitative rather than a quantitative analysis, we only focus on the relative differences between the parameters and combinations.

The halo parameters have better CRLBs than the perturbation parameters for the same number of combinations. The mock streams we identified as most informative, OC, Sagittarius, and GD-1, have individual constraints that can only be improved by

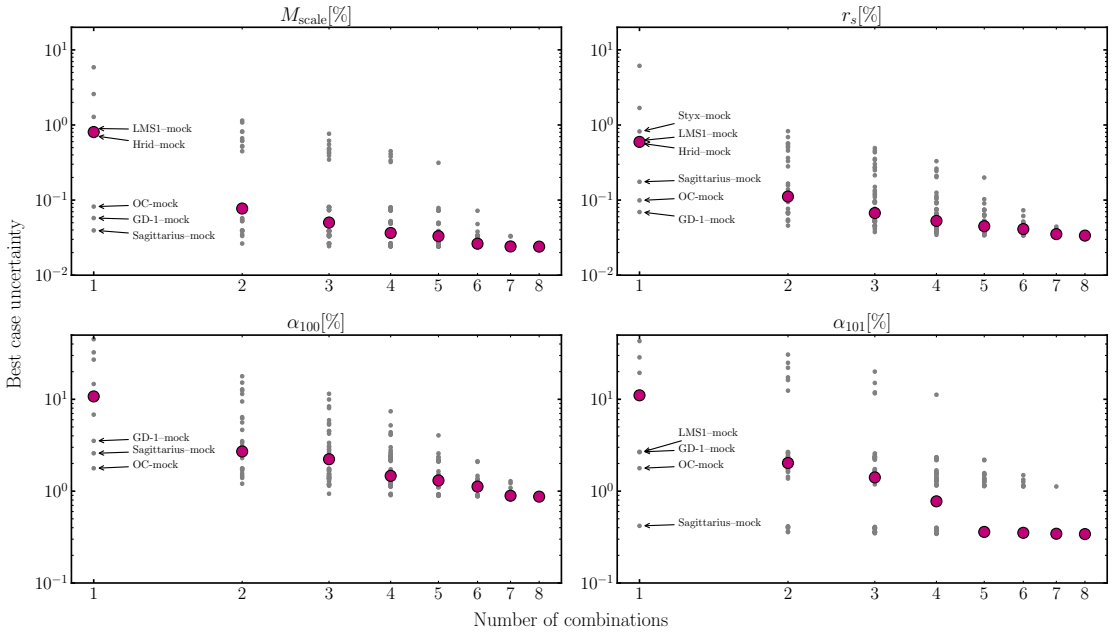

Figure 4.13: CRLBs of halo and perturbation parameters for combinations of streams. The parameters shown are the NFW scale mass *(top left)*, the NFW scale radius *(top right)*, and the perturbation parameters α_{100} *(bottom left)* and α_{101} *(bottom right)*. The number of combined streams is shown on the x-axis. The streams that we combine are the streams mentioned shown in Figures 4.8 and 4.9. The median of the combinations is indicated by the pink marker. As single mock streams, Sagittarius, GD-1, and OC are constraining for all shown parameters. The GD-1-mock is particularly informative, likely due to a larger width in the mock stream than its observed width. For all parameters, the median of combining at least 4 or more streams is better than any single stream constraint.

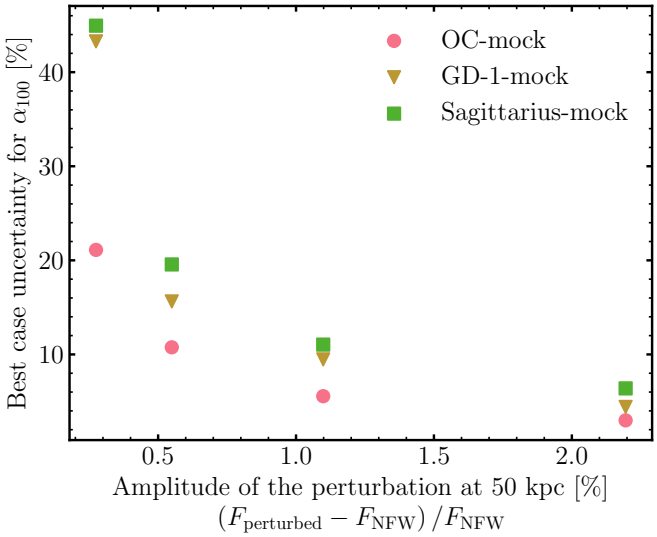

Figure 4.14: Best-case uncertainties for α_{100} for different force ratios of the perturbed potential to the NFW potential for the most constraining mock streams (OC, GD-1 and Sagittarius). This shows that for this toy potential, the force added by the perturbation needs to be at least 0.2 per cent of the force of the underlying potential to be significantly detectable with stellar streams with a parameter uncertainty of 20 per cent.

combining 4 or more streams. This improvement remains very small for most parameters; only α_{100} would improve significantly. This is in contradiction to the results from Bonaca & Hogg (2018), who find significant improvements for all halo parameters. Their CRLBs are generally larger than ours, allowing more room for improvement. Other differences are that they have a more realistic Milky Way model that includes stellar components and that they solely calculate the information for globular cluster streams. This contradiction could be solved by applying this methodology to mock streams that resemble the observed streams better in a more realistic Milky Way potential and splitting streams up between globular cluster and dwarf galaxy streams.

4.5.3 *Lower detection limit on the perturbation*

The perturbation can be scaled up or down by scaling the coefficients. We have scaled the perturbation so that its force amplitude matches the amplitude in the Lilleengen et al. (2023) Milky Way simulation. We scale the perturbations down to estimate a lower detection limit of the perturbation. We evolve the three most informative mock streams, OC, Sagittarius, and GD-1, in these scaled-down perturbed potentials and calculate their CRLBs. Figure 4.14 shows the information these streams contain given the

amplitude of the perturbation at 50 kpc. The rightmost points are calculated given the perturbation applied throughout the paper. The other points are calculated in perturbations with scaled-down coefficients, reduced at each step by a factor of two. In this toy potential and perturbation, the OC mock stream can constrain the perturbation with a 20 per cent CRLB at a perturbation amplitude of 0.25 per cent. At a half per cent amplitude, all three mock streams constrain the perturbation with a 20 per cent or better CRLB. However, given that the CRLBs are very small throughout this paper, these values should not be interpreted quantitatively but rather qualitatively.

4.5.4 *Realistic Milky Way–LMC system*

The analysis presented in this paper is based on a simple toy model. It includes an NFW halo describing the Milky Way's dark matter halo and a perturbation that is based on the Milky Way dipole induced by the LMC. We do not directly include the LMC, or the stellar components of the Milky Way, i.e. its disc, bulge, and its stellar halo.

So far, no stream model exists that can fit streams in a realistic, time-dependent, deforming Milky Way and LMC potential. This needs to be developed over the next years, using tools such as `EXP` (Petersen et al., 2022a) to create more deforming Milky Way–LMC models. The toy model in this chapter is selected to present this method's possibilities and provide a qualitative guide on which types of streams contain information on the perturbation. The streams identified as most informative can then be used to fit a more accurate, time-dependent Milky Way model.

4.6 CONCLUSIONS

The Milky Way halo experiences a perturbation due to the infalling LMC, and its dark matter halo deforms over time (Garavito-Camargo et al., 2019, 2021a; Erkal et al., 2021; Petersen & Peñarrubia, 2021; Conroy et al., 2021). This deformation affects stellar streams (Vasiliev et al., 2021; Lilleengen et al., 2023). Stellar streams have been used widely to constrain the Milky Way's dark matter halo (e.g. Johnston et al., 1999; Law & Majewski, 2010; Erkal et al., 2019; Koposov et al., 2023). The goal of this paper is to characterise how well streams can be used to measure these time-dependent deformations.

Bonaca & Hogg (2018) developed an information theory framework to better understand better the information that streams have about different parameters of stream models, focused on the Milky Way's dark matter halo. We expand their approach to investigate streams' information about the time-dependent perturbation and find the properties of the most informative streams. Our results are the following:

- We develop a flexible framework to calculate the information that stellar streams contain on their progenitor, the Milky Way halo, and a perturbation to the potential. It is implemented based on `gala` (Price-Whelan, 2017) and can be expanded to include more of `gala`'s functionality, such as a more realistic description of the Milky Way.

- We present a static and time-dependent perturbation to the potential described by multipole expansions (Figure 4.3).

- We show all constrained model parameters in a static potential for an example mock stream based on the OC stream (Figure 4.4) and compare the relative information in a static to a live potential. We find that in a potential with a static perturbation halo parameters are better constrained while in a potential with a time-dependent perturbation, the perturbation itself is better constrained (Figure 4.5).

- We create a set of mock streams that resemble the Milky Way streams and calculate the information each stream contains on the Milky Way halo and the time-dependent perturbation (Figures 4.1, 4.10). For a subset of these, we show that combining the streams results in better constraints on the model parameters (Figure 4.13).

- Focusing on information on the perturbation, we find that the longest streams hold the most information. Other informative stream properties are the stream's width and its apocentre. With increasing heliocentric distance to the progenitor, the information decreases. These properties are more informative in dwarf galaxy streams as they are generally longer and wider than globular cluster streams. This implies that streams that are used to constrain the Milky Way halo, i.e. the OC stream (Erkal et al., 2019; Koposov et al., 2023) and Sagittarius (Law & Ma-

jewski, 2010; Vasiliev et al., 2021), are the best streams to constrain the time-dependent perturbations (Figure 4.11). Combining several streams only leads to marginally better results for most parameters compared to the single most constraining stream (Figure 4.13).

- Within streams, the information is larger the further away particles are from the progenitor. Particles further away have left the progenitor earlier and orbited in the host potential for longer, thus having more time to gather information (Figure 4.9).

- In order to improve the information in streams, velocity and distance observables need better uncertainties. Future surveys and data releases, e.g. *Gaia* DR5 will improve the uncertainties by around a factor of 2–3 (Figure 4.7).

- With this method, it is possible to put a lower limit on the strength of the perturbation that the Milky Way streams are sensitive to. In this setup, the amplitude of the perturbation at 50 kpc has to be at least 0.3 per cent to be detectable with the OC-mock at a 20 per cent parameter uncertainty (Figure 4.14).

In this chapter, we evaluate numerical derivatives of a stream observable given the change of one model parameter. A more self-sufficient approach is to calculate the derivatives directly when creating the stream model rather than comparing different stream integrations. This can be done with automatic differentiation (Griewank & Walther, 2008), e.g. by implementing this framework in `JAX` (Bradbury et al., 2018). This is one of the most important steps going forward as CRLBs will be more reliable. It will also enable the development of novel stream-fitting techniques using e.g. Hamiltonian Monte Carlo methods that require a likelihood and its derivative.

There are two overarching goals for stellar streams in the time-dependent Milky Way potential: (i) fitting a Milky Way model that includes the most important aspects of the perturbations and (ii) detecting the dark matter deformations. This chapter offers intuition and insights into how well we can constrain the perturbations compared to other halo parameters and which streams offer the most insight. The next step is to build the tools to fit time-dependent models and repeat the analysis for more realistic models.

5

STELLAR STREAM FITTING METHODS ARE BIASED WHEN IGNORING THE TIME DEPENDENCE OF THE MILKY WAY

Stellar streams are powerful tracers of the Galactic halo potential. A variety of methods have been developed to fit streams; many streams have already been fit to measure the Milky Way's gravitational potential. A notoriously difficult parameter to fit is the flattening of the Milky Way halo, as it is often inconsistent between different methods and different streams. Furthermore, many of these fits imply that the Milky Way's disc is in an unstable dynamical configuration. The Large Magellanic Cloud (LMC) affects streams around the Milky Way due to its mass and closest approach distance with many streams. Furthermore, the dark matter haloes of both the Milky Way and the LMC are being deformed during the LMC's infall which also affects streams. In this paper, we investigate whether these time-dependent deformations can introduce biases in stream fits. To test this, we simulate the formation of a stellar stream in the presence of a deforming Milky Way–LMC system. We then make mock observations of this stream and fit them with state-of-the-art fitting methods. The inferred mass of the Milky Way is one-third lower than the true mass of the simulation, while the LMC's mass is twice as large. We investigate further results and implications and find that we cannot draw robust conclusions about the biases. We discuss possible solutions for how to improve the fits and to get more trustworthy interpretations.

Work shown in this chapter is being prepared for publication by Lilleengen, Erkal, et al. in MNRAS.

5.1 INTRODUCTION

Stellar tracers in the Milky Way halo hold clues about the Milky Way's formation and evolution and the distribution of dark matter in and around our Galaxy. We can measure the properties of the Milky Way's dark matter halo with these dynamical tracers. These measurements allow us to constrain different properties of dark matter.

Stellar streams are a particularly useful dynamical tracer. These streams form as globular clusters and dwarf galaxies disrupt in the Milky Way halo, forming long, filament-like structures. Stellar streams are highly sensitive to the gravitational potential they evolve in (Johnston et al., 1999). There are many different techniques of fitting stellar streams to constrain the potential, i.e. orbit-fitting (e.g. Koposov et al., 2010; Malhan & Ibata, 2019), action-angle tracks (e.g. Bovy, 2014; Sanders, 2014), action clustering (e.g. Sanderson et al., 2015; Reino et al., 2021, 2022), non-parametric models (e.g. Nibauer et al., 2022), and particle spray methods (e.g. Küpper et al., 2012; Bonaca et al., 2014; Gibbons et al., 2014; Fardal et al., 2015). Current state-of-the-art fits of streams that span large parts of the halo, e.g. to the Orphan–Chenab (OC) (Erkal et al., 2019, hereafter: E19; Koposov et al., 2023, hereafter: K23) and the Sagittarius streams (Law & Majewski, 2010; Vasiliev et al., 2021), find very flattened halo shapes, both for oblate and prolate halo models. These systems are often dynamically unstable as the disk will realign with the minor/major axes of these potentials (Debattista et al., 2013). These shapes disagree for fits to different streams (K23). Furthermore, the flattened haloes often point towards the Large Magellanic Cloud (LMC) or its orbital pole (Vasiliev et al., 2021; K23).

The effects of the LMC complicate the picture even further. A summary of the effects on the Milky Way can be found in Vasiliev (2023). While it has second-order effects on the Milky Way, such as the displacement of the disc (Erkal et al., 2021; Petersen & Peñarrubia, 2021) and overdensities in the stellar halo (Garavito-Camargo et al., 2019, 2021a; Conroy et al., 2021), its presence has direct effects on stellar streams. In an unperturbed stream, the proper motions align with the stream track. If the LMC passes close to a stellar stream, it induces a velocity kick in the stream, most clearly seen in a misalignment between the proper motions and the track. Streams such as the Sagittarius stream (Vasiliev et al., 2021), the OC stream (E19; K23), and several shorter

streams (Shipp et al., 2021) need the LMC included in their models to be successful. While in these models, the LMC is falling in and the Milky Way disc has a reflex motion, they assume rigid Milky Way and LMC haloes.

Lilleengen et al. (2023, hereafter: L23) show that not only the presence of the LMC affects the OC stream but that the stream is significantly perturbed by the deformations of the Milky Way and the LMC halo. To date, none of the state-of-the-art fits to stellar streams include these effects due to technological limitations. The effect of the deformations, together with clues from the alignment of the flattened haloes with the LMC, lead us to the question: *Are stream fits biased by not including the time-dependence of the Milky Way halo?* And if so, which specific parameters are biased and which ones are fit accurately?

To generate mock streams that are evolved in a time-dependent potential with an LMC perturbation, we use the N-body simulation of the Milky Way–LMC interaction presented in L23 as the underlying potential. In this simulation, the density and potential of the Milky Way and the LMC are described with basis function expansions (BFEs) using the software toolkit `EXP` (Petersen et al., 2022a). With BFEs, we have a compact and computationally efficient description of the potential and, thus, the acceleration fields in which we can evolve streams in time-dependent potentials.

In this paper, we fit a mock stream evolved in a time-dependent Milky Way and LMC with current state-of-the-art models which assume rigid haloes for the Milky Way and the LMC. We investigate which parameters the fit recovers correctly and which parameters are biased. For this, we follow the fitting procedure from K23 and qualitatively compare the interpretations of our results with theirs. The paper is structured as follows. In Section 5.2, we describe the Milky Way–LMC simulations, the generation of the mock stream data, and the fitting procedure. In Section 5.3, we present the stream fits, the inferred mass profiles for the Milky Way and the LMC and the flattening of the Milky Way halo. Section 5.4 contains the interpretation of the results, the comparison to the fits from K23 and a discussion of the biases we find in fitting this mock stream. Finally, in Section 5.5, we summarise and conclude our findings.

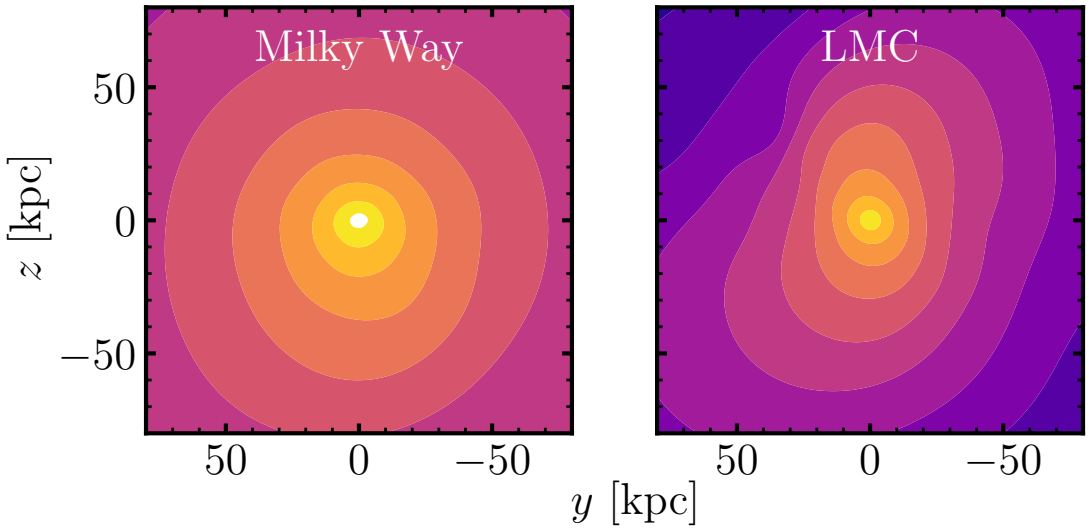

Figure 5.1: Density contours of the deforming Milky Way *(left)* and LMC *(right)* at t = 0 Gyr. In each panel, the zero point corresponds to the centre of each galaxy's halo expansion. While the Milky Way is slightly stretched in the negative z-direction, the LMC is highly stretched and twisted. The simulations are introduced in L23, and the initial halo profiles are based on the best spherical fit to the OC stream from E19.

5.2 METHODS

5.2.1 *Milky Way–LMC simulations*

The paper aims to uncover biases in stellar stream fits introduced by omitting the time dependence of the Milky Way and LMC haloes. To do this, we use a current state-of-the-art yet rigid model to fit a stream that evolved in a deforming Milky Way–LMC system. We simulate this system as an N-body simulation and describe its potential and density fields with basis function expansions using the `EXP` code (Petersen et al., 2022a). The simulation and the expansions are described in detail in L23[1]. We give a short summary here.

The Milky Way–LMC simulations are run for the best-fit reflexive spherical potential from E19 labelled 'sph. rMW+LMC'. For the Milky Way, they contain an Navarro–Frenk–White (NFW; Navarro et al., 1997) dark matter halo with $M_{\text{MW halo}} = 7.92 \times 10^{11}\,M_\odot$, $r_s = 12.8$ kpc, and $c = 15.3$, a Miyamoto Nagai (MN Miyamoto & Nagai, 1975) disc with $M_{\text{MW disc}} = 6.8 \times 10^{10}\,M_\odot$, $a = 3.0$ kpc, and $b = 0.28$ kpc, and a

1 The simulations presented here differ subtly from the simulations in L23. This is due to incorrect unit conversion for the models in that work. The scale radius of the NFW halo in L23 is $r_s = 18.43$ kpc.

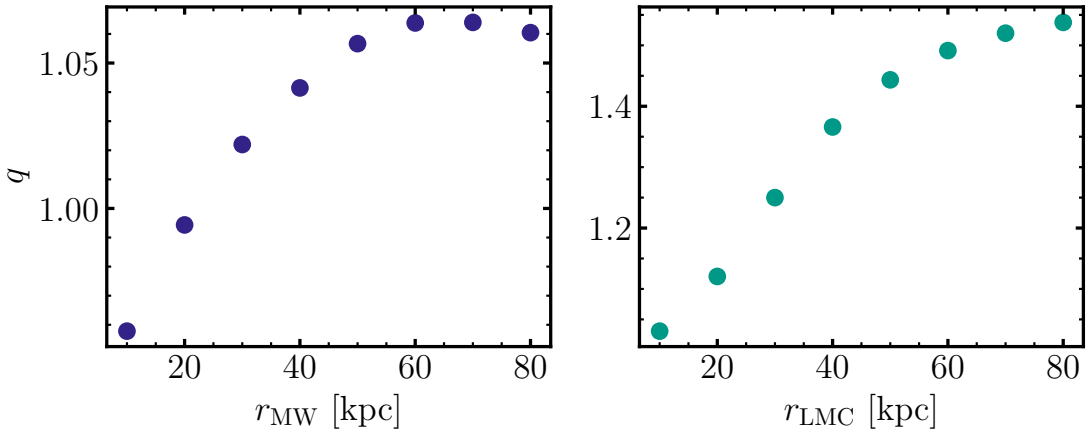

Figure 5.2: Flattenings of the simulated Milky Way *(left)* and LMC *(right)* at different radii of each galaxy at $t = 0$ Gyr. Despite the deformations, the Milky Way is essentially spherical. The LMC is almost spherical at the centre, but its flattening increases towards the outskirts of the LMC to highly prolate ($q > 1.5$). In the densities shown in Figure 5.1, this is seen as a strong elongation along its orbit.

Hernquist (Hernquist, 1990) bulge with $M_{\rm MW\ bulge} = 5 \times 10^9\ M_\odot$, $r_s = 0.5$ kpc. The LMC is modelled as a Hernquist halo with $M_{\rm LMC} = 1.25 \times 10^{11}\ M_\odot$ and $r_s = 14.9$ kpc. The disc and bulge components are based on the `MWPotential2014` implemented in `galpy` (Bovy, 2015). Due to the infinite mass profile of the NFW potential, a truncation is added as described in L23.

The simulations are evolved using `EXP` (Weinberg, 1999; Petersen et al., 2022a). In the `EXP` simulations, the system is expanded into three components: the Milky Way halo, the stellar component of the Milky Way containing the disc and the bulge, and the LMC halo. The potential and densities are represented with a set of basis functions where each potential–density pair solves Poisson's equation. The haloes are represented by a spherical basis where the angular dependence is described by spherical harmonics Y_l^m, and the radial functions are eigenfunctions of the Sturm-Liouville equation (for details, see Weinberg, 1999; Petersen et al., 2022a) The stellar component is represented as a cylindrical basis that is found by an optimisation process explained in Petersen et al. (2022a). The zeroth order of each expansion describes the equilibrium distribution and perturbations are described by higher-order functions. In order to describe an evolving system, the functions, which are fixed to their initial form, are weighted by their associated coefficients. The coefficients are calculated from the particle distribution at each time step and tabulated.

The simulations are set up so that the LMC matches its present-day observables: the centre position $(\alpha_{\rm LMC}, \delta_{\rm LMC}) = (78.76° \pm 0.52, -69.19° \pm 0.25)$ and its proper motions $(\mu_{\alpha^\star,\,\rm LMC}, \mu_{\delta,\,\rm LMC}) = (-1.91 \pm 0.02\ \rm mas/yr, 0.229 \pm 0.047\ \rm mas/yr)$ from Kallivayalil et al. (2013), the distance $d_{\rm LMC} = 49.59 \pm 0.54$ kpc, from Pietrzyński et al. (2019), and the line-of-sight velocity $v_{\rm los,\,LMC} = 262.2 \pm 3.4\,\rm km\,s^{-1}$ from van der Marel et al. (2002).

Figure 5.1 shows the present-day density contours of the Milky Way and the LMC in these simulations. The Milky Way is mostly spherical. Its deformation is governed by the induced dipole that is visible as a stretch of the contours in the negative z-direction. This is where the LMC fell in. The LMC is elongated and twisted. The dominant moment in the LMC is its quadrupole which corresponds to this stretching. The twisting in the inner parts is captured by higher-order moments. More details on the time evolution can be found in L23. The densities for both galaxies match the densities in similar simulations and numerical models (E19; Garavito-Camargo et al., 2019, 2021a; Rozier et al., 2022).

Previous fits to stellar streams in the outer Milky Way halo ($r \gtrsim 30$ kpc) have required a substantially flattened MW halo (e.g. Law & Majewski, 2010; Erkal et al., 2019; Vasiliev et al., 2021; Koposov et al., 2023). The shapes are often aligned with the position or the orbital angular momentum vector of the LMC. With these often unphysical results pointing towards the LMC, the flattening is one of the main parameters where we expect a bias. In order to compare it with the 'true' value, we calculate the flattening of both galaxies with their moment of inertia tensors (Frenk et al., 1988). The tensors are calculated from the density ρ following

$$I_{ij} = \iiint_V \rho\,(x, y, z)\ x_i\, x_j\, dx\, dy\, dz \tag{5.1}$$

using the `scipy.integrate.tplquad` function. This integral is done over a sphere between $r = 10$ kpc and $r = 80$ kpc in steps of $\Delta r = 10$ kpc for both galaxies.

The axis ratios of each galaxy are the eigenvalues of the moment of inertia tensor $a > b > c$, which are the axes of the halo itself. The sphericity q is calculated as the ratio of the short to the long axis c/a, but this value does not contain information about the shape of the system. The triaxiality $T = (a^2 - b^2)/(a^2 - c^2)$ (equation 10 in

Bett et al., 2007) gives a measure of the triaxiality and an estimate of the prolateness ($T = 1$) or oblateness ($T = 0$) of the halo. If the halo is prolate, i.e. $T > 0.5$, we invert q so that $q > 1$. In this notation, an oblate halo has a flattening of $q < 1$ and a spherical halo has $q = 1$. Figure 5.2 shows the flattening of the simulated Milky Way and LMC. The Milky Way remains essentially spherical ($0.96 < q_{MW} < 1.06$) while the LMC gets increasingly prolate with distance up to $q_{LMC} = 1.55$ at 80 kpc. This is seen in the densities where the inner contours are almost spherical, and the outer contours are very elongated. In the fits carried out in this paper, the flattening of the Milky Way NFW halo will be a free parameter. We compare the fit results to the true flattening in Section 5.3.3.

5.2.2 *Mock observations*

Next, we generate a stream that was evolved in the deforming Milky Way–LMC system and turn it into mock observables. The stream is generated using the modified Lagrange Cloud Stripping method (mLCS; Gibbons et al., 2014; E19; L23). Details on how this stream is generated are described in L23. In summary, we rewind the progenitor of the stream in the deforming Milky Way–LMC system for 4 Gyr. Then we integrate the progenitor forwards in time along the rewound orbit, while it constantly releases particles at its Lagrange points. Each particle is integrated forwards evaluating the forces of the Milky Way halo, disc, and the LMC halo. The progenitor uses an adaptive time step at which all particles are evaluated. To reduce the uncertainty that the model could introduce, we create the mock stream with 150 000 particles. This ensures that the data uncertainty (from K23) is at least five times as large as the model uncertainty for every data point.

Due to the earlier-mentioned conversion error in the scale radius of the Milky Way, we need to find new initial conditions that match the OC data. We rerun the grid search around the progenitor's initial conditions for the best fit spherical Milky Way halo with reflex motion from table A1 in E19. The new initial conditions of the mock stream progenitor are $\phi_1 = 6.340°$, $\phi_2 = -0.423°$, $d = 17.763$ kpc, $v_r = 85.232\,\mathrm{km\,s^{-1}}$, $\mu_\alpha^* = -3.757$ mas yr^{-1}, $\mu_\delta = 2.574$ mas yr^{-1}, following the notation of Koposov et al. (2019) and E19. The stream track coordinates (ϕ_1, ϕ_2) are given in a coordinate system aligned with the OC stream with its pole at $(\alpha_{OC}, \delta_{OC}) = (72°, -14°)$, and its origin

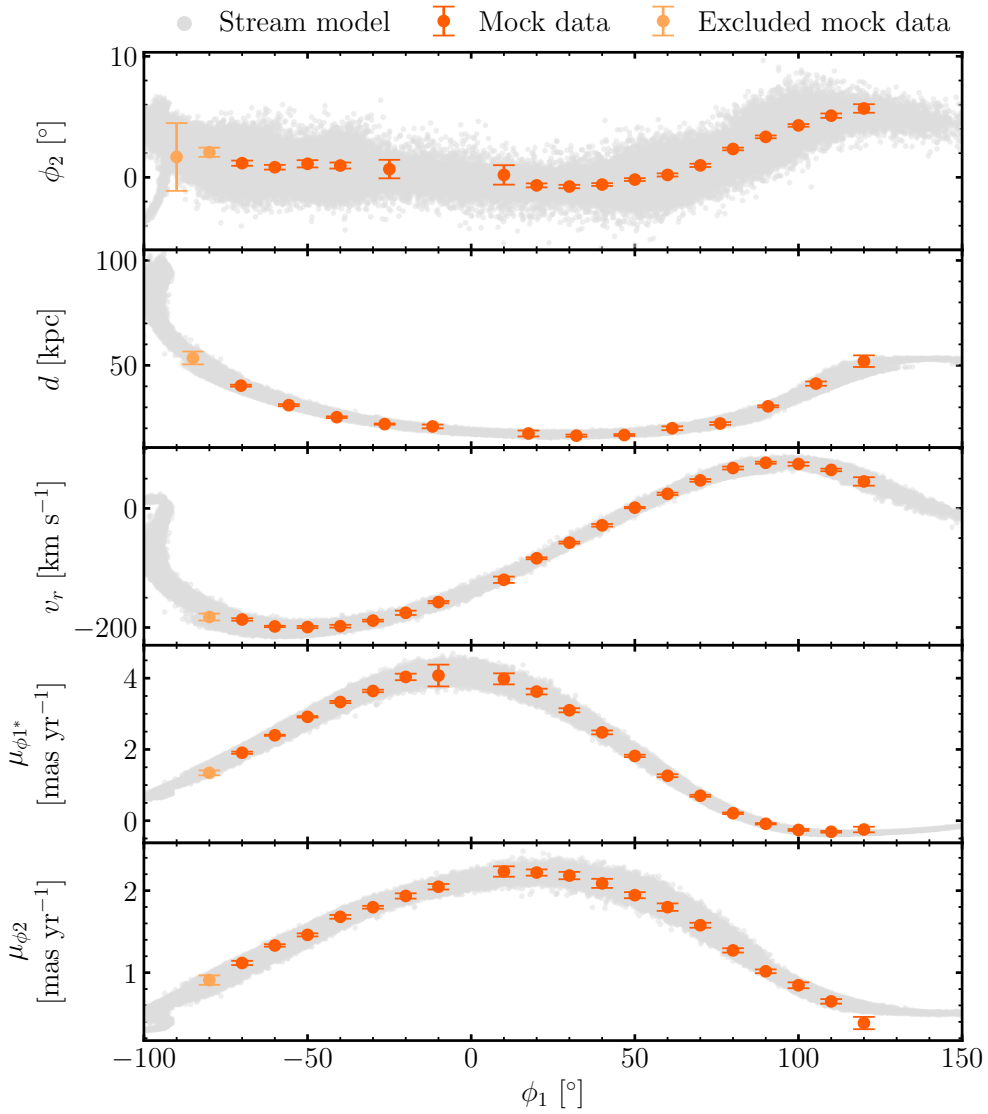

Figure 5.3: Stream model (grey) and constructed mock stream (orange) for the OC-like stream evolved in the deforming Milky Way–LMC simulation. Each row shows a different stream observable; track, distance, radial velocity, and proper motions along and perpendicular to the stream (top to bottom). The stream model consists of 150,000 particles in order to make the model uncertainty negligibly small. In light orange, the excluded mock data are shown following the same steps as K23. Section 5.2.2 explains the method to create mock observations from stream models. This is the stream we fit with current state-of-the-art fitting techniques.

at $(\alpha_0, \delta_0) = (191.10487°, -62.86084°)$. The rotation matrix is given in Appendix B of Koposov et al. (2019).

We create the mock data for this stream based on the OC data presented in K23. We first bin the stream data in all observables in the same bins as K23. Then, we fit a line to the particles each bin contains. The uncertainty in bin i is the square root of the observational uncertainty $\sigma_{i,\,\mathrm{data}}$ and the uncertainty of the mean $\sigma_{i,\,\mathrm{sim}}$,

$$\sigma_{i,\,\mathrm{tot}} = \sqrt{\sigma^2_{i,\,\mathrm{data}} + \sigma^2_{i,\,\mathrm{sim}}}. \tag{5.2}$$

To create the 'observations' for each bin, we draw one value from the normal distribution of the mean of the bin and its total uncertainty. Following the same process as K23, we do not include values at $\phi_1 \leqslant -80°$, K23 find a large spread in the stream track in ϕ_2 there (the 'kink'), which the observational measurements were not sensitive to. Figure 5.3 shows the stream model in grey, the mock data in orange and the excluded mock data in light orange.

5.2.3 *Stream fits*

In order to qualitatively compare our results to fits to real data, the fits are carried out similarly to K23. For the fits, the stream models are generated differently from the mock stream model. They are generated using the mLCS technique, but instead of aiming for a total number of stream stars, we release 12 000 particles per pericentre and evolve the stream with a fixed time step. More importantly, the Milky Way and LMC are now described by analytic expressions. The baryonic components, i.e. the disc and the bulge, follow the same profiles as in the simulations introduced in Section 5.2.1. Due to their high data quality, K23 introduce halo models with more flexibility.

The dark matter halo of the Milky Way is modelled as an axisymmetric, generalised NFW profile

$$\rho(m') = \frac{\rho_0}{\left(\frac{m'}{r_s}\right)^{\gamma_{\mathrm{NFW}}} \left(1 + \frac{m'}{r_s}\right)^{\beta_{\mathrm{NFW}} - \gamma_{\mathrm{NFW}}}} \exp\left(-\left(\frac{m'}{r_{\mathrm{cut}}}\right)^2\right), \tag{5.3}$$

with

$$\rho_0 = \frac{M_{NFW}}{4\pi r_s^3} \frac{1}{\ln(1+c_{NFW}) - \frac{c_{NFW}}{1+c_{NFW}}}. \tag{5.4}$$

Here, M_{NFW} is the halo mass, r_s the scale radius, and $c_{NFW} = 15$ the concentration that is fixed to avoid degeneracies between scale radius and halo mass. Other variables and parameters are the flattened radius $m' = \sqrt{x'^2 + y'^2 + z'^2/q^2}$, the flattening of the halo q, the inner (γ_{NFW}) and outer (β_{NFW}) slope of the profile, and the cutoff radius $r_{cut} = 500$ kpc. The primed coordinates $\vec{x}'$ allow the halo to be flattened in any direction $(x_{NFW}, y_{NFW}, z_{NFW})$. They are rotated from cartesian coordinates with the rotation matrix

$$R = \begin{pmatrix} \cos\phi\cos\theta & \cos\phi\sin\theta & -\sin\phi \\ -\sin\theta & \cos\theta & 0 \\ \sin\phi\cos\theta & \sin\phi\sin\theta & \cos\phi \end{pmatrix}, \tag{5.5}$$

where the coordinates of the direction are converted into polar coordinates with

$$\theta = \tan^{-1}\left(\frac{y_{NFW}}{x_{NFW}}\right), \tag{5.6}$$

$$\phi = \cos^{-1}\left(\frac{z_{NFW}}{\sqrt{x_{NFW}^2 + y_{NFW}^2 + z_{NFW}^2}}\right). \tag{5.7}$$

This Milky Way halo potential has 8 free parameters: M_{NFW}, r_s, q, γ_{NFW}, β_{NFW}, x_{NFW}, y_{NFW}, z_{NFW}.

To describe the LMC, K23 use a truncated NFW profile. However, for the fits in this work, we choose to describe the LMC with a generalised, spherical NFW, i.e. as in Equations 5.3, 5.4 but with the flattening set to 1 and a smaller cutoff radius of $r_{cut} = 100$ kpc. In addition, as in some of the fits in K23, we include a multiplier, λ_{DF}, for the dynamical friction experienced by the LMC. This multiplies the fiducial Chandrasekar dynamical friction experienced by the LMC, which was tuned with N-body simulations of the Milky Way-LMC encounter (see equation 3 of Jethwa et al., 2016). We note that this choice for the LMC model also matches that of Erkal et al. (in prep.), who are fitting an expanded data set for the OC stream and thus will serve as

a useful comparison. The potentials are constructed using `GALPOT` (Dehnen & Binney, 1998). We also include the LMC's proper motions, radial velocity and distance as free parameters, totalling nine free parameters for the LMC: M_{LMC}, $r_{s,LMC}$, γ_{LMC}, β_{LMC}, λ_{DF}, $\mu_{\alpha,LMC}$, $\mu_{\delta,LMC}$, $v_{r,LMC}$, d_{LMC}.

The progenitor's free parameters are its observables, adding another 5 free parameters to the model. Finally, we add nuisance parameters, σ, for all observables that cover an inadequate model, underestimated observational uncertainties and ignored correlations in measurements. They are added to the variance of the data σ_{data} and model σ_{sim} in quadrature. With a total of 27 parameters[2], the likelihood is defined as

$$\log \mathcal{L}_i = -\frac{1}{2}\log\left(2\pi\left(\sigma_{i,data}^2 + \sigma_{i,sim}^2 + \sigma^2\right)\right) - \frac{1}{2}\frac{\left(m_{i,data} - m_{i,sim}\right)^2}{\sigma_{i,data}^2 + \sigma_{i,sim}^2 + \sigma^2} \tag{5.8}$$

with the measurement $m_{i,data}$ at the ith knot and the corresponding value in the model $m_{i,sim}$. This likelihood is evaluated for each observable at each knot i and summed up to calculate the total likelihood of a stream realisation.

We explore the likelihood space of the stream models using `emcee` (Foreman-Mackey et al., 2013). Due to `emcee`'s unreliability with multimodal solutions, we split up the fits into three Milky Way halo models: oblate, prolate, and spherical. The spherical solution has 4 fewer model parameters, as the flattening is $q = 1$, and its direction is not relevant. We use approximately N_{param}^2 walkers, where N_{param} is the number of parameters in the model; for these fits, we use 625 walkers for each flattening setup. At the time of thesis submission, the walkers completed at least 6000 steps for the oblate, 5000 steps for the prolate, and 3000 steps for the spherical fits; none of the runs have converged yet. For the analysis presented here, we select the last 1000 steps of each run. In the next section, we present the results of these fits.

5.3 RESULTS

In this section, we present the results of the fits, including the best-fit stream, the inferred mass profiles for the Milky Way and the LMC, and the inferred halo flattenings of the Milky Way.

2 An overview of most parameters and their priors and their allowed ranges is presented in table 1 in K23. Only LMC parameters that changed due to using a generalised instead of a truncated NFW profile and the dynamical friction parameter are not listed.

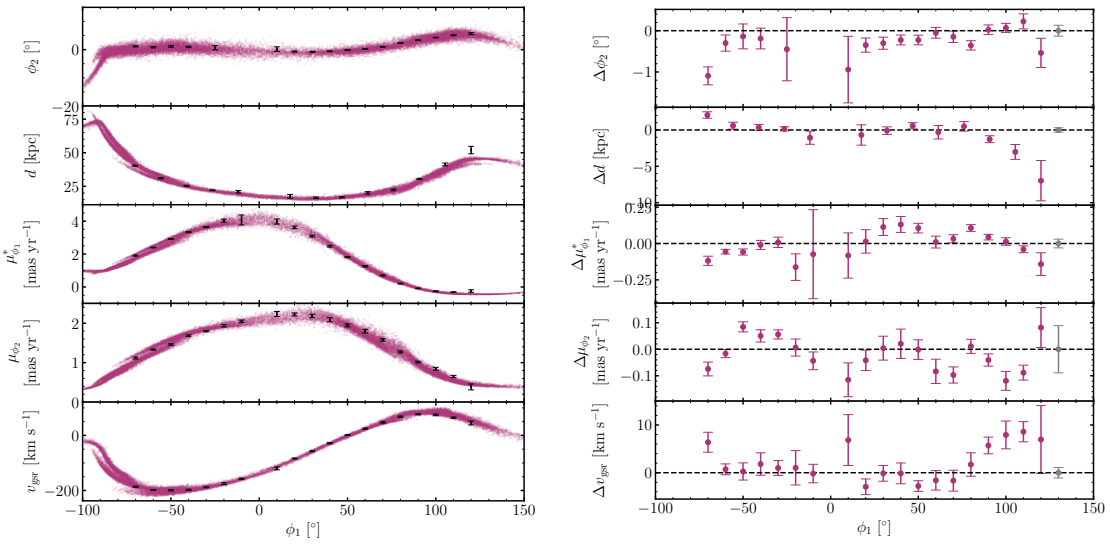

Figure 5.4: Observables *(left)* and residuals *(right)* of the best-fitting stream. In the observables plot, the mock data are shown as black error bars, and the particles of the best-fit stream are in purple. The residuals are shown as purple error bars. The best-fitting stream is evolved in the prolate potential and has the highest likelihood out of all three halo setups; oblate, prolate, and spherical. The grey error bars on the residuals plot represent the nuisance parameters for each observable that are fitted in order to allow the model to add unknown systematic errors.

5.3.1 *Best-fit stream*

The best-fit stream and its residuals are shown in Figure 5.4, and some key parameters are given in Table 5.1. This stream is evolved in the prolate halo. This stream has a marginally larger likelihood than the best solutions in the oblate and spherical haloes. The best-fit streams in the other halo setups not shown here look very similar to the stream observables and residuals in the prolate halo. The kink that is present in the other OC models (e.g. in K23) is also present here; however, the transition into the kink, at around $\phi_1 = -90°$, is smoother. The residuals are relatively large in all observables, particularly at $\phi_1 > 90°$.

5.3.2 *Mass profiles of the Milky Way and the LMC*

First, we want to investigate whether these fits give us reliable mass estimates. The quoted NFW masses for both galaxies in Table 5.1 are not easily interpretable since we use a more complicated generalised NFW potential. Mass profiles give us a more

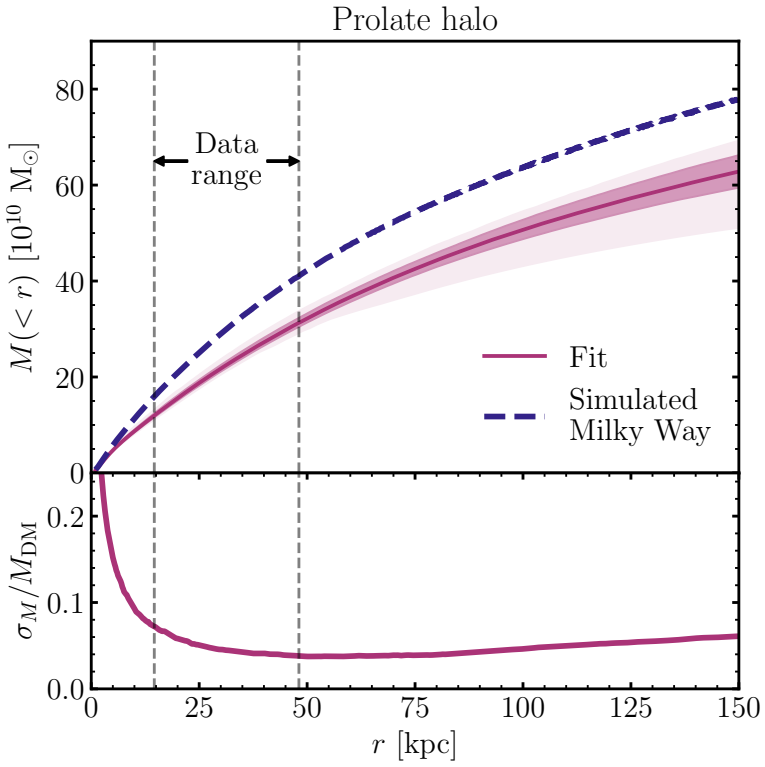

Figure 5.5: *Top panel:* Constraints on the mass profile of the simulated Milky Way from fitting a prolate halo. The lines are the enclosed mass profile of the entire mass with that radius, including all Galactic components. The purple line with the purple shaded regions indicates the median and the 1 sigma and 2 sigma uncertainties of the fits. The true mass profile is extracted from the rotation curves of the Milky Way simulation (indigo dashed line). In the best-fitting halo shape, the enclosed mass of the Milky Way is significantly underestimated. *Bottom panel:* Fractional uncertainty of the enclosed dark matter mass. The vertical grey dashed lines indicate the range in which we have observable data of the OC stream. In contrast to K23, whose constraints have the smallest uncertainty within the data range, our constraints have a very small uncertainty far into the halo. This flat uncertainty is comparable to the smallest uncertainty in K23.

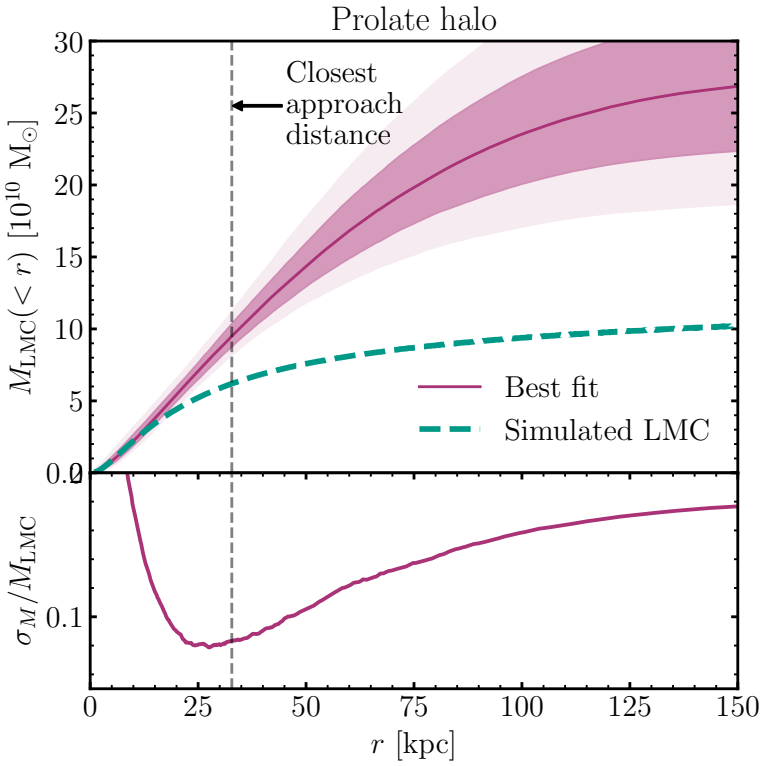

Figure 5.6: Constraints on the mass profile of the simulated LMC from fitting a prolate halo. Similar to Figure 5.5; the enclosed mass profile is shown in the *top panel* and the fractional uncertainty in the *bottom panel*. The true mass profile of the LMC (teal dashed line) is calculated from its rotation curve. The closest approach distance is the median closest approach distance from stream particles around the closest data point included in the fits, at $-75° \leqslant \phi_1 \leqslant -65°$, of the best-fit stream in the prolate Milky Way halo. While the Milky Way mass is underestimated, the LMC mass is overestimated by more than a factor of two outside of the inner 20 kpc of the LMC. There is a minimum in the fractional uncertainties further in than the closest approach distance. The uncertainty gradually rises to almost 20 per cent at 150 kpc.

Table 5.1: Key parameters from the posterior sampling. The first part of the table shows the fitted parameters and the second part shows the inferred enclosed masses of the Milky Way and the LMC at 50 kpc. The values are quoted as the median and one sigma uncertainties from the 15.9 and 84.1 percentiles. The last row shows the offset to the highest likelihood solution.

Parameter	Spherical	Oblate	Prolate
M_{NFW} $[10^{10}\ M_\odot]$	78 ± 15	88^{+22}_{-21}	72^{+16}_{-14}
r_s [kpc]	$13^{+1.9}_{-1.7}$	$13.9^{+3.0}_{-2.1}$	$14.8^{+2.7}_{-2.2}$
q_{NFW}	1	$0.90^{+0.05}_{-0.06}$	$1.18^{+0.11}_{-0.08}$
γ_{NFW}	0.6 ± 0.2	$0.72^{+0.21}_{-0.26}$	$0.79^{+0.19}_{-0.23}$
β_{NFW}	3.0 ± 0.1	$3.05^{+0.14}_{-0.15}$	$3.07^{+0.14}_{-0.16}$
M_{LMC} $[10^{10}\ M_\odot]$	$12.7^{+4.6}_{-3.8}$	11^{+4}_{-3}	10^{+4}_{-3}
M_{MW} (50 kpc) $[10^{10}\ M_\odot]$	$32.8^{+1.0}_{-0.9}$	$32.6^{+1.1}_{-0.9}$	$32.2^{+1.0}_{-0.9}$
M_{LMC} (50 kpc) $[10^{10}\ M_\odot]$	14.2 ± 1.1	13.5 ± 1.6	$14.4^{+1.6}_{-1.4}$
$\Delta \log \mathcal{L}$	-0.65	-0.84	0.0

physical estimate. Since we evolved the stream in a simulation, we can calculate the 'true' mass profiles. This is done via the rotation curve with

$$M_{encl}(r) = \frac{v_{circ}^2 \cdot r}{G} \tag{5.9}$$

at radius r with the gravitational constant G and the circular velocity $v_{circ} = \sqrt{-F_x \cdot x}$ calculated along the x-direction with the according force F_x. With the fitted stream parameters, we can calculate the enclosed mass profiles of the Milky Way and the LMC by integrating over the density of the generalised NFW profile given in Equation 5.3.

Figure 5.5 shows the inferred and true enclosed mass profiles of the Milky Way. There is an offset between both, with the inferred mass profile being significantly lower than the true profile. The fractional uncertainty in the bottom panel was first introduced by Bonaca & Hogg (2018), who showed that at the present-day position of the stream, it should be minimised. This bottom panel is also shown in K23, where the fractional uncertainties are the smallest within the data range. While the constraints are tight, there is no particular improvement of the mass in the data range. The mass profiles of the oblate and the spherical halo follow a similar trend.

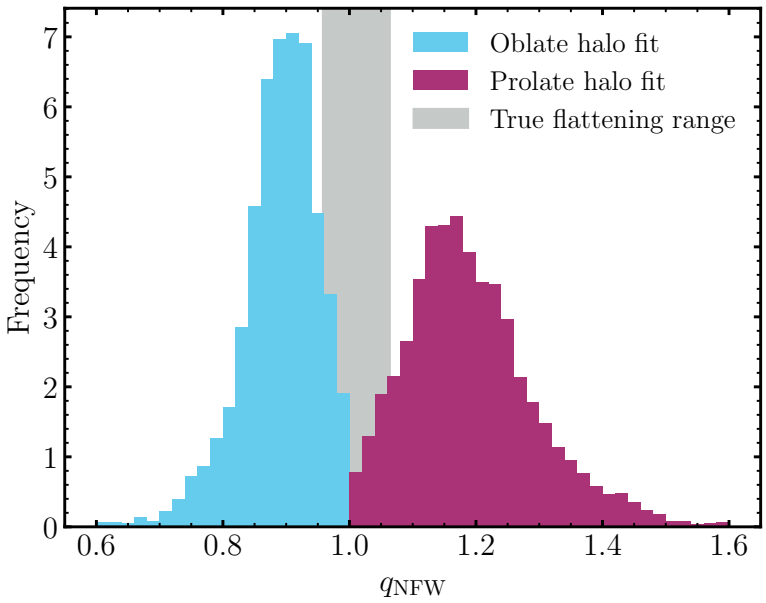

Figure 5.7: Inferred Milky Way halo flattenings from the fits in the prolate ($q > 1$) and oblate ($q < 1$) haloes. The flattening of the oblate halo (blue) has a very narrow distribution around $q = 0.9$. For the prolate halo (purple), the flattening peaks at $q = 1.2$, but it has a wide distribution out to $q = 1.6$. The true range of the flattening of the simulated Milky Way halo is shown as a grey band. The flattening is calculated every 10 kpc between 10 and 80 kpc, as shown in Figure 5.2, so that it covers the distance out to the apocentre of the stream. Only a few realisations of the fits produce almost spherical haloes that agree with the simulation.

Figure 5.6 shows the LMC's mass profile. The enclosed profiles match only in the very inner parts of the LMC. Further than $\sim$ 20 kpc from its centre, the LMC mass is overestimated by more than a factor of two. The fractional uncertainty dips further inwards than the closest approach distance and then increases similarly in shape and amplitude to K23. These mass profiles imply a heavy LMC with a mass ratio to the Milky Way of $\sim 1:3$. If the fits to these mock data are representative to the fits to real data, this implies that in fits to the real data, the mass of the Milky Way is underestimated and the mass of the LMC is overestimated.

5.3.3 *Flattening of the Milky Way halo*

Figure 5.7 shows the flattenings of the Milky Way halo inferred from the oblate and prolate fits. The oblate models find a flattening with a narrow distribution that peaks at $q = 0.90^{+0.05}_{-0.06}$. The prolate halo has a wider and flatter distribution that peaks at $q = 1.18^{+0.11}_{-0.08}$ but extends up to $q = 1.6$. These flattenings are significantly less flattened than in K23, who infer an oblate flattening of $q_{\mathrm{K23,\,obl}} = 0.55$ and a prolate flattening

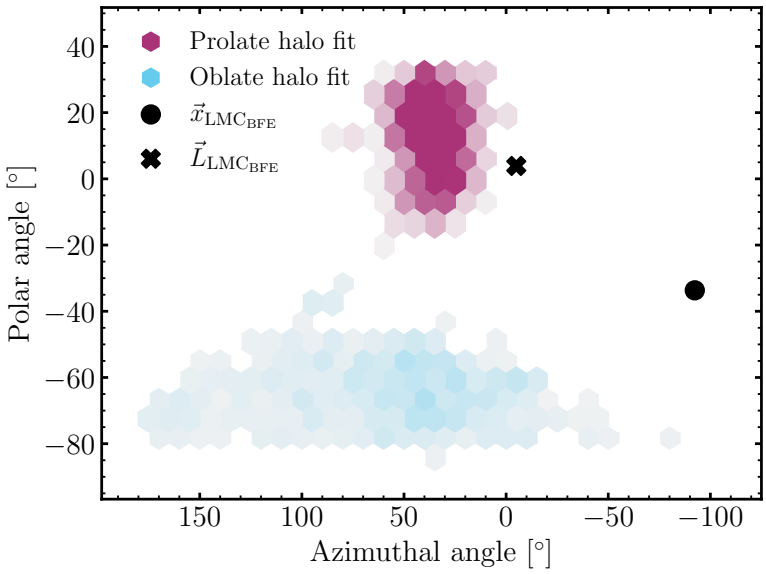

Figure 5.8: Directions of the flattenings of the oblate (blue) and prolate (prolate) haloes. The LMC position is marked with a black circle, and its angular momentum vector with a black cross. The prolate halo has a well-defined orientation, while the oblate halo allows for a wide range of the azimuthal angle. The prolate halo points close to the LMC's angular momentum vector, while the oblate halo does not exhibit any proximity to a phase-space property of the LMC. In previous work (Erkal et al., 2019; Vasiliev et al., 2021; Koposov et al., 2023), the proximity of the halo shapes to LMC properties was interpreted as a missed effect from the LMC.

of $q_{\mathrm{K23,\,prol}} = 1.4$. Given the relatively few steps of the fits and the initialisation of the walkers within $q = 1 \pm 0.1$, we expect these flattenings to move further away from $q = 1$ with longer fitting runs.

In previous works, flattened haloes often point towards the position of the LMC or its orbital angular momentum (e.g. Law & Majewski, 2010; Erkal et al., 2019; Vasiliev et al., 2021; Koposov et al., 2023). We show the orientation of the flattened haloes in Figure 5.8. Even though it has a wide range of flattening, the prolate halo points towards a very narrow region, close to the angular momentum vector of the LMC. The oblate halo has a wider preference for its angle and does not align with any LMC property.

5.4 DISCUSSION

The results we presented are peculiar. By knowing the parameters we fit from the simulations, we can evaluate the biases in our fits. As clearly seen throughout the results section in Figures 5.4, 5.5, 5.6, and 5.7, the fits are not recovering the true parameters

within any significance. First, assuming these results are reliable, we discuss their implications for stream fitting procedures, and for the flattening of the Milky Way halo and the difference between the oblate and prolate haloes. Then, we provide an explanation as to why these fits do not recover the true parameters. We summarise these caveats of why the results might not be reliable and propose further tests that should be carried out to confirm the results. Finally, we discuss the need to develop a time-dependent Milky Way–LMC model.

5.4.1 *Are stream fits biased?*

The results presented in Section 5.3.3 show that the fits do not recover the true parameters of the Milky Way and LMC halo including the flattening of the Milky Way halo and the mass estimates and enclosed mass profiles of the Milky Way and the LMC. This implies that the results of stream fits are biased. While we expected this bias for the Milky Way flattening due to inconsistent results in previous works (e.g. Law & Majewski, 2010, E19, Vasiliev et al., 2021, K23), we did not expect such a significant offset in the inferred masses of both galaxies.

The fits underestimate the Milky Way mass by around 20 per cent and overestimate the LMC mass by more than a factor of two. If these fits are representative of other fits, this would mean that stream fits underestimate the Milky Way mass. A comparison of different methods to estimate the Milky Way mass presented in figure 2 in Wang et al. (2020a) shows that methods using streams often estimate a slightly lower value of the Milky Way mass compared to other methods and tracers. Results from K23, however, generally agree well with some other selected Milky Way mass measurements but are on the lower end of the observations. They also match LMC mass measurements in the inner parts of the LMC, that do not have priors in their fits and are closer to the centre than the closest approach distance of the OC stream. While we match the inner LMC the best and only deviate strongly further out, the K23 Milky Way enclosed mass result agrees better with the data than our fits with the simulation. This reduces the significance of a possible bias in the enclosed mass of the Milky Way.

For the fits in the oblate and the prolate halo, we compared the inferred flattening to the true flattening of the simulation. We expect the flattening values we get from the stream fits to contain both the true flattening and the time dependence of the Milky

Way. The simulation initialises the Milky Way halo spherically (based on the spherical fit from E19). At the current-day position, the halo is still spherical with a small spread of flattenings around $q = 1$. Even though we used a spherical Milky Way in the mock, this does not mean there is no flattening in the Milky Way.

Both the prolate and oblate fits are initialised at $1 < q < 1.1$ and $0.9 < q < 1$, respectively, but quickly explore solutions further away from sphericity. Both solutions have flattenings that are weaker than the solutions in K23. Similarly to K23, we find that the likelihoods for the oblate and prolate solutions are almost equal which validates the weak flattening result. Running the fits for more steps could lead to an exploration of stronger flattenings. However, if we trust the currently recovered flattenings, while they are somewhat offset to the spherical offset, the bias for them is smaller than expected when compared to K23.

In the next sections, we compare our results to K23 to understand whether we see similar trends in both works. We also discuss why we see such differences between simulation and fit parameters and possible improvements to make the interpretation of these results more robust.

5.4.2 *Halo shape model setups*

Streams run in the different halo setups could explain why the fit parameters are so different from the true parameters. Figure 5.9 shows the best-fit stream track in each halo setup. We include the excluded mock data points for guidance in light grey. The stream tracks in all three setups look very similar. They have similar lengths and show similar features at both edges of the streams. A particularly insightful feature might be the 'kink' on the left edge of the stream. Follow-up observations of this feature will put stronger constraints on the stream fit (Erkal et al. in prep.). Within the range of the fitted data, no obvious feature unveils why the recovered parameters significantly deviate from the true parameters.

Following K23, we investigate the acceleration fields in the prolate and oblate halo. The accelerations are rotated into the plane of the OC stream with the rotation matrix from Koposov et al. (2019). In this plane, accelerations that point in the negative (positive) z-direction will also point down (up) in the sky in the OC coordinate system, pulling the stream particles off their track in the corresponding direction. We show the

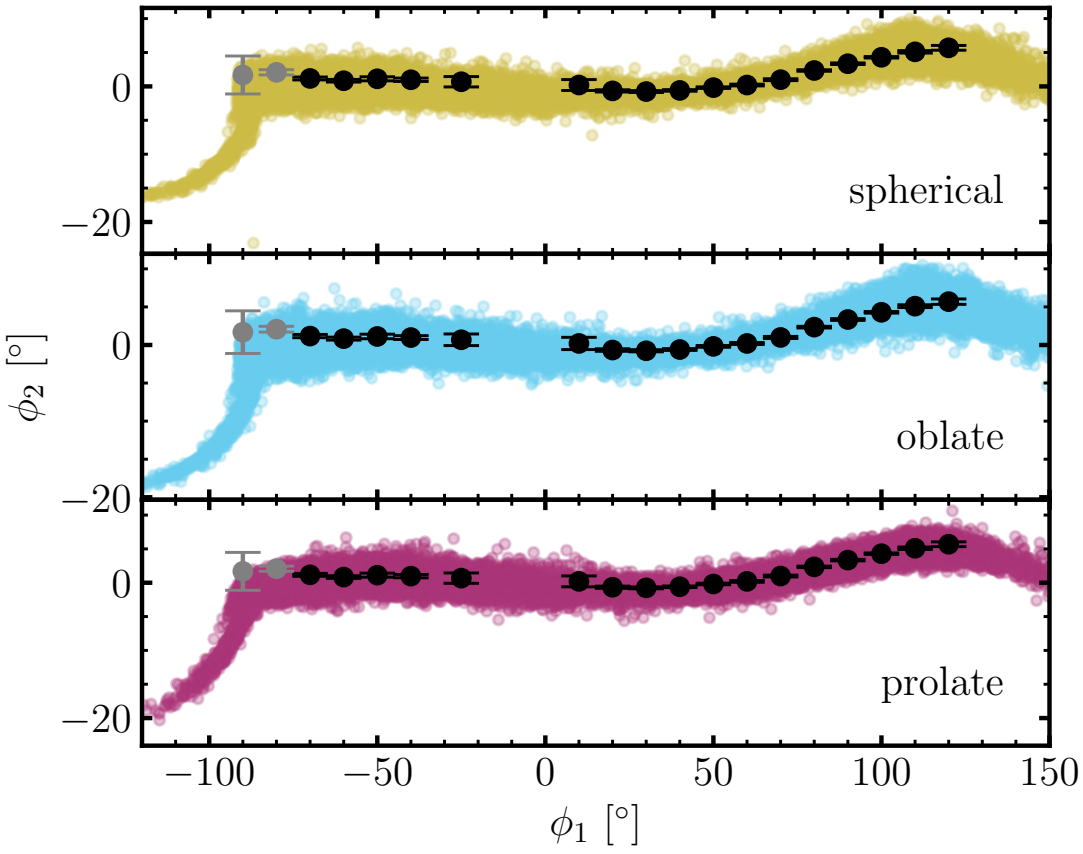

Figure 5.9: The best-fitting stream tracks in each Milky Way halo configuration. The spherical track is shown in the top panel in yellow; the oblate track in the middle panel in blue; and the prolate halo track in the bottom panel in purple. While the prolate halo produces the highest likelihood, the other two solutions have similar tracks. All streams produce the kink-like feature seen in the data and models (E19; L23; K23, Erkal et al. in prep.).

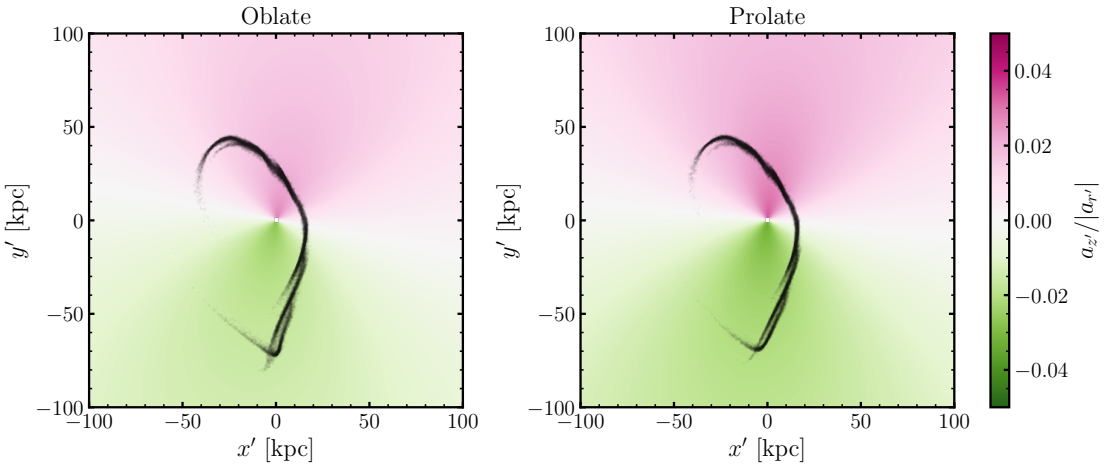

Figure 5.10: Ratio of vertical to radial accelerations in the OC stream plane in the oblate *(left)* and prolate *(right)* haloes. The best-fitting stream in each halo is shown with black points. This plot is similar to figure 21 in K23. The out-of-plane forces look similar for the prolate and oblate setup. However, the amplitudes of these ratios are very low, indicating no acceleration field is generated perpendicular to the stream's plane in either halo, in contrast to K23.

ratio of the out-of-plane acceleration to the radial accelerations in the stream plane in the oblate and prolate fits in Figure 5.10. Both setups have the same orientation of the forces. While K23 find force ratios of up to 20 per cent, the ratios in this work are less than 5 per cent. This is also consistent with the fact that the flattenings in this work are closer to 1 than in K23. This implies that streams in both setups do not experience a large perturbation perpendicular to the stream track.

In our fits, we include a dynamical friction multiplier as discussed in K23. Figure 5.11 shows the distribution of solutions for the multiplier. K23 find strong constraints for this multiplier with $\log_{10}\lambda_{\mathrm{DF}_{\mathrm{K23}}} = 0.31^{+0.20}_{-0.48}$. While we see a peak of solutions in the same region, our median solution, $\lambda_{\mathrm{DF}} = 1$, does not modify dynamical friction. Overall, our constraints are weaker with $\log_{10}\lambda_{\mathrm{DF}} = -0.04^{+0.47}_{-1.61}$, excluding very strong but allowing very weak dynamical friction.

5.4.3 *Orbit of the LMC*

The LMC can perturb the stream twofold: (i) the higher the LMC's mass, the higher its effect at a constant distance, and (ii) smaller distances between the stream and the LMC increase the LMC's effect at constant mass. The too-high mass estimate of the LMC indicates that, in the fits, the LMC does not come as close to the stream as it

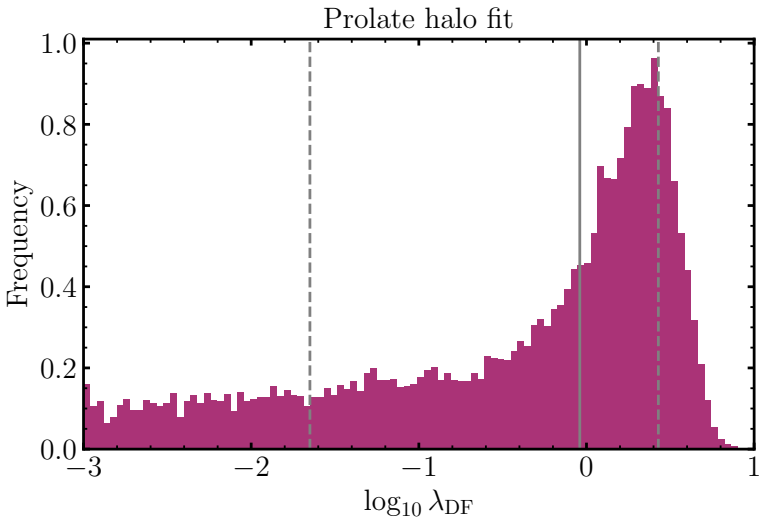

Figure 5.11: Dynamical friction multiplier in the prolate halo fit. This multiplier scales up or down the dynamical friction the LMC experiences during its infall. While there is a peak of solutions at $\log_{10}\lambda_{DF} \approx 0.5$, the median and the one sigma levels are at $\log_{10}\lambda_{DF} = -0.04^{+0.47}_{-1.61}$ as indicated by the grey lines.

does in the generation of the mock stream in the simulated Milky Way–LMC system. In order to get the same size velocity kick with a more massive LMC, its passage must be more distant. This means that the orbit of the LMC is not fitted correctly.

Figure 5.12 shows the orbit of the LMC in its galactocentric components in the simulation and in the three different fitting setups. The grey lines show the 'true' paths, while the coloured lines show the recovered paths in the fits. Particularly in the y and z-directions, there are large offsets between the fitted and the true orbits at larger lookback times. For small lookback times, e.g. the last 500 Myr, the orbits match well.

The LMC comes close and is thus relevant mainly for small lookback times. In Figure 5.13, we show the positional offset between the fits and the mock for the OC progenitor, the LMC and the Milky Way. The LMC has the smallest difference between the fits and the mock, while the Milky Way has the largest offset. This points towards a difference in the reflex motion of the disc, which we discuss in Section 5.4.4.

In Figure 5.14, we show the effect these orbital offsets have on how close the stream particles come to the LMC. At the closest approach, at around $\phi_1 \approx -90°$, the LMC comes the closest to all shown stream models. This is where the 'kink' we see in Figure 5.9 begins, indicating that this close approach to the LMC induces this kink.

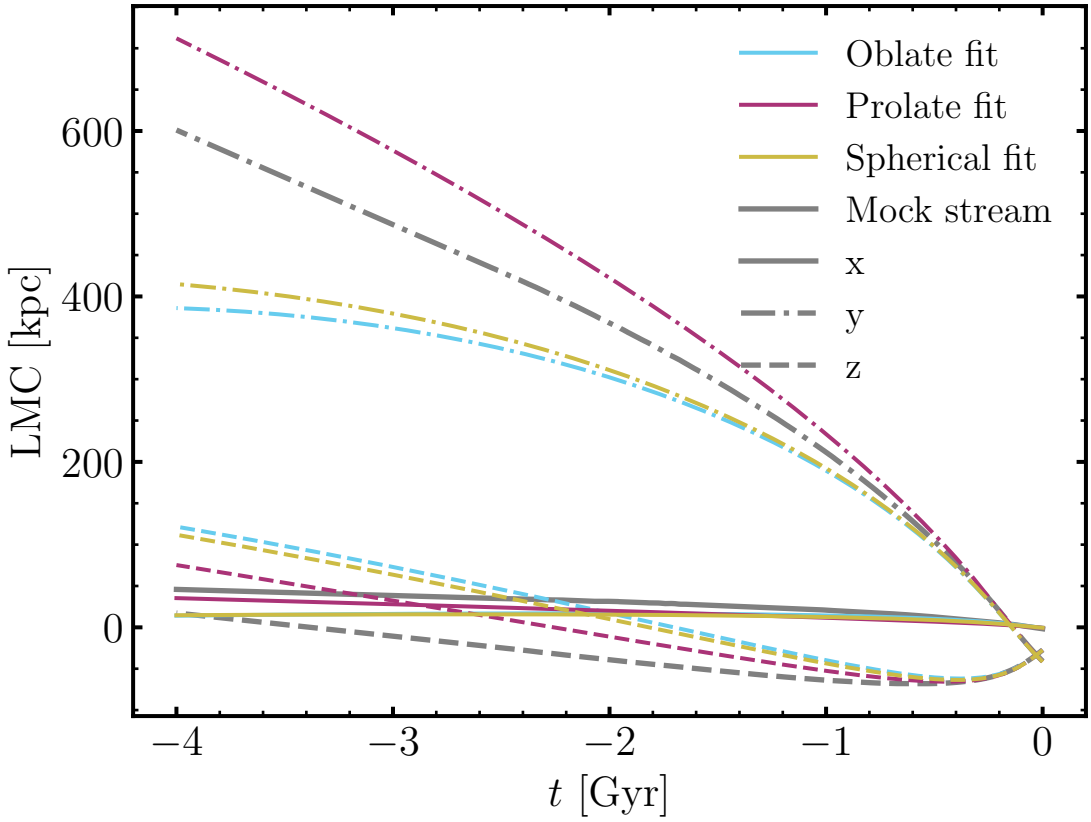

Figure 5.12: The inferred orbit of the LMC in cartesian coordinates. The full line shows its orbit in the x-direction, the dash-dotted line in the y-direction and the dashed line in the z-direction. The grey lines are from the 'true' orbit of the LMC in the simulation. The coloured lines are the orbits of the LMC in the best-fitting oblate (blue), prolate (purple), and spherical (yellow) halo. The x-direction is matched relatively well in all three fits. For all three halo shape fits, the LMC falls in from a higher z than in the simulation, with the orbit in the prolate halo matching the simulated LMC the best. In the y-direction, none of the orbit realisations match. While oblate and spherical configurations underestimate the orbit in y-direction, the prolate configuration overestimates it. The prolate orbit is overall the closest to the true orbit, which might explain the slightly better likelihood. Nevertheless, over the last 500 Myr, the period where the LMC comes the closest and has the biggest effect, all halo configurations match the simulated LMC's orbit still very well, as shown in Figure 5.13.

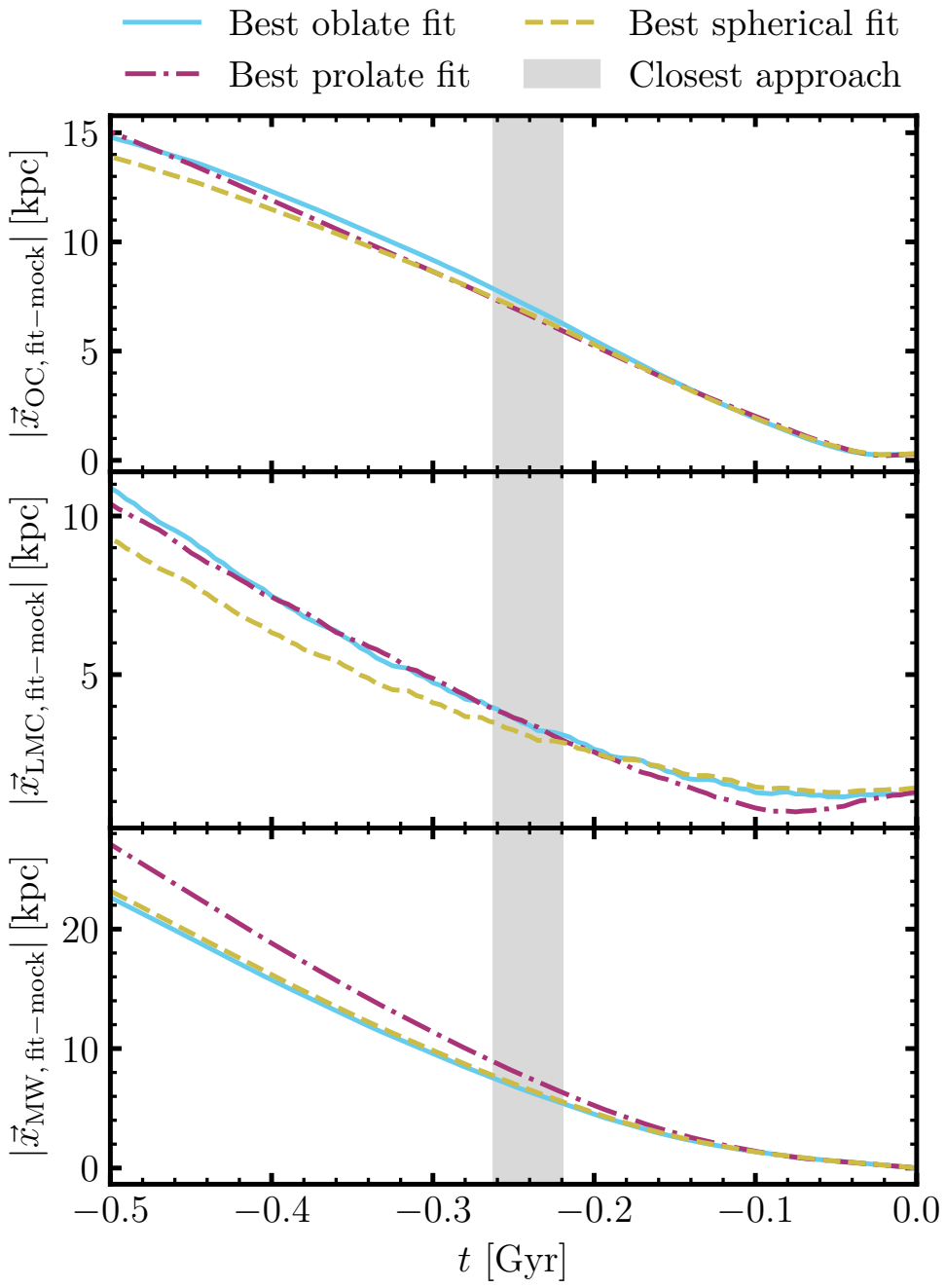

Figure 5.13: Positional offset between the best stream fits in each configuration and the mock for the OC progenitor *(top panel)*, the LMC *(middle panel)*, and the Milky Way *(bottom panel)*. The coloured dashed lines show the different halo configurations. The grey band shows the range of the times of the closest approach in the best fits and the mock. The smallest offset is seen in the LMC orbit which is less than 5 kpc. However, Figure 5.12 shows that the orbits get significantly offset for longer rewind times. The OC progenitor offset is less than 10 kpc, and the Milky Way's offset at closest approach times is the largest. This trend continues with larger lookback times.

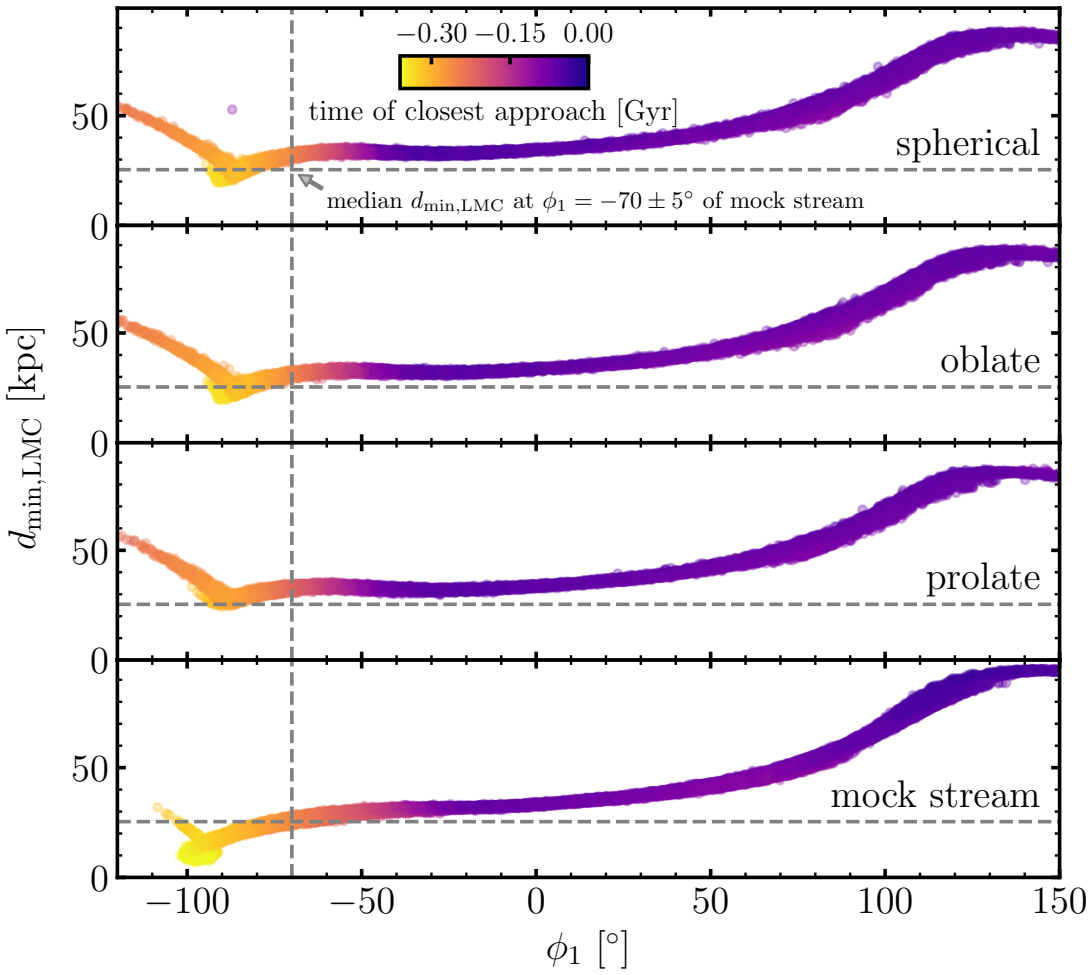

Figure 5.14: Closest approach distance between the OC stream and the LMC of the best-fit streams in the three halo configurations (*top panel:* spherical, *second panel:* oblate, *third panel:* prolate) and the mock stream *(bottom panel)*. The vertical grey lines show the position of the last data point that is included in the fits, ($\phi_1 = -70°$). The horizontal grey lines show the median closest approach distance of the mock particles in the bin of the last data point. While the mock OC stream gets very close to the LMC (within 10 kpc) more than 300 Myr ago, the fitted streams' closest approach is around 20 kpc and later in time. The prolate solution has the latest closest approach (~ 200 Myr ago) and the furthest away. Particles around the last data point included in the fits are the closest to the LMC within the fitting range and the most sensitive to its potential. Compared to the mock, these are still 10 kpc further away.

The last mock data point that we include in the fits is at $\phi_1 = -70°$. The horizontal lines show the closest approach distance to the LMC of the mock particles within this bin. At this position, the fitted stream particles are at distances around 10 kpc further away from the LMC. This explains the need for a higher LMC mass in the fits.

5.4.4 *Reflex motion in the stream models and Milky Way–LMC simulations*

The fits are unable to recover the true orbits of all components. The reflex motion of the Milky Way disc could introduce difficulties in the fits. In the Milky Way–LMC simulation, the reflex motion of the disc happens inherently due to the N-body nature of the simulation. In our fits, the phase-space position of the disc is calculated at each time step. The Milky Way–LMC simulation has a relatively small reflex motion, only finding a signature of $\sim 20\,\mathrm{km\,s^{-1}}$ in the outer halo. The bulk of this motion is in the y-direction. In the fits, the disc is moving significantly faster and more in the z-direction. The fits might not be able to reproduce a low enough signal that is given in the simulations. More robust results and interpretations of the bias in stream fits can be gained by simulating mock streams in different Milky Way–LMC simulations with a range of reflex motions.

Another insightful test for this bias will be fitting stellar streams with different methods in cosmological simulations (e.g. streams in the FIRE2 simulations; Panithanpaisal et al., 2021; Shipp et al., 2022; Arora et al., 2022). Reino et al. (2022) fit stellar streams in the FIRE simulations with an action-clustering approach. They find that fits to a full stream are not biased, but fitting streams near the pericentre has a systematic bias which leads to overestimating the host galaxy's mass. Future work could fit the same streams with the fitting technique presented here to test how well we recover the true parameters and to compare different stream fitting methods.

5.4.5 *Caveats of the results and tests for future confirmation*

In the first two sections of the discussion, I have discussed the implications of the results under the assumption they are correct. Then, I have shown that the LMC does not get close enough to the stream, which could explain the larger inferred LMC mass. Fi-

nally, I have discussed the differences between the reflex motion in the BFE simulation and the stream models which could be the reason for the mismatch.

There are several steps to testing the robustness of these results. The first problem could arise from marginally different implementations of the stream model. The main difference between the generation of the mock stream and the fitted streams is the integration of the stream particles. The particles of the streams evolved in the Milky Way–LMC simulation are integrated by time step. Testing whether we can fit and recover a mock stream that is created in a static, spherical potential should uncover any possible problems induced by this difference in stream modelling. Another test for this problem is to run a stream model with the fitting code with the according parameters of the mock stream and see whether the model stream matches the mock.

In order to test how the amount of reflex motion in the BFE simulation can affect a stream, we can model a different mock stream: Antlia 2 (Torrealba et al., 2019). Kinematic models of the stream require a reflex motion of the Milky Way disc of around $30\,\mathrm{km\,s^{-1}}$; otherwise, the proper motion vector of the model is misaligned with the observed spatial orientation of Antlia 2 (Ji et al., 2021). By evolving an Antlia 2-like stream in the Milky Way–LMC simulation and measuring the misalignment between the stream and its velocity vector, we will have an additional, different test of the amount of reflex motion in the Milky Way–LMC simulation.

If the smaller reflex motion in the current Milky Way–LMC simulation is the cause of the mismatch between the fitted and true potential parameters, we should look into evolving mock streams in different sets of simulations. One option is to expand all snapshots of the simulations presented in Garavito-Camargo et al. (2019, 2021a) where the orbit of the LMC matches the expectations better and which have a stronger reflex motion. Another option is to run new `EXP` simulations that focus on matching the LMC's orbit rather than the mass profiles of the Milky Way and the LMC. If similar mismatches still happen when the simulated reflex motion matches the Milky Way reflex motion better, this would confirm the results. Finally, as mentioned in the previous section, fits to stellar streams in cosmological simulations can uncover new, and confirm or disprove the current results.

Given the effect of the time-dependence of the Milky Way–LMC system on stellar streams presented in Chapter 3 and the possible bias in stream fitting methods found

in this chapter, we should aim to develop stream fitting techniques that take the deformations into account.

5.4.6 *Development of a time-dependent Milky Way–LMC model*

Current fits to stellar streams assume rigid haloes (e.g. E19; Shipp et al., 2021; Vasiliev et al., 2021; K23). In L23, we show that the deformations of the Milky Way and the LMC haloes have a significant effect on stellar streams. Thus, ideally, we fit streams with time-dependent haloes. This time-dependent model needs to provide cheap and fast force evaluations that come close to the performance of analytic solutions. A fully time-dependent Milky Way–LMC description that is functional in fitting streams is currently unachievable.

L23 have found that the dipole of the Milky Way has the most significant effect on the OC stream. Thus, implementing a simple dipole that can be fit is the first step in developing the desired model. Then, to get a more complete picture of the dynamical processes happening in this interaction, we can use multichannel singular spectrum analysis (mSSA; Weinberg & Petersen, 2021; Johnson et al., 2023). MSSA utilises principal component analysis of time series, finding relations in space and time and, thus, the clearest description of the dynamical system. This drastically reduces the number of coefficients needed to describe an evolving system. The dynamical features found with mSSA can be compared between different Milky Way–LMC simulations. Ideally, with a suite of Milky Way–LMC simulations, we will be able to use mSSA to interpolate between principal components of the BFEs. This would allow us to fit the mSSA coefficients and, ultimately, the time-dependent Milky Way–LMC model. This idea is not guaranteed to work, though, and needs considerable technical development and testing first.

5.5 CONCLUSIONS

This paper aims to uncover possible biases in fitting Milky Way and LMC properties with stellar streams by not including the time dependence of this interaction. We fit a mock stream evolved in a time-dependent Milky Way–LMC system with current state-

of-the-art stream fitting methods. Here, we summarise the results from these fitting efforts:

- We generate a stellar stream in a BFE simulation of the time-dependent Milky Way–LMC system. We turn this stream into mock data that includes realistic observational errors in order to fit the stream with current state-of-the-art fitting techniques (Figures 5.1–5.3).
- The stream model evolved in a prolate halo matches the stream observables fairly well (Figure 5.4).
- We compare the inferred model parameters with the BFE simulation's true parameters. The best-fit stream model recovers neither the enclosed mass profiles of the Milky Way and the LMC nor the flattening of the Milky Way halo (Figures 5.5–5.7).
- We compare results and implications of our fits with K23, who modelled the observed data of the OC stream with the same method. While their stream tracks can explain the difference in the likelihood between different halo setups, our stream tracks cannot (Figure 5.9). Furthermore, they find a strong out-of-plane acceleration in the stream plane. Our results do not imply such an acceleration (Figure 5.10).
- We find that the orbit of the LMC is not recovered correctly in the fits. The prolate halo fit matches the simulation orbit the best, which might explain the marginally higher likelihood for the prolate fit (Figure 5.12). The increased distance between the OC stream and the LMC can explain the higher LMC mass necessary for the stream to experience enough perturbation (Figure 5.14).
- We discuss the option that a difference in the reflex motion of the Milky Way disc in the fits and the simulation can affect the fits (Section 5.4.4, Figure 5.13) and discuss briefly the necessary technical developments to build a fittable time-dependent Milky Way–LMC model (Section 5.4.6).

While this chapter has been written as a paper draft, it clearly needs more work before being submitted for publication. We would like to understand more clearly

why these fits do not match the simulated parameters. We aim to better understand the effect of the different reflex motions in the fits and in the simulation. Future work will fit stellar streams in cosmological simulations to investigate similar questions as here so that we can paint a well-rounded picture of biases that are introduced in rigid stream fitting techniques. Once we know these biases, we can work towards developing workarounds and, ideally, a more realistic Milky Way model that includes some extent of the time dependence.

ACKNOWLEDGEMENTS

Facilities: Institute for Astronomy *cuillin* supercomputer (`https://cuillin.roe.ac.uk`), University of Surrey *Eureka* High Performance Computing cluster
Software: `astropy` (The Astropy Collaboration, 2013, 2018, 2022), `emcee` (Foreman-Mackey et al., 2013), `EXP` (Petersen et al., 2022a), `GALPOT` (Dehnen & Binney, 1998), `IPython` (Pérez & Granger, 2007), `Jupyter` (Kluyver et al., 2016), `matplotlib` (Hunter, 2007), `mpi4py` (Dalcin & Fang, 2021), `numpy` (Harris et al., 2020), `pandas` (McKinney, 2010; Reback et al., 2020), `pybind11` (Jakob et al., 2017), `schwimmbad` (Price-Whelan & Foreman-Mackey, 2017), `scipy` (Virtanen et al., 2020)

6

CONCLUSIONS AND OUTLOOK

In this thesis, I have presented work on stellar streams in the deforming dark matter haloes of the Milky Way and the Large Magellanic Cloud (LMC). Stellar streams are sensitive probes of the gravitational potential. Various streams have been used to fit properties of the Milky Way and the LMC halo. In this work, I have shown that stellar streams are significantly affected by these time-dependent deformations. This result presents us with problems regarding stream modelling and the parametrisation of the Milky Way's dark matter halo, but it also provides us with new possibilities to explore the nature of dark matter. In this concluding chapter, I summarise the work I have carried out and present the scope of future work based on these results.

6.1 RESULTS OF THIS THESIS

The OC stream in the deforming Milky Way–LMC system

In Chapter 3, I present a study on how the OC stream is affected by the deformations of the Milky Way and the LMC. We chose the OC stream as it spans large parts of the Milky Way halo, and it is affected by the LMC as a portion of the stream passes very close by the LMC. The infalling LMC has many effects on the Milky Way, e.g. the disc's reflex motion and overdensities in the halo. (Erkal & Belokurov, 2020; Petersen & Peñarrubia, 2020; Garavito-Camargo et al., 2021a; Conroy et al., 2021). Its presence also affects stellar streams (Erkal et al., 2019; Vasiliev et al., 2021; Shipp et al., 2021; Koposov et al., 2023). We ask, *are streams specifically affected by the deformations of the dark matter haloes of both galaxies?*

We investigate an OC-like stream in a basis function expansion (BFE) simulation of the Milky Way and the LMC that is time-dependent and includes the deformations of both galaxies. We find that these deformations significantly affect the OC stream,

with track offset far greater than observational uncertainties. This means that current inferences of the Milky Way and LMC potentials using stellar streams could be biased. The biggest effect on the stream comes from the Milky Way's dipole. Other smaller effects include the evolution of the LMC's monopole, the LMC's quadrupole, and even its higher moments.

With the LMC falling into the Milky Way, we have a dark matter collider in our backyard. Since stellar streams are sensitive probes to the gravitational potential they move in, and are affected by the dark matter halo deformations, they act as sensitive detectors in the Milky Way–LMC dark matter collider. This motivates future theoretical developments to utilise the high-quality current and future data to measure the time-dependent haloes of the Milky Way and the LMC. We need to improve BFE tools to create efficient models that can describe an arbitrary Milky Way–LMC encounter over a sufficiently large parameter space. Detecting the existence of these deformations and characterising their effects would be a spectacular test of the collisionless nature of dark matter. It would offer another window to probe different dark matter and alternative gravity models.

The information about the time-dependence of the Milky Way halo in stellar streams

In Chapter 4, I explore the information streams hold on a time-dependent Milky Way halo. Almost 100 streams have already been detected in the Milky Way halo, and more are expected with upcoming surveys. Each stream can give unique insights into the evolution of the Milky Way, yet some streams are particularly suited to infer properties of the Milky Way's dark matter halo. Bonaca & Hogg (2018) introduce a statistical approach to quantifying a stream's constraining power (i.e. its information content) on model parameters. They calculate the best-case uncertainty that model parameters can have given the quality of a data set. They find that streams have the best constraints over the distance range they currently cover and that combining streams improves the uncertainties significantly. While they included a potential that can include the effect of an external perturbation, this perturbation is rigid. We ask, *what information do streams hold on time-dependent perturbations of the Milky Way halo?*

We extend the methodology developed in Bonaca & Hogg (2018) to include time-dependent perturbations. We evolve streams in haloes with a rigid and time-dependent

perturbation and calculate the best-case uncertainties of several model parameters, focusing particularly on the perturbation coefficients. We chose a perturbation that matches the Milky Way dipole in the Milky Way–LMC simulation presented in Chapter 3, as we found that the dipole has the biggest effect on the stream. We find that streams that are currently used to fit the potential, such as Sagittarius, OC and GD-1 are also the most informative streams on the time-dependent perturbation. In our toy model setup, the OC-like mock stream has the best constraints on the first perturbation coefficient of the dipole, at the one per cent level. Only combining it with at least 3 other streams will improve the uncertainty. Further, we find that most of the information lies in the stream track for many streams. Finally, we estimated a lower limit of the perturbation in our toy models that streams are sensitive to within a 20 per cent best-case parameter uncertainty. This is for a relative force ratio of 0.5 per cent at 50 kpc. While these results are obtained for a toy model, they have important qualitative implications, such as informing us which streams are best to use when modelling a time-dependent Milky Way potential.

The bias in stream fitting methods from omitting the deformations

In Chapter 5, I investigate how stellar stream fits are affected by omitting the time-dependence of the Milky Way and the LMC haloes. There are a variety of stream-fitting methods (described in Chapter 2.2). Most of them assume analytic potentials with rigid halo shapes, including the widely used particle-spray method (Küpper et al., 2008, 2010, 2012; Gibbons et al., 2014; Fardal et al., 2015). In recent fitting efforts, the infalling LMC and the reflex motion of the Milky Way disc are included, but the dark matter haloes of both galaxies are still rigid (e.g. Erkal et al., 2019; Vasiliev et al., 2021; Koposov et al., 2023). The inferred Milky Way haloes – prolate and oblate – are strongly flattened, and their orientation often points towards the LMC. We ask, *are stream fits biased by not including the deformations of the dark matter haloes of the Milky Way and the LMC?*

To answer this question, we fit a mock stream evolved in a live Milky Way–LMC BFE simulation with current state-of-the-art fitting techniques. All halo shapes return similarly good fits, and the fitted streams match the mock data well. We compare the parameters and constraints from the fits with the 'true' values from the simulation. We

find that the fits do not recover the true parameters of the halo. The Milky Way halo mass is significantly underestimated, and the LMC mass is overestimated by more than a factor of two. The shape of the simulated Milky Way halo is close to spherical. The inferred flattenings are $q = 1.2$ in the prolate case and $q = 0.9$ in the oblate case. The flattenings measured in Koposov et al. (2023) are much stronger for both shapes.

In our fits, a problem could be induced by the small reflex motion in the BFE simulation, whereas the model cannot recreate a matching stream with such a small reflex motion. If these results are representative of this method, stream fits are more biased than expected. This approach needs to be repeated in different Milky Way–LMC simulations and other Milky Way-like simulations, e.g. cosmological zoom-in simulations, to test how common these biases are.

6.2 FUTURE DIRECTIONS OF WORK

The work I presented in this thesis offers many different directions for future research. I will now introduce some ideas my collaborators and I will work on over the next years. These aim to provide new tools to investigate the time dependence of the Milky Way halo and put constraints on dark matter particle models.

Technical development for BFEs

BFEs are a very useful tool to describe systems that are perturbed and to evolve other substructures in these systems. While they are accessible for fast and cheap evaluations of field values (potential, density, force, ...), this comes at the cost of needing $10^2 - 10^3$ coefficients to describe the system. Some of these coefficients hold substantial information about the system; others are merely noise. Ideally, this system can be described by fewer coefficients and functions that all hold information on the system's structure and evolution. This should allow for some physical interpretation of each coefficient.

Weinberg & Petersen (2021) developed a method that they adapted from geophysics, multichannel singular spectrum analysis (mSSA). MSSA is a non-parametric tool that finds correlations in space and time and drastically reduces the number of coefficients, similar to principal component analysis. It has a broad range of applications for dynamical systems that can are described with BFEs. Weinberg & Petersen (2021) apply

mSSA to barred galaxy simulations, finding that it extracts the dominant features in space and time. Johnson et al. (2023) present the application of mSSA to a simulated Milky Way-like system and extract signals for two dipole modes that occur. It can also be used to characterise the response of the MW halo to a satellite and vice versa.

For this, we will apply mSSA to the Milky Way–LMC simulations presented in this thesis and a Milky Way–LMC simulation suite that is currently being run. Applying mSSA to the simulation suite and correlating them together will identify the main dynamical processes that take place in the system and ideally provide a template to interpolate between different initial conditions for the Milky Way–LMC system (transfer learning technique). This method will drastically reduce the number of coefficients needed to describe the system. Together with identifying the dynamical features that affect stellar streams, we can develop tools to model the time-dependent Milky Way.

Developing a time-dependent Milky Way model

As shown in this work, stellar streams are affected by the deformations of the Milky Way and the LMC (Chapter 3) and hold information on the time-dependence of the Milky Way (Chapter 4), affecting our ability to model stellar streams and the Galaxy (Chapter 5). This calls for an updated Milky Way description that includes its time dependence.

With the Milky Way–LMC simulation suite, a reduced number of coefficients with mSSA, and the transfer learning technique, we will be able to interpolate between different setups for the Milky Way and the LMC, e.g. their halo masses and shapes. These setups can then be fitted with the streams that are the most informative of the time dependence of the Milky Way. With current and future high-quality data, this accurate Milky Way model is crucial for the reliability of any future work that requires a precise description of the Milky Way halo.

Constraining dark matter in the Milky Way using BFEs and stellar streams

One of the most exciting outlooks is that we will be able to test different dark matter and alternative gravity models. With the flexible form of BFEs, we can create Milky Way–LMC interactions with different setups that mimic warm, self-interacting (SIDM)

and fuzzy dark matter (FDM), and alternative gravities using EXP (Petersen et al., 2022a). This will enable us to understand how different parameters for each dark matter theory affect the interaction. These are e.g. the halo profile, mass and shape in cold dark matter (CDM), the dark matter particle mass for FDM, the cross-section for SIDM, and a_0 for modified Newtonian dynamics (MOND).

An unbiased measurement of the shape of the Milky Way halo distinguishes between e.g. CDM (triaxial) and SIDM (nearly spherical; Robles et al., 2017). This unbiased measurement is only possible if we understand the effect of the deformations and can contrast it clearly against the halo shape. Only the accurate time-dependent Milky Way model will allow us to measure the halo shape correctly and put these constraints on dark matter particle models.

Another strategy to distinguish between different dark matter particle and alternative gravity models is utilising different prescriptions of dynamical frictions in these theories (e.g. Lancaster et al., 2020 for FDM, and Bílek et al., 2018 for MOND). The dynamical friction experienced by the LMC has already been measured using stellar streams (Shipp et al., 2021; Koposov et al., 2023). This measurement was made possible since the streams have close passages with the LMC in the past, and thus the streams are sensitive to the LMC's past orbit. However, our work in Chapter 5 shows that while these measurements are precise, they might not be accurate. This past orbit highly depends on dynamical friction. A precise and robust measurement of dynamical friction will have strong implications for alternative gravity models, which should have very little dynamical friction at the radius of the LMC.

We are fortunate to live next to a dark matter collider that is the Milky Way–LMC interaction. Stellar streams are sensitive probes to the gravitational potential and the deformations of dark matter haloes, making them prime detectors in this collider. In the future, with new and improved technological tools, we will further investigate the time dependence and deformations of the Milky Way and LMC dark matter haloes with stellar streams, and turn these results into new constraints on dark matter particle models.

A

APPENDIX TO CHAPTER 3: THE OC STREAM IN DEFORMING DARK MATTER HALOES

This is the appendix to Chapter 3, published in Lilleengen et al. (2023).

A.1 BFE RECONSTRUCTIONS BY RADIAL ORDER

The spherical basis function expansions used in this paper correspond to harmonic indices l and m (which correspond to standard spherical harmonics) and radial index n, which broadly defines the spatial scale that a function is both sensitive to, and influences. The lowest-order radial function ($n = 0$) is sensitive to the largest scales, the next radial function ($n = 1$) is sensitive to slightly smaller scales, and so on. However, given that the basis is *global*, one cannot directly map radial functions to 'resolution'. To assist in physical interpretation, in this appendix, we visually demonstrate the effects on reconstructing the density field when including and excluding different radial orders. We restrict our detailed analysis with radial order to the largest-power harmonic subspaces for each component, as discussed in Sections 3.3.3 and 3.3.4 (i.e. dipole for the Milky Way, quadrupole for the LMC).

Figure A.1 shows the density reconstructions for the Milky Way and LMC, as well as the change in density for isolated n orders. Beginning with the upper row, we show the reconstruction of the Milky Way when including successively more terms, from the monopole (including all radial orders) in the left-most panel to the full density reconstruction over all functions (harmonic and radial) in the right-most panel. Intermediate panels (left to right) add dipole radial functions $n = 0$, $n \leqslant 1$, $n \leqslant 2$, and all radial dipole orders (second from right). One sees that the addition of functions adds features to the overall density profile that deform the Milky Way away from the initially spherical shape. To further illustrate the role different functions play in determining the overall structure, in the second row of panels, we show the contribution

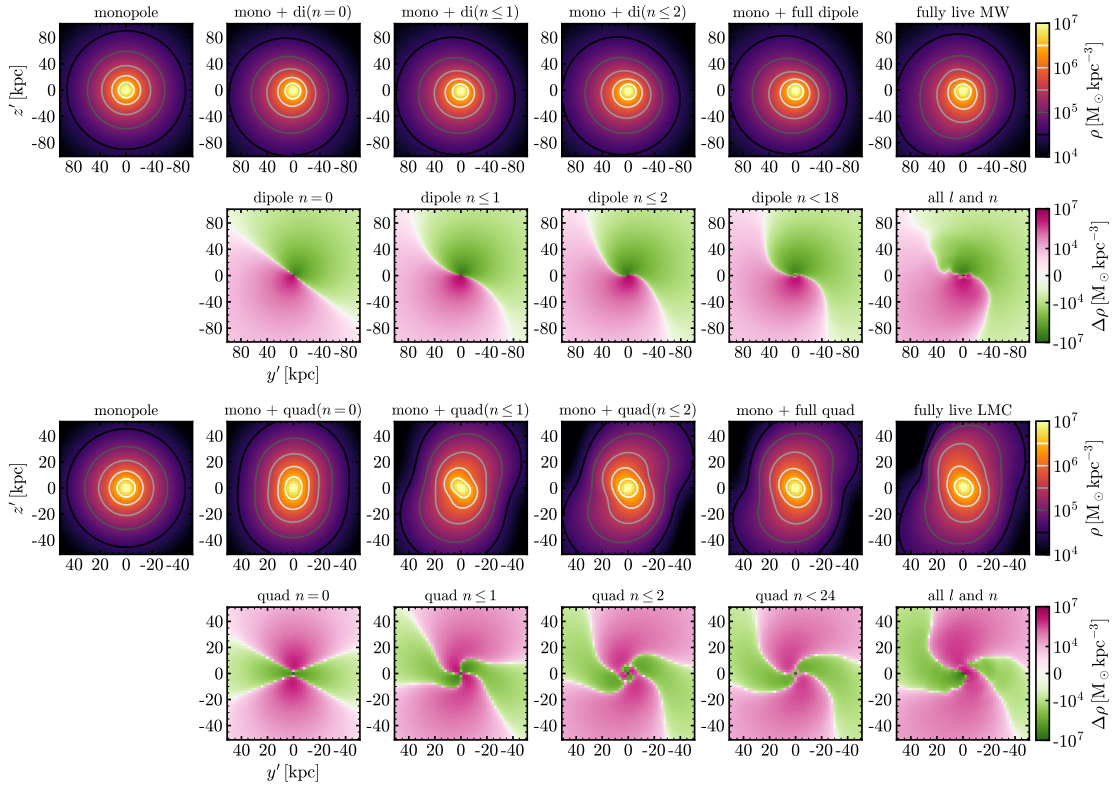

Figure A.1: Milky Way and Large Magellanic Cloud (LMC) density and change in density as a function of basis function n order at the present day ($T = 0$) in our model, for the largest-power harmonic subspace for each component. These are shown in the orbital plane of the LMC, defined in Appendix A.2. The upper two rows show the Milky Way reconstruction when adding successive *dipole* radial functions. The lower two rows show the LMC reconstruction when adding successive *quadrupole* functions. Both the Milky Way and LMC demonstrate the convergence of the series with the addition of radial orders (compare with the full reconstructions in the right-most row).

of specific sets of functions. The functions are shown in parallel with the total density reconstructions in the upper row, such that the left-most panel in the second row shows the contribution of the dipole $n = 0$ term, and the right-most panel shows the contribution of all non-monopole harmonic ($0 < l \leqslant 6$) and radial orders ($n < 18$).

We then show the same analysis for the LMC in the bottom two rows of panels of Figure A.1, except we focus on the quadrupole rather than the dipole. Moving from left to right in the panels reconstructing the total density, one sees that the addition of radial terms acts to twist the inner isodensity contours. The ability of multiple radial orders to act together is even more apparent in the density contribution of the isolated non-monopole functions (the bottom row of Figure A.1), where the full position angle of the LMC dipole requires the first few terms ($n \leqslant 2$) before it resembles the full reconstruction (the right-most panel). Figure A.1 also shows that the large-scale density fields of both the Milky Way and LMC are well described with the $n \leqslant 2$ expansions, while the higher order terms are responsible for smaller-scale features.

A.2 COORDINATE SYSTEM TRANSFORMATION

In order to study the effects of the deformations induced by the LMC, we rotate our coordinate system so that it is aligned with the LMC's orbital plane. First, we calculate the angular momentum of the LMC

$$\vec{L}_{\rm LMC} = \vec{x}_{\rm LMC} \times \vec{v}_{\rm LMC} = \begin{pmatrix} -15211 \\ 1133 \\ -1033 \end{pmatrix} \text{ kpc km s}^{-1} \tag{A.1}$$

from its current position $\vec{x}_{\rm LMC}$ and current velocity $\vec{v}_{\rm LMC}$. This angular momentum is defined by the angles $\theta = \arctan2(L_y, L_x)$[1] and $\phi = \arcsin(L_z/|\vec{L}|)$ that are used for the rotations. The first rotation is defined by the rotation matrices

$$M_1(\theta) = \begin{bmatrix} \cos(\chi(\theta)) & -\sin(\chi(\theta)) & 0 \\ \sin(\chi(\theta)) & \cos(\chi(\theta)) & 0 \\ 0 & 0 & 1 \end{bmatrix} \tag{A.2}$$

1 We choose the sequence of arguments (y, x) for the `arctan2` functions in line with the NUMPY definition.

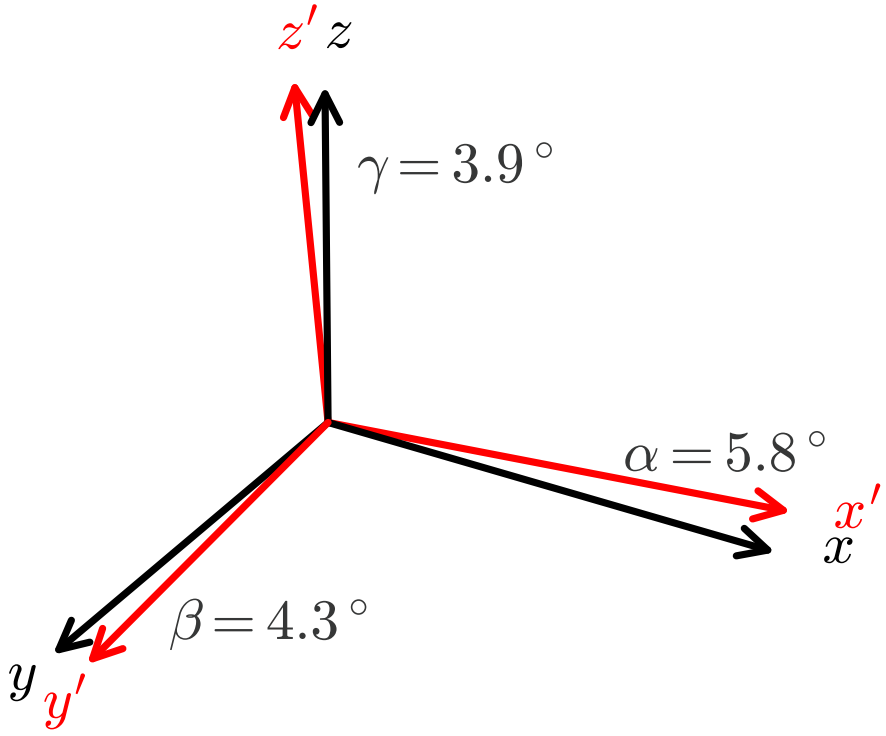

Figure A.2: Comparison of coordinate systems: Galactocentric *(black)* and the rotated system where the orbital plane of the LMC is aligned with the $y'z'$-plane such that the recent past LMC orbits in both frames are matching *(red)*. The frames are close, and the angles between the directions are small, but there are important features visible in the rotated frame that are not as clear in the Galactocentric frame.

$$M_2(\phi) = \begin{bmatrix} \cos(\phi) & 0 & -\sin(\phi) \\ 0 & 1 & 0 \\ \sin(\phi) & 0 & \cos(\phi) \end{bmatrix} \tag{A.3}$$

where $\chi(\theta) = \pi - \theta$. The matrix $M_{21}(\phi, \theta) = M_2(\phi)M_1(\theta)$ aligns the orbital plane of LMC with the yz'-plane, pointing towards the $-x$ direction. The position of the LMC in this new frame is calculated by $\vec{x}_{\mathrm{LMC,rot}}(\phi, \theta) = M_{21}(\phi, \theta) \times \vec{x}_{\mathrm{LMC}}$. The angle ψ is the angle between the y and z-components of the LMC's current position in Galactocentric coordinates and in the by M_{21} rotated frame

$$\psi(\phi, \theta) = -\arctan2\left(z_{\mathrm{LMC,rot}}(\phi, \theta), y_{\mathrm{LMC,rot}}(\phi, \theta)\right) + \arctan2\left(z_{\mathrm{LMC}}, y_{\mathrm{LMC}}\right). \tag{A.4}$$

With this angle, we rotate the frame around x' so that the LMC is at the same angle in both frames and their recent past orbits roughly match using the rotation matrix

$$M_3(\phi, \theta) = \begin{bmatrix} 1 & 0 & 0 \\ 0 & \cos(\psi(\phi, \theta)) & -\sin(\psi(\phi, \theta)) \\ 0 & \sin(\psi(\phi, \theta)) & \cos(\psi(\phi, \theta)) \end{bmatrix} \tag{A.5}$$

and the combined matrix

$$M(\phi, \theta) = M_3(\phi, \theta)M_{21}(\phi, \theta) \tag{A.6}$$

$$= \begin{bmatrix} 0.99496001 & -0.07410371 & 0.06755159 \\ 0.0741843 & 0.99724368 & 0.00131805 \\ -0.06746307 & 0.00369986 & 0.99771491 \end{bmatrix}. \tag{A.7}$$

The product of M and any vector (e.g. position, velocity, or force) rotates that vector into the orbital plane of the LMC. The transpose of M rotates the vector back into the Galactocentric coordinate frame. The new coordinate system is calculated by

$$\vec{r}' = M(\phi, \theta)\vec{r}. \tag{A.8}$$

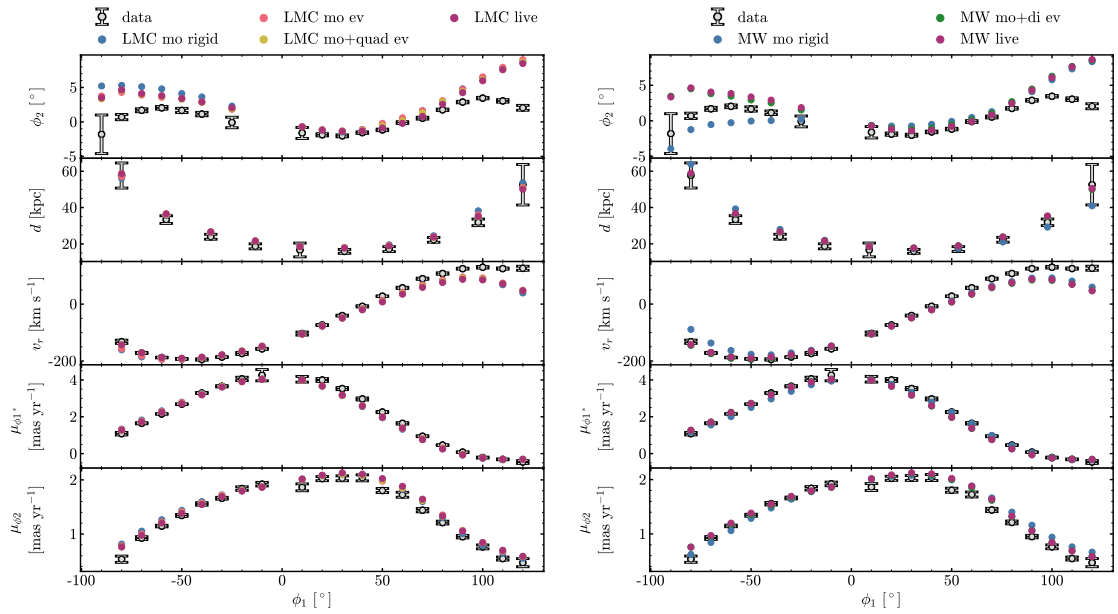

Figure A.3: Observables of the OC stream in different LMC and Milky Way potentials. The panels and data are the same as in Figure 3.4. We show the moments with the highest impact on the stream, identified in Figures 3.5 and 3.6. *Left panel:* The OC stream is evolved in a live Milky Way, and different moments from the LMC are shown. The moments with the highest impact are turning on the time-dependence (blue to red) and then including the quadrupole (red to yellow and purple). *Right panel:* The LMC is kept live while the OC stream is evolving in different Milky Way moments. The most important moment is the dipole (blue to green and purple). For both potential setups (Milky Way live vs LMC live), the track is the observable with the biggest changes, as seen in Figure 3.5. The other observables mostly do not differ significantly more than the data uncertainty.

In order to show how this new coordinate system looks, we transform the unit vectors in the prime coordinates system to vectors in the Galactocentric system in Figure A.2. We note that the required rotations are relatively small, and the Galactocentric cartesian axes are within 6° of the rotated Cartesian axes.

A.3 STREAM OBSERVABLES

Figure A.3 shows the observables (i.e. stream track, distance, proper motions, and radial velocity) for the data and the modelled streams in the BFE moments of each galaxy with the largest impact on the stream. The most affected observable is the stream track (which is the focus of this work), but we see other observables are also affected, and thus, fitting all observables should provide stringent constraints on these deforming haloes.

B

APPENDIX TO CHAPTER 4: THE INFORMATION CONTENT IN STELLAR STREAMS IN TIME-DEPENDENT POTENTIALS

This is the appendix to Chapter 4, currently being prepared for publication in the Astrophysical Journal.

B.1 ESTIMATION OF THE POLYNOMIAL COEFFICIENTS

Here, we show how we estimate the polynomial coefficients of the perturbation multipole potential. We fit the Milky Way dipole coefficients from the basis function expansion (BFE) simulation in Lilleengen et al. (2023) in Figure B.1. As the underlying functions are different for the basis function and the multipole expansions, we need to scale the parameters so that the force fields are similar for both setups. With a scaling coefficient of 0.025, the force amplitude of the change due to the perturbations are similar, shown in Figure B.2.

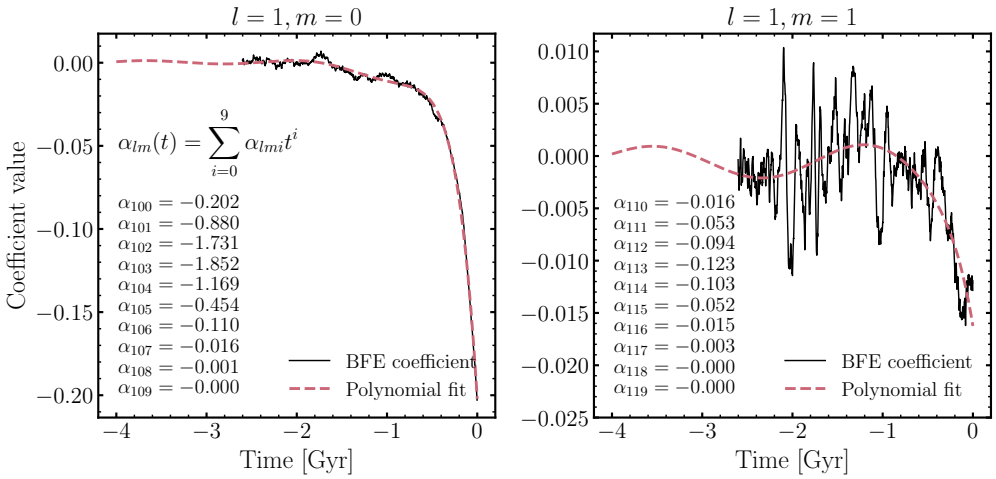

Figure B.1: Polynomial fit of the BFE dipole coefficients. Both panels show the time evolution of a dipole coefficient of the Milky Way simulation presented in Lilleengen et al. (2023). *Left panel:* Dipole with the $m = 0$ order for the zeroth radial order ($n = 0$). This is the deformation with the strongest effect in the simulation. It is represented in this paper by the parameter α_{10}. *Right panel:* Dipole with the $m = \pm 1$ orders, represented by the coefficient α_{11}. Both are fitted with a 9th-order polynomial. The values for the polynomial coefficients are given in each panel. While the BFE coefficients are noisy, the polynomial fits smooths out the evaluation.

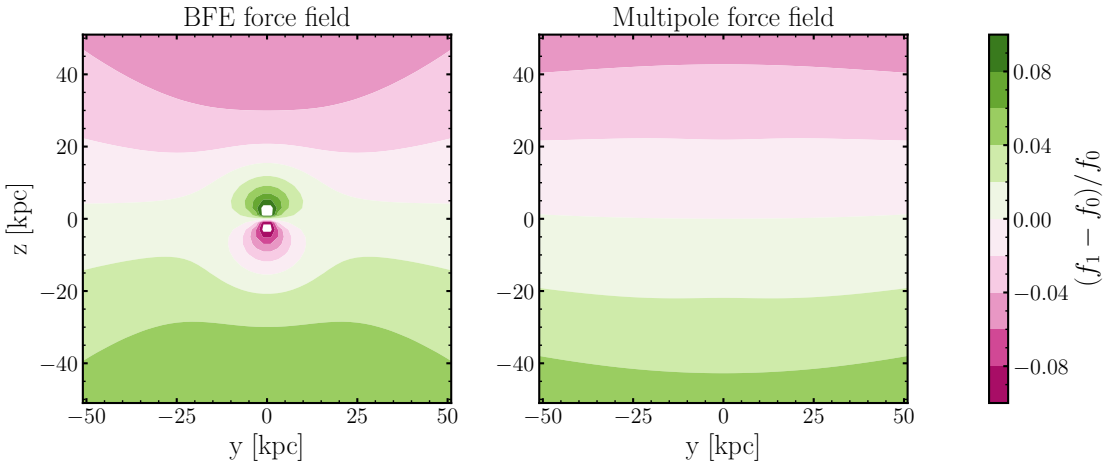

Figure B.2: Fields of the basis function and the multipole expansion for the dipole. The colours represent the relative amplitude of the dipole forces. While the BFE field (*left panel*; from Lilleengen et al., 2023) has more structure, the multipole field *(right panel)* recovered with the polynomial parameters α_{10} and α_{11} shows a similar amplitude distribution over large scales.

BIBLIOGRAPHY

Aarseth S. J., 1963, MNRAS, 126, 223

Aarseth S. J., 2003, Gravitational N-Body Simulations

Ackerman L., Buckley M. R., Carroll S. M., Kamionkowski M., 2009, Phys. Rev. D, 79, 023519

Adhikari R., et al., 2017, J. Cosmology Astropart. Phys., 2017, 025

Afonso G. B., 2006, EDIÇÃO ESPECIAL SCIENTIFIC AMERICAN BRASIL, 14, 46–55

Ahmad A., Cohen L., 1973, Journal of Computational Physics, 12, 389

Akerib D. S., et al., 2017, Phys. Rev. Lett., 118, 021303

Al Sufi A.-a.-R., 964, Book of Fixed Stars. Isfahan, Persia

Allen R. H., 1963, Star names. Their lore and meaning

Amorisco N. C., Gómez F. A., Vegetti S., White S. D. M., 2016, MNRAS, 463, L17

Angulo R. E., Hahn O., Abel T., 2013, MNRAS, 434, 3337

Antoja T., et al., 2018, Nature, 561, 360

Antoja T., Ramos P., Mateu C., Helmi A., Anders F., Jordi C., Carballo-Bello J. A., 2020, A&A, 635, L3

Aprile E., et al., 2018, Phys. Rev. Lett., 121, 111302

Arora A., Sanderson R. E., Panithanpaisal N., Cunningham E. C., Wetzel A., Garavito-Camargo N., 2022, ApJ, 939, 2

Athanassoula E., 2005, MNRAS, 358, 1477

Bahcall J. N., 1984a, ApJ, 276, 169

Bahcall J. N., 1984b, ApJ, 287, 926

Banik N., Bovy J., 2019, MNRAS, 484, 2009

Barbuy B., Chiappini C., Gerhard O., 2018, ARA&A, 56, 223

Bartelmann M., Schneider P., 2001, Phys. Rep., 340, 291

Bayer J., 1603, Uranometria: omnium asterismorum continens schemata, nova methodo delineata, aereis laminis expressa. Augsburg, Germany

Behroozi P. S., Wechsler R. H., Conroy C., 2013, ApJ, 770, 57

Bekenstein J. D., 2004, Phys. Rev. D, 70, 083509

Bekenstein J., Milgrom M., 1984, ApJ, 286, 7

Bekki K., Chiba M., 2005, MNRAS, 356, 680

Belokurov V., et al., 2006, ApJ, 642, L137

Belokurov V., et al., 2007a, ApJ, 657, L89

Belokurov V., et al., 2007b, ApJ, 658, 337

Belokurov V., Erkal D., Evans N. W., Koposov S. E., Deason A. J., 2018, MNRAS, 478, 611

Belokurov V., Deason A. J., Erkal D., Koposov S. E., Carballo-Bello J. A., Smith M. C., Jethwa P., Navarrete C., 2019, MNRAS, 488, L47

Belokurov V., Sanders J. L., Fattahi A., Smith M. C., Deason A. J., Evans N. W., Grand R. J. J., 2020, MNRAS, 494, 3880

Bertone G., Hooper D., 2018, Reviews of Modern Physics, 90, 045002

Bertone G., Tait T. M. P., 2018, Nature, 562, 51

Bertone G., Hooper D., Silk J., 2005, Phys. Rep., 405, 279

Besla G., Kallivayalil N., Hernquist L., Robertson B., Cox T. J., van der Marel R. P., Alcock C., 2007, ApJ, 668, 949

Besla G., Kallivayalil N., Hernquist L., van der Marel R. P., Cox T. J., Kereš D., 2010, ApJ, 721, L97

Besla G., Kallivayalil N., Hernquist L., van der Marel R. P., Cox T. J., Kereš D., 2012, MNRAS, 421, 2109

Best E., 1922, The Astronomical Knowledge of the Maori, Genuine and Empirical. Dominion Museum monograph, New Zealand Electronic Text Collection 2005, Wellington New Zealand, http://nzetc.victoria.ac.nz/tm/scholarly/tei-BesAstro.html

Bett P., Eke V., Frenk C. S., Jenkins A., Helly J., Navarro J., 2007, MNRAS, 376, 215

Bílek M., Thies I., Kroupa P., Famaey B., 2018, A&A, 614, A59

Binney J., 2005, in Turon C., O'Flaherty K. S., Perryman M. A. C., eds, ESA Special Publication Vol. 576, The Three-Dimensional Universe with Gaia. p. 89 (arXiv:astro-ph/0411229), doi:10.48550/arXiv.astro-ph/0411229

Binney J., 2010, MNRAS, 401, 2318

Binney J., 2012, MNRAS, 426, 1324

Binney J., Tremaine S., 2008, Galactic Dynamics: Second Edition

Bland-Hawthorn J., Gerhard O., 2016, ARA&A, 54, 529

Bland-Hawthorn J., Tepper-García T., 2021, MNRAS, 504, 3168

Blandford R. D., Narayan R., 1992, ARA&A, 30, 311

Blumenthal G. R., Pagels H., Primack J. R., 1982, Nature, 299, 37

Blumenthal G. R., Faber S. M., Primack J. R., Rees M. J., 1984, Nature, 311, 517

Bode P., Ostriker J. P., Turok N., 2001, ApJ, 556, 93

Bonaca A., Hogg D. W., 2018, ApJ, 867, 101

Bonaca A., Geha M., Kallivayalil N., 2012, ApJ, 760, L6

Bonaca A., Geha M., Küpper A. H. W., Diemand J., Johnston K. V., Hogg D. W., 2014, ApJ, 795, 94

Bonaca A., Hogg D. W., Price-Whelan A. M., Conroy C., 2019, ApJ, 880, 38

Bonaca A., et al., 2021, ApJ, 909, L26

Bosma A., 1978, PhD thesis, University of Groningen, Netherlands

Bovy J., 2014, ApJ, 795, 95

Bovy J., 2015, ApJS, 216, 29

Bovy J., et al., 2012, ApJ, 759, 131

Bovy J., Bahmanyar A., Fritz T. K., Kallivayalil N., 2016, ApJ, 833, 31

Bovy J., Erkal D., Sanders J. L., 2017, MNRAS, 466, 628

Bowden A., Belokurov V., Evans N. W., 2015, MNRAS, 449, 1391

Boyarsky A., Ruchayskiy O., Iakubovskyi D., Franse J., 2014, Phys. Rev. Lett., 113, 251301

Bradač M., Allen S. W., Treu T., Ebeling H., Massey R., Morris R. G., von der Linden A., Applegate D., 2008, ApJ, 687, 959

Bradbury J., et al., 2018, JAX: composable transformations of Python+NumPy programs, http://github.com/google/jax

Bromm V., Larson R. B., 2004, ARA&A, 42, 79

Brownstein J. R., Moffat J. W., 2007, MNRAS, 382, 29

Buckley M. R., Peter A. H. G., 2018, Phys. Rep., 761, 1

Buist H. J. T., Helmi A., 2014, A&A, 563, A110

Buist H. J. T., Helmi A., 2015, A&A, 584, A120

Buist H. J. T., Helmi A., 2017, A&A, 601, A37

Bulbul E., Markevitch M., Foster A., Smith R. K., Loewenstein M., Randall S. W., 2014, ApJ, 789, 13

Bullock J. S., Boylan-Kolchin M., 2017, ARA&A, 55, 343

Cantat-Gaudin T., et al., 2020, A&A, 640, A1

Chakrabarti S., et al., 2020, ApJ, 902, L28

Chakrabarti S., Chang P., Lam M. T., Vigeland S. J., Quillen A. C., 2021, ApJ, 907, L26

Chandrasekhar S., 1943, Reviews of Modern Physics, 15, 1

Chiappini C., Matteucci F., Gratton R., 1997, ApJ, 477, 765

Choi J.-H., Weinberg M. D., Katz N., 2007, MNRAS, 381, 987

Choi J.-H., Weinberg M. D., Katz N., 2009, MNRAS, 400, 1247

Chua K. T. E., Pillepich A., Vogelsberger M., Hernquist L., 2019, MNRAS, 484, 476

Ciotti L., Binney J., 2004, MNRAS, 351, 285

Clarkson W., et al., 2008, ApJ, 684, 1110

Clowe D., Gonzalez A., Markevitch M., 2004, ApJ, 604, 596

Clowe D., Bradač M., Gonzalez A. H., Markevitch M., Randall S. W., Jones C., Zaritsky D., 2006, ApJ, 648, L109

Clutton-Brock M., 1972, Ap&SS, 16, 101

Clutton-Brock M., 1973, Ap&SS, 23, 55

Collette A., 2013, Python and HDF5. O'Reilly Media, Incorporated, https://books.google.co.uk/books?id=a_yXngEACAAJ

Conroy C., Naidu R. P., Garavito-Camargo N., Besla G., Zaritsky D., Bonaca A., Johnson B. D., 2021, Nature, 592, 534

Cramér H., 1946, Mathematical Methods of Statistics. Princeton University Press
Crnojević D., et al., 2016, ApJ, 823, 19
Cullinane L. R., Mackey A. D., Da Costa G. S., Erkal D., Koposov S. E., Belokurov V., 2022, MNRAS, 510, 445
Dai B., Robertson B. E., Madau P., 2018, ApJ, 858, 73
Dalcin L., Fang Y.-L. L., 2021, Computing in Science Engineering, 23, 47
Dark Energy Survey Collaboration 2016, MNRAS, 460, 1270
Davis M., Efstathiou G., Frenk C. S., White S. D. M., 1985, ApJ, 292, 371
De Leo M., Carrera R., Noël N. E. D., Read J. I., Erkal D., Gallart C., 2020, MNRAS, 495, 98
Deason A. J., Belokurov V., Evans N. W., An J., 2012, MNRAS, 424, L44
Debattista V. P., Roškar R., Valluri M., Quinn T., Moore B., Wadsley J., 2013, MNRAS, 434, 2971
de Boer T. J. L., Erkal D., Gieles M., 2020, MNRAS, 494, 5315
Dehnen W., Binney J., 1998, MNRAS, 294, 429
Dehnen W., Read J. I., 2011, European Physical Journal Plus, 126, 55
Dehnen W., Odenkirchen M., Grebel E. K., Rix H.-W., 2004, AJ, 127, 2753
Dennefeld M., 2020, The Messenger, 181, 37
Dey A., et al., 2019, AJ, 157, 168
Diemand J., Kuhlen M., Madau P., Zemp M., Moore B., Potter D., Stadel J., 2008, Nature, 454, 735
Dodelson S., 2011, International Journal of Modern Physics D, 20, 2749
Donaldson K., Petersen M. S., Peñarrubia J., 2022, MNRAS, 513, 46
Eadie G. M., Harris W. E., 2016, ApJ, 829, 108
Earn D. J. D., 1996, ApJ, 465, 91
Eckner C., Calore F., Erkal D., Lilleengen S., Petersen M. S., 2023, MNRAS, 518, 4138
Eddington A. S., 1916, MNRAS, 76, 572
Efstathiou G., 1992, MNRAS, 256, 43P
Eggen O. J., Lynden-Bell D., Sandage A. R., 1962, ApJ, 136, 748
Eilers A.-C., Hogg D. W., Rix H.-W., Ness M. K., 2019, ApJ, 871, 120
Einstein A., 1917, Sitzungsberichte der Königlich Preussischen Akademie der Wissenschaften, pp 142–152
Erkal D., Belokurov V. A., 2020, MNRAS, 495, 2554
Erkal D., Belokurov V., Bovy J., Sanders J. L., 2016, MNRAS, 463, 102
Erkal D., Koposov S. E., Belokurov V., 2017, MNRAS, 470, 60
Erkal D., et al., 2019, MNRAS, 487, 2685
Erkal D., Belokurov V. A., Parkin D. L., 2020, MNRAS, 498, 5574
Erkal D., et al., 2021, MNRAS, 506, 2677
Eskridge P. B., et al., 2000, AJ, 119, 536
Event Horizon Telescope Collaboration 2022, ApJ, 930, L12

Eyre A., Binney J., 2011, MNRAS, 413, 1852

Faber S. M., Gallagher J. S., 1979, Annual Review of Astronomy and Astrophysics, 17, 135

Famaey B., McGaugh S. S., 2012, Living Reviews in Relativity, 15, 10

Fardal M. A., Huang S., Weinberg M. D., 2015, MNRAS, 452, 301

Fellhauer M., et al., 2006, ApJ, 651, 167

Filipovic M. D., White G. L., Jones P. A., Haynes R. F., Pietsch W. N., Wielebinski R., Klein U., 1996, in Burkert A., Hartmann D. H., Majewski S. A., eds, Astronomical Society of the Pacific Conference Series Vol. 112, The History of the Milky Way and Its Satellite System. p. 91

Fisher R. A., 1925, Proceedings of the Cambridge Philosophical Society, 22, 700

Forbes D. A., et al., 2018, Proceedings of the Royal Society of London Series A, 474, 20170616

Foreman-Mackey D., 2016, The Journal of Open Source Software, 1, 24

Foreman-Mackey D., Hogg D. W., Lang D., Goodman J., 2013, PASP, 125, 306

Fragkoudi F., et al., 2020, MNRAS, 494, 5936

Fragkoudi F., Grand R. J. J., Pakmor R., Springel V., White S. D. M., Marinacci F., Gomez F. A., Navarro J. F., 2021, A&A, 650, L16

Frebel A., Norris J. E., 2015, ARA&A, 53, 631

Freeman K. C., 1970, ApJ, 160, 811

Freeman K., Bland-Hawthorn J., 2002, ARA&A, 40, 487

Frenk C. S., White S. D. M., Davis M., Efstathiou G., 1988, ApJ, 327, 507

Frieman J. A., Turner M. S., Huterer D., 2008, ARA&A, 46, 385

Frommert, H. and Kronberg, C. 2007, Abd-al-Rahman Al Sufi (December 7, 903 - May 25, 986 A.D.), http://www.messier.seds.org/xtra/Bios/alsufi.html

Furlanetto S. R., Loeb A., 2002, ApJ, 565, 854

Gaia Collaboration 2016, A&A, 595, A1

Gaia Collaboration 2018, A&A, 616, A1

Gaia Collaboration 2021a, A&A, 649, A1

Gaia Collaboration 2021b, A&A, 649, A9

Garavito-Camargo N., Besla G., Laporte C. F. P., Johnston K. V., Gómez F. A., Watkins L. L., 2019, ApJ, 884, 51

Garavito-Camargo N., Besla G., Laporte C. F. P., Price-Whelan A. M., Cunningham E. C., Johnston K. V., Weinberg M., Gómez F. A., 2021a, ApJ, 919, 109

Garavito-Camargo N., Patel E., Besla G., Price-Whelan A. M., Gómez F. A., Laporte C. F. P., Johnston K. V., 2021b, ApJ, 923, 140

Garrison-Kimmel S., et al., 2017, MNRAS, 471, 1709

Gaskins J. M., 2016, Contemporary Physics, 57, 496

Gatto A., Fraternali F., Read J. I., Marinacci F., Lux H., Walch S., 2013, MNRAS, 433, 2749

Genzel R., Eisenhauer F., Gillessen S., 2010, Reviews of Modern Physics, 82, 3121

Ghez A. M., et al., 2008, ApJ, 689, 1044

Gibbons S. L. J., Belokurov V., Evans N. W., 2014, MNRAS, 445, 3788

Gibbons S. L. J., Belokurov V., Evans N. W., 2017, MNRAS, 464, 794

Gieles M., Erkal D., Antonini F., Balbinot E., Peñarrubia J., 2021, Nature Astronomy, 5, 957

Gillessen S., et al., 2017, ApJ, 837, 30

Gómez F. A., Besla G., Carpintero D. D., Villalobos Á., O'Shea B. W., Bell E. F., 2015, ApJ, 802, 128

Grand R. J. J., et al., 2017, MNRAS, 467, 179

GRAVITY Collaboration 2018, A&A, 615, L15

GRAVITY Collaboration 2019, A&A, 625, L10

GRAVITY Collaboration 2020, A&A, 636, L5

Griewank A., Walther A., 2008, Evaluating Derivatives, second edn. Society for Industrial and Applied Mathematics (https://epubs.siam.org/doi/pdf/10.1137/1.9780898717761), doi:10.1137/1.9780898717761, https://epubs.siam.org/doi/abs/10.1137/1.9780898717761

Grillmair C. J., 2006, ApJ, 645, L37

Grillmair C. J., 2009, ApJ, 693, 1118

Grillmair C. J., Carlin J. L., 2016, in Newberg H. J., Carlin J. L., eds, Astrophysics and Space Science Library Vol. 420, Tidal Streams in the Local Group and Beyond. p. 87 (arXiv:1603.08936), doi:10.1007/978-3-319-19336-6_4

Grillmair C. J., Dionatos O., 2006, ApJ, 643, L17

Guedes J., Callegari S., Madau P., Mayer L., 2011, ApJ, 742, 76

Gunn J. E., Knapp G. R., Tremaine S. D., 1979, AJ, 84, 1181

Guth A. H., 1981, Phys. Rev. D, 23, 347

Han J. J., et al., 2022, ApJ, 934, 14

Harris W. E., 1996, AJ, 112, 1487

Harris C. R., et al., 2020, Nature, 585, 357

Hattori K., Erkal D., Sanders J. L., 2016, MNRAS, 460, 497

Haywood M., Di Matteo P., Lehnert M. D., Katz D., Gómez A., 2013, A&A, 560, A109

Haywood M., Di Matteo P., Lehnert M. D., Snaith O., Khoperskov S., Gómez A., 2018, ApJ, 863, 113

Helmi A., 2004, ApJ, 610, L97

Helmi A., White S. D. M., 1999, MNRAS, 307, 495

Helmi A., Babusiaux C., Koppelman H. H., Massari D., Veljanoski J., Brown A. G. A., 2018, Nature, 563, 85

Hendel D., et al., 2018, MNRAS, 479, 570

Hernquist L., 1990, ApJ, 356, 359

Hernquist L., Ostriker J. P., 1992, ApJ, 386, 375

Hernquist L., Katz N., Weinberg D. H., Miralda-Escudé J., 1996, ApJ, 457, L51

Herschel J., 1847, Results of Astronomical Observations Made During the Years 1834, 5, 6, 7, 8, at the Cape of Good Hope; Being the Completion of a Telescopic Survey of the Whole Surface of the Visible Heavens, Commenced in 1825. Smith, Elder and Company, https://books.google.com/books?id=El0y9Y8hCF4C

Hogg D. W., Foreman-Mackey D., 2018, ApJS, 236, 11

Hogg D. W., Bovy J., Lang D., 2010, arXiv e-prints, p. arXiv:1008.4686

Holl B., et al., 2018, A&A, 618, A30

Holley-Bockelmann K., Weinberg M., Katz N., 2005, MNRAS, 363, 991

Hopkins P. F., Kereš D., Oñorbe J., Faucher-Giguère C.-A., Quataert E., Murray N., Bullock J. S., 2014, MNRAS, 445, 581

Hu W., Barkana R., Gruzinov A., 2000, Phys. Rev. Lett., 85, 1158

Hubble E., 1929, Proceedings of the National Academy of Science, 15, 168

Hubble E., Humason M. L., 1931, ApJ, 74, 43

Hui L., Ostriker J. P., Tremaine S., Witten E., 2017, Phys. Rev. D, 95, 043541

Hunter J. D., 2007, Computing in Science & Engineering, 9, 90

Ibata R. A., Gilmore G., Irwin M. J., 1994, Nature, 370, 194

Ibata R., Irwin M., Lewis G., Ferguson A. M. N., Tanvir N., 2001, Nature, 412, 49

Ibata R. A., Lewis G. F., Irwin M. J., Quinn T., 2002, MNRAS, 332, 915

Ibata R. A., Malhan K., Martin N. F., 2019, ApJ, 872, 152

Ibata R., Bellazzini M., Thomas G., Malhan K., Martin N., Famaey B., Siebert A., 2020, ApJ, 891, L19

Ibata R., et al., 2021, ApJ, 914, 123

Iršič V., et al., 2017a, Phys. Rev. D, 96, 023522

Iršič V., Viel M., Haehnelt M. G., Bolton J. S., Becker G. D., 2017b, Phys. Rev. Lett., 119, 031302

Ivezić Ž., et al., 2019, ApJ, 873, 111

Jakob W., Rhinelander J., Moldovan D., 2017, pybind11 – Seamless operability between C++11 and Python

Jeans J. H., 1915, MNRAS, 76, 70

Jeans J. H., 1922, MNRAS, 82, 122

Jee M. J., Hughes J. P., Menanteau F., Sifón C., Mandelbaum R., Barrientos L. F., Infante L., Ng K. Y., 2014, ApJ, 785, 20

Jethwa P., Erkal D., Belokurov V., 2016, MNRAS, 461, 2212

Ji A. P., et al., 2021, ApJ, 921, 32

Johnson A. C., Petersen M. S., Johnston K. V., Weinberg M. D., 2023, MNRAS, 521, 1757

Johnston K. V., 1998, ApJ, 495, 297

Johnston K. V., 2016, in Newberg H. J., Carlin J. L., eds, Astrophysics and Space Science Library Vol. 420, Tidal Streams in the Local Group and Beyond. p. 141 (arXiv:1603.06601), doi:10.1007/978-3-319-19336-6_6

Johnston K. V., Carlberg R. G., 2016, in Newberg H. J., Carlin J. L., eds, Astrophysics and Space Science Library Vol. 420, Tidal Streams in the Local Group and Beyond.

p. 169 (arXiv:1603.06602), doi:10.1007/978-3-319-19336-6_7

Johnston K. V., Hernquist L., Bolte M., 1996, ApJ, 465, 278

Johnston K. V., Zhao H., Spergel D. N., Hernquist L., 1999, ApJ, 512, L109

Johnston K. V., Spergel D. N., Haydn C., 2002, ApJ, 570, 656

Johnston K. V., Law D. R., Majewski S. R., 2005, ApJ, 619, 800

Jungman G., Kamionkowski M., Griest K., 1996, Phys. Rep., 267, 195

Kahlhoefer F., 2017, International Journal of Modern Physics A, 32, 1730006

Kallivayalil N., van der Marel R. P., Alcock C., Axelrod T., Cook K. H., Drake A. J., Geha M., 2006, ApJ, 638, 772

Kallivayalil N., van der Marel R. P., Besla G., Anderson J., Alcock C., 2013, ApJ, 764, 161

Kallivayalil N., et al., 2018, ApJ, 867, 19

Kalnajs A. J., 1976, ApJ, 205, 745

Kanas N., 2012, Star Maps: History, Artistry, and Cartography (Second Edition)

Kaplinghat M., Tulin S., Yu H.-B., 2016, Phys. Rev. Lett., 116, 041302

Kerr F. J., 1957, AJ, 62, 93

King I., 1962, AJ, 67, 471

Klein A., et al., 2023, imageio, doi:10.5281/zenodo.1488561, https://doi.org/10.5281/zenodo.1488561

Kluyver T., et al., 2016, in Loizides F., Scmidt B., eds, Positioning and Power in Academic Publishing: Players, Agents and Agendas. IOS Press, Netherlands, pp 87–90, https://eprints.soton.ac.uk/403913/

Klypin A., Kravtsov A. V., Valenzuela O., Prada F., 1999, ApJ, 522, 82

Kolb E. W., Turner M. S., 1990, The early universe. Frontiers in Physics Vol. 69

Koposov S. E., Rix H.-W., Hogg D. W., 2010, ApJ, 712, 260

Koposov S. E., Irwin M., Belokurov V., Gonzalez-Solares E., Yoldas A. K., Lewis J., Metcalfe N., Shanks T., 2014, MNRAS, 442, L85

Koposov S. E., et al., 2019, MNRAS, 485, 4726

Koposov S. E., et al., 2023, MNRAS, 521, 4936

Kormendy J., Kennicutt Robert C. J., 2004, ARA&A, 42, 603

Küpper A. H. W., MacLeod A., Heggie D. C., 2008, MNRAS, 387, 1248

Küpper A. H. W., Kroupa P., Baumgardt H., Heggie D. C., 2010, MNRAS, 401, 105

Küpper A. H. W., Lane R. R., Heggie D. C., 2012, MNRAS, 420, 2700

Küpper A. H. W., Balbinot E., Bonaca A., Johnston K. V., Hogg D. W., Kroupa P., Santiago B. X., 2015, ApJ, 803, 80

Lancaster L., Giovanetti C., Mocz P., Kahn Y., Lisanti M., Spergel D. N., 2020, J. Cosmology Astropart. Phys., 2020, 001

Laporte C. F. P., Gómez F. A., Besla G., Johnston K. V., Garavito-Camargo N., 2018, MNRAS, 473, 1218

Laporte C. F. P., Minchev I., Johnston K. V., Gómez F. A., 2019, MNRAS, 485, 3134

Laureijs R., et al., 2011, arXiv e-prints, p. arXiv:1110.3193

Law D. R., Majewski S. R., 2010, ApJ, 714, 229

Law D. R., Johnston K. V., Majewski S. R., 2005, ApJ, 619, 807

Lee B. W., Weinberg S., 1977, Phys. Rev. Lett., 39, 165

Lemaître G., 1927, Annales de la Société Scientifique de Bruxelles, 47, 49

Li T. S., et al., 2019, MNRAS, 490, 3508

Li T. S., et al., 2021, ApJ, 911, 149

Li T. S., et al., 2022, ApJ, 928, 30

Liddle A. R., Lyth D. H., 2000, Cosmological Inflation and Large-Scale Structure

Lilleengen S., Trick W., van de Ven G., 2020, in Valluri M., Sellwood J. A., eds, Proceedings of the IAU Vol. 353, Galactic Dynamics in the Era of Large Surveys. pp 266–270 (arXiv:1909.04673), doi:10.1017/S1743921319008196

Lilleengen S., et al., 2023, MNRAS, 518, 774

Lilley E. J., van de Ven G., 2023, A&A, 672, A91

Lilley E. J., Evans N. W., Sanders J. L., 2018a, MNRAS, 476, 2086

Lilley E. J., Sanders J. L., Evans N. W., Erkal D., 2018b, MNRAS, 476, 2092

Lilley E. J., Sanders J. L., Evans N. W., 2018c, MNRAS, 478, 1281

Lovell M. R., Frenk C. S., Eke V. R., Jenkins A., Gao L., Theuns T., 2014, MNRAS, 439, 300

Lowing B., Jenkins A., Eke V., Frenk C., 2011, MNRAS, 416, 2697

Lynden-Bell D., 1962, MNRAS, 124, 1

Lynds R., 1971, ApJ, 164, L73

Majewski S. R., Skrutskie M. F., Weinberg M. D., Ostheimer J. C., 2003, ApJ, 599, 1082

Malhan K., Ibata R. A., 2018, MNRAS, 477, 4063

Malhan K., Ibata R. A., 2019, MNRAS, 486, 2995

Malhan K., Ibata R. A., Martin N. F., 2018, MNRAS, 481, 3442

Malhan K., Ibata R. A., Carlberg R. G., Valluri M., Freese K., 2019, ApJ, 881, 106

Malhan K., Valluri M., Freese K., 2021, MNRAS, 501, 179

Malhan K., et al., 2022a, ApJ, 926, 107

Malhan K., Valluri M., Freese K., Ibata R. A., 2022b, ApJ, 941, L38

Markevitch M., Gonzalez A. H., David L., Vikhlinin A., Murray S., Forman W., Jones C., Tucker W., 2002, ApJ, 567, L27

Markevitch M., Gonzalez A. H., Clowe D., Vikhlinin A., Forman W., Jones C., Murray S., Tucker W., 2004, ApJ, 606, 819

Martin N. F., et al., 2022, MNRAS, 516, 5331

Martínez-Delgado D., et al., 2010, AJ, 140, 962

Martínez-Delgado D., et al., 2012, ApJ, 748, L24

Martínez-Delgado D., D'Onghia E., Chonis T. S., Beaton R. L., Teuwen K., GaBany R. J., Grebel E. K., Morales G., 2015, AJ, 150, 116

Martínez-Delgado D., et al., 2023, A&A, 671, A141

Massari D., Koppelman H. H., Helmi A., 2019, A&A, 630, L4

Massey R., Kitching T., Richard J., 2010, Reports on Progress in Physics, 73, 086901

Mateo M. L., 1998, ARA&A, 36, 435

Mateu C., 2023, MNRAS, 520, 5225

McConnachie A. W., 2012, AJ, 144, 4

McKinney W., 2010, in van der Walt S., Millman J., eds, Proceedings of the 9th Python in Science Conference. pp 56 – 61, doi:10.25080/Majora-92bf1922-00a

McMillan P. J., 2017, MNRAS, 465, 76

McWilliam A., Zoccali M., 2010, ApJ, 724, 1491

Meiksin A. A., 2009, Reviews of Modern Physics, 81, 1405

Milgrom M., 1983, ApJ, 270, 365

Milgrom M., 2020, Studies in the History and Philosophy of Modern Physics, 71, 170

Miller M. J., Bregman J. N., 2015, ApJ, 800, 14

Miyamoto M., Nagai R., 1975, PASJ, 27, 533

Mocz P., et al., 2019, Phys. Rev. Lett., 123, 141301

Moore B., Ghigna S., Governato F., Lake G., Quinn T., Stadel J., Tozzi P., 1999, ApJ, 524, L19

Moster B. P., Naab T., White S. D. M., 2013, MNRAS, 428, 3121

Naab T., Ostriker J. P., 2017, ARA&A, 55, 59

Naidu R. P., Conroy C., Bonaca A., Johnson B. D., Ting Y.-S., Caldwell N., Zaritsky D., Cargile P. A., 2020, ApJ, 901, 48

Nataf D. M., Udalski A., Gould A., Fouqué P., Stanek K. Z., 2010, ApJ, 721, L28

Natarajan P., Zhao H., 2008, MNRAS, 389, 250

Navarro J. F., Frenk C. S., White S. D. M., 1996, ApJ, 462, 563

Navarro J. F., Frenk C. S., White S. D. M., 1997, ApJ, 490, 493

Neumayer N., Seth A., Böker T., 2020, A&ARv, 28, 4

Newberg H. J., et al., 2002, ApJ, 569, 245

Newberg H. J., Yanny B., Willett B. A., 2009, ApJ, 700, L61

Newberg H. J., Willett B. A., Yanny B., Xu Y., 2010, ApJ, 711, 32

Ngan W., Bozek B., Carlberg R. G., Wyse R. F. G., Szalay A. S., Madau P., 2015, ApJ, 803, 75

Ngan W., Carlberg R. G., Bozek B., Wyse R. F. G., Szalay A. S., Madau P., 2016, ApJ, 818, 194

Nibauer J., Belokurov V., Cranmer M., Goodman J., Ho S., 2022, ApJ, 940, 22

Nibauer J., Bonaca A., Johnston K. V., 2023, arXiv e-prints, p. arXiv:2303.17406

Niederste-Ostholt M., Belokurov V., Evans N. W., 2012, MNRAS, 422, 207

Nipoti C., Ciotti L., Binney J., Londrillo P., 2008, MNRAS, 386, 2194

Odenkirchen M., et al., 2001, ApJ, 548, L165

Ortolani S., Renzini A., Gilmozzi R., Marconi G., Barbuy B., Bica E., Rich R. M., 1995, Nature, 377, 701

Pace A. B., Erkal D., Li T. S., 2022, ApJ, 940, 136

Panithanpaisal N., Sanderson R. E., Wetzel A., Cunningham E. C., Bailin J., Faucher-Giguère C.-A., 2021, ApJ, 920, 10

Patel E., et al., 2020, ApJ, 893, 121

Peñarrubia J., Belokurov V., Evans N. W., Martínez-Delgado D., Gilmore G., Irwin M., Niederste-Ostholt M., Zucker D. B., 2010, MNRAS, 408, L26

Peñarrubia J., Gómez F. A., Besla G., Erkal D., Ma Y.-Z., 2016, MNRAS, 456, L54

Pearson S., Price-Whelan A. M., Johnston K. V., 2017, Nature Astronomy, 1, 633

Pearson S., Clark S. E., Demirjian A. J., Johnston K. V., Ness M. K., Starkenburg T. K., Williams B. F., Ibata R. A., 2022a, ApJ, 926, 166

Pearson S., Price-Whelan A. M., Hogg D. W., Seth A. C., Sand D. J., Hunt J. A. S., Crnojević D., 2022b, ApJ, 941, 19

Pease F. G., 1918, Proceedings of the National Academy of Science, 4, 21

Peccei R. D., Quinn H. R., 1977, Phys. Rev. Lett., 38, 1440

Peebles P. J. E., 1982, ApJ, 263, L1

Peebles P. J., Ratra B., 2003, Reviews of Modern Physics, 75, 559

Pérez F., Granger B. E., 2007, Computing in Science and Engineering, 9, 21

Perlmutter S., et al., 1999, ApJ, 517, 565

Petersen M. S., Peñarrubia J., 2020, MNRAS, 494, L11

Petersen M. S., Peñarrubia J., 2021, Nature Astronomy, 5, 251

Petersen M. S., Weinberg M. D., Katz N., 2016, MNRAS, 463, 1952

Petersen M. S., Weinberg M. D., Katz N., 2019, MNRAS, 490, 3616

Petersen M. S., Weinberg M. D., Katz N., 2021, MNRAS, 500, 838

Petersen M. S., Weinberg M. D., Katz N., 2022a, MNRAS, 510, 6201

Petersen M. S., Peñarrubia J., Jones E., 2022b, MNRAS, 514, 1266

Pietrzyński G., et al., 2019, Nature, 567, 200–203

Pigafetta A., 1522, Journal of Magellan's voyage. https://www.loc.gov/item/2021667606

Pillepich A., Kuhlen M., Guedes J., Madau P., 2014, ApJ, 784, 161

Planck Collaboration 2016, A&A, 594, A13

Planck Collaboration 2020, A&A, 641, A6

Plummer H. C., 1911, MNRAS, 71, 460

Posti L., Helmi A., 2019, A&A, 621, A56

Pozo Menares G., Canio Llanquinao M., 2014, Wenumapu. Astronomía y cosmología mapuche, first edn. Ocho Libros Editores, https://biblioquinoa.com/libros/MM0090/wenumapu-astronomia-y-cosmologia-mapuche/

Press W. H., Schechter P., 1974, ApJ, 187, 425

Price-Whelan A. M., 2017, The Journal of Open Source Software, 2

Price-Whelan A. M., Bonaca A., 2018, ApJ, 863, L20

Price-Whelan A. M., Foreman-Mackey D., 2017, The Journal of Open Source Software, 2

Price-Whelan A. M., Hogg D. W., Johnston K. V., Hendel D., 2014, ApJ, 794, 4

Price-Whelan A. M., Johnston K. V., Valluri M., Pearson S., Küpper A. H. W., Hogg D. W., 2016a, MNRAS, 455, 1079

Price-Whelan A. M., Sesar B., Johnston K. V., Rix H.-W., 2016b, ApJ, 824, 104

Price-Whelan A., et al., 2022, adrn/gala: v1.6.1, doi:10.5281/zenodo.7299506, https://doi.org/10.5281/zenodo.7299506

Quercellini C., Amendola L., Balbi A., 2008, MNRAS, 391, 1308

Ramos P., Mateu C., Antoja T., Helmi A., Castro-Ginard A., Balbinot E., Carrasco J. M., 2020, A&A, 638, A104

Ramos P., et al., 2022, A&A, 666, A64

Randall S. W., Markevitch M., Clowe D., Gonzalez A. H., Bradač M., 2008, ApJ, 679, 1173

Rao C. R., 1945, Bulletin of Calcutta Mathematical Society, 37, 81–89

Read J. I., 2014, Journal of Physics G Nuclear Physics, 41, 063101

Reback J., et al., 2020, pandas-dev/pandas: Pandas 1.0.3, doi:10.5281/zenodo.3715232

Reid M. J., Brunthaler A., 2004, ApJ, 616, 872

Reino S., Rossi E. M., Sanderson R. E., Sellentin E., Helmi A., Koppelman H. H., Sharma S., 2021, MNRAS, 502, 4170

Reino S., Sanderson R. E., Panithanpaisal N., Rossi E. M., Kuijken K., 2022, MNRAS, 509, 5365

Remmen G. N., Carroll S. M., 2014, Phys. Rev. D, 90, 063517

Riess A. G., et al., 1998, AJ, 116, 1009

Rimoldini L., et al., 2019, A&A, 625, A97

Roberts M. S., 1966, ApJ, 144, 639

Roberts M. S., Rots A. H., 1973, A&A, 26, 483

Robertson A., Massey R., Eke V., 2017, MNRAS, 465, 569

Robles V. H., et al., 2017, MNRAS, 472, 2945

Rocha M., Peter A. H. G., Bullock J. S., Kaplinghat M., Garrison-Kimmel S., Oñorbe J., Moustakas L. A., 2013, MNRAS, 430, 81

Rockosi C. M., et al., 2002, AJ, 124, 349

Rogstad D. H., Shostak G. S., 1972, ApJ, 176, 315

Rozier S., Famaey B., Siebert A., Monari G., Pichon C., Ibata R., 2022, ApJ, 933, 113

Rubin V. C., 2004, in , The Dark Universe. p. 1

Rubin V. C., Ford W. Kent J., 1970, ApJ, 159, 379

Rubin V. C., Ford W. K. J., Thonnard N., 1978, ApJ, 225, L107

Ruiz-Lara T., Gallart C., Bernard E. J., Cassisi S., 2020, Nature Astronomy, 4, 965

Saha P., 1993, MNRAS, 262, 1062

Sanders R. H., 2003, MNRAS, 342, 901

Sanders J. L., 2014, MNRAS, 443, 423
Sanders J. L., Binney J., 2013a, MNRAS, 433, 1813
Sanders J. L., Binney J., 2013b, MNRAS, 433, 1826
Sanders J. L., Binney J., 2015a, MNRAS, 447, 2479
Sanders J. L., Binney J., 2015b, MNRAS, 449, 3479
Sanders J. L., Binney J., 2016, MNRAS, 457, 2107
Sanders J. L., Lilley E. J., Vasiliev E., Evans N. W., Erkal D., 2020, MNRAS, 499, 4793
Sanderson R. E., Helmi A., Hogg D. W., 2015, ApJ, 801, 98
Sawala T., et al., 2015, MNRAS, 448, 2941
Sawala T., et al., 2016, MNRAS, 457, 1931
Schaye J., et al., 2015, MNRAS, 446, 521
Schee J., Stuchlík Z., Petrásek M., 2013, J. Cosmology Astropart. Phys., 2013, 026
Schive H.-Y., Chiueh T., Broadhurst T., 2014, Nature Physics, 10, 496
Schneider P., Ehlers J., Falco E. E., 1992, Gravitational Lenses, doi:10.1007/978-3-662-03758-4.
Schönrich R., Dehnen W., 2018, MNRAS, 478, 3809
Schönrich R., Binney J., Dehnen W., 2010, MNRAS, 403, 1829
Sesar B., et al., 2017, AJ, 153, 204
Shao S., Cautun M., Deason A., Frenk C. S., 2021, MNRAS, 504, 6033
Shih D., Buckley M. R., Necib L., Tamanas J., 2022, MNRAS, 509, 5992
Shih D., Buckley M. R., Necib L., 2023, arXiv e-prints, p. arXiv:2303.01529
Shipp N., et al., 2018, ApJ, 862, 114
Shipp N., et al., 2019, ApJ, 885, 3
Shipp N., et al., 2021, ApJ, 923, 149
Shipp N., et al., 2022, arXiv e-prints, p. arXiv:2208.02255
Sikivie P., 2008, in Kuster M., Raffelt G., Beltrán B., eds, , Axions: Theory, Cosmology, and Experimental Searches. Springer Berlin Heidelberg, Berlin, Heidelberg, pp 19–50, doi:10.1007/978-3-540-73518-2_2, https://doi.org/10.1007/978-3-540-73518-2_2
Silverwood H., Easther R., 2019, Publ. Astron. Soc. Australia, 36, e038
Simion I. T., Belokurov V., Irwin M., Koposov S. E., 2014, MNRAS, 440, 161
Simon J. D., Geha M., 2007, ApJ, 670, 313
Simon J. D., et al., 2020, ApJ, 892, 137
Skordis C., Złośnik T., 2021, Phys. Rev. Lett., 127, 161302
Smith S., 1936, ApJ, 83, 23
Smith-Orlik A., et al., 2023, arXiv e-prints, p. arXiv:2302.04281
Somerville R. S., Davé R., 2015, ARA&A, 53, 51
Spergel D. N., Steinhardt P. J., 2000, Phys. Rev. Lett., 84, 3760
Spergel D., et al., 2013, arXiv e-prints, p. arXiv:1305.5422
Spitoni E., Silva Aguirre V., Matteucci F., Calura F., Grisoni V., 2019, A&A, 623, A60

Springel V., 2005, MNRAS, 364, 1105
Springel V., et al., 2005, Nature, 435, 629
Springel V., et al., 2008, MNRAS, 391, 1685
The Astropy Collaboration 2013, A&A, 558, A33
The Astropy Collaboration 2018, AJ, 156, 123
The Astropy Collaboration 2022, ApJ, 935, 167
Torrealba G., et al., 2019, MNRAS, 488, 2743
Tremaine S., 1999, MNRAS, 307, 877
Trick W. H., Coronado J., Rix H.-W., 2019, MNRAS, 484, 3291
Tulin S., Yu H.-B., 2018, Phys. Rep., 730, 1
Valluri M., Price-Whelan A. M., Snyder S. J., 2021, ApJ, 910, 150
van der Marel R. P., Alves D. R., Hardy E., Suntzeff N. B., 2002, AJ, 124, 2639
van der Marel R. P., Kallivayalil N., 2014, ApJ, 781, 121
van de Hulst H. C., Muller C. A., Oort J. H., 1954, Bull. Astron. Inst. Netherlands, 12, 117
Vasiliev E., 2019, MNRAS, 482, 1525
Vasiliev E., 2023, Galaxies, 11, 59
Vasiliev E., Baumgardt H., 2021, MNRAS, 505, 5978
Vasiliev E., Belokurov V., Erkal D., 2021, MNRAS, 501, 2279
Vegetti S., Koopmans L. V. E., Bolton A., Treu T., Gavazzi R., 2010, MNRAS, 408, 1969
Vera-Ciro C., Helmi A., 2013, ApJ, 773, L4
Virtanen P., et al., 2020, Nature Methods, 17, 261
Vivas A. K., et al., 2001, ApJ, 554, L33
Vogelsberger M., et al., 2014, MNRAS, 444, 1518
Vogelsberger M., Marinacci F., Torrey P., Puchwein E., 2020, Nature Reviews Physics, 2, 42
von Humboldt A., 1852, Cosmos: A sketch of a physical description of the Universe (Volume 4)
Wang L., Spurzem R., Aarseth S., Nitadori K., Berczik P., Kouwenhoven M. B. N., Naab T., 2015, MNRAS, 450, 4070
Wang W., Han J., Cautun M., Li Z., Ishigaki M. N., 2020a, Science China Physics, Mechanics, and Astronomy, 63, 109801
Wang J., Bose S., Frenk C. S., Gao L., Jenkins A., Springel V., White S. D. M., 2020b, Nature, 585, 39
Watkins L. L., Evans N. W., An J. H., 2010, MNRAS, 406, 264
Watkins L. L., van der Marel R. P., Sohn S. T., Evans N. W., 2019, ApJ, 873, 118
Wegg C., Gerhard O., 2013, MNRAS, 435, 1874
Weinberg M. D., 1989, MNRAS, 239, 549
Weinberg M. D., 1994, ApJ, 421, 481
Weinberg M. D., 1996, ApJ, 470, 715

Weinberg M. D., 1998, MNRAS, 299, 499
Weinberg M. D., 1999, AJ, 117, 629
Weinberg M. D., Katz N., 2002, ApJ, 580, 627
Weinberg M. D., Katz N., 2007a, MNRAS, 375, 425
Weinberg M. D., Katz N., 2007b, MNRAS, 375, 460
Weinberg M. D., Petersen M. S., 2021, MNRAS, 501, 5408
Wetzel A. R., Hopkins P. F., Kim J.-h., Faucher-Giguère C.-A., Kereš D., Quataert E., 2016, ApJ, 827, L23
White S. D. M., 1976, MNRAS, 177, 717
White S. D. M., Rees M. J., 1978, MNRAS, 183, 341
Wilkinson M. I., Evans N. W., 1999, MNRAS, 310, 645
Wu X., Famaey B., Gentile G., Perets H., Zhao H., 2008, MNRAS, 386, 2199
Xiang M., Rix H.-W., 2022, Nature, 603, 599
Xue X.-X., Rix H.-W., Ma Z., Morrison H., Bovy J., Sesar B., Janesh W., 2015, ApJ, 809, 144
Yanny B., et al., 2009, ApJ, 700, 1282
Yoachim P., Dalcanton J. J., 2006, AJ, 131, 226
York D. G., et al., 2000, AJ, 120, 1579
Yuan Z., Chang J., Beers T. C., Huang Y., 2020, ApJ, 898, L37
Yuan Z., et al., 2022, ApJ, 930, 103
Zavala J., Frenk C. S., 2019, Galaxies, 7, 81
Zwicky F., 1933a, Helvetica Physica Acta, 6, 110
Zwicky F., 1933b, Physical Review, 43, 147
Zwicky F., 1937, ApJ, 86, 217

COLOPHON

This document was typeset using the typographical look-and-feel `classicthesis` developed by André Miede. The style was inspired by Robert Bringhurst's seminal book on typography *"The Elements of Typographic Style"*. `classicthesis` is available for both LaTeX and LyX:

https://bitbucket.org/amiede/classicthesis/

Final Version as of 12 July 2023.